Fall 2016

Flexible multibody dynamics approach for tire dynamics simulation

Hiroki Yamashita
University of Iowa

Recommended Citation

Yamashita, Hiroki. "Flexible multibody dynamics approach for tire dynamics simulation." PhD (Doctor of Philosophy) thesis, University of Iowa, 2016.
https://doi.org/10.17077/etd.gfixb2od

Follow this and additional works at: https://ir.uiowa.edu/etd
Part of the Mechanical Engineering Commons

FLEXIBLE MULTIBODY DYNAMICS APPROACH FOR TIRE DYNAMICS SIMULATION

by

Hiroki Yamashita

A thesis submitted in partial fulfillment
of the requirements for the Doctor of
Philosophy degree in Mechanical Engineering
in the Graduate College of
The University of Iowa

December 2016

Thesis Supervisor: Associate Professor Hiroyuki Sugiyama

Graduate College
The University of Iowa
Iowa City, Iowa

CERTIFICATE OF APPROVAL

PH.D. THESIS

This is to certify that the Ph.D. thesis of

Hiroki Yamashita

has been approved by the Examining Committee
for the thesis requirement for the Doctor of Philosophy
degree in Mechanical Engineering at the December 2016 graduation.

Thesis Committee:

Hiroyuki Sugiyama, Thesis Supervisor

Kyung K. Choi

Paramsothy Jayakumar

Jia Lu

Shaoping Xiao

ACKNOWLEDGMENTS

I would like to express my deepest gratitude to my advisor Professor Hiroyuki Sugiyama for giving me not only invaluable guidance on my PhD research, but also continuous support for my study at the University of Iowa. I could not have kept pursuing my PhD research without his support. I would also like to thank Dr. Paramsothy Jayakumar from US Army TARDEC for providing me with constructive suggestions and various advice to my research. I would also like to thank Dr. Ryoji Hanada from Yokohama Rubber Co., Ltd. for giving me invaluable technical advice on developing the high-fidelity tire model. I would like to thank Professors Kyung K. Choi, Jia Lu, and Shaoping Xiao for serving on my thesis defense committee. I wish to thank all my friends and colleagues who have encouraged me and provided insight into my research. In particular, I would like to thank my labmates, Huaxia Lee, Chris Feldmeier, Bryan Peterson, and Xiangkang Chen.

This research was supported by the Automotive Research Center (ARC) in accordance with Cooperative Agreement W56HZV-04-2-0001 U.S. Army Tank Automotive Research, Development and Engineering Center (TARDEC) and Yokohama Rubber Co., Ltd. These financial supports are greatly acknowledged.

ABSTRACT

The objective of this study is to develop a high-fidelity physics-based flexible tire model that can be fully integrated into multibody dynamics computer algorithms for use in on-road and off-road vehicle dynamics simulation without ad-hoc co-simulation techniques. Despite the fact detailed finite element tire models using explicit finite element software have been widely utilized for structural design of tires by tire manufactures, it is recognized in the tire industry that existing state-of-the-art explicit finite element tire models are not capable of predicting the transient tire force characteristics accurately under severe vehicle maneuvering conditions due to the numerical instability that is essentially inevitable for explicit finite element procedures for severe loading scenarios and the lack of transient (dynamic) tire friction model suited for FE tire models. Furthermore, to integrate the deformable tire models into multibody full vehicle simulation, co-simulation technique could be an option for commercial software. However, there exist various challenges in co-simulation for the transient vehicle maneuvering simulation in terms of numerical stability and computational efficiency. The transient tire dynamics involves rapid changes in contact forces due to the abrupt braking and steering input, thus use of co-simulation requires very small step size to ensure the numerical stability and energy balance between two separate simulation using different solvers.

In order to address these essential and challenging issues on the high-fidelity flexible tire model suited for multibody vehicle dynamics simulation, a physics-based tire model using the flexible multibody dynamics approach is proposed in this study. To this end, a continuum mechanics based shear deformable laminated composite shell element is developed based on the finite element absolute nodal coordinate formulation for modeling the complex fiber reinforced rubber tire structure. The assumed natural strain (ANS) and enhanced assumed strain (EAS) approaches are introduced for alleviating element lockings exhibited in the element. Use of the concept of the absolute nodal coordinate formulation leads to various advantages for tire dynamics simulation in that (1) constant mass matrix can be obtained for fully nonlinear dynamics simulation; (2) exact modeling of rigid body motion is ensured when strains are zero; and (3) non-

incremental solution procedure utilized in the general multibody dynamics computer algorithm can be directly applied without specialized updating schemes for finite rotations. Using the proposed shear deformable laminated composite shell element, a physics-based flexible tire model is developed. To account for the transient tire friction characteristics including the friction-induced hysteresis that appears in severe maneuvering conditions, the distributed parameter LuGre tire friction model is integrated into the flexible tire model. To this end, the contact patch predicted by the structural tire model is discretized into small strips across the tire width, and then each strip is further discretized into small elements to convert the partial differential equations of the LuGre tire friction model to the set of first-order ordinary differential equations. By doing so, the structural deformation of the flexible tire model and the LuGre tire friction force model are dynamically coupled in the final form of the equations, and these equations are integrated simultaneously forward in time at every time step.

Furthermore, a systematic and automated procedure for parameter identification of LuGre tire friction model is developed. Since several fitting parameters are introduced to account for the nonlinear friction characteristics, the correlation of the model parameters with physical quantities are not clear, making the parameter identification of the LuGre tire friction model difficult. In the procedure developed in this study, friction parameters in terms of slip-dependent friction characteristics and adhesion parameter are estimated separately, and then all the parameters are identified using the nonlinear least squares fitting. Furthermore, the modified friction characteristic curve function is proposed for wet road conditions, in which the linear decay in friction is exhibited in the large slip velocity range. It is shown that use of the proposed numerical procedure leads to an accurate prediction of the LuGre model parameters for measured tire force characteristics under various loading and speed conditions. Furthermore, the fundamental tire properties including the load-deflection curve, the contact patch lengths, contact pressure distributions, and natural frequencies are validated against the test data. Several numerical examples for hard braking and cornering simulation are presented to demonstrate capabilities of the physics-based flexible tire model developed in this study.

Finally, the physics-based flexible tire model is further extended for application to off-road mobility simulation. To this end, a locking-free 9-node brick element with the

curvature coordinates at the center node is developed and justified for use in modeling a continuum soil with the capped Drucker-Prager failure criterion. Multiplicative finite strain plasticity theory is utilized to consider the large soil deformation exhibited in the tire/soil interaction simulation. In order to identify soil parameters including cohesion and friction angle, the triaxial soil test is conducted. Using the soil parameters identified including the plastic hardening parameters by the compression soil test, the continuum soil model developed is validated against the test data. Use of the high-fidelity physics-based tire/soil simulation model in off-road mobility simulation, however, leads to a very large computational model to consider a wide area of terrains. Thus, the computational cost dramatically increases as the size of the soil model increases. To address this issue, the component soil model is proposed such that soil elements far behind the tire can be removed from the equations of motion sequentially, and then new soil elements are added to the portion that the tire is heading to. That is, the soil behavior only in the vicinity of the rolling tire is solved in order to reduce the overall model dimensionality associated with the finite element soil model. It is shown that use of the component soil model leads to a significant reduction in computational time while ensuring the accuracy, making the use of the physics-based deformable tire/soil simulation capability feasible in off-road mobility simulation.

PUBLIC ABSTRACT

This study aims to develop a high-fidelity physics-based tire model that can be fully integrated into multibody dynamics computer algorithms for the transient on-road and off-road vehicle dynamics simulation. Due to the essential difference in formulations and solution procedures traditionally used in multibody dynamics and classical finite element approaches, integration of existing finite element tire models into multibody vehicle dynamics simulation is not straightforward and requires special treatments including co-simulation techniques.

In the tire model proposed in this study, the detailed tire structure considering the fiber-reinforced rubber material is modeled by the shear deformable laminated composite shell element using the flexible multibody dynamics approach. To account for the dynamic coupling of the structural tire deformation and the transient tire friction behavior, spatially discretized LuGre tire friction model is integrated into the flexible tire model. The tire model developed is validated against the test data, and numerical examples are presented in order to demonstrate the use of the flexible tire model for the transient braking and cornering analysis. The tire model is further extended for application to off-road mobility simulation. The continuum soil model using the capped Drucker-Prager failure criterion based on the multiplicative plasticity theory is developed and validated against the triaxial soil test data. To reduce the computational time, the soil behavior only in the vicinity of the rolling tire is solved and the moving soil patch is updated sequentially. This allows for the use of the physics-based deformable tire/soil simulation capability feasible for off-road mobility simulation.

TABLE OF CONTENTS

LIST OF TABLES

LIST OF FIGURES

CHAPTER 1
INTRODUCTION

This study is aimed to develop a high-fidelity physics-based tire model that can be fully integrated into multibody dynamics computer algorithms for the transient on-road and off-road vehicle dynamics simulation. While detailed finite element tire models using explicit finite element software have been widely used for structural design of tires by tire manufactures, they are not suited for the analysis of transient tire dynamics under severe vehicle maneuvers, in which the transient tire force characteristics and the interaction with deformable terrains for off-road vehicles play a crucial role in predicting the overall vehicle performance. Furthermore, due to the essential difference in formulations and solution procedures traditionally used in multibody dynamics and classical finite element approaches, integration of existing finite element tire models into multibody vehicle dynamics simulation is not straightforward and requires special treatments including a reliance on co-simulation techniques. Use of the co-simulation, however, leads to very small step size to ensure the numerical stability and energy balance between two separate simulation (i.e., finite element tire simulation and multibody vehicle simulation) in severe vehicle maneuvering conditions. In the tire model proposed in this study, the detailed tire structure consisting of the fiber-reinforced rubber material is modeled by the shear deformable laminated composite shell element based on the absolute nodal coordinate formulation developed in this study. The shell element developed allows for the use of non-incremental solution procedures suited for general multibody dynamics computer algorithms. Furthermore, to account for the transient tire friction characteristics including the friction-induced hysteresis that appears in severe braking and cornering conditions, the distributed parameter LuGre tire friction model is integrated into the flexible tire model. By doing so, the structural deformation of the flexible tire model and the LuGre tire friction force model are dynamically coupled in the final form of the equations. Furthermore, using the tire model based on the flexible multibody dynamics approach, a physics-based tire/soil interaction simulation capability is developed for prediction of off-road mobility in various terrain condition without resorting to ad-hoc co-simulation procedures.

1.1 Background and Motivation

1.1.1 Tire Dynamics Simulation

Tire models play an essential role in virtual prototyping of ground vehicles and they are classified according to the frequency range to be considered in the analysis [1]. The rigid ring tire model accounts for the frequency range up to approximately 80 Hz associated with the tire sidewall stiffness, while the tire belt flexibility is assumed to be negligible [2]. Because of the rigid tire belt assumption, the contact pressure distribution is assumed by a prescribed function, preventing the consideration of the dynamic change in the contact pressure distribution in the analysis. To account for more detailed deformation modes of the complex tire structure, high-fidelity finite-element (FE) tire models are constructed and used for design and analysis of tires [3,4]. In particular, an accurate modeling of the complex tire geometry and the anisotropic material properties of the tire structure is essential to the tire performance evaluation including the tire contact pressure and the braking/traction and cornering forces. Since a tire consists of layers of plies and steel belts embedded in rubber, the tire structure needs to be modeled by cord-rubber composite materials and various fiber-reinforced rubber material models are proposed for use in detailed finite element tire models. Since Young's modulus of the steel cord is significantly higher than that of the rubber material, mechanical property of the fiber-reinforced rubber is highly nonlinear [5]. Furthermore, the tire cross-section geometry and stiffness distribution are of significant importance in characterizing the normal contact pressure distribution, and the in-plane shear deformation of the carcass contributes to the cornering stiffness of tires. For this reason, high-fidelity finite element tire models that account for the tire geometric and material nonlinearities have been developed and used extensively in automotive and aerospace industry [6-9]. It is, however, known that these computational tire models encounter difficulties in predicting the transient tire force characteristics under severe vehicle maneuvering conditions such as braking with antilock braking control due to the numerical instability that could occur in the time-domain analysis and the lack of transient tire friction model fully integrated into finite element tire models. In such transient vehicle maneuvering conditions, structural tire deformation due to the large load transfer causes an abrupt change in normal contact pressure and slip distribution in the contact patch, and it has a dominant effect on characterizing the transient braking and cornering forces including the history-dependent friction-induced hysteresis effect. Furthermore, co-simulation techniques, which are widely used to incorporate finite element tire models into multibody vehicle simulation, could require very small step size to ensure the numerical stability in the severe transient tire dynamics simulation, involving rapid changes in normal and tangential contact forces due to the abrupt braking and steering input.

To overcome these fundamental and essential issues in the tire dynamics simulation, various types of flexible tire models have been proposed for use in vehicle dynamics simulation. Among others, FTire [10], CDTire [11], RMOD-K [12] are widely used and they have an interface to various multibody dynamics software. In the FTire model, the flexible belt is modeled using a large number of rigid segments that are connected together by springs and dampers. Such a modeling procedure for a flexible body is often called finite segment method in multibody dynamics community [13]. 80-200 segments are usually used for the discretization of a flexible belt [10], and this leads to a large number of degrees of freedom even for a single tire modeling. CDTire and RMOD-K tire models, on the other hand, use a finite element description for modeling the tire structure and these models are integrated into vehicle dynamics simulation framework via co-simulation techniques. Recently, a shell element based tire model was proposed by Roller, et al. using the geometrically exact shell formulation with inextensible directors for multibody vehicle dynamics simulation [14,15]. The inextensibility conditions of the directors are imposed on the nodal points to ensure zero through-thickness strain by introducing constraint equations, and the unilateral frictional contact model is employed in the contact patch [15].

1.1.2 Off-Road Mobility Simulation

The vehicle-terrain interaction model is essential to demonstrate vehicle mobility capability on deformable terrains in various scenarios, and the overall vehicle performance on sand and rough dirt roads needs to be carefully evaluated at various design stages, including drawbar pull, tire sinkage, and rolling resistance. Over the past decades, empirical models, analytical models based on terramechanics [16,17], and numerical simulation models using finite element and discrete element methods [18-26] have been proposed and utilized for modeling the vehicle and deformable terrain interaction. Empirical terramechanics models, for which model parameters are based on experimental results such as the cone index to characterize the soil properties, allows for a quick prediction of off-road mobility performance. Among others, a NATO Reference Mobility Model (NRMM) has been used for various military scenarios. Analytical and semi-empirical models, on the other hand, were developed by Bekker [16] and Wong [17] to better understand the tire/soil interaction mechanics and the principles behind, and those models are developed based on terramechanics theories. However, it is known that empirical and analytical terramechanics models do not capture many of the soil deformation modes that can be captured by numerical models [18].

For this reason, physics-based numerical models have been utilized to understand more details on the tire soil interaction behavior quantitatively and many different models with different level of fidelity have been proposed. The high-fidelity computational soil models are classified into continuum-based finite element (FE) models and discrete element (DE) models. In the finite element soil model, a soil is assumed to be ideal continuum and the soil behavior is modeled by the elasto-plasticity model such as Mohr-Coulomb or capped Drucker-Prager models. The contact between deformable tires and soil models is defined on continuous surfaces and, therefore, the normal and tangential contact forces can be modeled accurately using computational contact mechanics theories [19]. Shoop [20] developed the computational model for predicting the vehicle mobility on snow using the standard finite element approach, and the results were validated against the test data. Xia, et al. used the tire/soil interaction model to predict the soil compaction using finite element models [19]. Furthermore, to circumvent the fine mesh due to the large element distortion in the Lagrangian approach, Arbitrary Lagrangian Eulerian (ALE) approach is applied to the tire/soil interaction model [21], where the wheel is formulated in the Lagrangian description, while the soil is formulated in the Eulerian description to allow for relatively coarse mesh for soil. On the other hand, a discrete element method (DEM) has been also investigated extensively using high-performance computing (HPC) techniques. In the DEM, soil is modeled by many particles contacting each other. The contact between particles is modeled by either the penalty approach [22] or constraint approach [23]. Use of the penalty approach introduces high frequencies to the equations of motion due to the multiple elastic impacts of particles, requiring small stepsize in the time integration. On the other hand, rigid contact is assumed between particles in the constraint contact approach, allowing for large stepsize in the time integration due to the elimination of high frequencies arising from impacts of particles. This approach, however, requires more computationally intensive solution procedures to solve nonlinear complementary contact problems, and use of GPU computing has been investigated in the context of multibody dynamics problem in the literature [23,24]. A rigid tire model is integrated into the DEM computational framework in a straightforward manner since all the bodies (particles) are rigid [22,23]. Integration of DEM approach with a finite element flexible tire model requires addressing a challenging numerical issue. This is due to the fact that implicit time integrators are suited for the finite element equations (FE tire models), while the discrete element equations can be solved efficiently by an explicit time integration. Nakashima et al. developed the two-dimensional coupled discrete and finite element tire/soil contact model [25]. In addition, smooth particle hydrodynamics (SPH) method, which is a meshless approach, is applied to model large soil deformation together with the finite element tire model [26]. Most existing approaches rely on co-simulation techniques which could lead to computationally intensive procedures to ensure the accuracy and numerical stability. For this reason, a new high-fidelity physics-based tire/soil interaction simulation capability that can be fully integrated into multibody dynamics computer algorithms are pursued in this study without ad-hoc co-simulation techniques.

1.1.3 Needs for Flexible Multibody Dynamics Approach for Tire Dynamics Simulation

Tire dynamics simulation calls for addressing many challenging issues in the flexible body dynamics. A tire rotates at high speed, thus the gyroscopic nonlinear inertia effects arising from the large reference motion need to be precisely described in the model. This is not a trivial issue when existing structural finite elements based on the incremental solution procedure are used [27] since the flexible body kinematics are either linearized or simplified when the reference configuration, from which motion of the flexible body is described, is updated every time step. In other words, exact modeling of the rigid body dynamics cannot be ensured due to the approximation utilized in the finite element updating scheme for structural elements. For this reason, in the multibody dynamics simulation, a method called the floating frame of reference formulation has been widely used for modelling flexible bodies in multibody dynamics simulation [28]. In this approach, deformation of a flexible body is defined with respect to the body coordinate system using the local elastic coordinates and the assumed mode method is used to reduce the overall model dimensionality. The general motion description utilized in the floating frame of reference formulation allows for the integration with the general multibody dynamics simulation algorithm without resorting to the updating scheme of the reference configuration at every time step, and the exact modeling of the rigid body dynamics is ensured when strains are zero. However, despite the successful integration of the finite element models into the multibody dynamics simulation, strains are limited to small in this formulation and complex local deformation modes resulting from contact events (i.e., the rolling contact in the case of tires) cannot be efficiently described. Furthermore, the material behavior is limited to the linear strain range.

As a solution to overcome these difficulties in the flexible multibody dynamics simulation, the absolute nodal coordinate formulation (ANCF) has been proposed and proven to be successful in solving many challenging engineering problems that involve large deformable bodies in complex multibody systems [28,29]. This finite element procedure is developed for the nonlinear dynamics simulation of large deformable bodies. In the structural elements such as a beam and shell developed with the absolute nodal coordinate formulation, the finite rotation and deformation of the element are parameterized by the global position vector gradients, rather than the rotational nodal coordinates such as Euler angles. This parameterization leads to a constant mass matrix for fully nonlinear dynamics problems while ensuring the exact modeling of the rigid body reference motion. Since it is known that the displacement gradient tensor can be decomposed into the orthogonal rotation matrix and the stretch tensor that describes the most general six deformation modes using the polar decomposition theorem, it can be proved that use of the position vector gradient coordinates allows for describing the rotation and deformation within the element, thereby circumventing the complex nonlinear coupling of the rotation and deformation coordinates that appears in the inertia terms of flexible body models with rotational parameterization. The constant mass matrix of large deformable bodies not only leads to efficient solutions in nonlinear dynamics simulation, but also allows for the use of the non-incremental solution procedures utilized in general multibody dynamics computer algorithms. Using these important features and general motion description employed in the absolute nodal coordinate formulation, the structural beam and shell elements for modelling the detailed tire structures can be directly integrated into general multibody dynamics computer algorithms without resorting to ad hoc co-simulation procedures, and the flexible tire model based on the absolute nodal coordinate formulation was developed for multibody vehicle dynamics simulation by Sugiyama and Suda [31]. This in-plane tire model was further extended by Yamashita, et al. for transient longitudinal tire dynamics simulation by integrating the with LuGre tire friction model that allows for capturing the friction-induced hysteresis for an in-plane longitudinal tire dynamics problem [32]. This ANCF-LuGre tire model considers the nonlinear coupling between the dynamic structural deformation of the tire and its transient tire friction behavior in the contact patch, and the tire model is implemented directly in general multibody dynamics computer algorithms without resorting to ad hoc co-simulation techniques. It was shown that the ANCF-LuGre tire model has the potential of providing a better understanding of how structural deformation of tires under severe maneuvering conditions influences the transient tire force characteristics. This concept is further extended in this study to the three-dimensional high-fidelity flexible tire model as will be discussed in Chapter 4.

1.1.4 Finite Element Absolute Nodal Coordinate Formulation

The absolute nodal coordinate formulation (ANCF) has been widely used in the large deformation analysis of flexible multibody systems [28,29] due to following advantages for use in multibody dynamics simulation:

(1) Constant mass matrix can be obtained for fully nonlinear dynamics simulation

(2) Exact rigid body motion can be obtained when strains are zero

(3) Non-incremental solution procedure utilized in the general multibody dynamics computer algorithms can be directly applied without specialized updating schemes for finite rotations, thereby allowing for incorporating detailed finite element models into existing multibody dynamics simulation algorithms in a straightforward manner

Shell elements of the absolute nodal coordinate formulation can be classified into the fully parameterized shear deformable element [30,33] and the gradient deficient thin plate element [34,35]. While the fully parameterized element leads to a general motion description that accounts for complex coupled deformation modes of the plate/shell element, use of higher order polynomials and the coupled deformation modes exhibited in this type of element causes severe element locking and special care needs to be exercised to alleviate the locking [36]. The gradient deficient thin plate element, on the other hand, is developed by removing the position vector gradients along the thickness ($\partial \mathbf{r} / \partial z$). The global displacement field in the middle surface can be uniquely parameterized by the global position vector and the two gradient vectors ($\partial \mathbf{r} / \partial x$ and $\partial \mathbf{r} / \partial y$) which are both tangent to the surface. By doing so, the cross section is assumed to be rigid and the elastic forces are derived using a plane stress assumption with Kirchhoff-Love plate theory. This leads to the non-conforming plate element in which the inter-element continuity is not guaranteed, while the conforming thin plate element can be obtained by introducing the additional nodal coordinates $\partial^2 \mathbf{r} / \partial x \partial y$ with bi-cubic Hermite polynomials [34]. Despite the fact that the gradient deficient thin ANCF plate elements have proven to be successful in solving challenging engineering problems that involve large deformable thin plate and shell structures, consideration of general nonlinear material models requires special formulations and implementation due to the plane stress assumption.

Due to the severe element lockings and computational inefficiency of the fully parameterized ANCF elements utilizing three sets of gradient nodal coordinates ($\partial \mathbf{r} / \partial x$, $\partial \mathbf{r} / \partial y$, and $\partial \mathbf{r} / \partial z$), an ANCF parameterization which does not include the position vector gradients tangent to the beam centerline and the middle surface are investigated for shear deformable ANCF beam and plate elements. For beam problems, it is shown in the literature [37] that the elimination of the tangential slope vector along the beam centerline leads to an accurate elastic force description due to weaker polynomial coupling between the position and gradient fields, and use of the general continuum mechanics approach for the elastic forces calculation allows for modeling curved beam structures in a straightforward manner. The assumed displacement field on the beam centerline does not involve any gradient coordinates, while the transverse gradient coordinates are employed to parameterize the orientation and deformation of the beam cross section. For plate elements, on the other hand, the position vector gradient along the thickness can be used to describe the transverse shearing and the thickness stretch of the plate element, and this parameterization leads to a shear deformable shell element. That is, use of such an element parameterization leads to shear deformable plate/shell elements while reducing the number of coordinates per node as discussed in the literature [38]. For the shear deformable shell element, there are two approaches to formulate the elastic forces, *elastic middle surface approach* and *continuum mechanics approach*. In the former method, the six strain components are evaluated in the middle surface using Green-Lagrange strains and the approximated curvature expression is used to define the bending and twisting deformation of the shell. In other words, the strain distribution along the thickness is assumed to be constant in this approach based on the plane stress assumption, allowing for the evaluation of the elastic forces as an area element. Use of this element is limited to moderately thick plate problems and it requires special formulation and implementation to incorporate nonlinear material models. On the other hand, in the latter approach based on the continuum mechanics theory, the elastic forces of the shell element are evaluated as a continuum volume and various nonlinear material models can be considered in a way same as a solid element. This is an important requirement for shell elements utilized for tire models since cord-reinforced rubber material indispensable for modeling highly nonlinear material behavior of tires needs to be incorporated into the shell formulation.

It is also important to notice that there are a wide variety of continuum-based rotation-free shell elements proposed in the finite element community that have similar features to ANCF shell elements including the constant mass matrix and use of three-dimensional material laws without special modifications. Among others, solid shell elements [39-43] and shell elements utilizing extensible directors [44-46] can fall into this category. The configuration update schemes for the continuum-based shell elements were pursued in the literature to interface with incremental solution procedures of nonlinear finite element computer algorithms, including the updating scheme of extensible directors at every load step. On the other hand, the non-incremental solution procedure is adopted in the absolute nodal coordinate formulation to enable the straightforward implementation of elements in general multibody dynamics computer algorithms. Furthermore, various joint constraint formulations have been proposed specialized for ANCF elements to facilitate the integration with multibody dynamics software [47,48]. These important features of the absolute nodal coordinate formulation are utilized in this study for modeling the tire structure using the shear deformable shell element. In addition, the element locking remedy for the shear deformable ANCF shell element is addressed in Chapter 2 using the assumed natural strain (ANS) and the enhanced assumed strain (EAS) approaches to alleviate the transverse shear locking, thickness locking, Poisson’s locking, and the in-plain normal/shear locking.

1.2 Objective of the Study

This study is aimed to develop a high-fidelity physics-based tire/soil interaction simulation capability using flexible multibody dynamics techniques based on the finite element absolute nodal coordinate formulation. To this end, the following issues are addressed in this thesis:

(1) Development of a locking-free shear deformable laminated composite shell element based on the finite element absolute nodal coordinate formulation for modeling the complex fiber reinforced rubber tire structure

(2) Development and validation of a physics-based structural tire model that can be integrated into multibody dynamics computer algorithm

(3) Integration of the distributed parameter LuGre dynamic tire friction model into the physics-based structural tire model for transient braking and cornering simulation

(4) Development and validation of the continuum soil model based on the capped Drucker-Prager yield criterion using the multiplicative finite strain plasticity theory for multibody off-road vehicle dynamics simulation

(5) Development of a physics-based tire/soil interaction simulation capability for off-road mobility simulation

1.3 Organization of Thesis

This thesis is organized as follows: In Chapter 2, a new shear deformable laminated composite shell element based on the finite element absolute nodal coordinate formulation is developed for modeling the fiber reinforced rubber tire structure.

Numerical examples and accuracy of the shear deformable laminated composite shell element developed are demonstrated with several benchmark problems in Chapter 3. In Chapter 4, a high-fidelity physics-based flexible tire model is developed using the shear deformable laminated composite shell element and validated against test data. The distributed parameter LuGre tire friction model is integrated into the deformable tire model to capture the transient tire force characteristics for severe vehicle maneuvering scenarios. In Chapter 5, the parameter identification procedure for the LuGre tire friction model and numerical results of the transient tire dynamics simulation including hard braking and cornering scenarios are presented. A new brick element for modeling the continuum soil behavior using the capped Drucker-Prager yield criterion is developed based on multiplicative finite strain plasticity theory in Chapter 6. In this Chapter, the triaxial soil test results are also presented and those results are used to identify the parameters of the capped Drucker-Prager soil model. Furthermore, the continuum soil model developed is validated against the test results. In Chapter 7, the continuum based deformable tire/soil interaction simulation model is developed for multibody off-road mobility simulation, and the component soil model using the moving soil patch is introduced to reduce the computational time for use in the off-road mobility simulation. Summary, conclusions and the future works are provided in Chapter 8.

CHAPTER 2

DEVELOPMENT OF SHEAR DEFORMABLE LAMINATED COMPOSITE SHELL ELEMENT

2.1 Introduction

In this chapter, a continuum mechanics based shear deformable shell element is developed based on the absolute nodal coordinate formulation for use in the modeling of fiber-reinforced rubber structure of the physics-based tire model. The element consists of four nodes, each of which has the global position coordinates and the transverse gradient coordinates along the thickness introduced to describe the orientation and deformation of the cross section of the shell element. The global position field on the middle surface and the position vector gradient at a material point in the element are interpolated by the bi-linear polynomial. The continuum mechanics approach is used to formulate the generalized elastic forces, allowing for the consideration of nonlinear constitutive models in a straightforward manner. The element locking exhibited in the element can be eliminated using the assumed natural strain (ANS) and enhanced assumed strain (EAS) approaches. In particular, the combined ANS and EAS approach is introduced to alleviate both curvature and Poisson's thickness lockings arising from the erroneous transverse normal strain distribution [49].

2.2 Kinematics of Bi-linear Shear Deformable Shell Element

As shown in Fig. 2.1, the global position vector $\mathbf{r}^i$ of a material point $\mathbf{x}^i = [x^i \quad y^i \quad z^i]^{\mathrm{T}}$ in shell element *i* is defined as

$$\mathbf{r}^i = \mathbf{r}_m^i(x^i, y^i) + z^i \frac{\partial \mathbf{r}^i}{\partial z^i}(x^i, y^i) \tag{2.1}$$

where $\mathbf{r}_m^i(x^i, y^i)$ is the global position vector in the middle surface and $\partial \mathbf{r}^i(x^i, y^i) \big/ \partial z^i$ is the transverse gradient vector used to describe the orientation and deformation of the infinitesimal volume in the element. The preceding global displacement field is interpolated using the bi-linear polynomials as follows:

$$r^i = a_0 + a_1 x^i + a_2 y^i + a_3 x^i y^i + z^i (a_4 + a_5 x^i + a_6 y^i + a_7 x^i y^i) \tag{2.2}$$

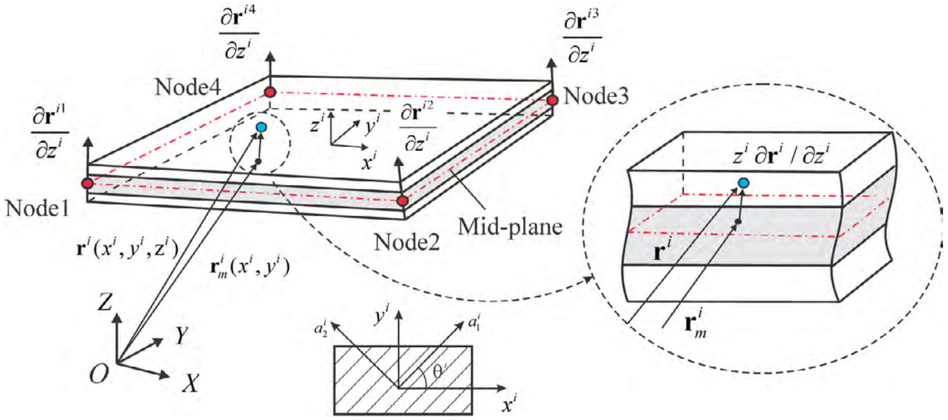

Figure 2.1 Kinematics of bi-linear shear deformable laminated composite shell element

from which, one can interpolate both position vector in the middle surface and the transverse gradient vector using the same bi-linear shape function matrix $\mathbf{S}_m^i$ as follows:

$$\mathbf{r}_m^i(x^i, y^i) = \mathbf{S}_m^i(x^i, y^i)\mathbf{e}_p^i, \qquad \frac{\partial \mathbf{r}^i}{\partial z^i}(x^i, y^i) = \mathbf{S}_m^i(x^i, y^i)\mathbf{e}_g^i \tag{2.3}$$

where $\mathbf{S}_m^i = \begin{bmatrix} S_1^i\mathbf{I} & S_2^i\mathbf{I} & S_3^i\mathbf{I} & S_4^i\mathbf{I} \end{bmatrix}$ and

$$\begin{aligned} S_1^i &= \frac{1}{4}\left(1-\xi^i\right)\left(1-\eta^i\right), S_2^i = \frac{1}{4}\left(1+\xi^i\right)\left(1-\eta^i\right), \\ S_3^i &= \frac{1}{4}\left(1+\xi^i\right)\left(1+\eta^i\right), S_4^i = \frac{1}{4}\left(1-\xi^i\right)\left(1+\eta^i\right) \end{aligned} \tag{2.4}$$

where $\xi^i = 2x^i / \ell^i$ and $\eta^i = 2y^i / w^i$. ℓ^i and w^i are lengths along the element x^i and y^i axes, respectively. In Eq. 2.3, the vectors $\mathbf{e}_p^i$ and $\mathbf{e}_g^i$ represent the element nodal coordinates associated with the global position vector in the middle surface and the transverse gradient vector. That is, for node k of element i, one has $\mathbf{e}_p^{ik} = \mathbf{r}^{ik}$ and $\mathbf{e}_g^{ik} = \partial \mathbf{r}^{ik} / \partial z^i$. It is important to notice here that the assumed displacement field $\mathbf{r}_m^i$ defined in the middle surface does not involve any gradient coordinates, while the orientation and deformation of the infinitesimal volume at the material point is parameterized by the transverse gradient coordinates only. Substitution of Eq. 2.3 into Eq. 2.1 leads to the following general expression for the global position vector used for the absolute nodal coordinate formulation:

$$\mathbf{r}^i(x^i, y^i, z^i) = \mathbf{S}^i(x^i, y^i, z^i)\mathbf{e}^i \tag{2.5}$$

where the shape function matrix $\mathbf{S}^i$ and the element nodal coordinate vector $\mathbf{e}^i$ are, respectively, defined as

$$\mathbf{S}^i = \begin{bmatrix} \mathbf{S}_m^i & z^i\mathbf{S}_m^i \end{bmatrix}, \qquad \mathbf{e}^i = [(\mathbf{e}_p^i)^T \quad (\mathbf{e}_g^i)^T]^T \tag{2.6}$$

It is important to notice here that the element parameterization and the assumed global displacement field defined in the ANCF shell element are essentially different from those of the degenerated shell elements [50]. For more details on the difference between the ANCF and degenerated shell elements, one can refer to the literature [51], in which a fully parameterized ANCF shell element [30] is used for comparison. The difference between the fully parameterized shell element [30] and the gradient deficient shear deformable bi-linear shell element considered in this study lies in the order of polynomials introduced to the global position field of the middle surface. The transverse position gradient vector is interpolated with the same bi-linear polynomial in the fully parameterized shell element, while the global position vector in the middle surface is interpolated by an incomplete bi-cubic polynomial.

2.3 Generalized Elastic Forces

2.3.1 Generalized Elastic Forces with Continuum Mechanics Approach

In the continuum mechanics approach, the elastic forces of the shell element are evaluated as a continuum volume and the Green-Lagrange strain tensor $\mathbf{E}$ at an arbitrary material point in element *i* is defined as follows:

$$\mathbf{E}^i = \frac{1}{2}\left((\mathbf{F}^i)^T\mathbf{F}^i - \mathbf{I}\right) \tag{2.7}$$

where $\mathbf{F}^i$ is the global position vector gradient tensor defined by

$$\mathbf{F}^i = \frac{\partial \mathbf{r}^i}{\partial \mathbf{X}^i} = \frac{\partial \mathbf{r}^i}{\partial \mathbf{x}^i}\left(\frac{\partial \mathbf{X}^i}{\partial \mathbf{x}^i}\right)^{-1} = \bar{\mathbf{J}}^i(\mathbf{J}^i)^{-1} \tag{2.8}$$

In the preceding equation, $\bar{\mathbf{J}}^i = \partial\mathbf{r}^i / \partial\mathbf{x}^i$ and $\mathbf{J}^i = \partial\mathbf{X}^i / \partial\mathbf{x}^i$, where the vector $\mathbf{X}^i$ represents the global position vector of element *i* at an arbitrary reference configuration. Substitution of Eq. 2.8 into Eq. 2.7 leads to

$$\mathbf{E}^i = (\mathbf{J}^i)^{-T}\tilde{\mathbf{E}}^i(\mathbf{J}^i)^{-1} \tag{2.9}$$

where $\tilde{\mathbf{E}}^i$ is the covariant strain tensor defined by

$$\tilde{\mathbf{E}}^i = \frac{1}{2}\left((\bar{\mathbf{J}}^i)^T \bar{\mathbf{J}}^i - (\mathbf{J}^i)^T \mathbf{J}^i\right) \tag{2.10}$$

The transformation (push-forward operation) of the covariant strain tensor $\tilde{\mathbf{E}}^i$ given by Eq. 2.10 can be re-expressed in a vector form by introducing the engineering covariant strain vector $\tilde{\boldsymbol{\varepsilon}}^i$ as

$$\boldsymbol{\varepsilon}^i = (\mathbf{T}^i)^{-T}\tilde{\boldsymbol{\varepsilon}}^i \tag{2.11}$$

where the vector $\boldsymbol{\varepsilon}$ in Eq. 2.11 is the engineering strain vector at the deformed configuration defined as

$$\boldsymbol{\varepsilon}^i = [\varepsilon_{xx}^i \quad \varepsilon_{yy}^i \quad \gamma_{xy}^i \quad \varepsilon_{zz}^i \quad \gamma_{xz}^i \quad \gamma_{yz}^i]^T \tag{2.12}$$

and the engineering covariant strain vector is defined as

$$\tilde{\boldsymbol{\varepsilon}}^i = [\tilde{\varepsilon}_{xx}^i \quad \tilde{\varepsilon}_{yy}^i \quad \tilde{\gamma}_{xy}^i \quad \tilde{\varepsilon}_{zz}^i \quad \tilde{\gamma}_{xz}^i \quad \tilde{\gamma}_{yz}^i]^T \tag{2.13}$$

The transformation matrix $\mathbf{T}^i$ in Eq. 2.11 can be expressed explicitly as

$$\mathbf{T}^i = \begin{bmatrix} (J_{11}^i)^2 & (J_{12}^i)^2 & 2J_{11}^i J_{12}^i & (J_{13}^i)^2 & 2J_{11}^i J_{13}^i & 2J_{12}^i J_{13}^i \\ (J_{21}^i)^2 & (J_{22}^i)^2 & 2J_{21}^i J_{22}^i & (J_{23}^i)^2 & 2J_{21}^i J_{23}^i & 2J_{22}^i J_{23}^i \\ J_{11}^i J_{21}^i & J_{12}^i J_{22}^i & J_{11}^i J_{22}^i + J_{12}^i J_{21}^i & J_{13}^i J_{23}^i & J_{11}^i J_{23}^i + J_{13}^i J_{21}^i & J_{12}^i J_{23}^i + J_{13}^i J_{22}^i \\ (J_{31}^i)^2 & (J_{32}^i)^2 & 2J_{31}^i J_{32}^i & (J_{33}^i)^2 & 2J_{31}^i J_{33}^i & 2J_{32}^i J_{33}^i \\ J_{11}^i J_{31}^i & J_{12}^i J_{32}^i & J_{11}^i J_{32}^i + J_{12}^i J_{31}^i & J_{13}^i J_{33}^i & J_{11}^i J_{33}^i + J_{13}^i J_{31}^i & J_{12}^i J_{33}^i + J_{13}^i J_{32}^i \\ J_{21}^i J_{31}^i & J_{22}^i J_{32}^i & J_{21}^i J_{32}^i + J_{22}^i J_{31}^i & J_{23}^i J_{33}^i & J_{21}^i J_{33}^i + J_{23}^i J_{31}^i & J_{22}^i J_{33}^i + J_{23}^i J_{32}^i \end{bmatrix} \tag{2.14}$$

and J_{ab}^i is the element in the a-th column and b-th row of matrix $\mathbf{J}^i$ which is constant in time. The generalized elastic forces can then be obtained using the virtual work as follows:

$$\mathbf{Q}_k^i = \int_{V_0^i} \left(\frac{\partial \boldsymbol{\varepsilon}^i}{\partial \mathbf{e}^i}\right)^T \boldsymbol{\sigma}^i dV_0^i \tag{2.15}$$

where $\boldsymbol{\sigma}^i$ is a vector of the second Piola–Kirchhoff stresses and dV_0^i is the infinitesimal volume at the reference configuration of element i. It is important to notice here that the element elastic forces are evaluated as a continuum volume, and the stress vector for the shell element can be obtained with various nonlinear material models for large deformation problems without ad hoc procedures.

2.3.2 Element Locking for Transverse Shear and In-Plane Shear/Normal Strains

As it has been addressed in literature of shell element formulations [41,42,44,45,52-57], the bi-linear quadrilateral shell element suffers from the transverse shear and the in-plane shear/normal lockings. The transverse shear locking can be eliminated using the assumed natural strain (ANS) approach proposed by Bathe and Dvorkin [55,56]. In this approach, the covariant transverse shear strains are interpolated using those evaluated at the sampling points *A*, *B*, *C* and *D* shown in Fig. 2.2 as follows:

$$\left.\begin{aligned} \tilde{\gamma}_{xz}^{ANS} &= \frac{1}{2}(1-\eta)\tilde{\gamma}_{xz}^{C} + \frac{1}{2}(1+\eta)\tilde{\gamma}_{xz}^{D} \\ \tilde{\gamma}_{yz}^{ANS} &= \frac{1}{2}(1-\xi)\tilde{\gamma}_{yz}^{A} + \frac{1}{2}(1+\xi)\tilde{\gamma}_{yz}^{B} \end{aligned}\right\} \tag{2.16}$$

where $\tilde{\gamma}_{xz}^{C}$, $\tilde{\gamma}_{xz}^{D}$, $\tilde{\gamma}_{yz}^{A}$ and $\tilde{\gamma}_{yz}^{B}$ are compatible covariant transverse shear strains at the sampling points.

The parasitic in-plane shear under pure bending loads is a typical locking problem exhibited in the bi-linear quadrilateral element [58], and the compatible in-plane strains (ε_{xx}, ε_{yy} and γ_{xy}) obtained by the assumed displacement field can be enhanced by introducing the enhanced assumed strains (EAS) $\boldsymbol{\varepsilon}^{EAS}$ as [44,54]

$$\boldsymbol{\varepsilon} = \boldsymbol{\varepsilon}^{c} + \boldsymbol{\varepsilon}^{EAS} \tag{2.17}$$

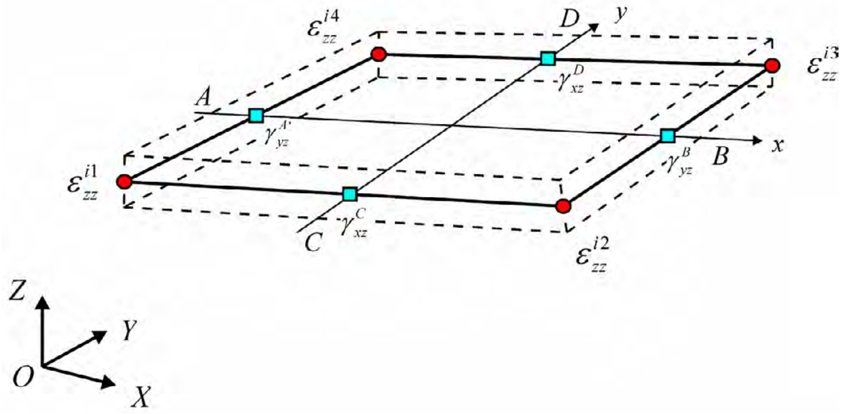

Figure 2.2 Sampling points for assumed natural strain

where $\boldsymbol{\varepsilon}^c$ indicates the compatible strain vector and the strain vector $\boldsymbol{\varepsilon}^{EAS}$ is defined by

$$\boldsymbol{\varepsilon}^{EAS}(\boldsymbol{\xi}) = \mathbf{G}(\boldsymbol{\xi})\boldsymbol{\alpha} \tag{2.18}$$

In the preceding equation, $\boldsymbol{\alpha}$ is a vector of internal parameters introduced to define the enhanced in-plane strain field and the matrix $\mathbf{G}(\boldsymbol{\xi})$ can be defined as [44,54]

$$\mathbf{G}(\boldsymbol{\xi}) = \frac{|\mathbf{J}_0|}{|\mathbf{J}(\boldsymbol{\xi})|}\mathbf{T}_0^{-\mathrm{T}}\mathbf{N}(\boldsymbol{\xi}) \tag{2.19}$$

where $\mathbf{J}(\boldsymbol{\xi})$ and $\mathbf{J}_0$ are the global position vector gradient matrices at the reference configuration evaluated at the Gaussian integration point $\boldsymbol{\xi}$ and at the center of element ($\boldsymbol{\xi} = \mathbf{0}$), respectively. $\boldsymbol{\xi}$ is a vector of the element coordinates in the parametric domain and $\mathbf{T}_0$ is the constant transformation matrix evaluated at the center of element as shown in Eq. 2.19. The matrix $\mathbf{N}(\boldsymbol{\xi})$ defines polynomials for the enhancement of the in-plane strain field in the parametric domain. For example, consideration of the linear distribution of in-plane strains (ε_{xx}, ε_{yy} and γ_{xy}) requires introducing the following interpolation matrix $\mathbf{N}(\boldsymbol{\xi})$:

$$\mathbf{N}(\boldsymbol{\xi}) = \begin{bmatrix} \xi & 0 & 0 & 0 \\ 0 & \eta & 0 & 0 \\ 0 & 0 & \xi & \eta \\ 0 & 0 & 0 & 0 \\ 0 & 0 & 0 & 0 \\ 0 & 0 & 0 & 0 \end{bmatrix} \tag{2.20}$$

where the additional four internal EAS parameters are introduced in this model. Using Eq. 2.14, the enhanced covariant strains are then pushed forward to those at the deformed configuration in the physical domain. It is important to notice here that the matrix $\mathbf{N}(\boldsymbol{\xi})$ needs to satisfy the following condition [44]:

$$\int \mathbf{N}(\boldsymbol{\xi})d\boldsymbol{\xi} = \mathbf{0} \tag{2.21}$$

such that the orthogonality condition between the assumed stress and strain is satisfied as

$$\int_{V_0} \boldsymbol{\sigma} \cdot \boldsymbol{\varepsilon}^{EAS} dV_0 = 0 \tag{2.22}$$

Using the preceding condition, the unknown assumed stress term that appears in Hu-Washizu mixed variational principle vanishes and one can obtain the generalized elastic force vector as follows [44]:

$$\mathbf{Q}_k^i = -\int_{V_0^i} \left(\frac{\partial \boldsymbol{\varepsilon}^c}{\partial \mathbf{e}^i} \right)^T \frac{\partial W^i (\boldsymbol{\varepsilon}^c + \boldsymbol{\varepsilon}^{EAS})}{\partial \boldsymbol{\varepsilon}^i} dV_0^i \tag{2.23}$$

where W is an elastic energy function. For example, the elastic energy function W of the compressible neo-Hookean material model is defined as follows [59]:

$$W = \frac{\mu}{2}\left(\mathrm{tr}(\mathbf{C}) - 3\right) - \mu \ln J + \frac{\lambda}{2}\left(\ln J\right)^2 \tag{2.24}$$

where μ and λ are the Lamé constants; $\mathbf{C} = \mathbf{F}^T\mathbf{F}$ is the right Cauchy-Green deformation tensor; and $J = \det(\mathbf{F}) = \sqrt{\det(\mathbf{C})}$. It is important to notice here that the right Cauchy-Green deformation tensor that accounts for the enhanced assumed strain modification is defined as follows:

$$\mathbf{C} = 2(\mathbf{E}^c + \mathbf{E}^{EAS}) + \mathbf{I} \tag{2.25}$$

2.3.3 Thickness Locking

Use of the transverse gradients in the shell element introduces the thickness stretch and the locking associated with the transverse normal strain is exhibited in the bi-linear shear deformable shell element. That is, the transverse gradient vectors can be erroneously elongated when the shell element is subjected to bending and twisting deformation. This phenomenon is called curvature thickness locking. The solid shell elements which consists of layers of translational nodal coordinates at the top and bottom surfaces of the element [41,42,52,53] and shell elements parameterized by extensible directors for capturing the transverse shearing and the thickness stretch [45,46,57] suffer from the similar thickness locking resulting from the erroneous transverse normal strain distribution. Use of the assumed natural strain (ANS) approach is proposed in the literature [45] to alleviate the curvature thickness locking of the shell element modeled by extensible directors and the transverse normal strain at a material point in the element is approximated as follows:

$$\varepsilon_{zz}^{ANS} = S_1^{ANS}\varepsilon_{zz}^1 + S_2^{ANS}\varepsilon_{zz}^2 + S_3^{ANS}\varepsilon_{zz}^3 + S_4^{ANS}\varepsilon_{zz}^4 \tag{2.26}$$

where ε_{zz}^{k} indicates the compatible transverse normal strain at node k as shown in Fig. 2.2 and S_{k}^{ANS} is the shape function associated with it. This approach is applied to the bi-linear shear deformable shell element based on the elastic middle surface approach shown in Appendix to alleviate the thickness locking problem. Since the strain distribution along the thickness is assumed to be constant and the stress is evaluated in the middle surface, use of the assumed natural strain approach can successfully alleviate the thickness locking if the compatible transverse normal strains at four corners are accurate.

In addition to the curvature thickness locking, use of a linear interpolation of the global position field along the shell thickness leads to locking called Poisson´s thickness locking because it is the Poisson´s ratio that introduces the coupling of the in-plane strains to the transverse normal strain. In the case of pure bending, the axial strains due to bending are linearly distributed along the thickness and it leads to the linearly varying transverse normal strain due to the coupling induced by Poisson’s ratio. However, the use of the linear interpolation along the thickness leads to constant thickness strains which make the element behave overly stiff since the thickness strain does not vanish on the neutral axis. It has been shown that the use of the enhanced assumed strain (EAS) approach alleviates the Poisson’s thickness locking effectively [41,46]. That is, the additional internal EAS parameters associated with the enhanced transverse normal strain are added to consider the linear distribution of the transverse normal strain along the thickness coordinate z^{i} . The interpolation matrix $\mathbf{N}(\xi)$ introduced for the in-plane normal/shear lockings in Eq. 2.20 is modified as

$$\mathbf{N}(\xi)=\begin{bmatrix} \xi & 0 & 0 & 0 & 0 \\ 0 & \eta & 0 & 0 & 0 \\ 0 & 0 & \xi & \eta & 0 \\ 0 & 0 & 0 & 0 & \zeta \\ 0 & 0 & 0 & 0 & 0 \\ 0 & 0 & 0 & 0 & 0 \end{bmatrix} \tag{2.27}$$

where $\zeta = 2z/h$. It is important to notice here that there are no strain enhancement terms associated with the transverse shear strains γ_{xz} and γ_{yz} defined in the fifth and sixth rows. In the literature [46], the transformation matrix $\mathbf{G}(\xi)$ associated with the enhanced in-plane and thickness strain terms are assumed to be decoupled and the approximated transformation matrix is used. In this investigation, the exact transformation matrix defined for the general three-dimensional stress state is considered.

Accordingly, the compatible transverse normal strain is replaced by the assumed natural strain defined by Eq. 2.26 to alleviate both curvature thickness locking and Poisson's thickness lockings as follows:

$$\varepsilon_{zz} = \varepsilon_{zz}^{ANS} + \varepsilon_{zz}^{EAS} \tag{2.28}$$

The similar approach is employed for solid shell elements in literature [41]. In this investigation, the combined ANS and EAS approach for the thickness locking is applied to the bi-linear shear deformable shell element. With this approach, the transverse normal strain improved by the ANS approach for the curvature thickness locking is further modified by the enhanced assumed strain approach to eliminate the Poisson's locking. For application of this approach to the continuum mechanics based ANCF shell element, the covariant strain components of the transverse shear and transverse normal strains are interpolated in the natural coordinate domain first and then the covariant strain vector given in Eq. 2.13 is replaced by the following strain vector:

$$\tilde{\boldsymbol{\varepsilon}} = \begin{bmatrix} \tilde{\varepsilon}_{xx} & \tilde{\varepsilon}_{yy} & \tilde{\gamma}_{xy} & \tilde{\varepsilon}_{zz}^{ANS} & \tilde{\gamma}_{xz}^{ANS} & \tilde{\gamma}_{yz}^{ANS} \end{bmatrix}^T \tag{2.29}$$

and then the strain field can be defined as follows:

$$\boldsymbol{\varepsilon} = \mathbf{T}^{-T}\,\tilde{\boldsymbol{\varepsilon}} + \boldsymbol{\varepsilon}^{EAS} \tag{2.30}$$

In the preceding equation, the enhanced assumed strain vector is defined as

$$\boldsymbol{\varepsilon}^{EAS} = \begin{bmatrix} \varepsilon_{xx}^{EAS} & \varepsilon_{yy}^{EAS} & \gamma_{xy}^{EAS} & \varepsilon_{zz}^{EAS} & 0 & 0 \end{bmatrix}^T \tag{2.31}$$

This leads to a systematic derivation of the generalized elastic forces of the locking-free continuum mechanics based shear deformable shell element.

2.4 Generalization to Laminated Composite Shell Element

In fiber-reinforced composite materials that are widely used in many engineering applications, laminae having different fiber angles are bonded together to produce desired material properties. Since many laminae are stacked at different fiber angles, the complex deformation coupling between the extension, shearing, bending and twisting occurs, and such a deformation coupling characterizes the mechanical behavior of fiber-reinforced composite materials [60]. To account for the laminated composite materials in shell elements, various formulations are proposed and one can refer to review articles on this topic [61,62]. The shell element used in this study is formulated as a continuum solid that accounts for the three-dimensional stress state, thus the complex deformation coupling exhibited in laminates can be automatically considered without specialized formulations for shell elements. That is, the generalized elastic force of the laminated composite shell element that consists of N layers can be defined as follows:

$$\mathbf{Q}_s^i = -\sum_{k=1}^{N} \int_{V_0^{ik}} \left(\frac{\partial \boldsymbol{\varepsilon}^{ik}}{\partial \mathbf{e}^i} \right)^T \frac{\partial W^{ik}(\boldsymbol{\varepsilon}^{ik})}{\partial \boldsymbol{\varepsilon}^{ik}} dV_0^{ik} \tag{2.32}$$

In the preceding equation, the integration interval for the k-th layer in the thickness direction is from z_{k-1} to z_k. In other words, the element generalized elastic forces are evaluated layer by layer, and the resulting generalized elastic forces of each layer are added together to define the elastic force vector of the laminated composite shell. Two Gaussian integration points are used along the thickness when the elastic forces of each layer are evaluated. It is important to notice here that there is no restriction in material models considered in each lamina, despite the fact that the orthotropic material law is the most popular material model used for reinforced composite materials.

For an orthotropic Saint-Venant-Kirchhoff material, the stress and strain relation is defined in the fiber coordinate system as [41]

$$\bar{S}^{ab} = \bar{C}^{abcd} \bar{E}_{cd} \tag{2.33}$$

where the material moduli $\bar{C}^{abcd}$ is defined in the fiber coordinate system as

$$[\bar{C}^{ijkl}] = \begin{bmatrix} \bar{C}^{1111} & \bar{C}^{1122} & 0 & \bar{C}^{1133} & 0 & 0 \\ \bar{C}^{1122} & \bar{C}^{2222} & 0 & \bar{C}^{2233} & 0 & 0 \\ 0 & 0 & \bar{C}^{1212} & 0 & 0 & 0 \\ \bar{C}^{1133} & \bar{C}^{2233} & 0 & \bar{C}^{3333} & 0 & 0 \\ 0 & 0 & 0 & 0 & \bar{C}^{2323} & 0 \\ 0 & 0 & 0 & 0 & 0 & \bar{C}^{1313} \end{bmatrix} \tag{2.34}$$

where

$$\begin{array}{lll} \bar{C}^{1111} = E_1(1-\nu_{23}\nu_{32})/\Delta & \bar{C}^{2222} = E_2(1-\nu_{13}\nu_{31})/\Delta & \bar{C}^{3333} = E_3(1-\nu_{12}\nu_{21})/\Delta \\ \bar{C}^{1122} = E_1(\nu_{21}+\nu_{31}\nu_{23})/\Delta & \bar{C}^{1133} = E_3(\nu_{13}+\nu_{12}\nu_{23})/\Delta & \bar{C}^{2233} = E_2(\nu_{32}+\nu_{12}\nu_{31})/\Delta \\ \bar{C}^{1212} = G_{12} & \bar{C}^{2323} = G_{23} & \bar{C}^{1313} = G_{13} \end{array} \tag{2.35}$$

and $\Delta = 1-\nu_{12}\nu_{21}-\nu_{23}\nu_{32}-\nu_{31}\nu_{13}-2\nu_{21}\nu_{32}\nu_{13}$. The orthogonal triad of the fiber coordinate system $[\mathbf{a}_1 \quad \mathbf{a}_2 \quad \mathbf{a}_3]$ is defined for the fiber angle θ as

$$\mathbf{a}_1 = \cos\theta\mathbf{i} + \sin\theta\mathbf{j}, \quad \mathbf{a}_2 = -\sin\theta\mathbf{i} + \cos\theta\mathbf{j} \quad \text{and} \quad \mathbf{a}_3 = \mathbf{k} \tag{2.36}$$

In the preceding equations, **i**, **j** and **k** are unit vectors along axes of the global coordinate system. On the other hand, using the covariant basis $\mathbf{J} = \partial\mathbf{X}/\partial\mathbf{x} = [\mathbf{b}_1 \quad \mathbf{b}_2 \quad \mathbf{b}_3]$ at the initially curved configuration, the stress and strain relation is expressed as

$$S^{ij} = C^{ijkl}E_{kl} \tag{2.37}$$

In the preceding equations, the second Piola-Kirchhoff stress tensor and the Green-Lagrange strain tensor can be defined with respect to these coordinate systems as follows [41]:

$$\mathbf{S} = \bar{S}^{ab}\mathbf{a}_a \otimes \mathbf{a}_b = S^{ij}\mathbf{b}_i \otimes \mathbf{b}_j \quad \text{and} \quad \mathbf{E} = \bar{E}_{cd}\mathbf{a}^c \otimes \mathbf{a}^d = E_{kl}\mathbf{b}^k \otimes \mathbf{b}^l \tag{2.38}$$

from which, one can obtain the elastic moduli of a fiber-reinforced lamina in the material frame as [41]

$$C^{ijkl} = (\mathbf{b}^i \cdot \mathbf{a}_a)(\mathbf{b}^j \cdot \mathbf{a}_b)(\mathbf{b}^k \cdot \mathbf{a}_c)(\mathbf{b}^l \cdot \mathbf{a}_d)\bar{C}^{abcd} \tag{2.39}$$

where $(\mathbf{J}^i)^{-1} = [\mathbf{b}^1 \quad \mathbf{b}^2 \quad \mathbf{b}^3]$.

For modeling incompressible materials such as rubbers in the composite tire structure, Mooney-Rivlin material model is widely used. The energy density function is defined as [63]

$$W = C_1(\bar{I}_1 - 3) + C_2(\bar{I}_2 - 3) + \frac{K}{2}(J-1)^2 \tag{2.40}$$

where C_1 and C_2 are material constants, $\bar{I}_1 = I_1/(I_3)^{1/3}$, $\bar{I}_2 = I_2/(I_3)^{2/3}$ and $J = (I_3)^{1/2}$, where I_1, I_2 and I_3 are invariants of right Cauchy-Green tensor [63]. K is a bulk modulus. The second Piola–Kirchhoff stress tensor **S** is obtained by differentiating the energy density function W with respect to Green-Lagrange strain tensor **E** as

$$\mathbf{S}=\frac{\partial W}{\partial \mathbf{E}}=2C_1\left(I_3\right)^{-1/3}\left(\mathbf{I}-\frac{1}{3}I_1\mathbf{C}^{-1}\right)+2C_2\left(I_3\right)^{-2/3}\left(I_1\mathbf{I}-\mathbf{C}-\frac{2}{3}I_2\mathbf{C}^{-1}\right)+KJ(\mathrm{J}-1)\mathbf{C}^{-1} \quad (2.41)$$

2.5 Equations of Motion and Solution Procedures

Using the principle of virtual work in dynamics, the equations of motion of the shear deformable laminated composite shell element *i* can be expressed as

$$\mathbf{M}^i\ddot{\mathbf{e}}^i=\mathbf{Q}_s^i(\mathbf{e}^i,\boldsymbol{\alpha}^i)+\mathbf{Q}_e^i(\mathbf{e}^i,\dot{\mathbf{e}}^i,t)+\mathbf{Q}_c^i \quad (2.42)$$

where the vectors $\mathbf{Q}_k^i$, $\mathbf{Q}_e^i$ and $\mathbf{Q}_c^i$ are respectively, vectors of the element elastic forces, external forces and constraint forces associated with connection to adjacent elements; and the matrix $\mathbf{M}^i$ is the constant element mass matrix defined by

$$\mathbf{M}^i=\sum_{k=1}^{N}\int_{V_0^{ik}}\rho_0^{ik}(\mathbf{S}^i)^T\mathbf{S}^i dV_0^{ik} \quad (2.43)$$

where ρ_0^{ik} is the material density of *k*-th layer at the reference configuration.

It is important to notice here that the generalized elastic forces are defined as a function of the nodal coordinates and the internal EAS parameters $\boldsymbol{\alpha}^i$. The parameter $\boldsymbol{\alpha}^i$ are determined by solving the following equation for each element:

$$\mathbf{h}^i(\mathbf{e}^i,\boldsymbol{\alpha}^i)=\int_{V_0^i}\left(\frac{\partial\boldsymbol{\varepsilon}^{EAS}}{\partial\boldsymbol{\alpha}^i}\right)^T\frac{\partial W^i(\boldsymbol{\varepsilon}^c+\boldsymbol{\varepsilon}^{EAS})}{\partial\boldsymbol{\varepsilon}^i}dV_0^i=\mathbf{0} \quad (2.44)$$

The nodal coordinates $\mathbf{e}^i$ and the EAS internal parameters $\boldsymbol{\alpha}^i$ are determined at every time step such that both Eqs. 2.42 and 2.43 are satisfied. Using the time integration scheme in Newmark-β family, the nodal acceleration and velocity vectors at time step t_{n+1} are discretized in time as

$$\left.\begin{aligned}\ddot{\mathbf{e}}_{n+1}&=\frac{1}{\beta h^2}(\mathbf{e}_{n+1}-\mathbf{e}_n)-\frac{1}{\beta h}\ \dot{\mathbf{e}}_n-(\frac{1}{2\beta}-1)\ddot{\mathbf{e}}_n\\ \dot{\mathbf{e}}_{n+1}&=\frac{\gamma}{\beta h}(\mathbf{e}_{n+1}-\mathbf{e}_n)-(\frac{\gamma}{\beta}-1)\ \dot{\mathbf{e}}_n-h(\frac{\gamma}{2\beta}-1)\ddot{\mathbf{e}}_n\end{aligned}\right\} \quad (2.45)$$

where h is the step size; and β and γ are integration coefficients. Using the preceding equations, the equations of motion given by Eq. 2.42 can be expressed as a function of the unknown system nodal coordinates $\mathbf{e}_{n+1}$ and EAS parameters $\boldsymbol{\alpha}_{n+1}$ for all the elements as follows:

$$\mathbf{f}(\mathbf{e}_{n+1}, \boldsymbol{\alpha}_{n+1}) = \mathbf{0} \tag{2.46}$$

In other words, one needs to seek solutions to the following equations at time step t_{n+1}:

$$\mathbf{g}(\mathbf{e}_{n+1}, \boldsymbol{\alpha}_{n+1}) = \begin{bmatrix} \mathbf{f}(\mathbf{e}_{n+1}, \boldsymbol{\alpha}_{n+1}) \\ \mathbf{h}(\mathbf{e}_{n+1}, \boldsymbol{\alpha}_{n+1}) \end{bmatrix} = \mathbf{0} \tag{2.47}$$

Using Newton-Raphson method, Newton difference for $\mathbf{e}_{n+1}$ and $\boldsymbol{\alpha}_{n+1}$ can be obtained by solving the following matrix equation:

$$\begin{bmatrix} \partial\mathbf{f}/\partial\mathbf{e}_n & \partial\mathbf{f}/\partial\boldsymbol{\alpha}_n \\ \partial\mathbf{h}/\partial\mathbf{e}_n & \partial\mathbf{h}/\partial\boldsymbol{\alpha}_n \end{bmatrix} \begin{bmatrix} \Delta\mathbf{e}_{n+1} \\ \Delta\boldsymbol{\alpha}_{n+1} \end{bmatrix} = -\begin{bmatrix} \mathbf{f}_n \\ \mathbf{h}_n \end{bmatrix} \tag{2.48}$$

By eliminating $\Delta\boldsymbol{\alpha}_{n+1}$ from the preceding equation, $\Delta\mathbf{e}_{n+1}$ can be obtained as a solution to the following equation:

$$\left(\frac{\partial\mathbf{f}_n}{\partial\mathbf{e}_n} - \frac{\partial\mathbf{f}_n}{\partial\boldsymbol{\alpha}_n} \left(\frac{\partial\mathbf{h}_n}{\partial\boldsymbol{\alpha}_n} \right)^{-1} \frac{\partial\mathbf{h}_n}{\partial\mathbf{e}_n} \right) \Delta\mathbf{e}_{n+1} = -\mathbf{f}_n + \frac{\partial\mathbf{f}_n}{\partial\boldsymbol{\alpha}_n} \left(\frac{\partial\mathbf{h}_n}{\partial\boldsymbol{\alpha}_n} \right)^{-1} \mathbf{h}_n \tag{2.49}$$

The system nodal coordinates can then be updated by $\mathbf{e}_{n+1} = \mathbf{e}_n + \Delta\mathbf{e}_{n+1}$, while the EAS parameters are updated as follows:

$$\boldsymbol{\alpha}_{n+1} = \boldsymbol{\alpha}_n - \left(\frac{\partial\mathbf{h}_n}{\partial\boldsymbol{\alpha}_n} \right)^{-1} \left(\mathbf{h}_n + \frac{\partial\mathbf{h}_n}{\partial\mathbf{e}_n} \Delta\mathbf{e}_{n+1} \right) \tag{2.50}$$

It is important to recall that the EAS parameters are introduced to each element and can be determined at the element level as internal variables. That is, for given element nodal coordinates $\mathbf{e}^i_{n+1}$ for element i obtained from the updated system nodal coordinates $\mathbf{e}_{n+1}$ (Eq. 2.49), the EAS parameters $\boldsymbol{\alpha}^i_{n+1}$ for element i can then be determined at the element level using Eq. 2.42 with the following updating scheme:

$$\boldsymbol{\alpha}^{i(k+1)}_{n+1} = \boldsymbol{\alpha}^{i(k)}_{n+1} - (\mathbf{H}^i)^{-1} \mathbf{h}^i (\mathbf{e}^i_{n+1}, \boldsymbol{\alpha}^{i(k)}_{n+1}) \tag{2.51}$$

where $\boldsymbol{\alpha}^{i(0)}_{n+1} = \boldsymbol{\alpha}^i_n$ and Jacobian matrix $\mathbf{H}^i$ in the preceding equation is defined by

$$\mathbf{H}^i = \frac{\partial\mathbf{h}^i}{\partial\boldsymbol{\alpha}^i} = \int_{V^i_0} (\mathbf{G}^i)^T \frac{\partial^2 W^i(\boldsymbol{\varepsilon}^c + \boldsymbol{\varepsilon}^{EAS})}{\partial{\boldsymbol{\varepsilon}^i}^2} \mathbf{G}^i \, dV^i_0 \tag{2.52}$$

where the matrix $\mathbf{G}^i$ is defined by Eq. 2.19. The term $\partial^2 W / \partial\boldsymbol{\varepsilon}^2$ leads to a material moduli matrix obtained by the second derivative of the elastic energy function. That is, for a linear Hookean material model, this matrix is constant. However, for general nonlinear material models, the material moduli matrix is no longer constant and the iterative solution procedure is required to determine the internal EAS parameters $\boldsymbol{\alpha}^i$ for each element. Using this procedure, the dimension of the governing equations remains the same as the number of the system nodal coordinates, while the EAS parameters can be determined element by element without solving the augmented large dimensional governing equations. This also allows for implementing the shell element formulated with the EAS approach in a straightforward manner without significant modifications of existing algorithms developed for ANCF elements.

CHAPTER 3

SHELL ELEMENT PERFORMANCE TEST

3.1 Benchmark Problems

In this chapter, several numerical examples are presented in order to demonstrate the accuracy and the rate of convergence of numerical solutions obtained by the continuum mechanics based shear deformable shell element developed in this investigation. The effect of the assumed natural strain (ANS) and enhanced assumed strain (EAS) approaches on the element accuracy is also discussed.

3.1.1 Cantilevered Plate and Shell Subjected to a Point Force

In the first problem, a rectangular cantilevered plate subjected to a vertical point force at one of the corners of the plate is considered as shown in Fig. 3.1 The length, width and thickness of the plate are assumed to be 1.0 m, 1.0 m and 0.01 m. The Young's modulus and Poisson's ratio are assumed to be 2.1×10^{8} Pa and 0.3, respectively. The vertical point force F_z defined at the corner is assumed to be 50 N. As shown in Fig. 3.1, the plate is subjected to large deformation at the static equilibrium state. The six models with different strain modifications discussed in Chapter 2 are considered to demonstrate the effect of the EAS and ANS approaches on the element convergence and accuracy. These models are summarized in Table 3.1. In Model-1, no strain modifications are made, while Model-2 is used to demonstrate the effect of the ANS approach to alleviate the transverse shear locking for the shell element. A comparison between Model-3 and 4 explains the effect of the in-plane shear/normal lockings alleviated by the EAS approach, while a comparison between Model-4, 5 and 6 explains the use of the three different approaches for elimination of the thickness locking, i.e., the ANS (Model-4), the EAS (Model-5), and the combined ANS and EAS (Model-6) approaches as discussed in Section 2.2.

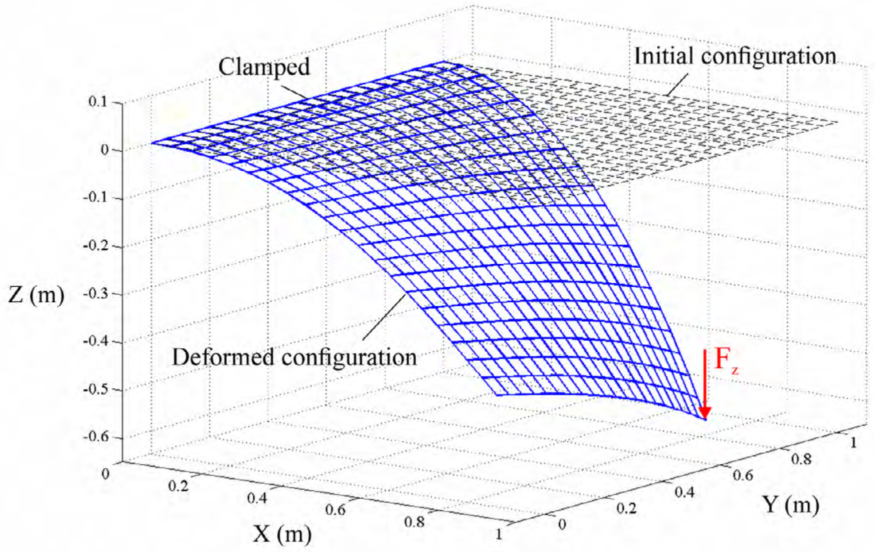

Figure 3.1 Deformed shape of a cantilevered plate subjected to a tip force

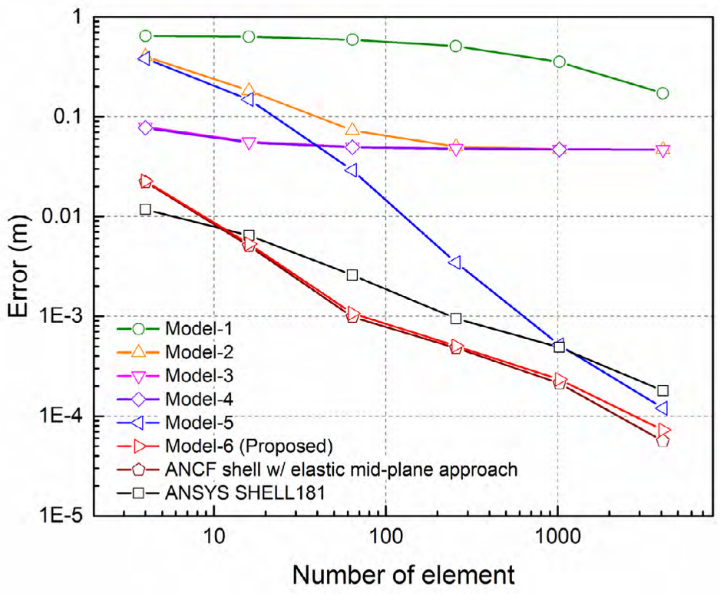

Figure 3.2 Numerical convergence of ANCF shell solutions: cantilevered plate subjected to a tip force with large deformation

Table 3.1 Strain modification for the continuum mechanics based ANCF bi-linear shell element

Model name	ANS for transverse shear strains ($\varepsilon_{xz}^{\mathrm{ANS}}, \varepsilon_{yz}^{\mathrm{ANS}}$)	EAS for in-plane strains ($\varepsilon_{xx}^{\mathrm{EAS}}, \varepsilon_{yy}^{\mathrm{EAS}}$, $\gamma_{xy}^{\mathrm{EAS}}$)	ANS for transverse normal strain ($\varepsilon_{zz}^{\mathrm{ANS}}$)	EAS for transverse normal strain ($\varepsilon_{zz}^{\mathrm{EAS}}$)	Combined EAS and EAS for transverse normal strain ($\varepsilon_{zz}^{\mathrm{ANS/EAS}}$)
Model-1	-	-	-	-	-
Model-2	Y	-	-	-	-
Model-3	Y	-	Y	-	-
Model-4	Y	Y	Y	-	-
Model-5	Y	Y	-	Y	-
Model-6	Y	Y	-	-	Y

To measure the accuracy, error in solution is defined by a deviation of the vertical deflection at the force application point on the plate from that of the reference solution obtained by ANSYS SHELL181 with 100×100 elements. The numerical convergence of the solution is presented in Fig. 3.2 for each model. The numerical result obtained by the bi-linear shear deformable ANCF plate element based on the elastic middle surface approach which is given in Appendix is also presented in this figure for comparison. It is observed from the comparison between Model-1 and Model-2 that the accuracy is improved by alleviating the transverse shear locking with the ANS approach. However, the solution is converged to the erroneous solution. While the use of the EAS for the in-plane shear/normal lockings and the ANS for the thickness locking slightly improve the rate of convergence, the convergent solutions are still incorrect. It is important to notice that use of Model-6 with the combined ANS and EAS approach leads to the same result with that of the locking-free ANCF plate element based on the elastic mid-plane approach shown in Appendix. This plate element employs ANS only for alleviating the curvature thickness locking. In other words, the strain modification used in the elastic mid-plane ANCF shell element corresponds to Model-4 in Table 3.1. However, Model-4 of the continuum mechanics based ANCF shell element leads to an erroneous solution due to the Poisson's locking. While the application of the EAS approach to the thickness locking improves the element performance as shown in the result of Model-5, the accuracy is not at satisfactory level especially when the small number of elements is used.

This result clearly indicates severity of the Poisson's locking exhibited in the continuum mechanics based shear deformable ANCF shell element and the locking for the continuum mechanics based ANCF shell element needs to be eliminated using the combined EAS and ANS approach as demonstrated by the result of Model-6.

In the second problem, the flat plate is replaced with the quarter cylinder modeled by the continuum mechanics based bi-linear ANCF shell elements as shown in Fig. 3.3, and the radius of curvature is assumed to be 1.0 m. The material properties, tip load, width and height are the same as the previous example. The deformed shape at the static equilibrium state is shown in Fig. 3.3 and the large deformation is exhibited in this problem. As in the previous example, error in solution is defined by a deviation of the vertical deflection at the force application point from that of the reference solution obtained by ANSYS SHELL181 with 100×100 elements. The numerical convergence in solution is presented in Fig. 3.4 for Models 1 to 6 and ANSYS SHELL181 for comparison. Furthermore, the numerical result obtained by the bi-linear shear deformable ANCF plate element based on the elastic middle surface approach is also presented in Fig. 3.3 for comparison. The overall trend of the numerical convergence of solutions obtained by different models is similar to that observed for the flat plate problem. The result clearly indicates that use of the combined EAS and ANS approach is necessarily to ensure the ideal rate of convergence and accuracy for the proposed shell element.

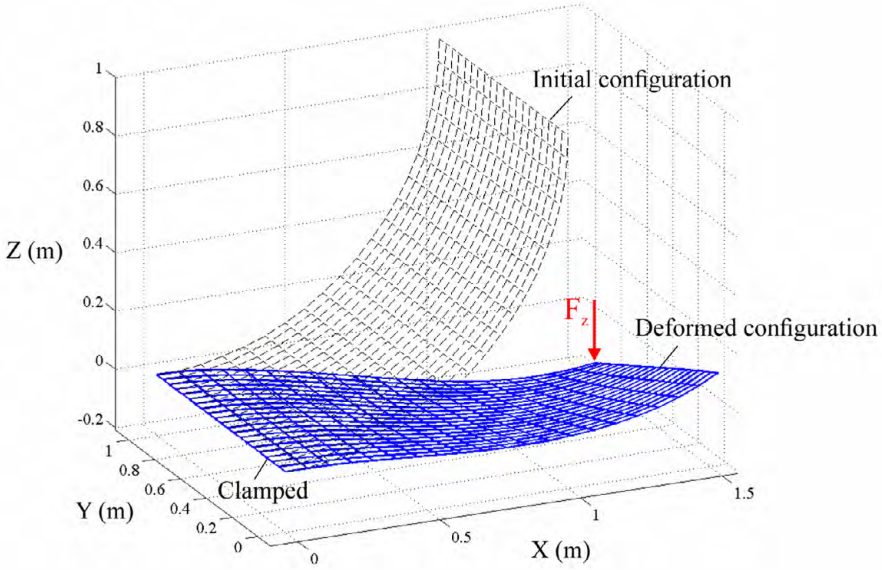

Figure 3.3 Deformed shape of a quarter cylinder subjected to a tip force

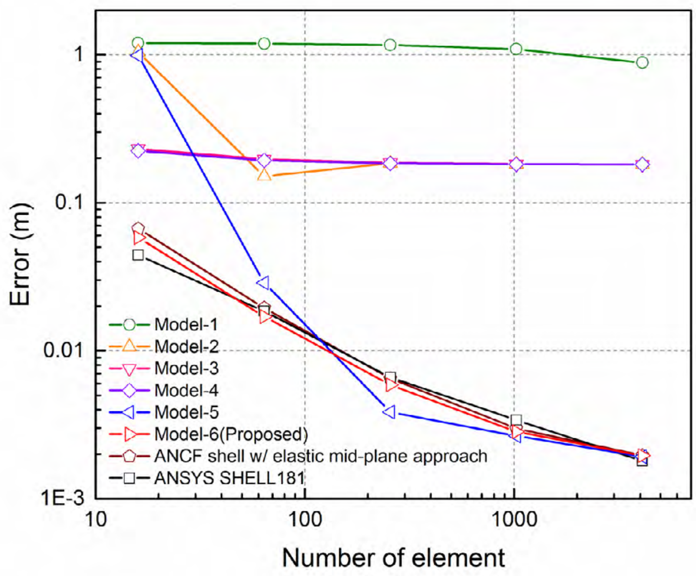

Figure 3.4 Numerical convergence of ANCF shell solutions:
quarter cylinder subjected to a tip force

3.1.2 Pinched Semi-Cylindrical Shell

A semi-cylindrical shell as shown in Fig. 3.5 subjected to a pinching force of 800 N at the middle of the free-hanging circumferential periphery is discussed. This problem is used as a benchmark problem for various shell elements [52,53,64,65] and the numerical solution obtained by the proposed continuum mechanics based bi-linear shear deformable shell element (Model-6) is compared with those in the literature [53,64,65]. The length, radius and thickness are assumed to be 3.048 m, 1.016 m and 0.03 m, respectively. Young's modulus and Poisson's ratio are assumed to be 2.0685×10^7 Pa and 0.3, respectively [52,53,64,65]. A quarter cylinder model with the symmetric boundary condition is used in the analysis. The deformed shape of the semi-cylindrical shell is shown in Fig. 3.5, and the nonlinear load-deflection curve shown in Fig. 3.6 agree well with those presented in the literature [53,64,65]. Use of the 16×16 elements leads to the convergent solution in the case of the continuum mechanics based bi-linear shear deformable ANCF shell element.

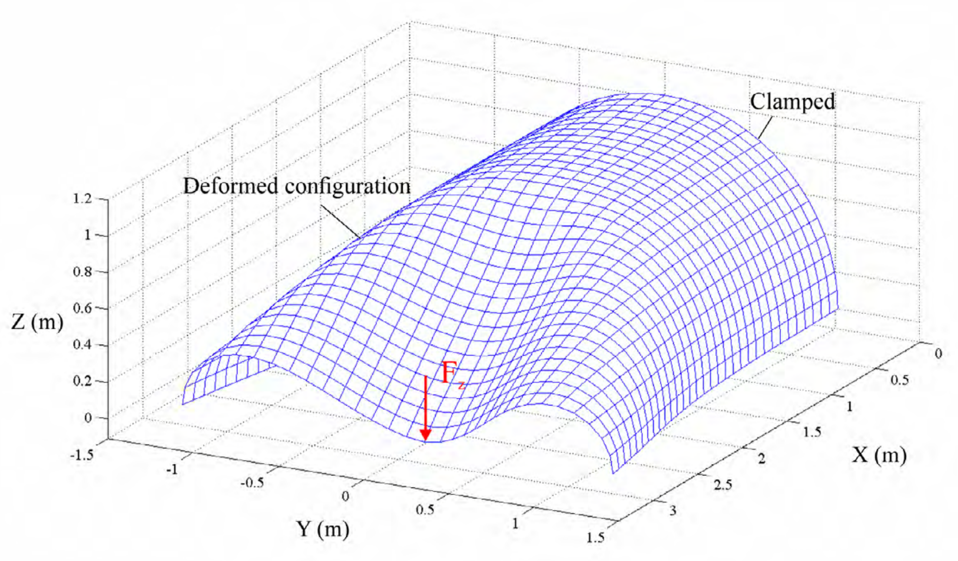

Figure 3.5 Deformed shape of pinched semi-cylindrical shell

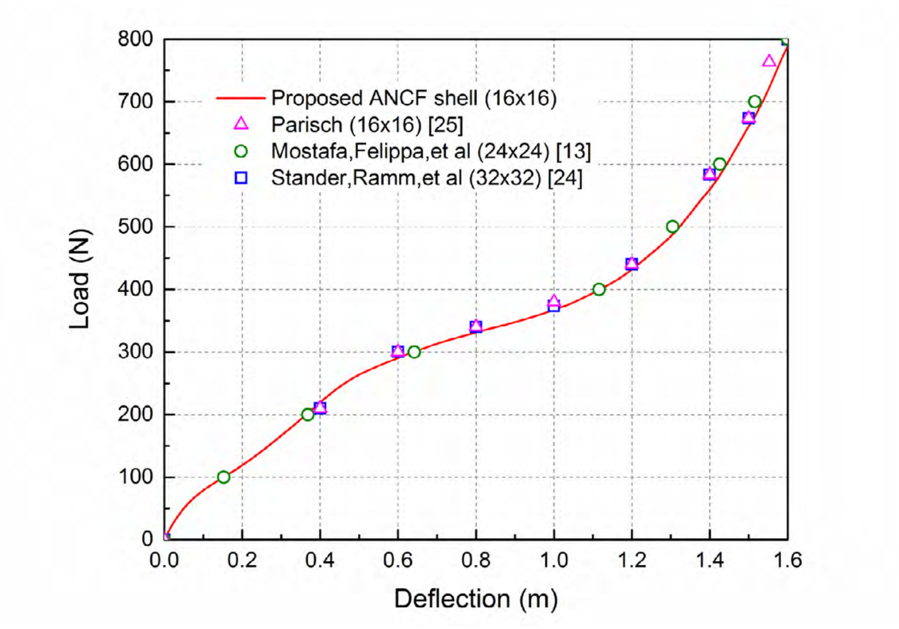

Figure 3.6 Load-deflection curve of pinched semi-cylindrical shell

3.1.3 Slit Annular Plate Subjected to Lifting Force

In the next example, a slit annular plate subjected to a lifting line force is considered as shown in Fig. 3.7. This problem is also widely used as a benchmark problem for shell elements [52]. The inside and outside radii of the annular plate are assumed to be 6.0 m and 10.0 m, respectively. Young's modulus and Poisson's ratio are assumed to be 2.1×10^{7} Pa and $\nu=0.0$, respectively [52]. One end of the slit is fully clamped, while the other end of the slit is subjected to the line force of 50 N. The load-deflection curves at Point A and B shown in Fig.3.8 are compared with those obtained using ANSYS SHELL181 with 10×60 elements as a reference solution and the results are in good agreement with those obtained by the continuum mechanics based bi-linear shear deformable ANCF shell element.

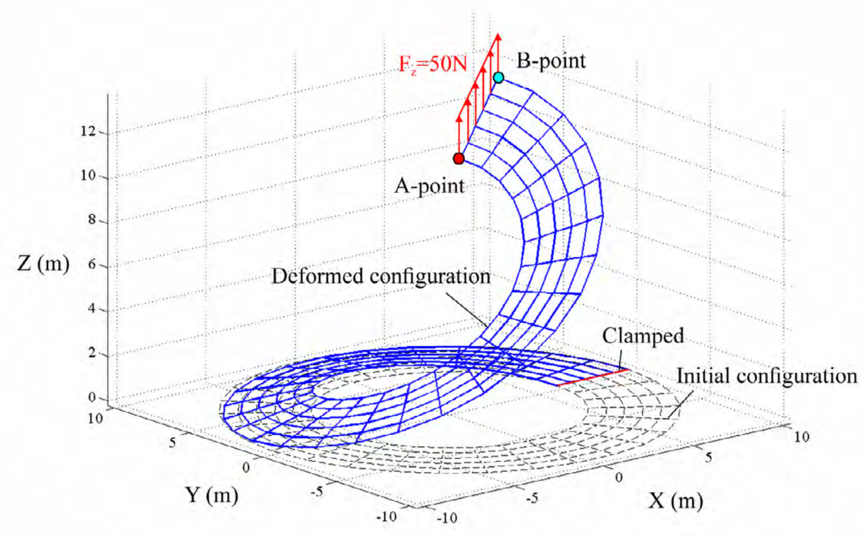

Figure 3.7 Deformed shape of slit annular plate subjected to lifting force

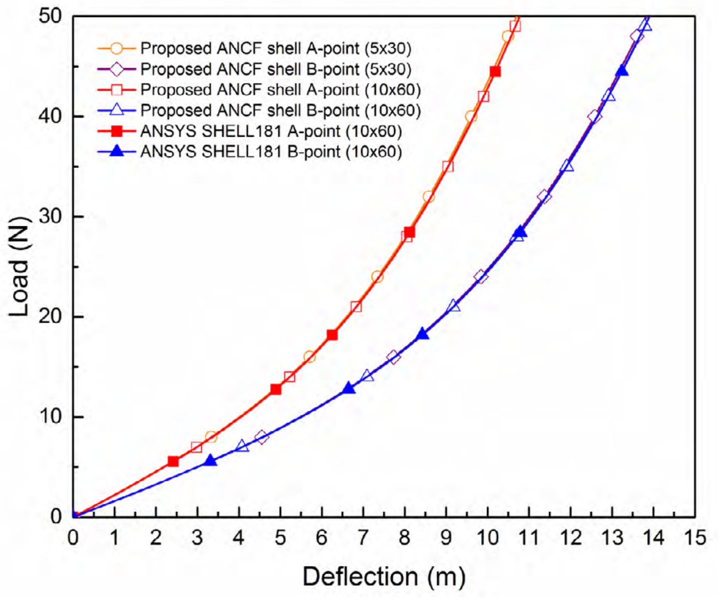

Figure 3.8 Load-deflection curve of slit annular plate subjected to lifting force

3.2 Numerical Examples of Laminated Composite Shell Element

In this section, the element accuracy of the shear deformable laminated composite shell element is discussed.

3.2.1 Extension and In-Plane Shear Coupling of Fiber-Reinforced Plate Subjected to Uniaxial Tensile Load

To discuss the extension and in-plane shear coupling of a fiber-reinforced rubber material, a uniaxial tension test as shown in Fig. 3.9 (a) is considered using the shear deformable ANCF shell element. The length, width and thickness of the plate are 2.0 m, 1.0 m, and 0.01 m, respectively. Young's modulus of the fiber and those of the matrix are, respectively, assumed to be $E_x = 1.8 \times 10^{11}$ Pa and $E_y = E_z = 1.3333 \times 10^7$ Pa. The shear modulus of rigidity and Poisson's ratio are assumed to be $G_{xy} = \mathrm{G}_{xz} = \mathrm{G}_{yz} = 3.33333 \times 10^6$ Pa and $\nu_{xy} = \nu_{xz} = \nu_{yz} = 0.4$, respectively. The tensile distributed uniaxial load of 5000 N/m is applied in the *X* direction. The in-plane shear strain of the plate is presented in Fig. 3.10 as a function of the fiber angle θ. In this figure, the in-plane shear strain obtained by the composite shell element is compared with the analytical solution given by [5]

$$\gamma_{xy} = \sin 2\theta \left(\frac{\cos^2\theta}{E_1} - \frac{\sin^2\theta}{E_2} + \frac{1}{2}\left(\frac{2\nu_{12}}{E_1} - \frac{1}{G_{12}} \right) \cos 2\theta \right) \sigma_x \tag{3.1}$$

It is observed from the preceding equation that the change in the shear strain is nonlinear in the fiber angle θ. The sign of the shear strain changes at $\theta = 54.7$ degrees [5] as shown by the magnified deformed shapes at $\theta = 20$, 54.7 and 70 degrees in Fig. 3.10. The results obtained by the ANCF shell element agree well with the analytical solution based on the assumption of Kirchhoff plate theory with infinitesimal deformation. Furthermore, using Eq. 3.1 the inflection points of the in-plane shear strain are obtained at $\theta = 25.5$ and 71.3 degrees, and they are also well predicted using the composite shell element discussed in this study.

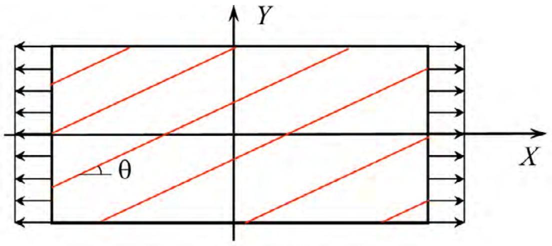

(a) One-layer orthotropic plate

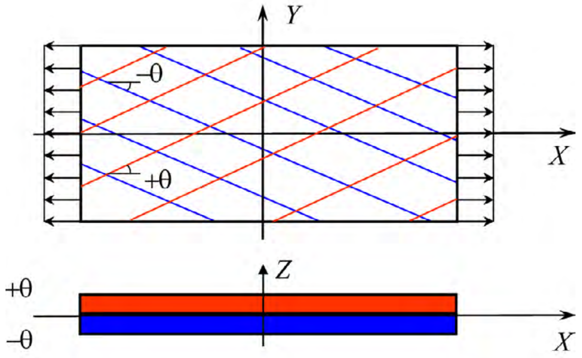

(b) Two-layer laminated composite plate

Figure 3.9 Uniaxial tensile test models

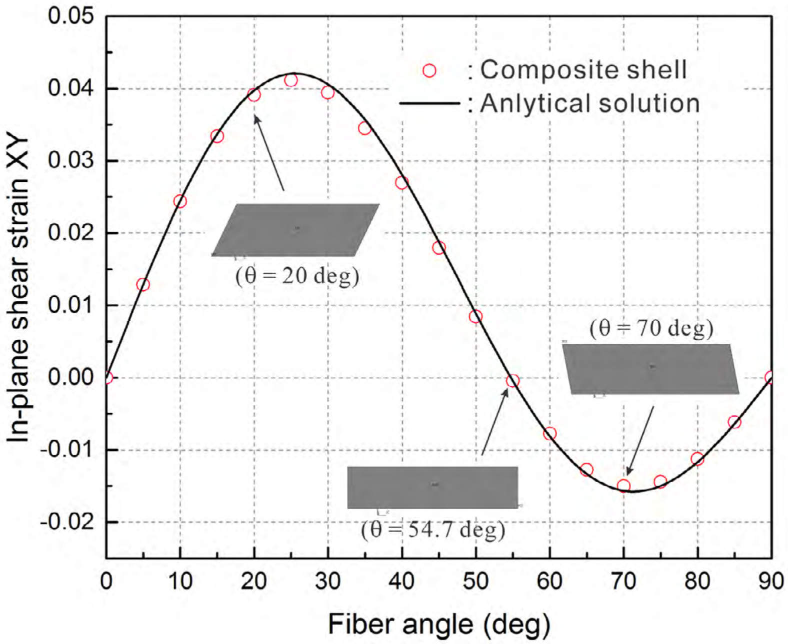

Figure 3.10 In-plane shear strain of one-layer orthotropic plate

3.2.2 Warpage of Two-Layer Laminated Composite Plate Subjected to Uniaxial Tensile Load

In the next example, a uniaxial tensile test of a two-layer laminate at $+/-\theta$ fiber angles is considered as shown in Fig. 3.9 (b) [60]. The length, width and thickness of the plate are same as the previous example in Section 3.1. The thicknesses of each layer is 0.005 m. The fiber angles of the upper and lower layers are same in magnitude, but opposite in direction as shown in Fig. 3.9 (b). The material properties of each layer are also same as the previous example in Section 3.2.1. The tensile distributed uniaxial load of 500 N/m is applied in the X direction. In this problem, the extension and bending/twisting coupling occurs in this laminate, and it causes the warpage (twisting) under the uniaxial tensile loading [60]. While the extension and shear coupling occurs in each lamina, shear deformation of the upper and lower layers caused by the uniaxial tensile load are same in magnitude, but opposite in direction. Thus, the shear deformations of both layers are canceled out and no in-plane shearing occurs in the laminated composite. To demonstrate this fundamental coupling behavior of the laminated composite material, the twisting angle and the in-plane shear strain of the two-layer laminated composite plate are presented in Fig. 3.11 as a function of the fiber angle θ. In this figure, results obtained by the laminated composite shell element are compared with the analytical model based on the classical lamination theory. In the analytical model, the warpage is defined by [60]

$$w = -\frac{1}{2}\left(\kappa_x x^2 + \kappa_y y^2 + \kappa_{xy} xy\right) \tag{3.2}$$

where the curvatures are determined by solving equilibrium equations of the force and moment resultants of fiber-reinforced composite [60]. It is observed from Fig. 3.11 that the twisting angles agree well with those based on the classical lamination theory, and the warpage developed by the uniaxial tensile load applied to the two-layer laminated composite plate is well predicted. The sign of the twisting angle of the composite plate changes at the fiber angle of $\theta = 54.7$ degrees [5], and this important fiber angle is also correctly predicted. Furthermore, zero in-plane shear strain is ensured in the results regardless of the fiber angle, and this result agrees with that of the analytical model based on the classical lamination theory.

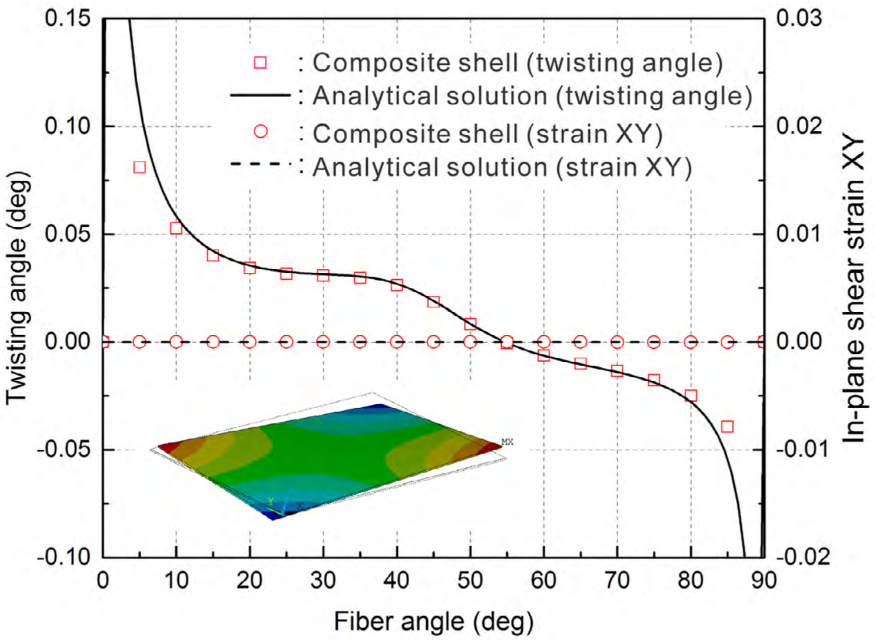

Figure 3.11 Twisting angle and in-plane shear strain of two-layer laminated composite plate subjected to uniaxial tensile load

3.2.3 Cantilevered Two-Layer Composite Shell Subjected to a Point Load

To demonstrate the accuracy of the composite shell element for large deformation problem of initially curved shell structures, a cantilevered quarter cylinder modeled by $+/-\theta$ two-layer composite shell is considered as shown in Fig. 3.12. The initial shape and the location of a subjected point load is the same as Section 3.1.1 shown in Fig. 3.3. The fiber angle of each layer is assumed to be 20°. The radius of curvature is assumed to be 1.0 m. The width and height are assumed to be 1.0 m and 0.01 m (i.e., 0.005 m thickness for each layer). Young's modulus of the fiber and those of the matrix are, respectively, assumed to be $E_x = 2.0 \times 10^8$ Pa and $E_y = E_z = 1.0 \times 10^8$ Pa. The shear modus of rigidity and Poisson's ratio are assumed to be $G_{xy} = \mathrm{G}_{xz} = \mathrm{G}_{yz} = 3.84615 \times 10^7$ Pa and $\nu_{xy} = \nu_{xz} = \nu_{yz} = 0.3$, respectively. The vertical point load of 10 N is applied to the corner of the shell as shown in Fig. 3.12. The deformed shape at the static equilibrium state is shown in Fig. 3.12, in which the large deformation is exhibited. The static deflections of the load application point obtained by the laminated composite shell element are compared with those of the shear deformable composite shell element of ANSYS (SHELL181) [63] in Table 3.2 for different number of elements. It is demonstrated in this Table that good agreements in solution are obtained with the MITC shell formulation [63] implemented in ANSYS. The numerical convergence of the finite element solutions are presented in Fig. 3.13 for errors defined by the deviation from the reference solution, where the reference solution of -0.80517 m is obtained by 100×100 elements using the ANSYS SHELL181 composite shell element. It is observed from this figure that the ideal linear rate of convergence is ensured in both models for the large deformation problem and it indicates that element lockings are properly eliminated in the ANCF laminated composite shell element discussed in this study. On the other hand, the fully parameterized ANCF shell element utilizing the bi-cubic polynomial does not converge to the reference solution, despite the fact that higher order polynomials are used due to the element lockings exhibited. Furthermore, the number of integration points for the elastic force calculation of each layer is 8 $(2\times2\times2)$ in the bi-linear shell element having 24 nodal coordinates per element, while 32 $(4\times4\times2)$ integration points are used in the bi-cubic fully parameterized shell element with 48 nodal coordinates per element. This has a significant impact on the computational efficiency for large scale problems including tire simulation.

Table 3.2 Static deflection of cantilevered two-layer composite shell subjected to point load (m)

Number of elements	ANCF composite shell	ANSYS composite shell (SHELL181)
4×4	-0.77157	-0.78262
8×8	-0.79931	-0.79786
16×16	-0.80310	-0.80220
32×32	-0.80414	-0.80619
50×50	-0.80452	-0.80473
64×64	-0.80469	-0.80493

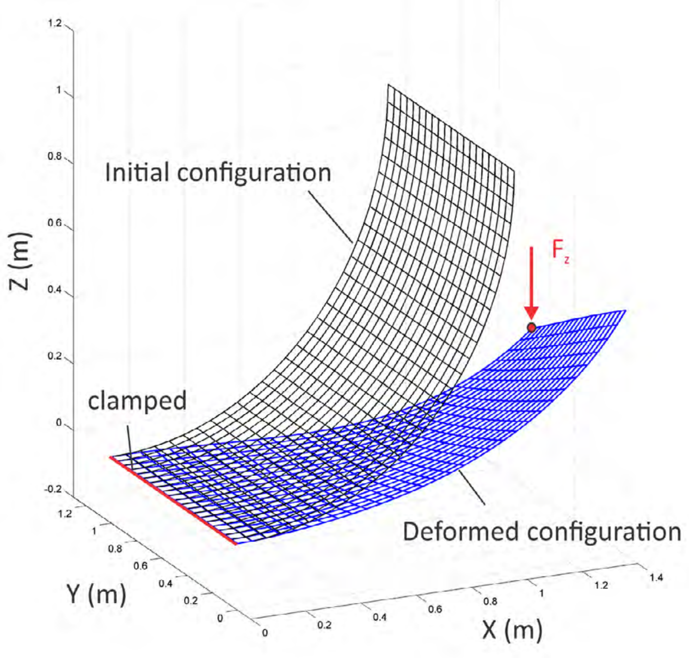

Figure 3.12 Deformed shape of cantilevered two-layer composite shell subjected to point load

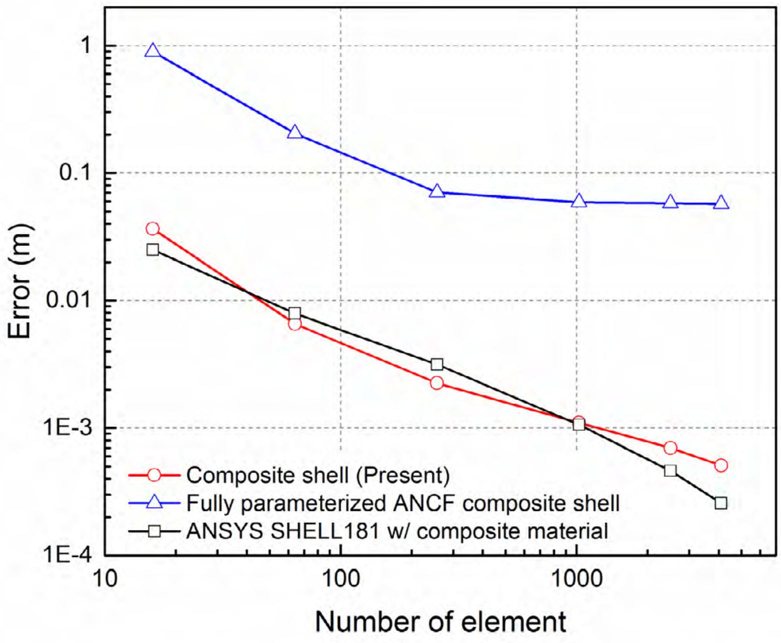

Figure 3.13 Numerical convergence of finite element solutions

3.2.4 Natural Frequencies of Laminated Composite Plate

The eigenfrequency analysis of the $+/-\theta$ two-layer composite plate is considered in this example. The fiber angle of each layer is assumed to be 20°. A free boundary condition is assumed. The length, width and thickness of the plate are 1.0 m, 1.0 m, and 0.01 m (i.e., 0.005 m thickness for each layer), respectively. Young's modulus of the fiber and those of the matrix are, respectively, assumed to be $E_x = 6.0\times10^7$ Pa and $E_y = E_z = 3.0\times10^7$ Pa. The shear modus of rigidity and Poisson's ratio are assumed to be $G_{xy} = \mathrm{G}_{xz} = \mathrm{G}_{yz} = 1.1538\times10^7$ Pa and $\nu_{xy} = \nu_{xz} = \nu_{yz} = 0.3$, respectively. The material density is assumed to be 500 kg/m^3. The first ten eigenfrequencies and their mode shapes are shown in Table 3.3 and Fig. 3.14, respectively. The eignfrequencies are compared with the reference solutions obtained by the 100×100 elements using the ANSYS SHELL181 composite shell element. The eigenfrequencies are also in good agreement with the reference solutions. Use of the proposed low-order continuum mechanics based shear deformable shell element leads to better rate of convergence than the higher-order fully parameterized ANCF element presented in literature [30].

Table 3.3 First ten eigenfrequencies of the laminated composite shell (Hz)

ANCF composite shell 2×2	ANCF composite shell 4×4	ANCF composite shell 8×8	ANCF composite shell 16×16	ANCF composite shell 32×32	ANSYS composite shell (SHELL181) 100×100
1.8168	1.7705	1.7385	1.7291	1.7295	1.7175
2.9444	2.6214	2.4887	2.4518	2.4296	2.4424
4.3411	3.7085	3.4579	3.3853	3.3642	3.3700
4.8487	4.6450	4.4097	4.3355	4.3088	4.2951
5.4240	5.0939	4.8413	4.7605	4.7412	4.7220
9.1235	9.3139	7.7790	7.2886	7.1604	7.1146
116.4075	9.7130	8.5528	8.3152	8.2496	8.2005
127.6218	10.7920	9.2868	8.8343	8.7120	8.6442
133.0542	12.3383	9.8813	9.2463	9.0973	9.0559
141.4632	14.1086	11.5408	10.8417	10.6750	10.6080

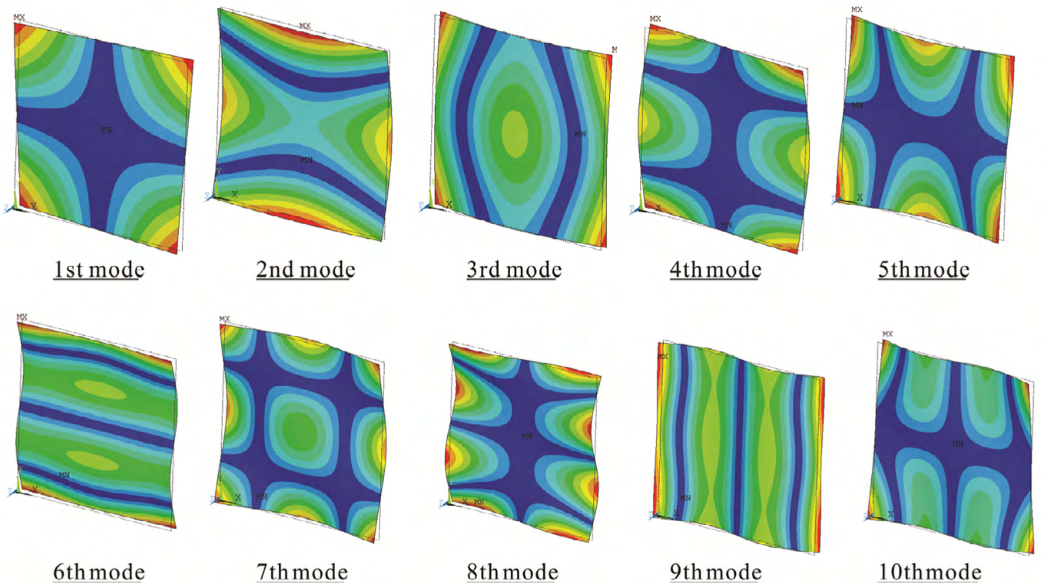

1st mode 2nd mode 3rd mode 4th mode 5th mode

6th mode 7th mode 8th mode 9th mode 10th mode

Figure 3.14 Vibration mode shapes of two-layer laminated composite shell

3.2.5 Quarter Cylinder Pendulum with Laminated Composite Material

In the last numerical example in this section, the nonlinear dynamic analysis of the $+/-\theta$ two-layer laminated composite shell structure (a quarter cylinder pendulum) is discussed as shown in Fig. 3.15. The radius of curvature is assumed to be 1.0 m. The fiber angle of each layer is assumed to be 20° and the material property including the material density of each layer is same as that of the previous example in Section 3.2.4. One corner of the composite quarter cylinder is connected to the ground by a spherical joint. HHT time integrator is used with variable step size [67], while the EAS parameters are determined at the element level at every time step as discussed in Chapter 2. The maximum step size for error control specified in this example is 1E-3 s. The deformed shapes under the effect of gravity are shown in Fig. 3.15, in which large deformation is observed. The global *X*, *Y* and *Z* positions at the corner point shown by a red circle in Fig. 3.15 are presented in Figs.3.16, 17 and 18, respectively. Despite the highly nonlinear dynamics problem involving the large deformation of composite materials, the numerical solution obtained by 10×10 elements are close to those of 30×30 elements.

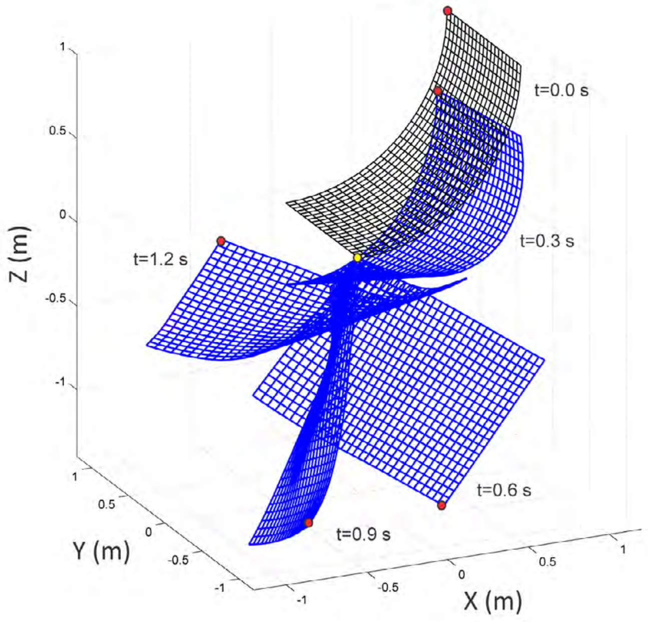

Figure 3.15 Deformed shapes

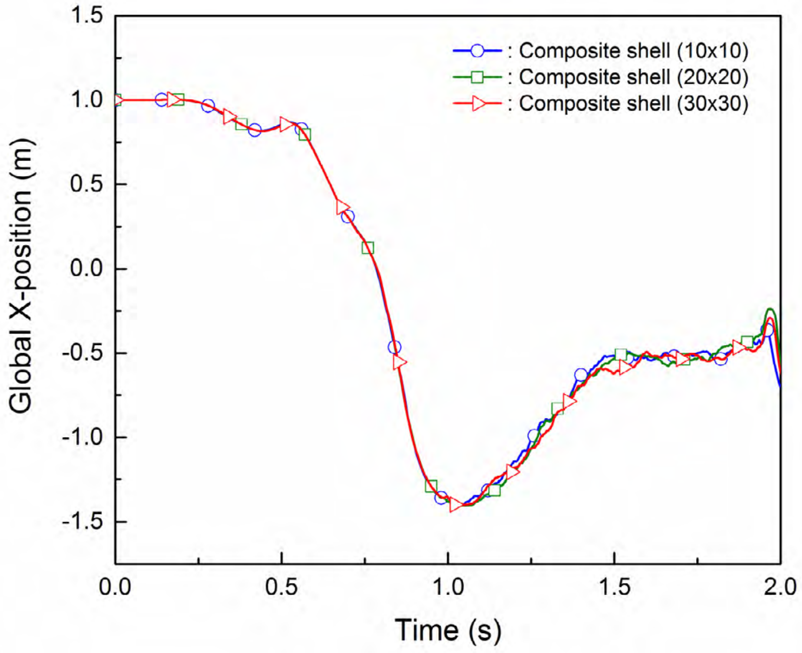

Figure 3.16 Global X-position at the tip point

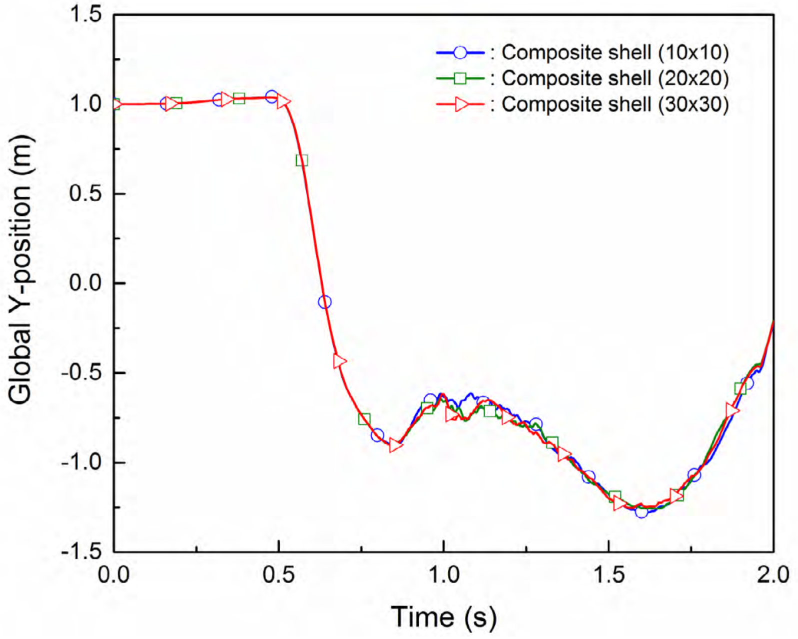

Figure 3.17 Global Y-position at the tip point

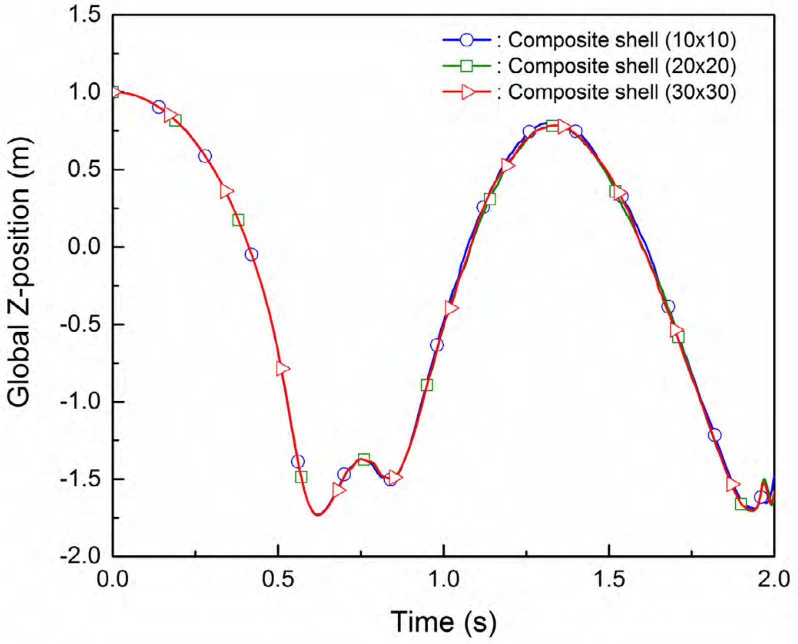

Figure 3.18 Global Z-position at the tip point

CHAPTER 4

PHYSICS-BASED FLEXIBLE TIRE MODEL FOR TRANSIENT BRAKING AND CORNERING ANALYSIS

4.1 Introduction

In this chapter, a high fidelity physics-based finite element tire model is developed using the shear deformable laminated composite shell element based on the absolute nodal coordinate formulation discussed in Chapter 2 and 3 for use in the transient braking and cornering analysis of multibody vehicle systems [66]. To account for the transient tire force characteristics, the distributed parameter LuGre tire friction model is introduced and then integrated into the physics-based flexible tire model. Using the LuGre tire friction model, the dynamic friction effect is modeled by the first order partial differential equation in terms of an internal friction parameter and, therefore, the history-dependent friction-induced hysteresis can be considered [68,69]. It is shown that the nonlinear structural tire deformation due a large load transfer in the severe maneuvers and the transient tire force characteristics are fully coupled in the final form of the governing equations. Furthermore, a modified friction characteristic curve function is proposed for wet road conditions, in which the linear decay in friction is exhibited in the large slip velocity range.

4.2 Structural Tire Model Using Laminated Composite Shell Element

4.2.1 Modeling of Tire Structure with Cord-Rubber Composite Materials

A tire has a complex structure that consists of layers of plies and steel belts that are embedded in rubber, thus an accurate modeling of the complex tire geometry and the anisotropic material properties is essential to the tire performance evaluation including the tire contact pressure and the braking/traction and cornering forces. While the in-plane tire belt deformation can be modeled by an equivalent material model [31,32], such a simplified material model cannot be used for predicting the overall tire structural deformation in the three-dimensional analysis. This is attributed to the fact that the tire section property in both geometry and material is of crucial importance in characterizing the contact pressure distribution.

In order to develop a physics-based flexible tire model, the tire cross section geometry is imported from the tire cut section and data points are interpolated by a cubic smoothing spline to extract the nodal position and slope coordinates. As shown in Fig. 4.1, the tire cross-section is divided into the tread, sidewall, and bead sections. The number of layers, cord angles, thickness, and material properties, which vary through the tire structure, are provided in each section to create the tire model data as shown in Fig. 4.1. The tread section consists of a carcass ply, two steel belts, a belt cover, and tread blocks. The carcass ply and steel belt are modeled as an orthotropic material with polyester and steel cords embedded in rubber, respectively. A rubber layer is considered between the upper and lower steel belts and between the carcass ply and the lower steel belt, and these rubber layers are modeled by Mooney-Rivlin material in the laminated composite shell element. The sidewall section is modeled by two carcass ply layers and a rubber layer that lies in between. The bead section is modeled by two carcass ply layers, a steel belt, and a rubber layer as shown in Fig. 4.2. Having created the cross-section geometry and material properties, the three-dimensional tire model data including the nodal position and slope coordinates is generated by rotating the tire section model as summarized in Fig. 4.1.

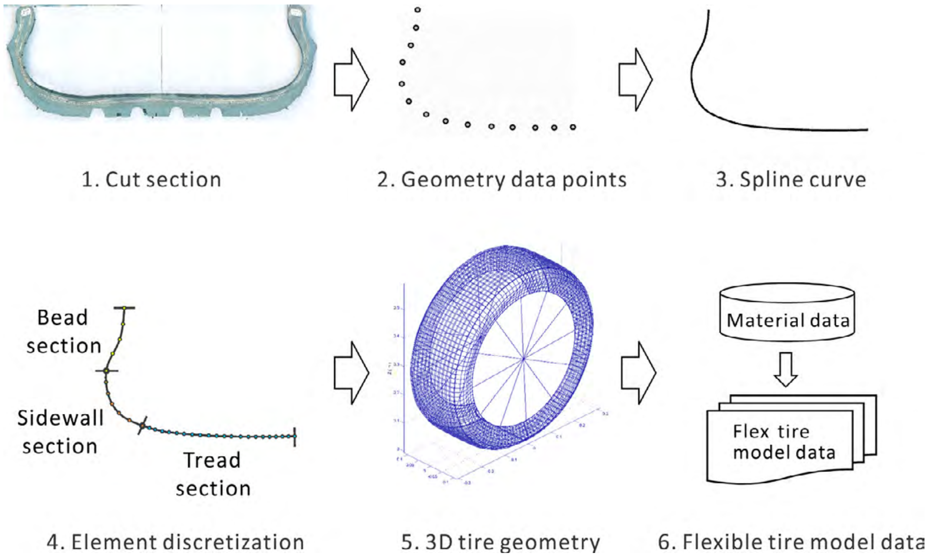

1. Cut section 2. Geometry data points 3. Spline curve

4. Element discretization 5. 3D tire geometry 6. Flexible tire model data

Figure 4.1 Tire model creation procedure

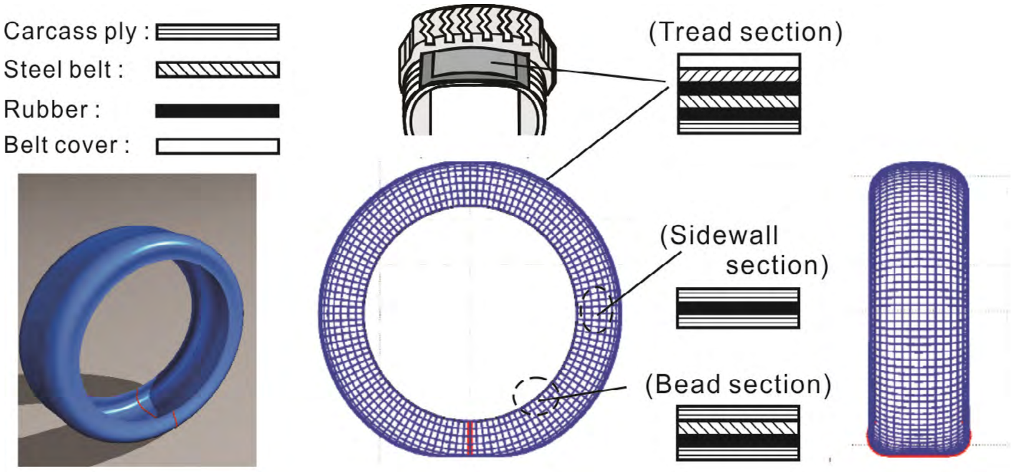

Figure 4.2 Physics-based tire model using the laminated composite shell element

4.2.2 Modeling of Air Pressure

The internal air pressure is modeled by the distributed load acting in the direction normal to the deformable inner tire surface, and the generalized force vector of element *i* for the air pressure is defined as

$$\mathbf{Q}_p^i = \int_a (\mathbf{S}^i)^T \mathbf{F}_p^i da^i \tag{4.1}$$

where $\mathbf{S}^i$ is the shape function of the shell element introduced in Section 2, da is the infinitesimal area at the current configuration, and

$$\mathbf{F}_p^i = f_p \mathbf{n}^i \tag{4.2}$$

In the preceding equation, f_p defines the air pressure and the unit normal is defined as

$$\mathbf{n}^i = \frac{\partial \mathbf{r}^i / \partial x^i \times \partial \mathbf{r}^i / \partial y^i}{\left| \partial \mathbf{r}^i / \partial x^i \times \partial \mathbf{r}^i / \partial y^i \right|} \tag{4.3}$$

Gaussian integration is used for the spatial integral of Eq 4.1. It is important to note here that the integral over the current area da^i is converted to that over the area at the reference configuration dA^i using Nanson's formula $da^i = \left(\det \mathbf{J}^i \Big/ \sqrt{(\mathbf{n}^i)^T \mathbf{J}^i (\mathbf{J}^i)^T \mathbf{n}^i} \right) dA^i$, where $\mathbf{J}^i$ is the position vector gradient tensor at the reference configuration. If the deformation is small, one can assume $da^i \approx dA^i$.

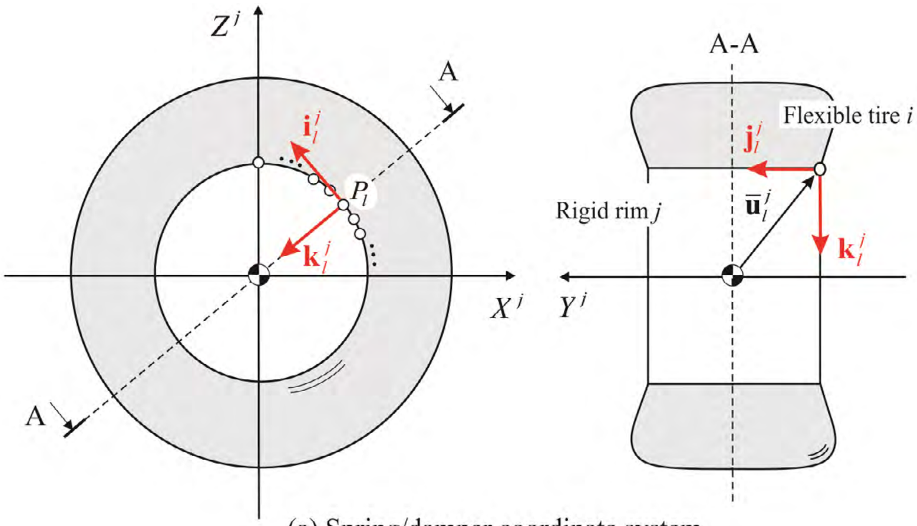

(a) Spring/damper coordinate system

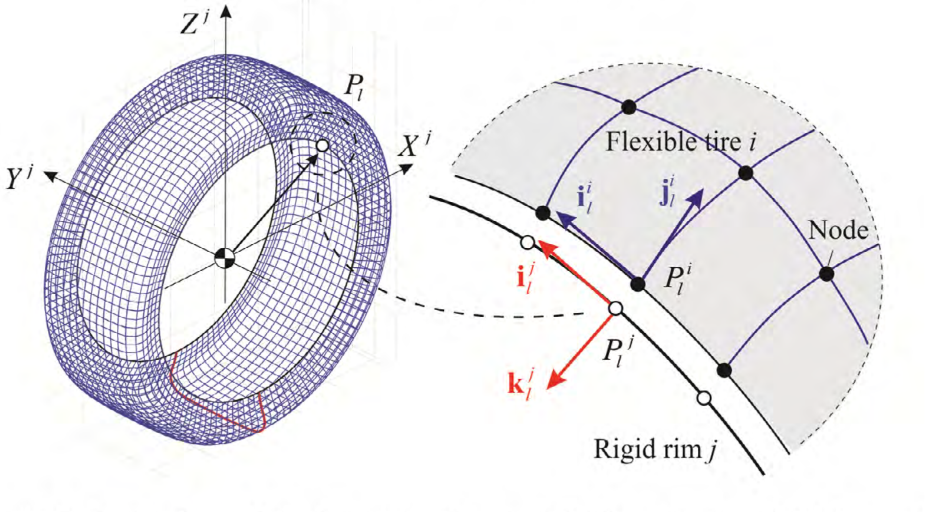

(b) Reference frame defined at spring/damper definition point l on shell element i

Figure 4.3 Assembly of flexible tire and rigid rim

4.2.3 Assembly of Flexible Tire and Rigid Rim

The bead part of the finite element tire model is connected to the rigid rim by multiple spring and damper elements as shown in Fig. 4.3. For a spring and damper element defined at point P_l^i on the finite element i of the deformable tire model, the global position vector is defined by $\mathbf{r}_l^i = \mathbf{S}^i(x_l^i, y_l^i, z_l^i)\mathbf{e}^i$ and the nodal point can also be selected as the force definition point. This point is connected to point P_l^j on the rigid rim j and the global position vector of this point on the rigid rim is written by $\mathbf{r}_l^j = \mathbf{R}^j + \mathbf{A}^j \bar{\mathbf{u}}_l^j$, where $\mathbf{R}^j$ is the global position vector of the origin of the body coordinate system of rigid rim j, $\mathbf{A}^j$ is the rotation matrix, and $\bar{\mathbf{u}}_l^j$ is the local position vector that defines the point P_l^j on the rigid rim j. Note that the subscript l indicates l-th force definition point along the circumference of the tire bead. The spring/damper coordinate system on the rigid rim at point l is given as follows:

$$\mathbf{A}_l^j = \mathbf{A}^j \bar{\mathbf{A}}_l^j \tag{4.4}$$

where $\bar{\mathbf{A}}_l^j$ defines the local spring/damper coordinate system defined with respect to the body coordinate system of rim body j. This coordinate system is defined such that the X-axis is tangent to circumference of the rim, while the Z-axis is aligned in a radial direction of the rim as shown in Fig. 4.3 (a). On the other hand, the spring/damper coordinate system at point P_l^i on the finite element i of the flexible tire model is defined using the gradient coordinates as shown in Fig. 4.3 (b) as follows:

$$\mathbf{A}_l^i = \begin{bmatrix} \mathbf{i}_l^i & \mathbf{j}_l^i & \mathbf{k}_l^i \end{bmatrix} \tag{4.5}$$

where

$$\mathbf{i}_l^i = \mathbf{j}_l^i \times \mathbf{k}_l^i, \quad \mathbf{j}_l^i = \frac{\partial \hat{\mathbf{r}}_l^i / \partial z^i \times \partial \hat{\mathbf{r}}_l^i / \partial x^i}{\left| \partial \hat{\mathbf{r}}_l^i / \partial z^i \times \partial \hat{\mathbf{r}}_l^i / \partial x^i \right|}, \quad \mathbf{k}_l^i = \frac{\partial \mathbf{r}_l^i / \partial z^i}{\left| \partial \mathbf{r}_l^i / \partial z^i \right|} \tag{4.6}$$

In the preceding equation, $\partial \hat{\mathbf{r}}_l^i / \partial z^i$ and $\partial \hat{\mathbf{r}}_l^i / \partial x^i$, respectively, indicate unit vectors of the global position vector gradients $\partial \mathbf{r}_l^i / \partial z^i$ and $\partial \mathbf{r}_l^i / \partial x^i$. Accordingly, the relative deformation and deformation rate between the point P_l^i on the finite element i and P_l^j on the rigid rim j are defined with respect to the local spring/damper coordinate system attached to the rigid rim j as follows:

$$\bar{\boldsymbol{\delta}}_l^{ij} = (\mathbf{A}_l^j)^T \left(\mathbf{r}_l^i - \mathbf{r}_l^j \right) \quad \text{and} \quad \dot{\bar{\boldsymbol{\delta}}}_l^{ij} = (\mathbf{A}_l^j)^T \left(\dot{\mathbf{r}}_l^i - \dot{\mathbf{r}}_l^j \right) \tag{4.7}$$

Furthermore, the relative rotation matrix of the spring/damper coordinate system of the finite element i with respect to the spring/damper coordinate system of the rigid rim j is defined as follows:

$$\mathbf{A}_l^{ij} = (\mathbf{A}_l^j)^T \mathbf{A}_l^i \tag{4.8}$$

From which, relative rotation angles $\bar{\boldsymbol{\theta}}_l^{ij} = \begin{bmatrix} \bar{\theta}_x^{ij} & \bar{\theta}_y^{ij} & \bar{\theta}_z^{ij} \end{bmatrix}^T$ about the three axes can be extracted from the relative rotation matrix $\mathbf{A}_l^{ij}$ and used for defining the restoring torque about each axis. Rotational deformation rate can be defined as

$$\bar{\boldsymbol{\omega}}_l^{ij} = (\mathbf{A}_l^{j})^T \left(\boldsymbol{\omega}_l^{i} - \boldsymbol{\omega}^{j} \right) \tag{4.9}$$

where $\boldsymbol{\omega}_l^i$ and $\boldsymbol{\omega}^j$ are the angular velocity vectors of the force application point l on the shell element i and rigid rim j, respectively. It is important to notice here that $\boldsymbol{\omega}_l^i$ can be obtained from the skew-symmetric matrix $\tilde{\boldsymbol{\omega}}_l^i = \dot{\mathbf{A}}_l^i (\mathbf{A}_l^i)^T$. It is important to notice here that $\boldsymbol{\omega}_l^i$ can be obtained from the skew-symmetric matrix

$$\tilde{\boldsymbol{\omega}}_l^i = \dot{\mathbf{A}}_l^i (\mathbf{A}_l^i)^T \tag{4.10}$$

where the time derivative of the tangent frame is given as

$$\dot{\mathbf{A}}_l^i = \begin{bmatrix} \dot{\mathbf{i}}_l^i & \dot{\mathbf{j}}_l^i & \dot{\mathbf{k}}_l^i \end{bmatrix} \tag{4.11}$$

In the preceding equation, one has

$$\left.\begin{aligned} \dot{\mathbf{i}}_l^i &= \dot{\mathbf{j}}_l^i \times \mathbf{k}_l^i + \mathbf{j}_l^i \times \dot{\mathbf{k}}_l^i \\ \dot{\mathbf{j}}_l^i &= \frac{1}{\sin\alpha}\left(\dot{\hat{\mathbf{r}}}_z^i \times \hat{\mathbf{r}}_x^i + \hat{\mathbf{r}}_z^i \times \dot{\hat{\mathbf{r}}}_x^i \right) - \frac{\cos\alpha}{\sin^2\alpha}\left(\hat{\mathbf{r}}_z^i \times \hat{\mathbf{r}}_x^i \right)\dot{\alpha} \\ \dot{\mathbf{k}}_l^i &= \frac{1}{\sqrt{\mathbf{r}_z^{i^T}\mathbf{r}_z^i}}\left(\mathbf{I} - \left(\mathbf{r}_z^{i^T}\mathbf{r}_z^i \right)^{-1} \left(\mathbf{r}_z^i \mathbf{r}_z^{i^T} \right) \right) \dot{\mathbf{r}}_z^i \end{aligned}\right\} \tag{4.12}$$

where $\mathbf{r}_z^i = \partial \mathbf{r}^i / \partial z^i$; $\mathbf{r}_x^i = \partial \mathbf{r}^i / \partial x^i$; $\dot{\alpha} = (\partial\alpha / \partial \mathbf{r}_z^i) \cdot \dot{\mathbf{r}}_z^i + (\partial\alpha / \partial \mathbf{r}_x^i) \cdot \dot{\mathbf{r}}_x^i$; $\cos\alpha = \hat{\mathbf{r}}_z^{i^T} \hat{\mathbf{r}}_x^i$; $\partial\alpha / \partial \mathbf{r}_z^i = (-1/\sin\alpha) \dot{\mathbf{r}}_x^{i^T} (\partial \hat{\mathbf{r}}_z^i / \partial \mathbf{r}_z^i)$; and $\partial\alpha / \partial \mathbf{r}_x^i = (-1/\sin\alpha) \dot{\mathbf{r}}_z^{i^T} (\partial \hat{\mathbf{r}}_x^i / \partial \mathbf{r}_x^i)$.

Using the deformation and deformation rate at the spring and damper definition point, the spring and damping forces and torques defined with respect to the local spring and damper coordinate system are defined as follows:

$$\bar{\mathbf{F}}_l^{ij} = -\mathbf{K}_r \bar{\boldsymbol{\delta}}_l^{ij} - \mathbf{C}_r \dot{\bar{\boldsymbol{\delta}}}_l^{ij} \quad \text{and} \quad \bar{\mathbf{N}}_l^{ij} = -\mathbf{K}_\theta (\bar{\boldsymbol{\theta}}_l^{ij} - \bar{\boldsymbol{\theta}}_{0l}^{ij}) - \mathbf{C}_\theta \bar{\boldsymbol{\omega}}_l^{ij} \tag{4.13}$$

where $\mathbf{K}_r$ and $\mathbf{K}_\theta$ are the translational and rotational spring constant matrices, while $\mathbf{C}_r$ and $\mathbf{C}_\theta$ are translational and rotational damping coefficient matrices, respectively. $\bar{\boldsymbol{\theta}}_{0l}^{ij}$ is the initial relative rotation angle vector of the spring/damper coordinate systems at P_l^i

and P_l^j . The preceding force and torque vectors are defined with respect to the global coordinate system as

$$\begin{bmatrix} \mathbf{F}_l^{ij} \\ \mathbf{N}_l^{ij} \end{bmatrix} = \begin{bmatrix} \mathbf{A}_l^j \overline{\mathbf{F}}_l^{ij} \\ \mathbf{A}_l^j \overline{\mathbf{N}}_l^{ij} \end{bmatrix} \tag{4.14}$$

and then the generalized forces can be obtained for both element i and rigid rim j using the virtual work.

4.3 LuGre Tire Friction Model

4.3.1 LuGre Tire Friction Model for Combined Slip

In existing deformable tire models, the steady-state tire friction model are widely used and the tire frictional force is defined by the product of the friction coefficient and the normal contact force at discretized points in the contact patch. The friction coefficient is defined in many cases as a multi-variable function of the contact pressure, slip velocity, temperature, etc. While such a frictional contact model leads to a straightforward implementation, it requires a large set of test data prepared *a priori* to define the multi-variable friction function. Furthermore, it does not account for the history-dependent dynamic friction effect needed for the severe transient maneuver simulation due to the steady-state assumption made. For this reason, to account for the transient tire friction effect for severe braking and cornering analysis, the distributed parameter LuGre tire friction model [68,69] is introduced in this study and a numerical procedure to integrate the LuGre tire friction model into the finite-element based deformable tire model is proposed.

In the LuGre tire force model originally proposed for rigid-body based tire models, the state of friction between a tire tread and road is described by internal friction parameters $z_x(\zeta,t)$ and $z_y(\zeta,t)$ defined in time and space, where ζ is a spatial coordinate defined along the contact patch longitudinal axis ($0 \le \zeta \le L$) as shown in Fig. 4.4. The longitudinal and lateral tire forces are then defined using the following equations [68,69]:

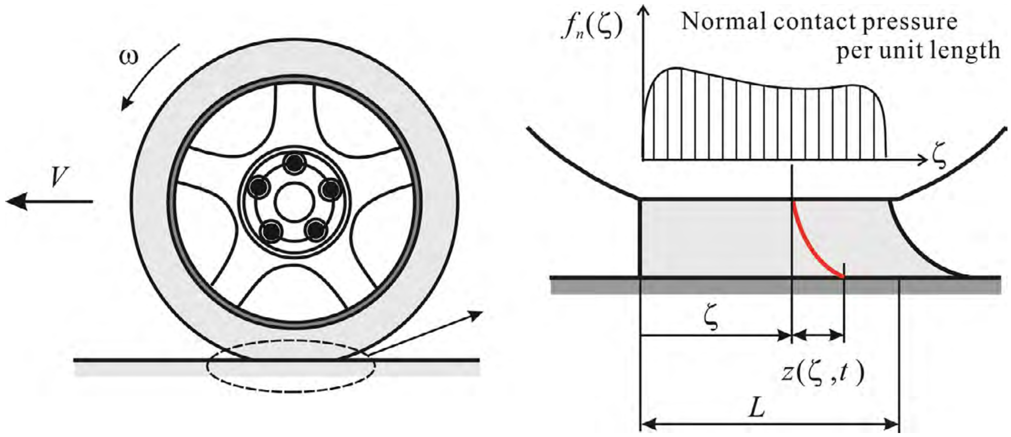

Figure 4.4 LuGre tire friction model

$$\left.\begin{aligned} F_x &= \int_0^L \int_{-W/2}^{W/2} \left(\sigma_{0x}\, z_x(\zeta,t) + \sigma_{1x} \frac{\partial z_x}{\partial t}(\zeta,t) + \sigma_{2x} v_{rx} \right) p_n(\zeta) d\eta d\zeta \\ F_y &= \int_0^L \int_{-W/2}^{W/2} \left(\sigma_{0y}\, z_y(\zeta,t) + \sigma_{1y} \frac{\partial z_y}{\partial t}(\zeta,t) + \sigma_{2y} v_{ry} \right) p_n(\zeta) d\eta d\zeta \end{aligned}\right\} \tag{4.15}$$

where L and W are, respectively, the length and width of the contact patch, and $-W/2 \le \eta \le W/2$. v_{rk} ($k = x, y$) is the slip velocity in the longitudinal ($k = x$) and lateral ($k = y$) directions, respectively; σ_{0k} and σ_{1k} are, respectively, coefficients associated with z_k and $\dot{z}_k$, where $k = x, y$; and σ_{2k} ($k = x, y$) is a coefficient describing viscous friction effect between the tread and road. $p_n(\zeta)$ is the normal contact pressure in the contact patch. The internal friction parameter $z_x(\zeta,t)$ and $z_y(\zeta,t)$ are given as solution to the following partial differential equations [68,69]:

$$\left.\begin{aligned} \frac{\partial z_x(\zeta,t)}{\partial t} &= v_{rx} - \frac{\sigma_{0x}|v_{rx}|}{g_x(v_{rx})} z_x(\zeta,t) - \frac{\partial z_x(\zeta,t)}{\partial \zeta}|r\omega| \\ \frac{\partial z_y(\zeta,t)}{\partial t} &= v_{ry} - \frac{\sigma_{0y}|v_{ry}|}{g_y(v_{ry})} z_y(\zeta,t) - \frac{\partial z_y(\zeta,t)}{\partial \zeta}|r\omega| \end{aligned}\right\} \tag{4.16}$$

where $|r\omega|$ is the circumferential velocity; and $g_x(v_{rx})$ and $g_y(v_{ry})$ are functions that define the longitudinal and lateral slip-dependent friction coefficient characteristics. In this study, the friction characteristics are identified at pure braking conditions, and then friction curves for the longitudinal and lateral frictions under combined slip conditions are defined as follows [69]:

$$g_x(v_{rx}) = \left|\frac{v_{rx}}{v_r}\right| g(v_r) \quad \text{and} \quad g_y(v_{ry}) = \left|\frac{v_{ry}}{v_r}\right| g(v_r) \tag{4.17}$$

where $v_r = \sqrt{(v_{rx})^2 + (v_{ry})^2}$ and the function $g(v_r)$ characterizes the slip-dependent friction coefficient and is given as

$$g(v_r) = \mu_c + \left(\mu_s - \mu_c\right)\exp\left(-\left|v_r / v_s\right|^{\alpha}\right) \tag{4.18}$$

where μ_c and μ_s are, respectively, the kinetic and static friction coefficients; v_s is Stribeck velocity; and α is Stribeck exponent [68,69].

4.3.2 Steady-State LuGre Tire Friction Model

The steady-state LuGre tire friction model required for the parameter identification of LuGre tire model can be obtained by assuming $\partial z_k / \partial t = 0$ in Eq. 4.16 as follows:

$$\frac{\partial z_k(\zeta)}{\partial \zeta} = \frac{1}{|r\omega|}\left(v_{rk} - \sigma_{0k}\frac{|v_{rk}|}{g_k(v_{rk})} z_k(\zeta)\right), \quad k = x, y \tag{4.19}$$

By solving the preceding equation with $z_k(0,t) = 0$, $k = x, y$ on the leading edge of the contact patch, one can obtain the following steady-state solution [68]:

$$z_{ssk}(\zeta) = \mathrm{sgn}(v_{rk}) \cdot \frac{g_k(v_r)}{\sigma_{0k}}\left[1 - \exp\left(-\frac{\sigma_{0k}}{g_k(v_r)}\left|\frac{v_{rk}}{r\omega}\right|\zeta\right)\right], \quad k = x, y \tag{4.20}$$

from which, the following steady-state tire force can be obtained by assuming a parabolic normal contact pressure distribution:

$$(F_k)_{ss} = \left[\mathrm{sgn}\left(v_{rk}\right) \cdot g_k\left(v_r\right)\left(1 - 6\left(\frac{\gamma_k}{L}\right)^2\left(1 + e^{-L/\gamma_k}\right) + 12\left(\frac{\gamma_k}{L}\right)^3\left(1 - e^{-L/\gamma_k}\right)\right) + \sigma_2 v_{rk}\right] F_n, \quad k = x, y \tag{4.21}$$

where F_n is a normal contact force and γ is given as

$$\gamma_k = \frac{g_k(v_r)}{\sigma_{0k}}\left|\frac{1+s}{s}\right|, \quad k = x, y \tag{4.22}$$

Note here that the slip ratio is defined by $s = v_r / V$.

4.3.3 Slip Dependent Characteristics for Wet Condition

The longitudinal tire force measured by a tire test rig on a wet condition is shown in Fig. 4.5. The forward velocity is assumed to be 100 km/h (27.8 m/s) and the tire size is 195/65/R15. It is observed from this figure that the tire force builds up as the slip ratio increases and then it drops after it reaches the maximum point, which is the typical braking force characteristic on wet road conditions. Furthermore, it is important to note here that the tire force decreases linearly as the slip ratio increases in the large slip ratio regime. Such a linear decay in the tire force in the large slip ratio range is also observed in the literature [70] for the measured tire forces on wet road conditions. However, since the slip-dependent friction characteristics given in Eq. 4.18 are approximated by an exponential function, the linear decay of the tire force in the large slip ratio range cannot be described. In order to account for the linear decay of the friction coefficient in the large slip ratio range, the function $g(v_r)$ is modified in this investigation as follows:

$$g(v_r) = h(v_r) + (\mu_s - h(v_r))\exp\left(-\left|v_r / v_s\right|^{\alpha}\right) \tag{4.23}$$

where the linear change in the friction coefficient is modeled by the following function $h(v_r)$ as

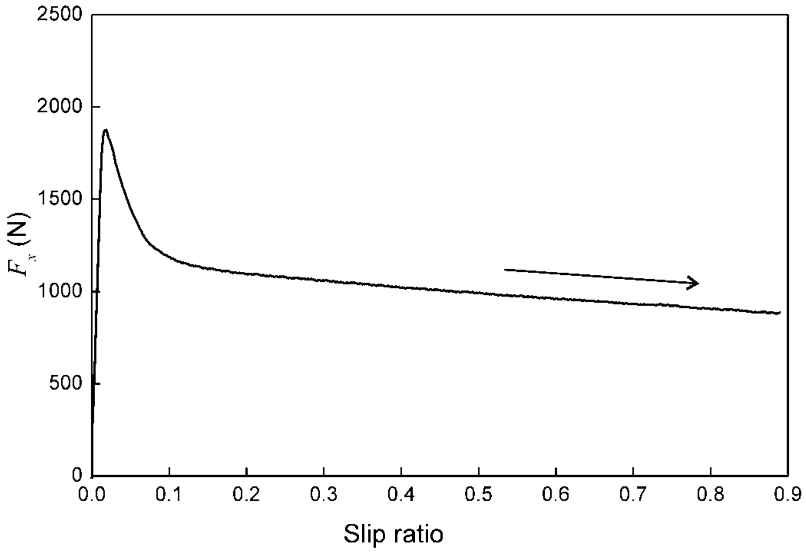

Figure 4.5 Longitudinal tire force on wet surface

$$h(v_r) = -\beta \left| \frac{v_r}{v_s} \right| + \mu_\beta \tag{4.24}$$

where β and μ_β are the model parameters that need to be identified. Using the preceding equations, the friction coefficient can decrease exponentially in small slip range, while in the large slip range, the friction coefficient decreases linearly as defined by the function $h(v_r)$. Since the exponential function that appears in the second term of Eq. 4.23. approaches to zero as the slip velocity increases, the function $h(v_r)$ has a dominant effect in the large slip range, allowing for the accurate modeling of the slip-dependent friction coefficient characteristics which involve the linear decay in the large slip range. It is important to notice here that the original function proposed in the literature [68] can be recovered if β in Eq. 4.24 is equal to zero.

4.4 Integration of LuGre Tire Friction Model into Deformable Tire Model

In most literature that discuss the LuGre tire friction model using rigid-body based tire models, the tangential tire force distribution across the contact patch width is assumed to be constant and the spatial distribution of the friction parameter $z(\zeta, t)$ is approximated by a single mean friction parameter $\bar{z}(t)$ such that the tire force can be determined as a solution to the ordinary differential equation in terms of the single friction variable $\bar{z}(t)$ [68,69]. This leads to a straightforward implementation of the LuGre tire friction model in rigid-body based tire models. However, the shear contact stress distribution over the contact patch cannot be evaluated and the slip velocity is approximated at a single contact point. For this reason, to account for the effect of the change in the normal contact pressure and slip distributions over the contact patch predicted by the flexible tire model, spatially discretized form of the LuGre tire friction model is derived and integrated into the flexible tire model developed in this study. Since the state of friction is dependent on the longitudinal and transverse coordinates as $z_k(\zeta, \eta, t)$, one has

$$\frac{dz_k}{dt} = \frac{\partial z_k}{\partial \zeta}\frac{\partial \zeta}{\partial t} + \frac{\partial z_k}{\partial \eta}\frac{\partial \eta}{\partial t} + \frac{\partial z_k}{\partial t}, \qquad k = x, y \tag{4.25}$$

In rolling contact problems, $\partial\zeta / \partial t$ term defines the velocity of the contact patch coordinate system in the rolling direction ζ. However, the lateral velocity of the contact patch coordinate system represented by $\partial\eta / \partial t$ in the second term is assumed to be small enough as compared to $\partial\zeta / \partial t$ and $\partial z_k / \partial t$ describing the transient effect of the friction parameter in rolling contact problems. Thus, one can assume $\partial\eta / \partial t \approx 0$ as in the original LuGre tire friction model. However, this does not mean that distribution of the friction parameters z_x and z_y in the width direction is neglected since the contact pressure and slip velocity distributions obtained from the finite element tire model are defined as a function of ζ and η in this study, i.e., $p_n(\zeta,\eta)$ and $v_r(\zeta,\eta)$. For this reason, the contact patch predicted by the flexible tire model is discretized into strips across the tire width first to account for the shear contact stress distribution along the transverse axis of the contact patch, and then shear contact stresses are evaluated strip by strip as shown in Fig. 4.6. This strip is called "LuGre strip" in this study. For each LuGre strip *j* defined at $\eta = \eta^j$ shown in Fig. 4.6, the state of friction is defined by the following partial differential equations in terms of the two parameters z_x^j and z_y^j associated with the longitudinal and lateral shear stresses:

$$\left.\begin{aligned} \frac{\partial z_x^j}{\partial t} &= v_{rx}^j - \frac{\sigma_{0x}\left|v_{rx}^j\right|}{g_x(v_{rx}^j)} z_x^j - \frac{\partial z_x^j}{\partial \zeta^j}\left|r^j \omega^j\right|, \quad j = 1, \cdots, m \\ \frac{\partial z_y^j}{\partial t} &= v_{ry}^j - \frac{\sigma_{0y}\left|v_{ry}^j\right|}{g_y(v_{ry}^j)} z_y^j - \frac{\partial z_y^j}{\partial \zeta^j}\left|r^j \omega^j\right|, \quad j = 1, \cdots, m \end{aligned}\right\} \tag{4.26}$$

where the superscript *j* indicates the quantity on the *j*-th LuGre strip along the longitudinal axis of the contact patch. In order to solve the preceding partial differential equations of the LuGre tire friction model, Eq. 4.26 is spatially discretized as $\partial z^j / \partial \zeta^j = (z^{ij} - z^{i-1,j}) / \Delta L^{ij}$ and then converted to the set of first-order ordinary differential equations as follows:

$$\left.\begin{aligned} \frac{dz_x^{ij}}{dt} &= v_{rx}^{ij} + \frac{\left|r^{ij}\omega^{ij}\right|}{\Delta L^{ij}} z_x^{i-1,j} - \left(\frac{\sigma_{0x}\left|v_{rx}^{ij}\right|}{g_x\left(v_{rx}^{ij}\right)} + \frac{\left|r^{ij}\omega^{ij}\right|}{\Delta L^{ij}}\right) z_x^{ij}\,, \quad i=1,\cdots,n\,; \quad j=1,\cdots,m \\ \frac{dz_y^{ij}}{dt} &= v_{ry}^{ij} + \frac{\left|r^{ij}\omega^{ij}\right|}{\Delta L^{ij}} z_y^{i-1,j} - \left(\frac{\sigma_{0y}\left|v_{ry}^{ij}\right|}{g_y\left(v_{ry}^{ij}\right)} + \frac{\left|r^{ij}\omega^{ij}\right|}{\Delta L^{ij}}\right) z_y^{ij}\,, \quad i=1,\cdots,n\,; \quad j=1,\cdots,m \end{aligned}\right\} \quad (4.27)$$

where the superscript i and j, respectively, indicate the i-th discretized element ($i=1,\cdots,n$) in the j-th LuGre strip ($j=1,\cdots,m$). ΔL^{ij} is the length of the LuGre element ij shown in Fig. 4.6. $z_x^{0j} = z_y^{0j} = 0$ is assumed on the leading edge. The preceding

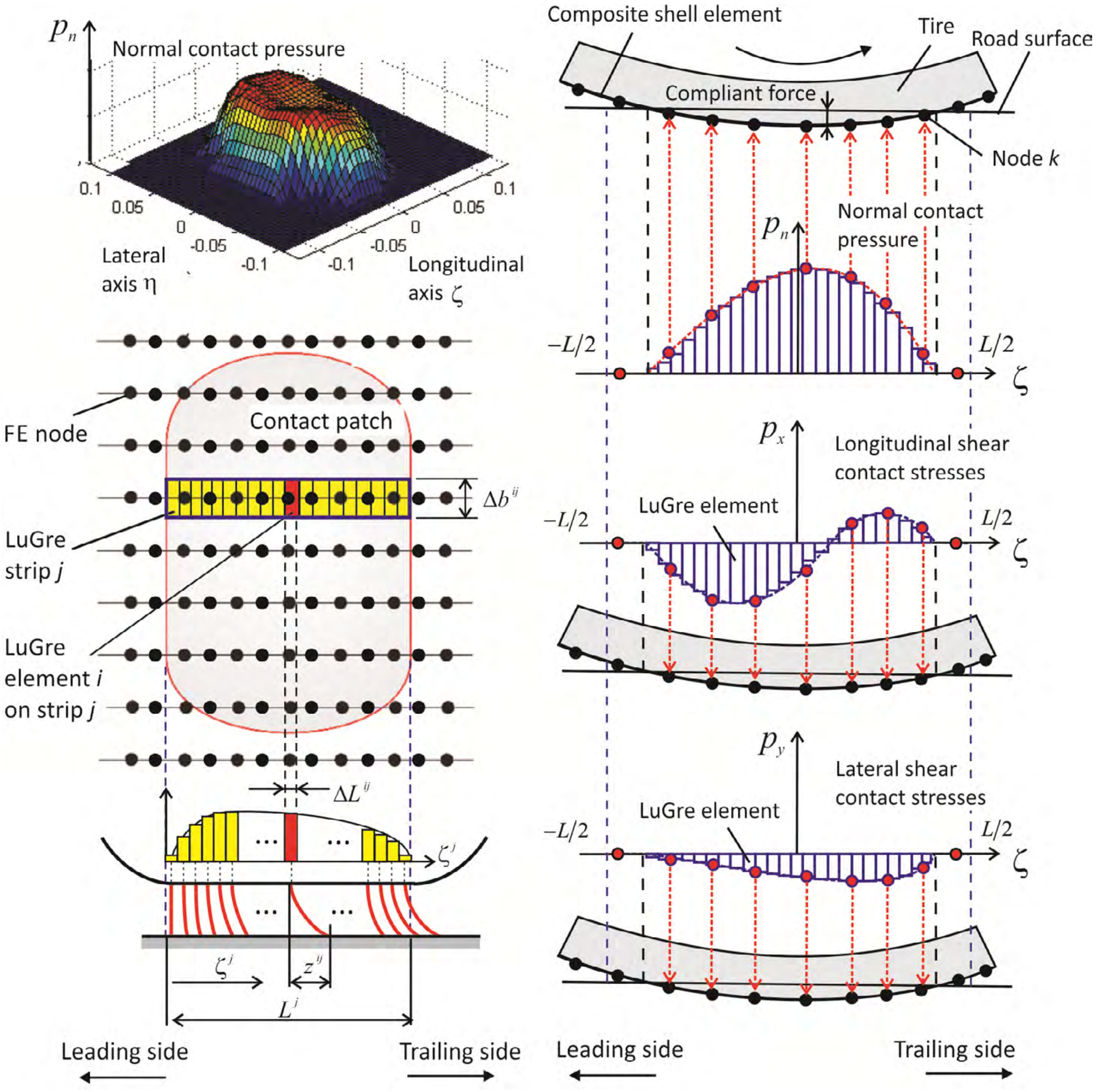

Figure 4.6 Integration of LuGre tire friction model in flexible tire model

equations are expressed in the following matrix form for all the discretized LuGre elements in the contact patch:

$$\dot{\mathbf{z}} = \mathbf{A}\,\mathbf{z} + \mathbf{b} \tag{4.28}$$

where the vector $\mathbf{z}$ contains all the LuGre friction variables z_x^{ij} and z_y^{ij} for $i = 1, \cdots, n$ and $j = 1, \cdots, m$. $\mathbf{A}$ is the square matrix of $mn \times mn$ and $\mathbf{b}$ is the vector of slip velocities v_{rx}^{ij} and v_{ry}^{ij} defined in the discretized element *ij*. Accordingly, the longitudinal and lateral shear contact stresses in the LuGre element *ij* are defined as

$$\left.\begin{aligned} p_x^{ij} &= \left(\sigma_{0x} z_x^{ij} + \sigma_{1x} \dot{z}_x^{ij} + \sigma_{2x} v_{rx}^{ij}\right) p_n^{ij} \\ p_y^{ij} &= \left(\sigma_{0y} z_y^{ij} + \sigma_{1y} \dot{z}_y^{ij} + \sigma_{2y} v_{ry}^{ij}\right) p_n^{ij} \end{aligned}\right\} \tag{4.29}$$

where p_n^{ij} is the normal contact pressure acting on the LuGre element *ij*. From which, the longitudinal and lateral contact forces defined in the LuGre element *ij* can be obtained as

$$F_x^{ij} = p_x^{ij} \Delta L^{ij} \Delta b^{ij}, \qquad F_y^{ij} = p_y^{ij} \Delta L^{ij} \Delta b^{ij} \tag{4.30}$$

where Δb^{ij} is the width of LuGre element *ij*. It is important to notice here that the finite element nodes in contact and LuGre elements in the contact patch do no coincide as shown in Fig. 4.6, and finer LuGre mesh is required to obtained accurate shear contact stress distribution. For this reason, the contact pressure and slip velocity predicted at each finite element node in contact are spatially interpolated to evaluate those at discretized LuGre elements to construct the set of ordinary differential equations associated with the dynamic tire friction for each LuGre element defined by Eq. 4.27. On the other hand, to define the nodal tangential contact forces applied to the flexible tire model, the shear contact stresses evaluated at the discretized LuGre elements are then interpolated to define the LuGre tangential tire forces acting on each finite element node in the contact patch as shown in Fig. 4.6. These nodal tangential contact forces are added to the right hand side of the equations of motion of the flexible tire model. By doing so, the structural deformation of the flexible tire model can be dynamically coupled with the LuGre tire friction model in the final form of the equations as follows:

$$\left.\begin{aligned} \mathbf{M}\ddot{\mathbf{e}} &= \mathbf{Q}_s(\mathbf{e}, \boldsymbol{\alpha}) + \mathbf{Q}_e(\mathbf{e}, \dot{\mathbf{e}}, \mathbf{z}, \dot{\mathbf{z}}) \\ \dot{\mathbf{z}} &= \mathbf{A}(\dot{\mathbf{e}})\mathbf{z} + \mathbf{b}(\dot{\mathbf{e}}) \end{aligned}\right\} \tag{4.31}$$

and these two sets of equations are integrated forward in time simultaneously. To numerically integrate the preceding equations of the tire model with spatially discretized LuGre tire friction model in time, the nodal acceleration vector $\ddot{\mathbf{e}}$, nodal velocity vector $\dot{\mathbf{e}}$ and time derivative of the friction parameter vector $\dot{\mathbf{z}}$ at time step t_{n+1} are defined using the time integration scheme of Newmark-β family as

$$\left.\begin{aligned}
\ddot{\mathbf{e}}_{n+1} &= \frac{1}{\beta h^2}(\mathbf{e}_{n+1}-\mathbf{e}_n)-\frac{1}{\beta h}\ \dot{\mathbf{e}}_n-(\frac{1}{2\beta}-1)\ddot{\mathbf{e}}_n \\
\dot{\mathbf{e}}_{n+1} &= \frac{\gamma}{\beta h}(\mathbf{e}_{n+1}-\mathbf{e}_n)-(\frac{\gamma}{\beta}-1)\ \dot{\mathbf{e}}_n-h(\frac{\gamma}{2\beta}-1)\ddot{\mathbf{e}}_n \\
\dot{\mathbf{z}}_{n+1} &= \frac{\gamma}{\beta h}(\mathbf{z}_{n+1}-\mathbf{z}_n)-(\frac{\gamma}{\beta}-1)\ \dot{\mathbf{z}}_n
\end{aligned}\right\} \tag{4.32}$$

where h is the step size; and β and γ are integration coefficients. Using the preceding equations, Eq. 4.31 is expressed in terms of unknown vectors $\mathbf{e}_{n+1}$ and $\mathbf{z}_{n+1}$ in a vector form as

$$\begin{bmatrix} \mathbf{f}_{\text{FE tire}}(\mathbf{e}_{n+1},\mathbf{z}_{n+1}) \\ \mathbf{g}_{\text{LuGre}}(\mathbf{e}_{n+1},\mathbf{z}_{n+1}) \end{bmatrix} = \mathbf{0} \tag{4.33}$$

The preceding discretized equations are solved iteratively at every time step using the following equations:

$$\begin{bmatrix} \partial\mathbf{f}_{\text{FE tire}}/\partial\mathbf{e}_n & \partial\mathbf{f}_{\text{FE tire}}/\partial\mathbf{z}_n \\ \partial\mathbf{g}_{\text{LuGre}}/\partial\mathbf{e}_n & \partial\mathbf{g}_{\text{LuGre}}/\partial\mathbf{z}_n \end{bmatrix} \begin{bmatrix} \Delta\mathbf{e}_{n+1} \\ \Delta\mathbf{z}_{n+1} \end{bmatrix} = -\begin{bmatrix} (\mathbf{f}_{\text{FE tire}})_n \\ (\mathbf{g}_{\text{LuGre}})_n \end{bmatrix} \tag{4.34}$$

and then the nodal coordinates and LuGre friction parameters are updated as $\mathbf{e}_{n+1}=\mathbf{e}_n+\Delta\mathbf{e}_{n+1}$ and $\mathbf{z}_{n+1}=\mathbf{z}_n+\Delta\mathbf{z}_{n+1}$ until the norm of the residual vector becomes smaller than the error tolerance. It is important to notice here that the elastic forces involve the internal EAS parameters $\boldsymbol{\alpha}$ as discussed in Chapter 2 that need to be determined at every time step to satisfy Eq. 2.44 for each element. For this reason, EAS equations (Eq. 2.44) need to be considered when evaluating the Jacobian matrix and the residual vector of the elastic forces (i.e., $\partial\mathbf{f}_{\text{FE tire}}/\partial\mathbf{e}_n$ and $(\mathbf{f}_{\text{FE tire}})_n$) in a way described in Chapter 2.

It is also important to notice here that the steady state tire model can be obtained systematically by assuming $\dot{\mathbf{z}}=\mathbf{0}$ in the preceding equations and then state of friction $\mathbf{z}$

can be uniquely determined by solving the linear algebraic equations $\mathbf{A}(\dot{\mathbf{e}})\mathbf{z}+\mathbf{b}(\dot{\mathbf{e}})=\mathbf{0}$ if the transient tire friction effect is considered negligible for some simulation scenarios. That is, the steady-state model of the spatially discretized LuGre tire friction can be obtained by assuming that the transient term of the friction parameters equal zero, i.e., $dz_x^{ij}/dt=dz_y^{ij}/dt=0$ in Eq. 4.27. This assumption leads to the following equations:

$$\left.\begin{array}{l} \left(\dfrac{\sigma_{0x}\left|v_{rx}^{ij}\right|}{g_x\left(v_{rx}^{ij}\right)}+\dfrac{\left|r^{ij}\omega^{ij}\right|}{\Delta L^{ij}}\right)z_x^{ij}=v_{rx}^{ij}+\dfrac{\left|r^{ij}\omega^{ij}\right|}{\Delta L^{ij}}z_x^{i-1,j}\ , \quad i=1,\cdots,n\,; \quad j=1,\cdots,m \\ \left(\dfrac{\sigma_{0y}\left|v_{ry}^{ij}\right|}{g_y\left(v_{ry}^{ij}\right)}+\dfrac{\left|r^{ij}\omega^{ij}\right|}{\Delta L^{ij}}\right)z_y^{ij}=v_{ry}^{ij}+\dfrac{\left|r^{ij}\omega^{ij}\right|}{\Delta L^{ij}}z_y^{i-1,j}\ , \quad i=1,\cdots,n\,; \quad j=1,\cdots,m \end{array}\right\} \tag{4.35}$$

It is important to notice here that the preceding equations can be solved for z_x^{ij} and z_y^{ij} without any time-integration procedures from the leading edge ($i=1$) to the trailing edge ($i=n$) recursively for each LuGre strip j with the boundary condition $z_x^{0j}=z_y^{0j}=0$ on the leading edge. This indicates that the leading edge of the contact patch is in adhesion. The shear contact stresses can then be defined by Eq. 4.29. Since the state of shear contact stress distribution over the contact patch is defined by algebraic equations, friction parameters are no longer treated as system coordinates, resulting in a smaller number of equations being solved. The steady-state tire friction model is, however, unable to incorporate the history-dependent friction-induced hysteresis since friction state can be uniquely determined without the state at previous time step through time integration.

CHAPTER 5

PARAMETER IDENTIFICATION AND TIRE DYNAMICS SIMULATION

5.1 Introduction

For use of LuGre tire friction model, the parameter identification is crucial to accurate and reliable prediction of transient tire forces under various driving conditions [70]. Since governing equations of LuGre tire friction model are highly nonlinear and several fitting parameters are introduced to account for the nonlinear friction characteristics, the correlation of the model parameters with physical quantities are not clear, making the parameter identification of the LuGre tire friction model difficult [70]. That is, inappropriate initial estimates may lead to parameters that have nothing to do with physical quantities even though the LuGre model are fitted well with measured tire force curves. For this reason, a systematic and automated procedure for parameter identification of LuGre tire friction model is developed in this chapter. Furthermore, the fundamental tire characteristics including the normal contact pressure distribution and load-deflection curve of the physics-based flexible tire model discussed in Chapter 4 are validated against the tire test data, and then the nonlinear tire dynamic simulation under abrupt braking and cornering scenarios on a rigid ground are presented to demonstrate the tire model capability for transient maneuvering scenarios developed in this study.

5.2 Parameter Identification Procedure of LuGre Tire Friction Model

Since the basic tire force characteristics are, in most cases, evaluated using tire test rigs in the steady state condition, the steady state model given by Eq. 4.21 is introduced for the purpose of the parameter identification of the LuGre tire friction model. The parameters identified in the steady state condition are then introduced to the transient LuGre tire friction model in the time-domain analysis. It is important to notice here that the steady-state model is derived as a special case of the general transient model, thus all the LuGre model parameters for describing the tire tread friction characteristics are, in principle, consistent in both models to ensure that the steady state tire force characteristics can be recovered from the transient tire force model.

In the steady-state LuGre tire friction model given by Eq. 4.21 with the modified function $g(v_r)$ (Eqs. 4.23 and 4.24), the following 7 parameters need to be identified using the measurement data:

$$\mathbf{p} = [\sigma_{0x} \quad \sigma_{0y} \quad \mu_s \quad \mu_\beta \quad \beta \quad v_s \quad \alpha]^T \tag{5.1}$$

While the first two parameters σ_{0x} and σ_{0y} are identified in the longitudinal and lateral directions separately, the rest of the friction parameters are determined in a pure slip condition and then slip-dependent friction curves in the longitudinal and lateral directions are assumed by Eq. 4.17. In this study, the steady-state friction-slip curve for the longitudinal tire force is used to identify the tire friction characteristics. For example, using Eq. 4.21, the tangential force coefficient (ratio of tire force to normal force) at the steady state condition can be obtained by assuming that the viscous friction effect is negligibly small as follows:

$$\mu_x^{LG}(\mathbf{p}_x) = \left|\frac{F_{ssx}}{F_n}\right| = g(v_r)\left(1-6\left(\frac{\gamma_x}{L}\right)^2\left(1+e^{-L/\gamma_x}\right)+12\left(\frac{\gamma_x}{L}\right)^3\left(1-e^{-L/\gamma_x}\right)\right) \tag{5.2}$$

where $\gamma_x = \dfrac{g(v_r)}{\sigma_{0x}}\left|\dfrac{1+s}{s}\right|$ since $g_x(v_{rx}) = g(v_r)$ at the pure slip state. In the preceding equation, the unknown LuGre parameter vector $\mathbf{p}_x = [\sigma_{0x} \quad \mu_s \quad \mu_c \quad \beta \quad v_s \quad \alpha]^T$ is identified such that an error function defined by the difference between the tangential force coefficient obtained by Eq. 5.2 and the measurement data can be minimized in the entire slip range. That is,

$$J(\mathbf{p}_x) = \frac{1}{2}\sum_{k=1}^{ns}\left(\frac{\mu_k^{LG}(\mathbf{p}_x) - \mu_k^{EXP}}{\mu_k^{EXP}}\right)^2 \rightarrow \min\left(J(\mathbf{p}_x)\right) \tag{5.3}$$

where *ns* is the number of data points used for the parameter identification, and all the components of the vector $\mathbf{p}_x$ need to be positive. In order to solve the preceding nonlinear optimization problem, iterative solution procedures are employed. Since there are many local minima in the error function, appropriate initial estimates for iterative solution procedures are crucial to accurate and reliable identification of the LuGre tire friction model parameters. Although the model curve can be fitted to the measurement data, it is not guaranteed that the model parameters identified are physically consistent.

Furthermore, all the LuGre model parameters are not necessarily correlated to measureable physical quantities, making the determination of the initial estimates for the nonlinear parameter identification difficult. For this reason, initial estimates provided for solving Eq. 5.2 need to be accurately predicted first, and it allows for developing a systematic and automated procedure for estimating parameters of the LuGre tire friction model. The proposed slip-dependent friction coefficient given by function $g(v_r)$ is defined by the five parameters μ_s, μ_β, β, v_s and α. Since these parameters can be identified solely by the measured slip-dependent friction characteristics, they can be estimated first and then adhesion parameters σ_{0x} and σ_{0y} are identified by the traction/braking and cornering stiffness extracted from the measured data. Since one has $g(v_r)=\mu_s$ for $v_r=0$ using Eq. 4.23, μ_s can be estimated by finding the point of intersection between the function $g(v_r)$ and its ordinate axis. To find the point of intersection, the friction coefficient of the measured data denoted by $g^{EXP}(v_r)$ in the small slip velocity range is approximated by a linear function as shown at the top left corner of Fig. 5.1 (also denoted as (A)) using the least square method, and then the point of intersection with the ordinate axis that defines μ_s can be obtained as

$$\mu_{s0}=\frac{\sum_{k=1}^{N_s}{v_{rk}}^2\sum_{k=1}^{N_s}g^{EXP}(v_{rk})-\sum_{k=1}^{N_s}v_{rk}\,g^{EXP}(v_{rk})\sum_{k=1}^{N_s}v_{rk}}{N_s\sum_{k=1}^{N_s}{v_{rk}}^2-\left(\sum_{k=1}^{N_s}v_{rk}\right)^2} \tag{5.4}$$

where N_s is the number of data points used for defining a linear function around the left end of the $g^{EXP}(v_{rk})$ and v_{rk} $(k=1,\cdots,N_s)$ indicates the slip velocity at data point *k*.

In the next step, μ_β and β are estimated by approximating g^{EXP} in the large slip velocity range as a linear function as shown at the bottom right corner of Fig. 5.1 (also denoted as (B)). As a result, the intercept μ_β and the slope β/v_s of the function $h(v_r)=-\beta\left|v_r/v_s\right|+\mu_\beta$ can be estimated by the linear regression as follow:

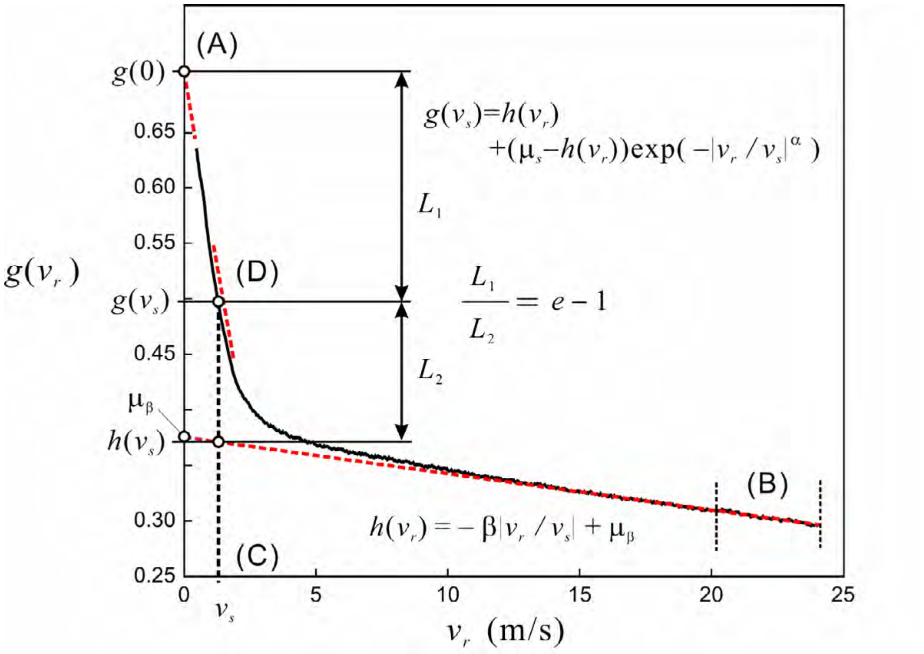

Figure 5.1 Slip-dependent friction coefficient

$$\mu_{\beta 0}=\frac{\sum_{k=1}^{N_\beta} v_{rk}{}^2 \sum_{k=1}^{N_\beta} g^{EXP}(v_{rk})-\sum_{k=1}^{N_\beta} v_{rk}\, g^{EXP}(v_{rk}) \sum_{k=1}^{N_\beta} v_{rk}}{N_\beta \sum_{k=1}^{N_\beta} v_{rk}{}^2-\left(\sum_{k=1}^{N_\beta} v_{rk}\right)^2} \tag{5.5}$$

and

$$\frac{\beta_0}{v_{s0}}=-\frac{N_\beta \sum_{k=1}^{N_\beta} v_{rk}\, g^{EXP}(v_{rk})-\sum_{k=1}^{N_\beta} v_{rk} \sum_{k=1}^{N_\beta} g^{EXP}(v_{rk})}{N_\beta \sum_{k=1}^{N_\beta} v_{rk}{}^2-\left(\sum_{k=1}^{N_\beta} v_{rk}\right)^2} \tag{5.6}$$

An additional equation needs to be introduced to uniquely determine β_0 and v_{s0} using Eq. 4.23. To this end, the L_1 / L_2 ratio as shown in Fig. 5.1 is defined as follows:

$$\frac{L_1}{L_2}=\frac{g(0)-g(v_s)}{g(v_s)-h(v_s)} \tag{5.7}$$

where

$$g(0)=\mu_s\,, \qquad g(v_s)=h(v_s)+\frac{\mu_s-h(v_s)}{\mathrm{e}} \qquad \text{and} \qquad h(v_s)=-\beta+\mu_\beta \tag{5.8}$$

Substituting the preceding equations into the right hand side in Eq. 5.7, one can prove the following identity:

$$\frac{L_1}{L_2} = \mathrm{e} - 1 = \text{constant} \tag{5.9}$$

The preceding equation indicates that the L_1 / L_2 ratio defined by Fig. 5.1 is always constant if the slip-dependent friction characteristics is approximated by Eqs. 4.23 and 4.24. In other words, Stribeck velocity v_s can be found such that Eq. 5.9 is satisfied. Since the initial estimate for μ_s is given by μ_{s0} (Eq. 5.4), one has $g(0) = \mu_{s0}$. Furthermore, using Eq. 5.6, $h(v_{s0})$ can be defined as a function of v_{s0} as $h(v_{s0}) = -c\, v_{s0} + \mu_{\beta 0}$, where c is the right-hand side of Eq. 5.6 evaluated with the measurement data. Consequently, the initial estimate for the Stribeck velocity v_{s0} can be defined such that the following equation is satisfied:

$$\frac{L_1}{L_2} \equiv \frac{\mu_{s0} - g^{EXP}(v_{s0})}{g^{EXP}(v_{s0}) + c\, v_{s0} - \mu_{\beta 0}} = \mathrm{e} - 1 \tag{5.10}$$

where $g^{EXP}(v_{s0})$ indicates the measured *g*-function evaluated at the slip velocity of v_{s0} (see (C) in Fig. 5.1). The Stribeck velocity v_{s0} can be determined such that the difference of the both sides of the preceding equation can be minimized.

To determine the parameter α, the function $g(v_r)$ is differentiated with respect to the slip velocity v_r and one can obtain

$$g'(v_r) = h'(v_r) - h'(v_r)\exp\left(-\left|v_r / v_s\right|^{\alpha}\right) - \left(\mu_s - h(v_r)\right)\frac{\alpha}{v_s}\left|v_r / v_s\right|^{\alpha-1}\exp\left(-\left|v_r / v_s\right|^{\alpha}\right) \tag{5.11}$$

where $h'(v_r) = dh(v_r)/dv_r = -\beta / v_s$. By evaluating the preceding equation at $v_r = v_s$, one can obtain the following equation:

$$g'(v_s) = -\frac{\beta(e-1) + \alpha(\mu_s - \mu_\beta + \beta)}{e\, v_s} \tag{5.12}$$

Since all the estimated parameters on the right hand side of Eq. 5.12 are already given except for α, the parameter α can be uniquely determined as follows:

$$\alpha_0 = -\frac{e v_{s0}(g(v_{s0})^{EXP})' + \beta_0(e-1)}{\mu_{s0} - \mu_{\beta 0} + \beta_0} \tag{5.13}$$

where $(g(v_{s0})^{EXP})'$ is the slope of the measurement data evaluated at $v_r = v_{s0}$ and a numerical differentiation is used to evaluate the derivative. As a result, all the estimated parameters associated with the function $g(v_r)$ can be obtained by Eqs. 5.4, 5.5, 5.6, 5.10 and 5.13. Using the initial estimates provided, the following nonlinear least square problem is solved such that the following error function associated with function $g(v_r)$ can be minimized:

$$R(\mathbf{p}_g) = \frac{1}{2}\sum_{k=1}^{ns}\left(\frac{g_k(\mathbf{p}_g) - g_k^{EXP}}{g_k^{EXP}}\right)^2 \rightarrow \min\left(R(\mathbf{p}_g)\right) \tag{5.14}$$

where $\mathbf{p}_g = [\mu_s \quad \mu_\beta \quad \beta \quad v_s \quad \alpha]^T$.

Since σ_{0x} represents the stiffness associated with the friction parameter $z_x(\zeta, t)$ as shown in Eq. 4.15, σ_{0x} indicates longitudinal traction/braking stiffness [70]. For this reason, using the correlation between the slope of the tire force characteristic curve around the zero slip ratio and the parameter σ_{0x}, one can estimate the parameter σ_{0x}. To this end, the slope of the tire force around the zero slip ratio $K_{Fx} = \lim_{s \to 0}\left|dF_x / ds\right|$ is calculated using the linear regression of the measured data and the parameter σ_{0x} around the zero slip ratio can be estimated by the following equation [69]

$$\sigma_{0x} = \frac{2K_{Fx}}{LF_n} \tag{5.15}$$

where L is the contact patch length. With all these parameters estimated, σ_{0x} and $\mathbf{p}_g$ given by Eq. 5.14 are further used as initial estimates for Eq. 5.3 to determine the final parameters that fit with the measurement tire force characteristic curve. It is important to note here that the parameters σ_{0x} and $\mathbf{p}_g$ are estimated separately based on the adhesive force characteristics and the slip-dependent friction coefficient characteristics. However, this does not necessarily lead to an accurate prediction of the maximum peak of the tire force. For this reason, Eq. 5.3 is solved with all the parameters estimated in the entire slip range such that the maximum peak also agrees with the measurement data. In the same way, the rest of unknown LuGre parameter σ_{0y} which represents the cornering stiffness is determined as

$$\sigma_{0y} = \frac{2K_{Fy}}{LF_n} \tag{5.16}$$

where the slope of the cornering force around the zero slip ratio $K_{Fy} = \lim_{s \to 0} \left| dF_y / ds \right|$ is calculated using the linear regression of the measured data. Using the procedure proposed in this chapter, all the LuGre parameters can be systematically estimated by exploiting important mathematical features of the functions used in the LuGre tire friction model and correlating them to the measured data. Furthermore, providing proper initial estimates improves the numerical convergence of iterative solution procedures for the nonlinear least square problem.

5.3 Parameter Identification Results of LuGre Tire Friction Model

5.3.1 Pure Slip

The measurement data of a tire for passenger cars as previously shown in Fig. 4.5 on a wet road condition is used to demonstrate the use of the parameter identification procedure proposed in this study. The slip-dependent friction coefficient (i.e., tangential force coefficient) is shown as a function of the slip velocity in Fig. 5.2, while the longitudinal tire force is shown as a function of slip ratio in Fig. 5.3. The nonlinear least square problems given by Eqs. 5.3 and 5.14 are solved by *lsqnonlin* function in MATLAB™. In these figures, numerical results obtained using the original function $g(v_r)$ given by Eq. 4.18 (i.e., $\beta = 0$ in Eq. 4.23) and the proposed one given by Eq. 4.23 are compared. It is observed from these figures that use of the modified *g*-function leads to good agreement with the one obtained by measurement. In the use of the original *g*-function, noticeable difference from the measurement data is exhibited. Since the change in the tangential force coefficient in the entire slip velocity range needs to be described by an exponential function, the tangential force coefficient that linearly decays with the slip velocity cannot be accurately described with the original function. As a result, the model does not agree well with the measurement data in both small and large slip velocity regimes since the overall errors in the entire slip velocity range are minimized in the optimization process. Furthermore, it is observed from Fig. 5.3 that use of the original *g*-function also leads to noticeable difference in the maximum peak of the tire force, which leads to less accurate prediction of the traction and braking performance of tires. On the other hand, using the modified *g*-function along with the parameter estimation procedure for LuGre tire friction model, the model curve is well fitted to the measured tire force characteristic curve.

In order to demonstrate the use of the proposed parameter identification procedure for LuGre tire friction model with the modified *g*-function for a wide variety of loading and forward speed conditions, friction characteristic curves of a tread rubber are measured in a wet road condition and used for demonstrating the accuracy of the proposed parameter identification procedure. As shown in Fig. 5.4, a tread rubber is glued on a small rigid wheel and the friction characteristics of a tread rubber are measured by changing the slip ratio. This testing allows to measure the pure tangential

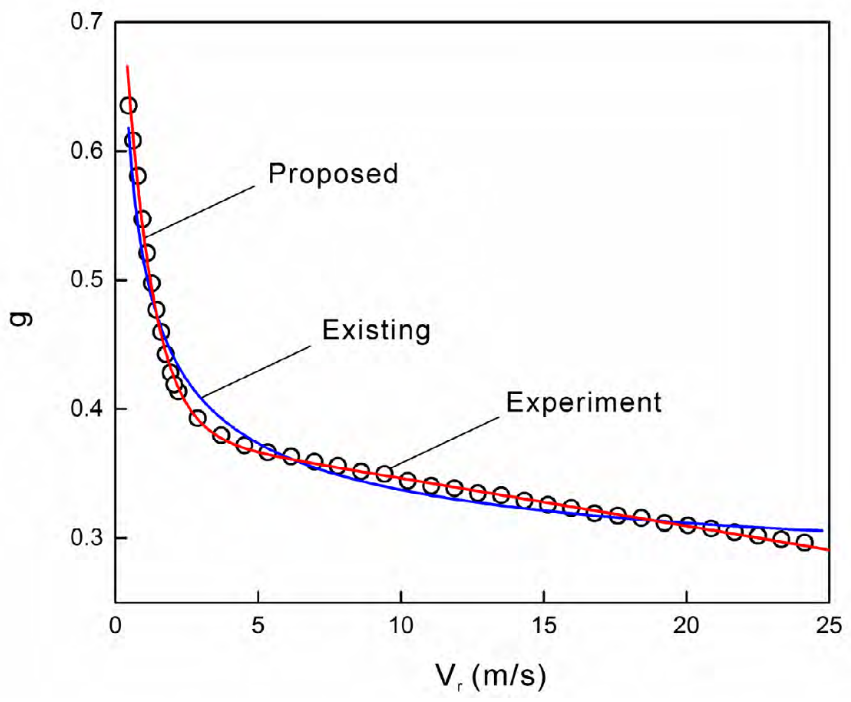

Figure 5.2 Slip-dependent friction coefficient modeled by exiting and modified $g(v_r)$-function

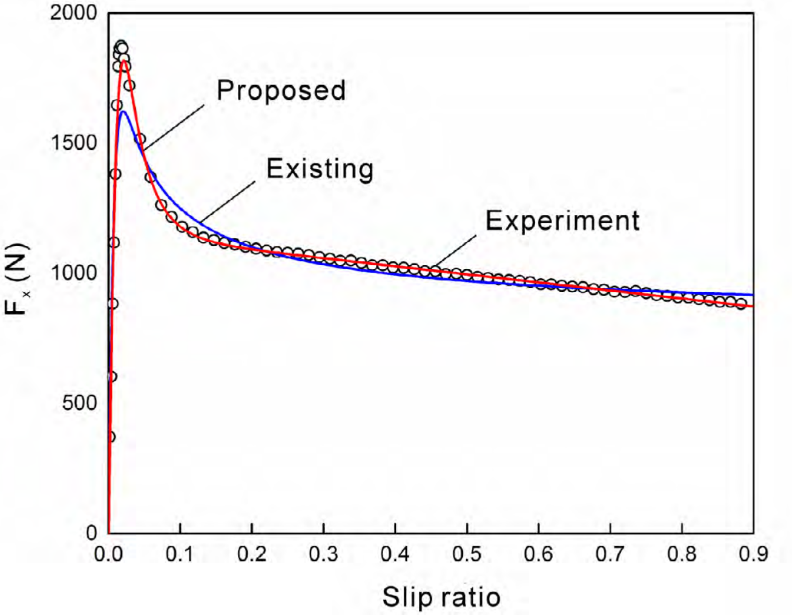

Figure 5.3 Longitudinal tire force with exiting and modified $g(v_r)$-function

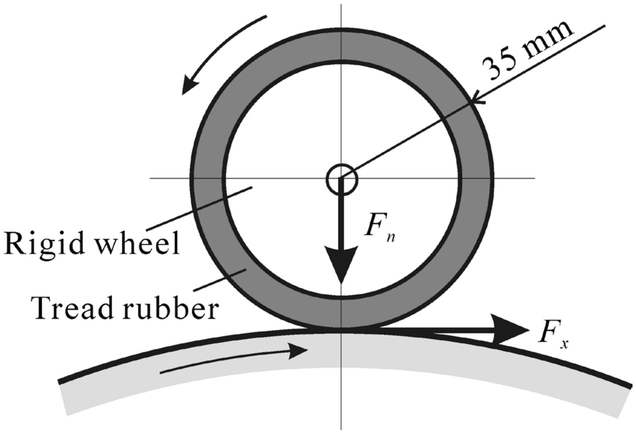

Figure 5.4 Friction testing of tread rubber

force characteristics for the tread rubber under consideration. The wheel is pressed on a drum and the slip ratio is quasi-statically changed by controlling the brake torque of the wheel. The outside diameter of the wheel is 70 mm and the forward velocities are 20 km/h (5.6 m/s), 30 km/h (8.3 m/s) and 40 km/h (11.1 m/s), while the vertical loads are changed to 4 kgf (39.2 N), 5 kgf (49.1 N) and 6 kgf (58.9 N). The tangential force coefficients in different wheel load conditions are shown in Figs. 5.5, 5.6 and 5.7. In each figure, results obtained for different forward velocities are presented. It is observed from these figures that the linear decay in the tangential force in the large slip range is exhibited due to the wet road condition and the tangential forces are well described using the LuGre tire friction model with model parameters identified regardless of the load and speed condition.

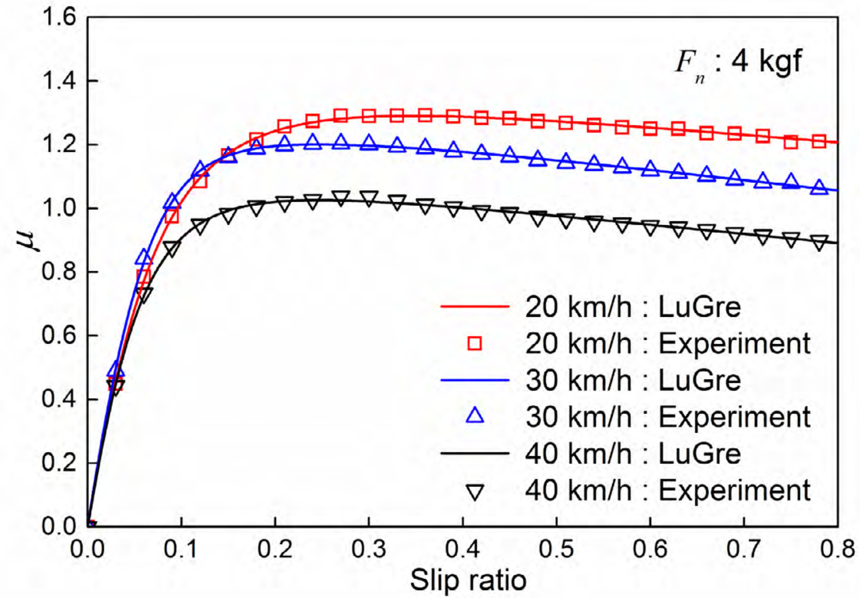

Figure 5.5 Tangential force coefficients for 4 kgf

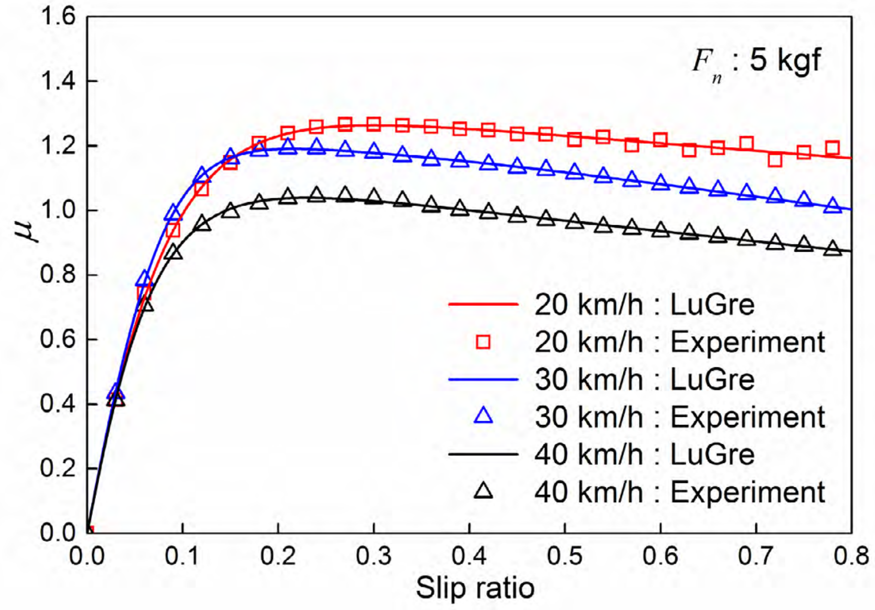

Figure 5.6 Tangential force coefficients for 5 kgf

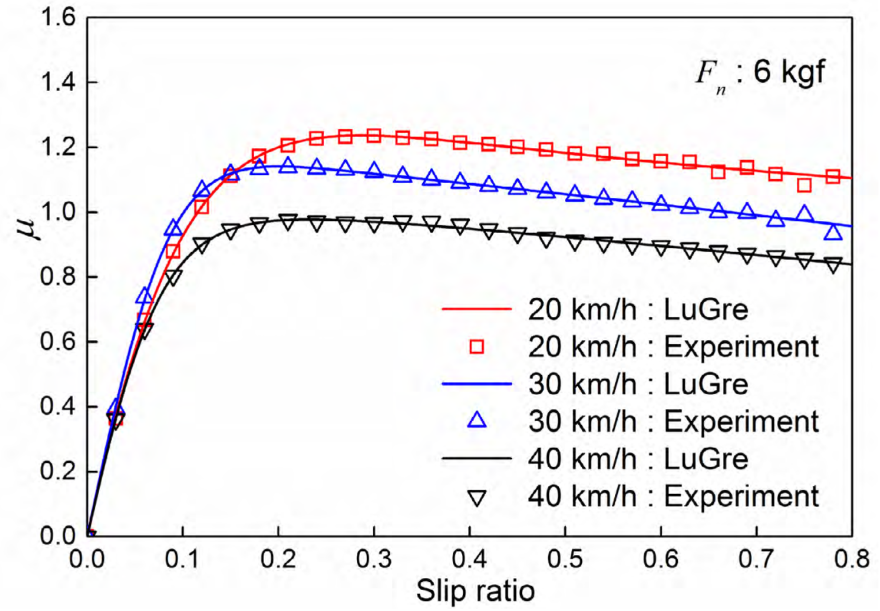

Figure 5.7 Tangential force coefficients for 6 kgf

5.3.2 Combined Slip

The longitudinal and lateral tire forces are presented for slip angles of 1, 3, 5 and 7 degrees and compared with those obtained by the tire test in Fig. 5.8, showing good agreement with the tire test results. It is important to notice here that tire force characteristics differ in traction ($-F_x$) and braking ($+F_x$) in the test result, while numerical results in this figure are obtained using parameters identified for braking conditions. For the slip angle of 1 degree, the longitudinal and cornering tangential force coefficients under combined slips (i.e., longitudinal and lateral slips occur simultaneously) are compared with the test results in Fig. 5.9 for vertical load of 4 kN. The longitudinal and lateral tire forces characteristics are well predicted using the LuGre tire friction model with the parameters identified.

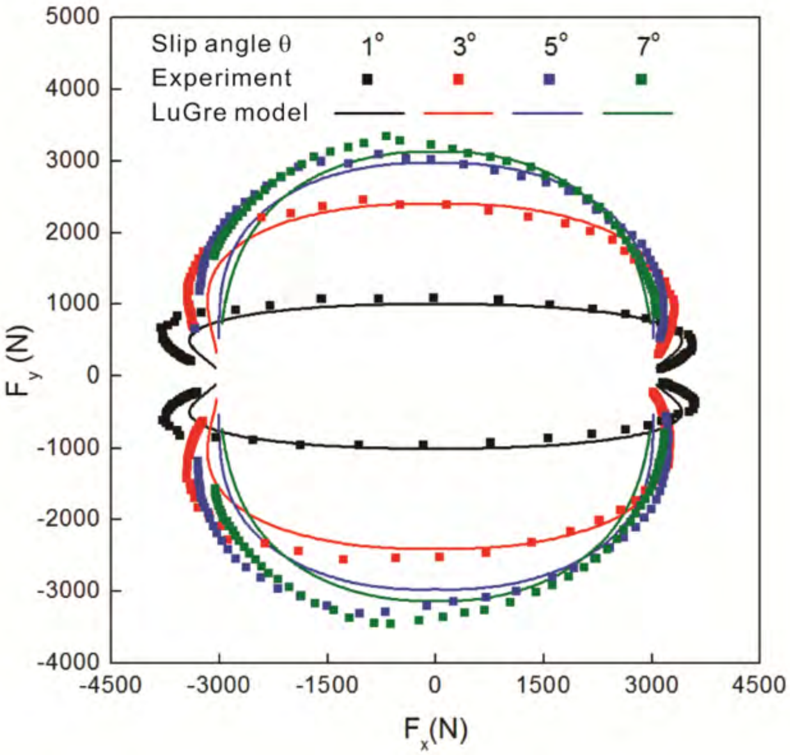

Figure 5.8 Tire force characteristics under combined slip condition

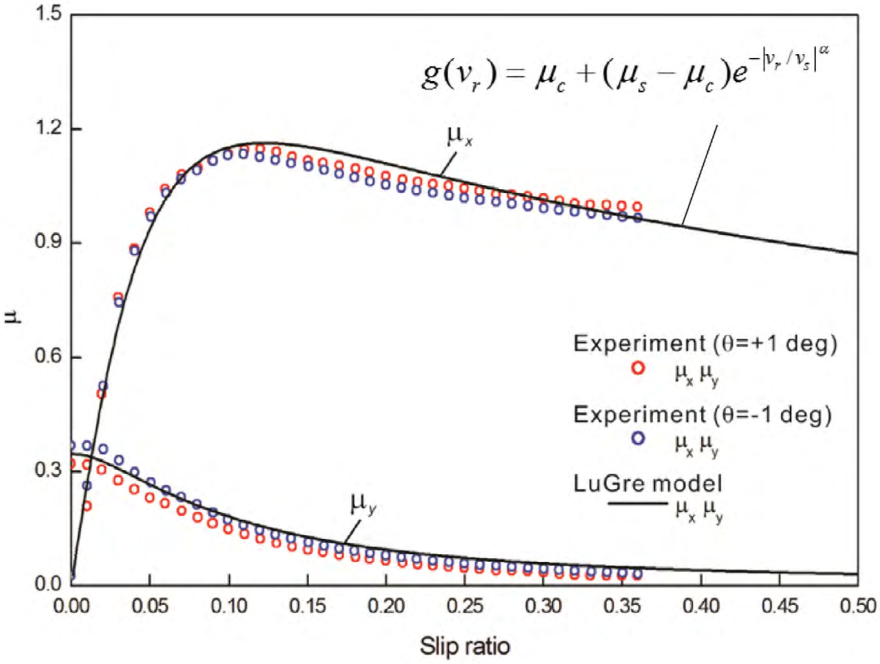

Figure 5.9 Tangential force coefficient under combined slip condition

5.4 Tire Dynamics Simulation

5.4.1 Structural Tire Characteristics and Validation

The tire considered in the numerical example is 215/45R17. The air pressure of 220 kPa is considered by distributed pressure loads applied normal to the inner surface of the tire. The penalty approach is used to define the normal contact forces in the contact patch. The load-deflection curve is used to validate fundamental structural properties of tires. The lateral and vertical deflections of the tire model shown in Fig. 5.10 are compared with the test results in Figs. 5.11 and 5.12. It is observed from these figures that the lateral and vertical tire deflections are in good agreement with test results for the various wheel loads. Furthermore, the lengths of the contact patch in the longitudinal and lateral axes also agree well with those of the test results as shown in Fig. 5.13 and 5.14. The two-dimensional normal contact pressure distribution defined along the longitudinal and lateral axes of the contact patch coordinate system are also compared with those of the test data for the vertical load of 4 kN in Figs. 5.15 and 5.16.

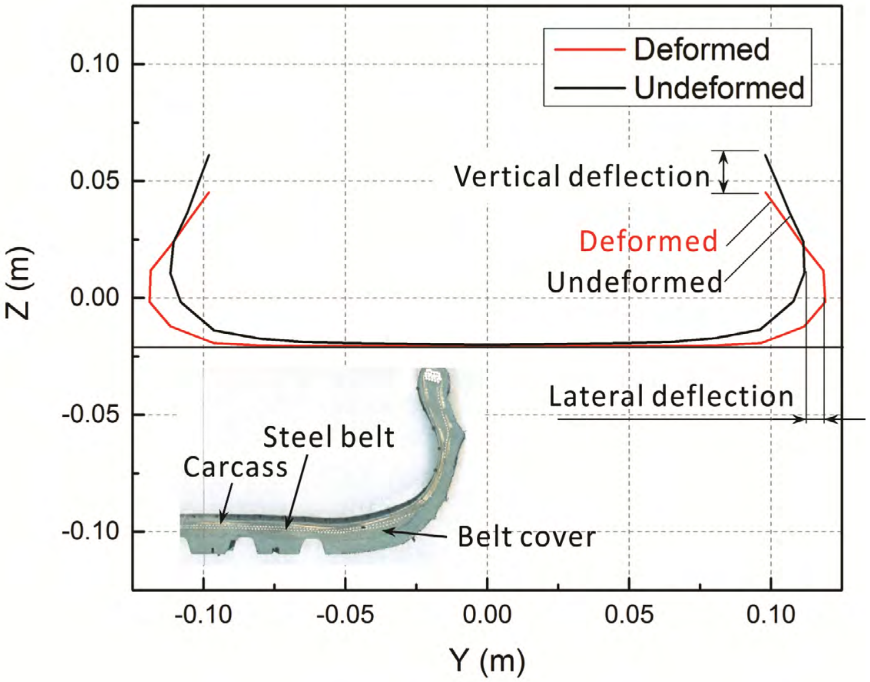

Figure 5.10 Deformed shape of tire cross section

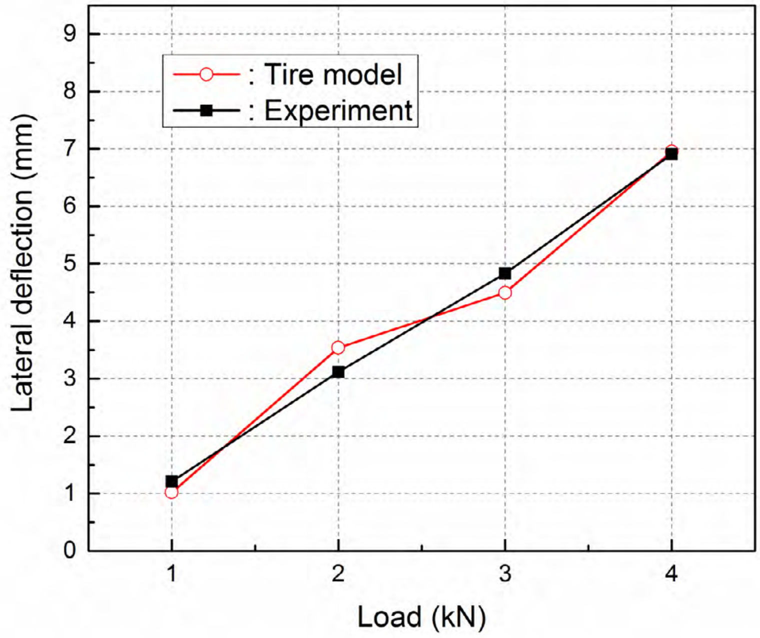

Figure 5.11 Lateral deflection of tire for various wheel loads

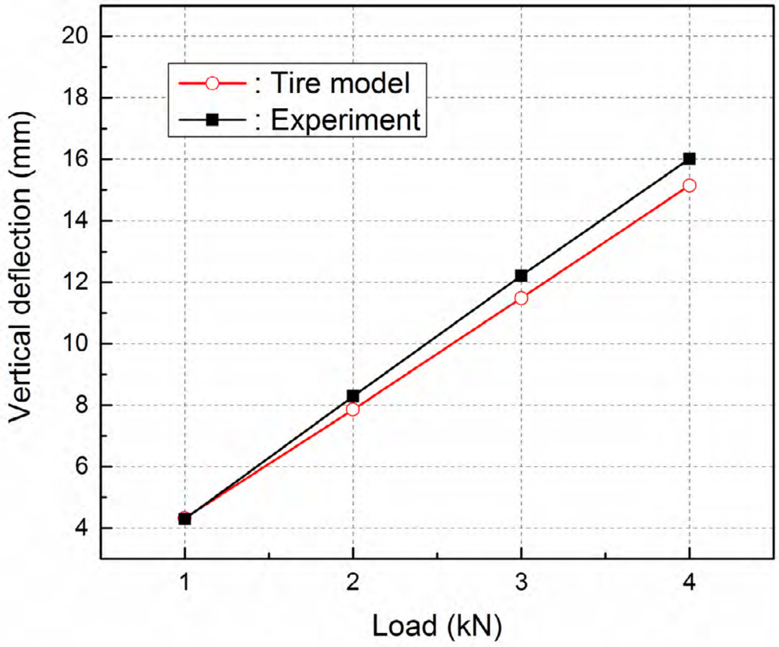

Figure 5.12 Vertical deflection of tire for various wheel loads

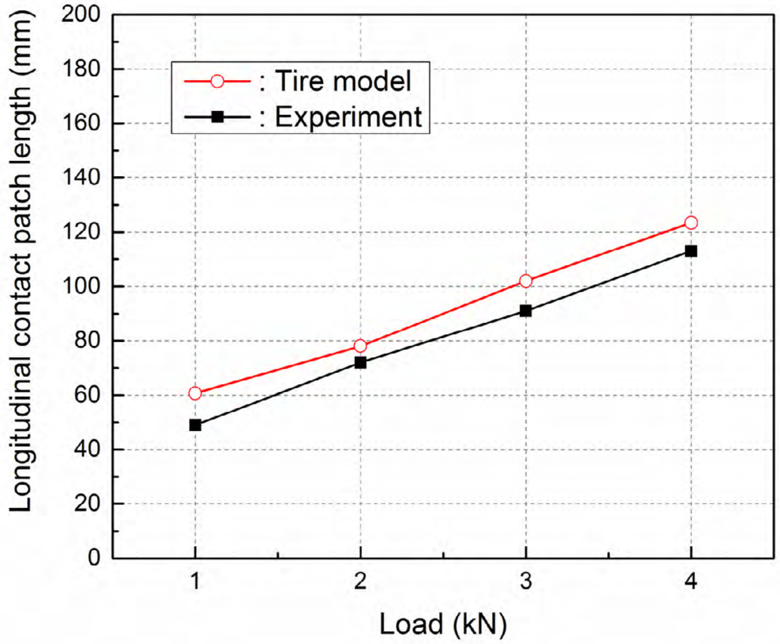

Figure 5.13 Longitudinal contact patch length for various wheel loads

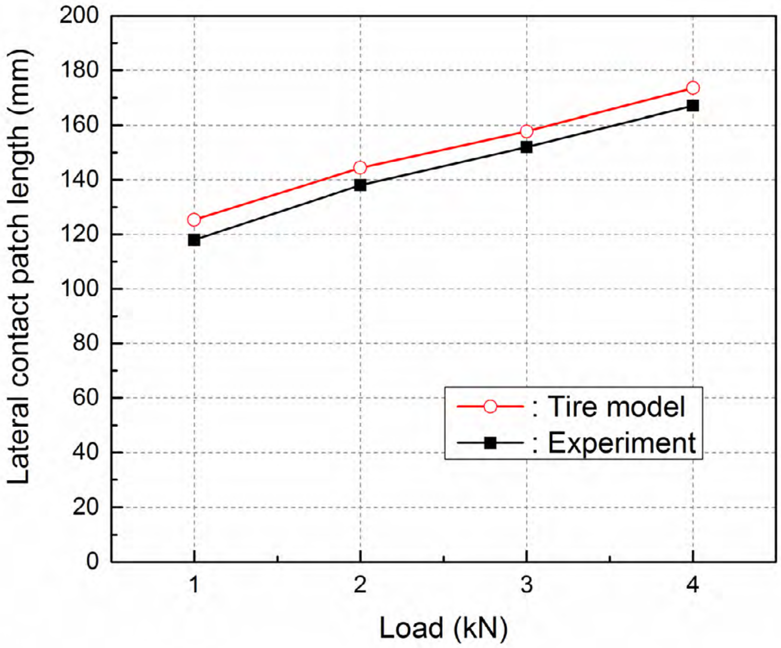

Figure 5.14 Lateral contact patch length for various wheel loads

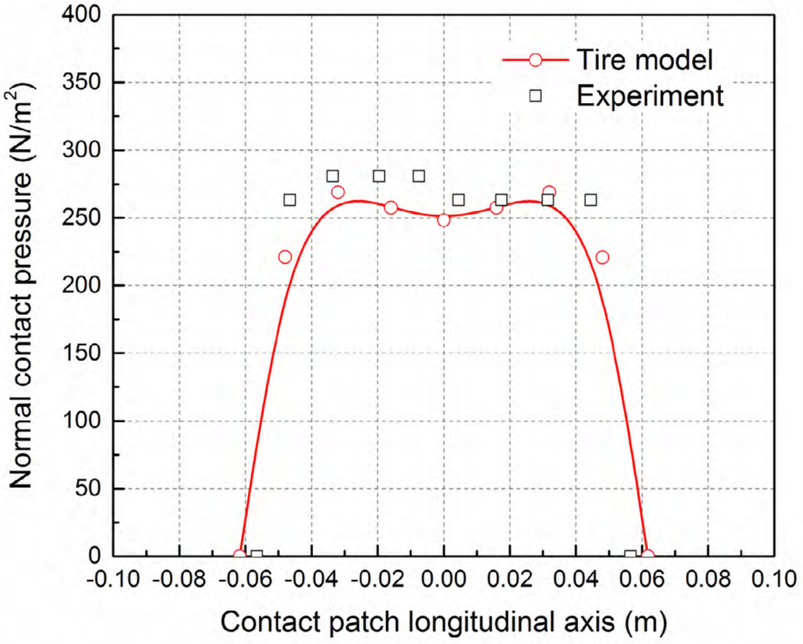

Figure 5.15 Normal contact pressure distribution in the longitudinal direction

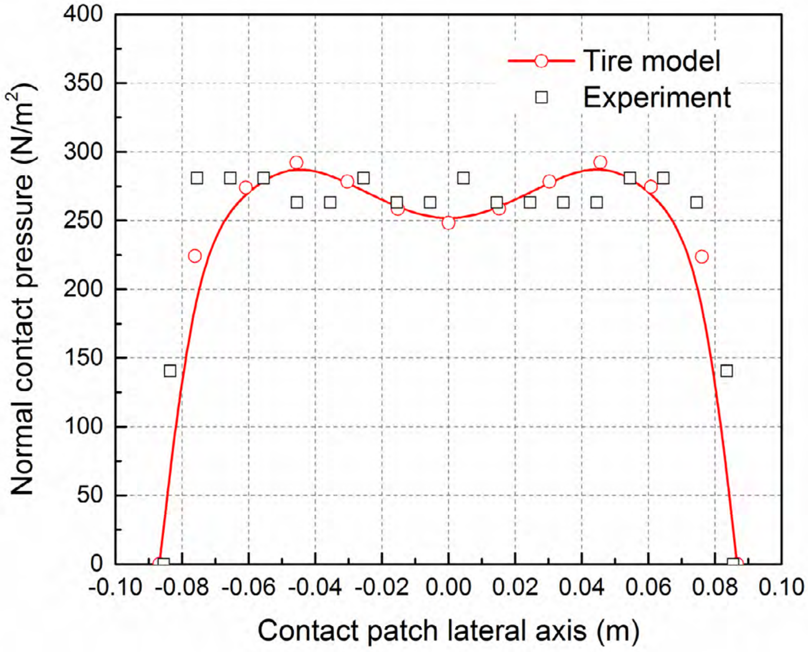

Figure 5.16 Normal contact pressure distribution in the lateral direction

In Fig. 5.17, the contour plot of the normal contact pressure is presented considering the tread patter of tire as shown in Fig. 5.18 for a static wheel load of 3 kN. Furthermore, the normal contact pressure distribution is compared with high-fidelity LS-DYNA FE tire model validated and used in tire design by a tire manufacture in Fig. 5.18. It is observed from this figure that a good agreement is obtained between both models and effect of the tread pattern is captured using the tire model developed in this study.

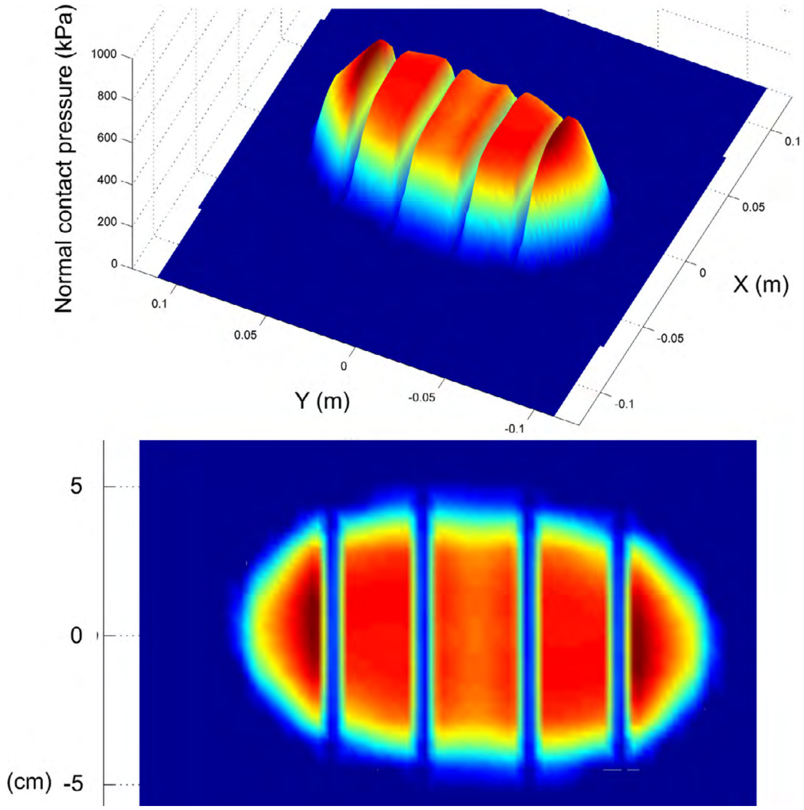

Figure 5.17 Normal contact pressure distribution considering tread pattern

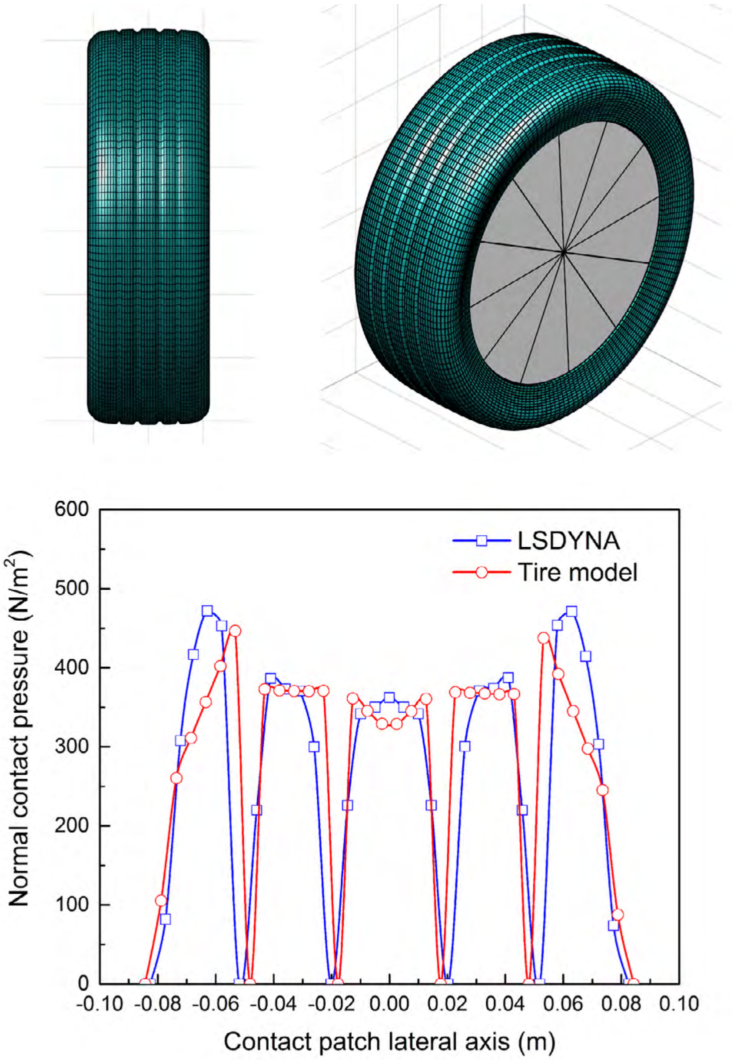

Figure 5.18 Comparison of normal contact pressure distribution with LS-DYNA FE tire model

To validate the vibration characteristics of the tire model, natural frequencies and associated mode shapes are identified by the experimental modal analysis in the free boundary condition and then the first three in-plane and out-of-plane elastic deformation modes are compared with those obtained by the tire model developed in this study as shown in Fig. 5.19. It is observed from this figure that good agreements are obtained for both in-plane and out-of-plane natural frequencies.

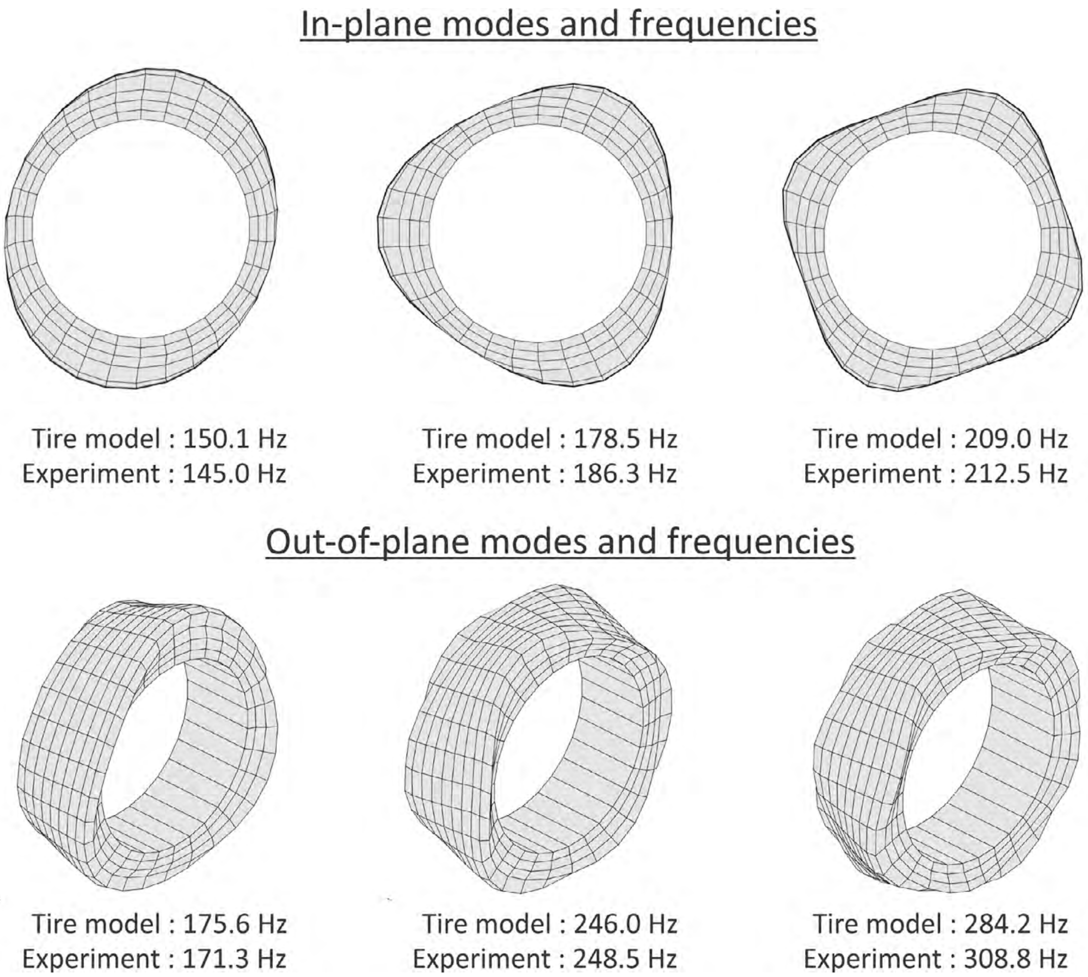

Figure 5.19 In-plane and out-of-plane natural frequencies

5.4.2 Transient Braking Simulation

To demonstrate the shear contact stresses under hard braking maneuvers using the flexible tire model with the distributed parameter LuGre tire friction model, the transient braking analysis is carried out. The constant traveling velocity of 22.6 m/s is prescribed and then external braking torque is applied to the rigid rim to completely lock the rotation of the rigid rim. The circumferential velocity and braking force predicted by the proposed tire model is presented in Fig. 5.20. As shown in this figure, the braking force builds up right after the braking torque is applied to the rim at t = 0.1 s and increases until it exceeds the maximum peak around t = 0.4 s. The braking force then drops when it goes beyond the peak, which is a typical behavior of the braking force of tires. The tire rim is finally locked completely around t = 0.47 s and the tire is skidding at the prescribed constant speed of 22.6 m/s. In this simulation, HHT time integration scheme is used with variable step size control. CPU time for this hard braking simulation was 8175 seconds using single processor (Intel Core i7-3770, 3.4GHz). The shear contact stresses acting on the tire in this transient braking scenario are shown in Fig. 5.21 at various instants of time. In each figure, the longitudinal (braking) components of the mean shear contact stresses are also plotted along the longitudinal axis of the contact patch. In the steady state rolling, the shear contact stresses around the center of the contact patch is small, while large contact stresses occur around the shoulder of the tire due to larger slips. The similar shear contact stress distribution is obtained using the detailed finite element tire model as presented in the literature [8] at the steady state rolling condition. After the braking toque is applied to the rim, the trailing contact zone starts sliding and the shear contact stresses increase, while contact stresses in the leading region are small since it is still in adhesion. For example, as shown in the result at *t* = 0.22 s, the shear contact stress increases linearly from the leading edge until it reaches the friction bound, and then sliding region appears. Finally, all the contact regions become sliding zone and the shear contact stress arrows get aligned, pointing to the direction opposite to the traveling direction (i.e., braking direction). It is also important to notice here that the shear contact stress at this

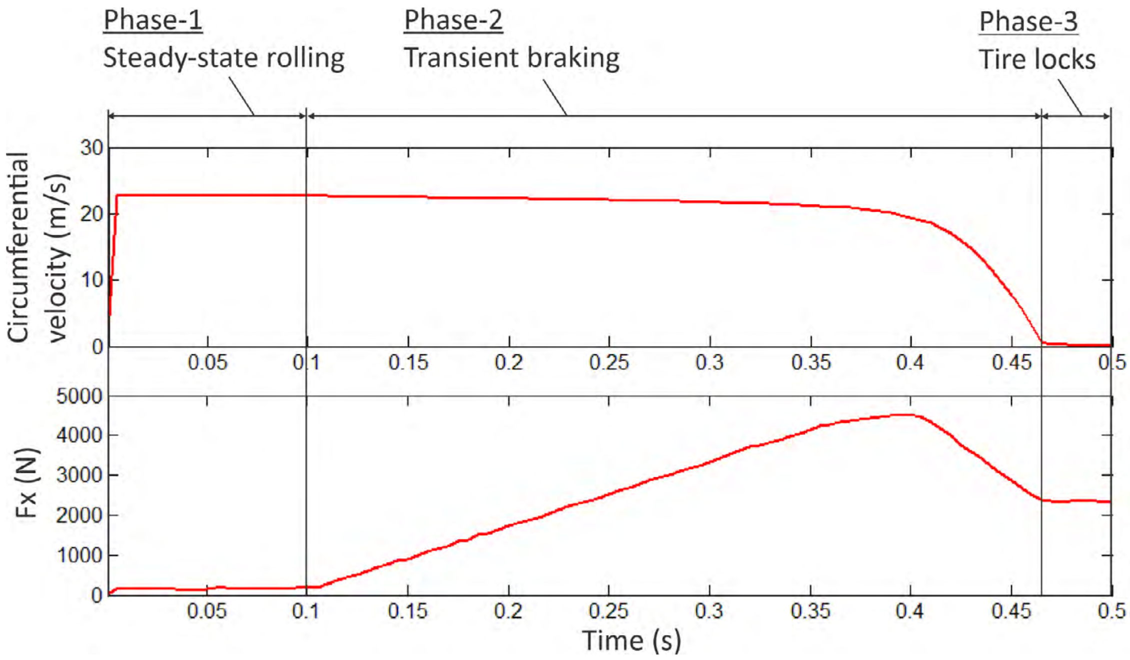

Figure 5.20 Transient braking analysis results

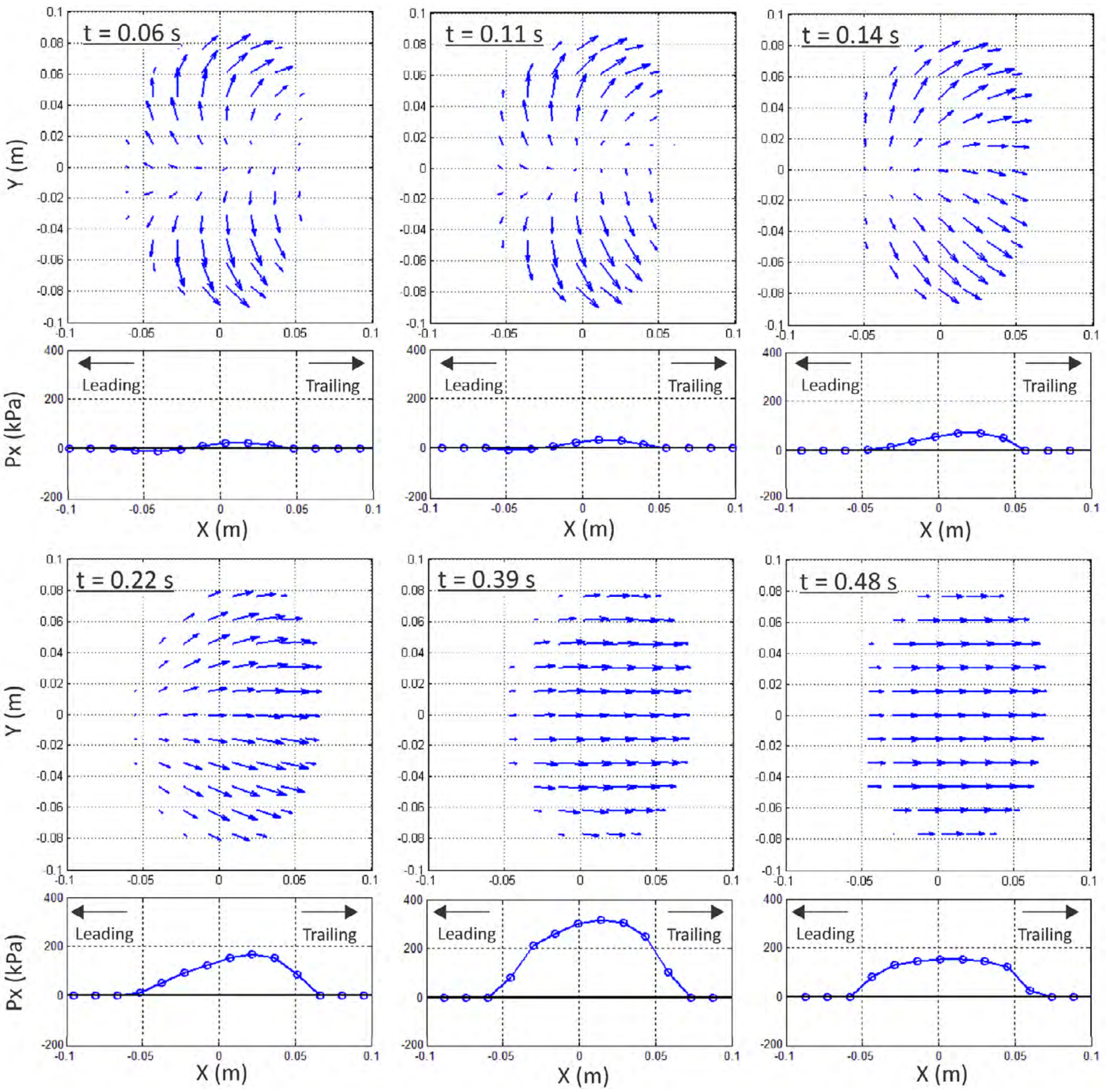

Figure 5.21 Shear contact stress distribution in the transient braking analysis

state (t = 0.48 s) is smaller than that at t = 0.39 s, at which the maximum peak of the braking force occurs. Furthermore, it is observed that the contact patch is pulled backward due to the tire deformation after the braking torque is applied.

5.4.3 Antilock Braking System (ABS) Simulation

To further discuss the simulation capability of the flexible tire model proposed in this study, an antilock braking system (ABS) control is considered. Using the ABS control, the braking torque is controlled to prevent a tire from being locked completely and the tire force around the peak friction can be generated during braking to minimize the braking distance. While there are various ABS control algorithms proposed in the past, a simplified slip-based on/off control algorithm is used in this study to focus on the tire model simulation capability under the severe braking scenario. In the numerical example, it is assumed that the braking torque T is defined as follows:

$$\begin{aligned}
&\text{If } T(t_n)=T_{up}(t_n)\\
&\quad T(t_{n+1})=\begin{cases} T_{up}(t_{n+1}) & \text{if } s(t_{n+1})<s_2 \\ T_{down}(t_{n+1}) & \text{if } s(t_{n+1})\geq s_2 \end{cases}\\
&\text{If } T(t_n)=T_{down}(t_n)\\
&\quad T(t_{n+1})=\begin{cases} T_{down}(t_{n+1}) & \text{if } s(t_{n+1})>s_1 \\ T_{up}(t_{n+1}) & \text{if } s(t_{n+1})\leq s_1 \end{cases}
\end{aligned} \tag{5.17}$$

where s_1=0.08 and s_2=0.14 such that the braking force is kept in that target slip range during braking and the target slip range is selected around the peak friction in the μ-slip curve. In the preceding equation, $T_{up}(t)$ and $T_{down}(t)$ are assumed to be a linear function having the positive and negative slopes, respectively. In Fig. 5.22, the slip ratio, the tangential force coefficient, and braking torque under the ABS control are shown as a function of time. It is observed from this figure that the slip ratio lies in the target range ($0.08 \leq s \leq 0.14$) during the braking, while the tire completely locks if the ABS control is off (i.e., the slip ratio becomes one), as shown in the dotted line. Furthermore, the braking torque changes up and down according to the change in the slip ratio by following the ABS control algorithm defined by Eq. 5.17. Furthermore, the change in the tangential force coefficient follows the change in the braking torque.

The forward velocity at the rim center and the circumferential velocity of the rim are presented in Fig. 5.23 for cases with and without ABS control. As shown in this figure, rotation of the rim is locked at t = 0.47 s if ABS is off and the tire continues skidding until it stops as presented in this figure. On the other hand, the tangential velocity in the case of ABS control decreases almost linearly to zero, indicating that a nearly constant braking force is ideally generated to stop the tire. This results in a shorter braking distance as demonstrated in Fig. 5.23. It is important to notice here that the circumferential velocity of the tire changes very frequently due the frequent switching of braking torque based on the ABS control. That is, as observed in Fig. 5.23, when the deviation of the circumferential velocity from the forward velocity gets larger due to the

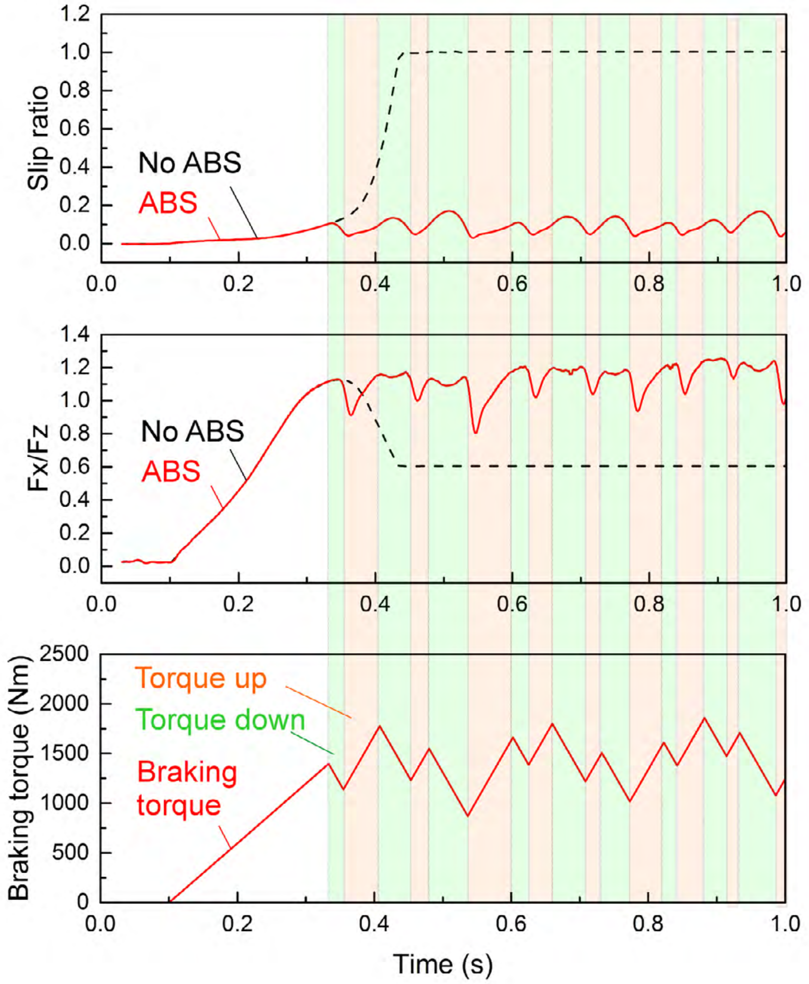

Figure 5.22 Simplified slip-based ABS control algorithm

increase in slip, the braking torque decreases until the circumferential velocity gets closer to the forward velocity. This process is repeated in order for the slip ratio to always lie in the target slip range. The μ-slip curve obtained using this time-domain ABS analysis is presented in Fig. 5.24. It is clearly observed from this figure that the tangential force coefficient (μ) lies in the target slip range if ABS control is used and it changes back and forth to keep generating the peak braking force during braking. If the ABS control is off, the tangential force coefficient sharply drops beyond the peak point and continue to decreases to the kinetic friction as discussed in the previous braking simulation scenario. It is also important to notice here that the tangential force coefficient gradually increases during the operation of the ABS control. Since the coefficient of friction increases as an increases in the slip velocity, the tangential force coefficient increase as the tire speed decreases. It is known that this friction behavior is observed in braking tests, and this typical friction behavior is captured in this physics-based tire dynamics simulation. As it is demonstrated in this ABS transient tire dynamics simulation that is challenging for existing finite element based tire models, the flexible tire model developed in this study is computationally robust and is capable of predicting the transient tire dynamics behavior.

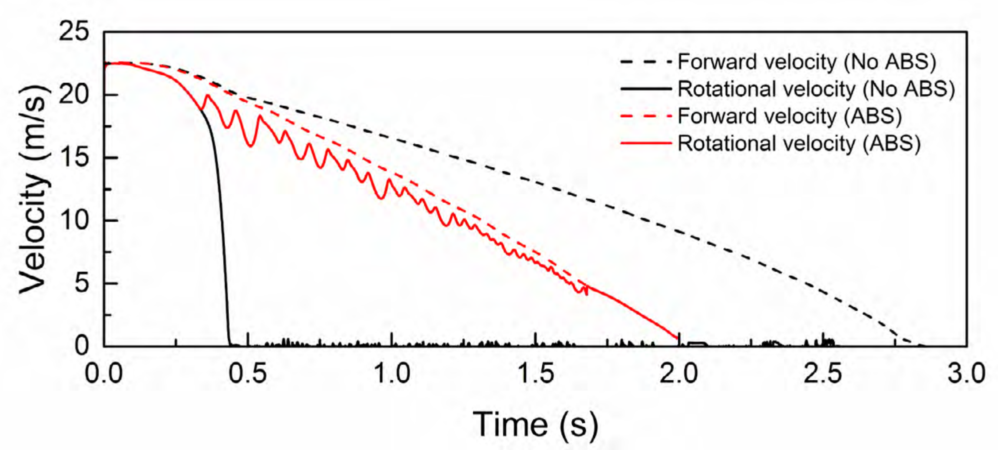

Figure 5.23 Forward and circumferential velocities of tire with and without ABS control

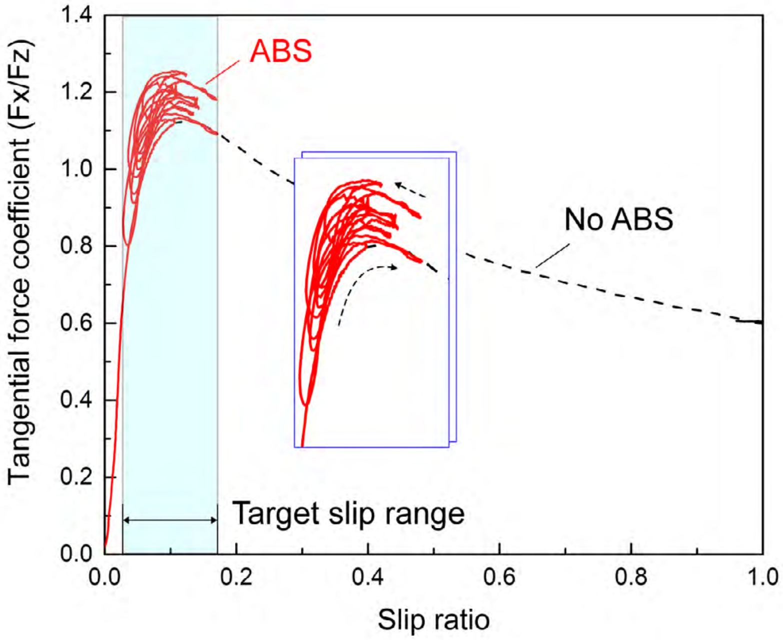

Figure 5.24 μ-slip curve with and without ABS control

5.4.4 Transient Cornering Simulation

To evaluate the transient cornering force characteristics, frequency response of a cornering force to an oscillatory steering input is evaluated. The cornering force responses for different steering (slip) angle path frequencies are shown in Fig. 5.25. The path frequency is defined by a frequency of the slip angle input divided by the forward velocity and its unit is cycle/m. The steering (slip) angle is assumed to be 1 degree in both directions. It is observed from this figure that the cornering force amplitude decreases and the phase lag increases as the path frequency increases. To validate the cornering force response, the cornering force gain and phase lag are presented in Fig.

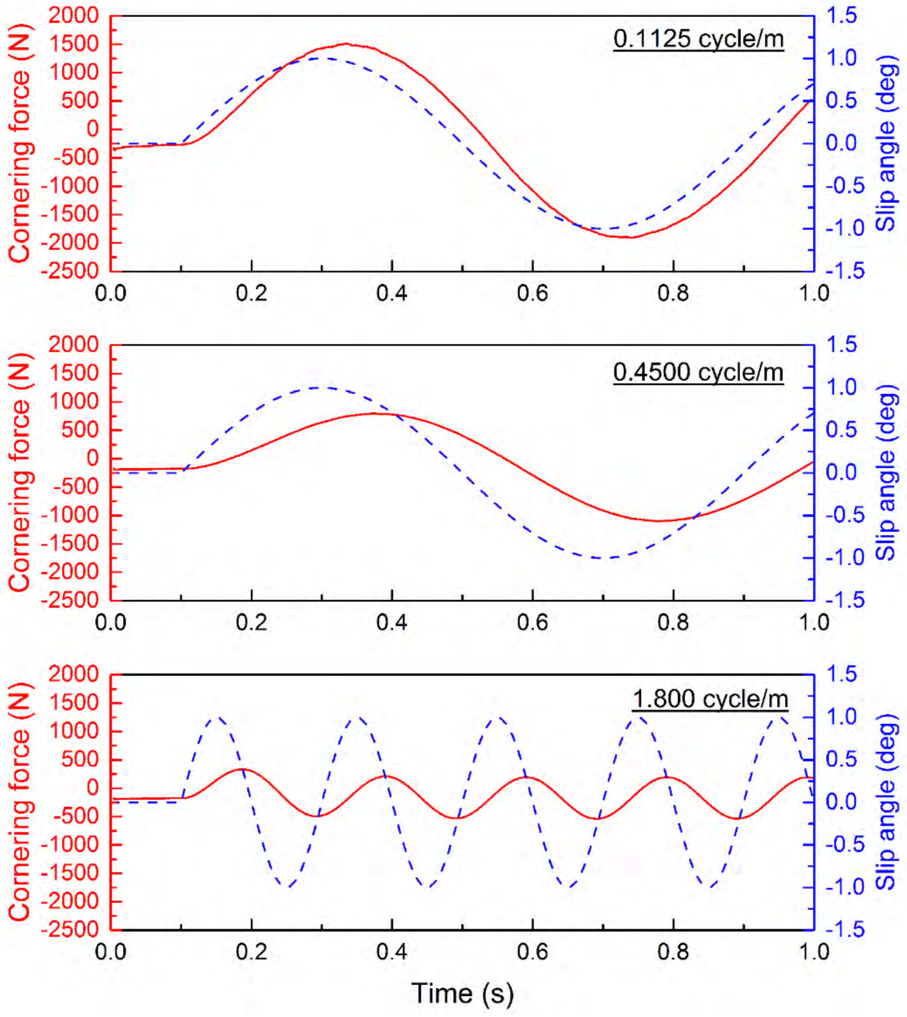

Figure 5.25 Cornering force responses to oscillatory steering input

5.26 as a function of the input path frequency. It is observed from these figures that very good agreements are obtained in the cornering force gain and the phase lag for a wide range of path frequency using the physics-based flexible tire model developed in this study.

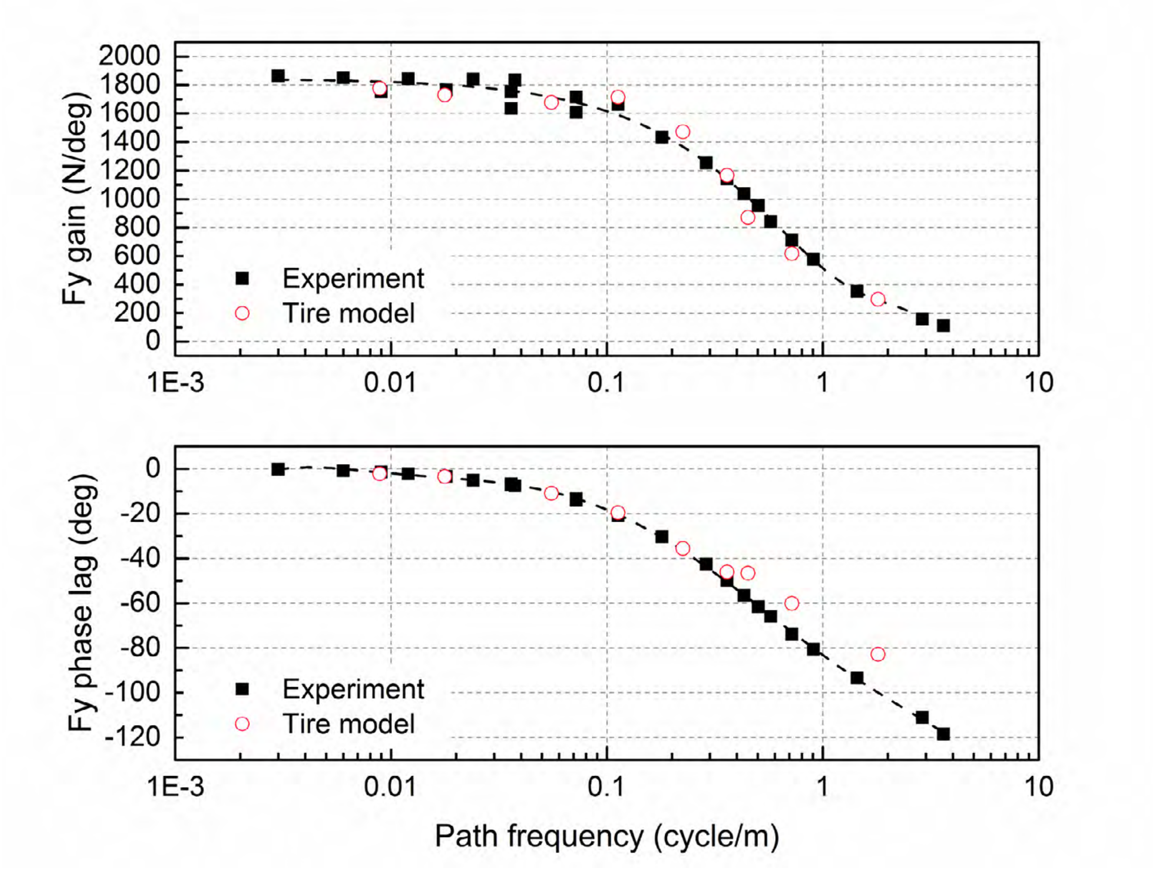

Figure 5.26 Cornering force responses and phase lag

In the last example, a hard cornering maneuver is considered as shown in Fig. 5.27, where the slip angle changes from zero to one degree in 0.2 seconds. CPU time for this transient cornering simulation was 8427 seconds using single processor (Intel Core i7-3770, 3.4GHz). It is observed from the shear contact stresses shown in Fig. 5.28 that the shear contact stresses are pointing to the cornering direction (right to the direction of travel) as the slip angle increases. Furthermore, the shear contact stresses increase on the right side of the contact patch due to the increase in the normal contact pressure in this region for the steering input.

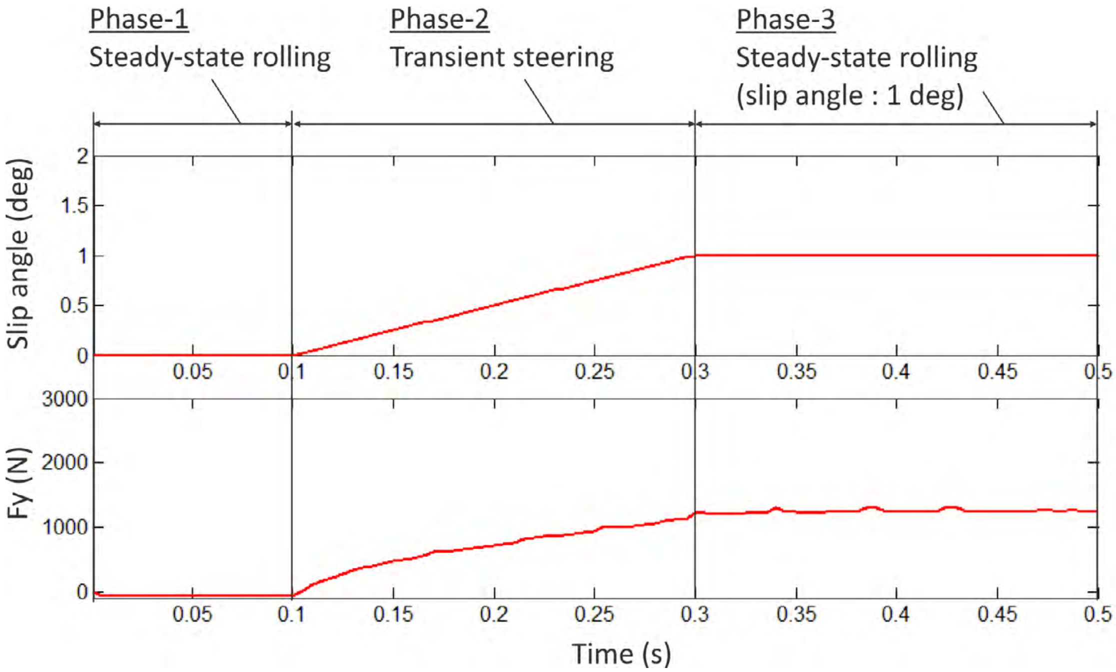

Figure 5.27 Transient cornering analysis results

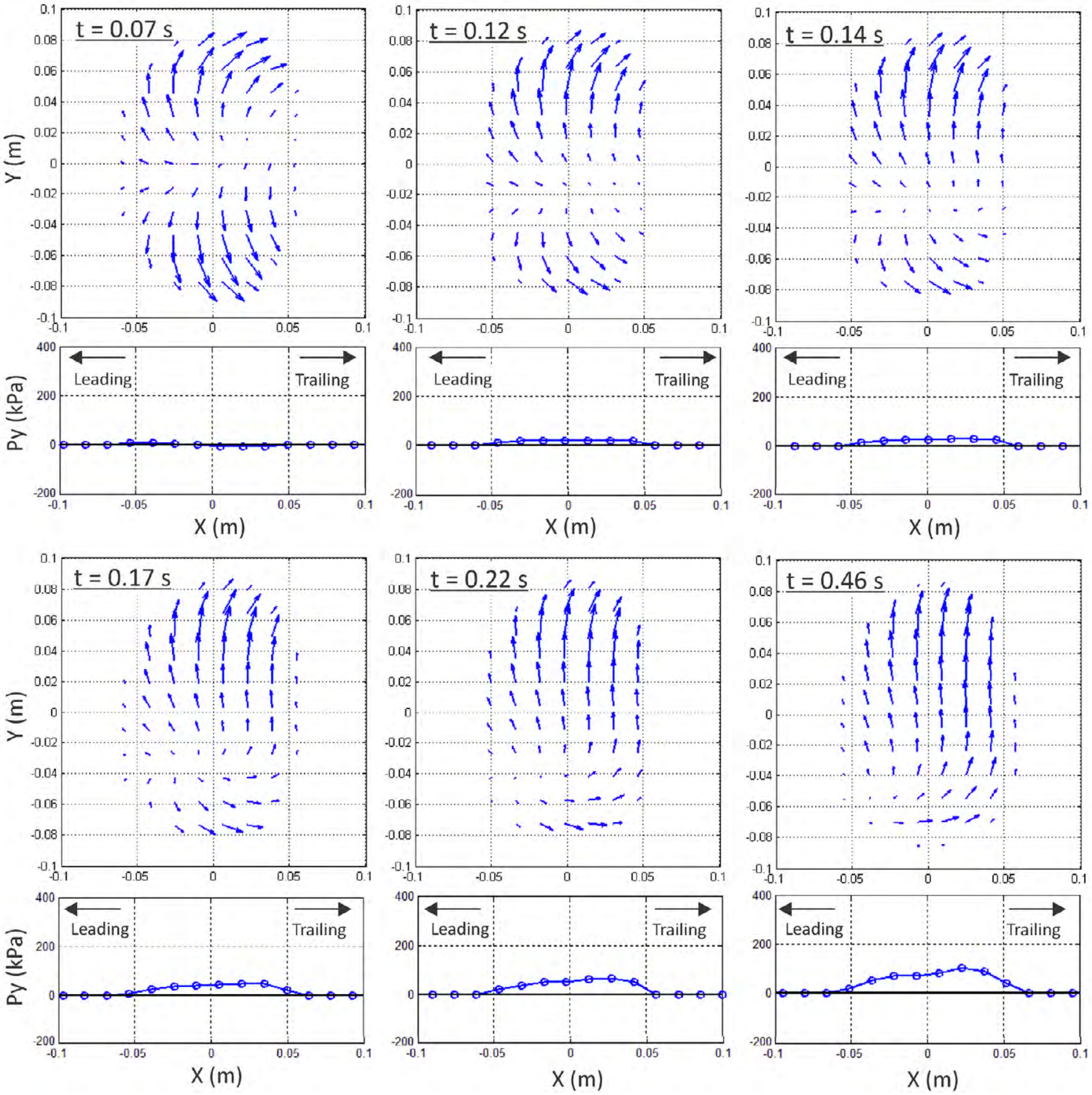

Figure 5.28 Shear contact stress distribution in the transient cornering analysis

CHAPTER 6

CONTINUUM BASED SOIL MODEL AND VALIDATION

6.1 Introduction

In this chapter, a continuum based finite element soil model is developed for use in off-road mobility simulation using the physics-based flexible tire model discussed in previous chapters. For modeling deformable soil, a 9-node brick element is proposed by introducing the additional curvature coordinates at the center node to the standard tri-linear 8-node brick element. It is shown that the 9-node brick element does not suffer from the element lockings exhibited in the standard 8-node tri-linear brick element caused by the incapability of describing the linear stress and strain distribution over the volume, thereby making the implementation of the plasticity material model straightforward for soil model. The capped Drucker-Prager failure material model based on the multiplicative finite strain plasticity theory is applied to the 9-node brick element to develop the large deformable continuum soil model for off-road mobility simulation. Using the triaxial soil test data, parameters of the capped Drucker-Prager model are identified and used for validating the soil behavior under the triaxial test condition.

6.2 Brick Elements for Modeling Continuum Soil

6.2.1 Tri-linear 8-Node Brick Element (Brick24)

The global position vector of the standard 8-node 24-DOF brick element is defined using the tri-linear polynomial as

$$r = a_0 + a_1\xi + a_2\eta + a_3\zeta + a_4\xi\eta + a_5\xi\zeta + a_6\eta\zeta + a_7\xi\eta\zeta \tag{6.1}$$

Each corner node has three degrees of freedom describing the global position at the node as shown in Fig. 6.1, thus only C^0 continuity is ensured at nodal points. Using the preceding polynomial, the global position vector is defined as

$$\mathbf{r}^i(\xi^i,\eta^i,\zeta^i) = \mathbf{S}^i(\xi^i,\eta^i,\zeta^i)\mathbf{e}^i \tag{6.2}$$

where $\mathbf{e}^i$ is the element nodal coordinate vector and each nodal coordinate at node k ($k = 1,\cdots,8$) include three position coordinates only as $\mathbf{e}^{ik} = \mathbf{r}^{ik}$. The matrix $\mathbf{S}^i$ is the shape function matrix given by

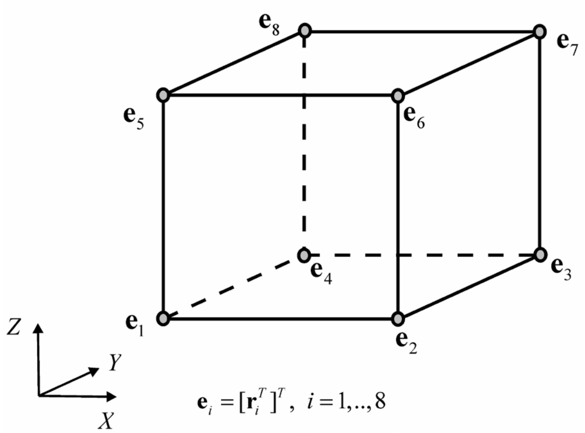

Figure 6.1 Kinematics of 8-node tri-linear brick element

(Brick24)

$$\mathbf{S}^i = \begin{bmatrix} S_1^i\mathbf{I} & S_2^i\mathbf{I} & S_3^i\mathbf{I} & S_4^i\mathbf{I} & S_5^i\mathbf{I} & S_6^i\mathbf{I} & S_7^i\mathbf{I} & S_8^i\mathbf{I} \end{bmatrix} \tag{6.3}$$

and

$$\left.\begin{aligned} S_1^i &= \frac{1}{8}(1-\xi^i)(1-\eta^i)(1-\zeta^i), & S_2^i &= \frac{1}{8}(1+\xi^i)(1-\eta^i)(1-\zeta^i) \\ S_3^i &= \frac{1}{8}(1+\xi^i)(1+\eta^i)(1-\zeta^i), & S_4^i &= \frac{1}{8}(1-\xi^i)(1+\eta^i)(1-\zeta^i) \\ S_5^i &= \frac{1}{8}(1-\xi^i)(1-\eta^i)(1+\zeta^i), & S_6^i &= \frac{1}{8}(1+\xi^i)(1-\eta^i)(1+\zeta^i) \\ S_7^i &= \frac{1}{8}(1+\xi^i)(1+\eta^i)(1+\zeta^i), & S_8^i &= \frac{1}{8}(1-\xi^i)(1+\eta^i)(1+\zeta^i) \end{aligned}\right\} \tag{6.4}$$

The elastic forces of the brick element are evaluated using the continuum mechanics approach and the Green-Lagrange strain tensor at an arbitrary material point in element *i* is defined as follows:

$$\mathbf{E}^i = \frac{1}{2}\left((\mathbf{F}^i)^T\mathbf{F}^i - \mathbf{I}\right) \tag{6.5}$$

where $\mathbf{F}^i$ is the global position vector gradient tensor defined by

$$\mathbf{F}^i = \frac{\partial \mathbf{r}^i}{\partial \mathbf{X}^i} = \frac{\partial \mathbf{r}^i}{\partial \mathbf{x}^i}\left(\frac{\partial \mathbf{X}^i}{\partial \mathbf{x}^i}\right)^{-1} = \bar{\mathbf{J}}^i(\mathbf{J}^i)^{-1} \tag{6.6}$$

In the preceding equation, $\bar{\mathbf{J}}^i = \partial \mathbf{r}^i / \partial \mathbf{x}^i$ and $\mathbf{J}^i = \partial \mathbf{X}^i / \partial \mathbf{x}^i$, where the vector $\mathbf{X}^i$ represents the global position vector of element i at an arbitrary reference configuration. Strain tensor $\mathbf{E}^i$ can be re-expressed in a vector form as

$$\boldsymbol{\varepsilon}^i = (\mathbf{T}^i)^{-T} \tilde{\boldsymbol{\varepsilon}}^i \tag{6.7}$$

where the vectors of the Green-Lagrange strains and covariant strains are, respectively, given as

$$\boldsymbol{\varepsilon}^i = [\varepsilon^i_{xx} \quad \varepsilon^i_{yy} \quad \gamma^i_{xy} \quad \varepsilon^i_{zz} \quad \gamma^i_{xz} \quad \gamma^i_{yz}]^T \tag{6.8}$$

and

$$\tilde{\boldsymbol{\varepsilon}}^i = [\tilde{\varepsilon}^i_{xx} \quad \tilde{\varepsilon}^i_{yy} \quad \tilde{\gamma}^i_{xy} \quad \tilde{\varepsilon}^i_{zz} \quad \tilde{\gamma}^i_{xz} \quad \tilde{\gamma}^i_{yz}]^T \tag{6.9}$$

The transformation matrix $\mathbf{T}^i$ in Eq. 6.7 is be expressed as

$$\mathbf{T}^i = \begin{bmatrix} (J^i_{11})^2 & (J^i_{12})^2 & 2J^i_{11}J^i_{12} & (J^i_{13})^2 & 2J^i_{11}J^i_{13} & 2J^i_{12}J^i_{13} \\ (J^i_{21})^2 & (J^i_{22})^2 & 2J^i_{21}J^i_{22} & (J^i_{23})^2 & 2J^i_{21}J^i_{23} & 2J^i_{22}J^i_{23} \\ J^i_{11}J^i_{21} & J^i_{12}J^i_{22} & J^i_{11}J^i_{22}+J^i_{12}J^i_{21} & J^i_{13}J^i_{23} & J^i_{11}J^i_{23}+J^i_{13}J^i_{21} & J^i_{12}J^i_{23}+J^i_{13}J^i_{22} \\ (J^i_{31})^2 & (J^i_{32})^2 & 2J^i_{31}J^i_{32} & (J^i_{33})^2 & 2J^i_{31}J^i_{33} & 2J^i_{32}J^i_{33} \\ J^i_{11}J^i_{31} & J^i_{12}J^i_{32} & J^i_{11}J^i_{32}+J^i_{12}J^i_{31} & J^i_{13}J^i_{33} & J^i_{11}J^i_{33}+J^i_{13}J^i_{31} & J^i_{12}J^i_{33}+J^i_{13}J^i_{32} \\ J^i_{21}J^i_{31} & J^i_{22}J^i_{32} & J^i_{21}J^i_{32}+J^i_{22}J^i_{31} & J^i_{23}J^i_{33} & J^i_{21}J^i_{33}+J^i_{23}J^i_{31} & J^i_{22}J^i_{33}+J^i_{23}J^i_{32} \end{bmatrix} \tag{6.10}$$

and J^i_{ab} is the element in the *a*-th column and *b*-th row of matrix $\mathbf{J}^i$ which is constant in time. The generalized elastic forces can then be obtained using the virtual work as follows:

$$\mathbf{Q}^i_k = -\int_{V^i_0} \left(\frac{\partial \boldsymbol{\varepsilon}^i}{\partial \mathbf{e}^i} \right)^T \frac{\partial W^i}{\partial \boldsymbol{\varepsilon}^i} dV^i_0 \tag{6.11}$$

where W is an elastic energy function and dV^i_0 is the infinitesimal volume at the reference configuration of element *i*. It is important to notice here that, because of the tri-linear polynomial utilized, the strains are constant over the volume, causing the element lockings. To alleviate the locking, the 9-parameter enhanced assumed strain (EAS) are introduced as follows:

$$\boldsymbol{\varepsilon} = \boldsymbol{\varepsilon}^c + \boldsymbol{\varepsilon}^{EAS} \tag{6.12}$$

where $\boldsymbol{\varepsilon}^c$ indicates the compatible strain vector and one has

$$\boldsymbol{\varepsilon}^{EAS}(\xi) = \mathbf{G}(\xi)\boldsymbol{\alpha} \tag{6.13}$$

In the preceding equation, $\boldsymbol{\alpha}$ is a vector of internal parameters introduced to define the enhanced strain field of the brick element and the matrix $\mathbf{G}(\boldsymbol{\xi})$ can be defined as [54,73]

$$\mathbf{G}(\boldsymbol{\xi}) = \frac{|\mathbf{J}_0|}{|\mathbf{J}(\boldsymbol{\xi})|}\mathbf{T}_0^{-\mathrm{T}}\mathbf{N}(\boldsymbol{\xi}) \tag{6.14}$$

where $\mathbf{J}(\boldsymbol{\xi})$ and $\mathbf{J}_0$ are the global position vector gradient matrices at the reference configuration evaluated at the Gaussian integration point $\boldsymbol{\xi}$ and at the center of element ($\boldsymbol{\xi} = \mathbf{0}$), respectively. $\boldsymbol{\xi}$ is a vector of the element coordinates in the parametric domain and $\mathbf{T}_0$ is the constant transformation matrix evaluated at the center of element. The matrix $\mathbf{N}(\boldsymbol{\xi})$ defines polynomials for the enhancement of the strain field in the parametric domain as follows:

$$\mathbf{N}(\boldsymbol{\xi}) = \begin{bmatrix} \xi & 0 & 0 & 0 & 0 & 0 & 0 & 0 & 0 \\ 0 & \eta & 0 & 0 & 0 & 0 & 0 & 0 & 0 \\ 0 & 0 & \xi & \eta & 0 & 0 & 0 & 0 & 0 \\ 0 & 0 & 0 & 0 & \zeta & 0 & 0 & 0 & 0 \\ 0 & 0 & 0 & 0 & 0 & \xi & \zeta & 0 & 0 \\ 0 & 0 & 0 & 0 & 0 & 0 & 0 & \eta & \zeta \end{bmatrix} \tag{6.15}$$

6.2.2 Tri-cubic 8-Node ANCF Brick Element (Brick96)

The concept of the fully parameterized beam and shell elements of the absolute nodal coordinate formulation utilizing the three sets of the global position vector gradients along the element *x*, *y* and *z* coordinates can be extended to the 8-node brick element [74]. In other words, the three sets of gradient vector coordinates, $\partial\mathbf{r}/\partial x$, $\partial\mathbf{r}/\partial y$ and $\partial\mathbf{r}/\partial z$ are introduced to the nodal coordinates of each node as shown in Fig. 6.2, thus C^1 continuity is automatically ensured due to the use of position vector gradient at all the nodal points. This leads to the 8-node 96-DOF brick element using the following polynomial:

$$\begin{aligned} r = {} & a_0 + a_1\xi + a_2\eta + a_3\zeta + a_4\xi\eta + a_5\xi\zeta + a_6\eta\zeta + a_7\xi\eta\zeta + a_8\xi^2 + a_9\eta^2 + a_{10}\zeta^2 \\ & + a_{11}\xi\eta^2 + a_{12}\xi^2\eta + a_{13}\eta\zeta^2 + a_{14}\eta^2\zeta + a_{15}\zeta\xi^2 + a_{16}\xi\zeta^2 + a_{17}\xi^3 + a_{18}\eta^3 + a_{19}\zeta^3 \\ & + a_{20}\xi^3\eta + a_{21}\xi\eta^3 + a_{22}\zeta^3\eta + a_{23}\eta^3\zeta + a_{24}\zeta^3\xi + a_{25}\xi^3\zeta + a_{26}\xi^2\eta\zeta + a_{27}\xi\eta^2\zeta \\ & + a_{28}\xi^3\eta\zeta + a_{29}\xi\eta^3\zeta + a_{30}\zeta^2\eta\xi + a_{31}\zeta^3\eta\xi \end{aligned} \tag{6.16}$$

Using the preceding polynomial, the global position vector is defined as

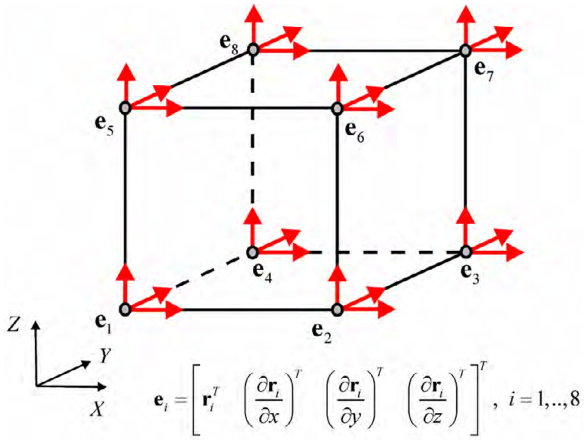

Figure 6.2 Kinematics of 8-node tri-cubic ANCF brick element (Brick96)

$$\mathbf{r}^i(\xi^i,\eta^i,\zeta^i) = \mathbf{S}^i(\xi^i,\eta^i,\zeta^i)\mathbf{e}^i \tag{6.17}$$

where $\mathbf{e}^i$ is the element nodal coordinate vector and each nodal coordinate at node k ($k = 1,\cdots,8$) is defined as

$$\mathbf{e}^{ik} = [(\mathbf{r}^{ik})^T \quad (\partial\mathbf{r}^{ik}/\partial x^i)^T \quad (\partial\mathbf{r}^{ik}/\partial y^i)^T \quad (\partial\mathbf{r}^{ik}/\partial z^i)^T]^T \tag{6.18}$$

The shape function matrix $\mathbf{S}^i$ in Eq. 6.17 is given by

$$\mathbf{S}^i = \left[S_1^i\mathbf{I} \quad S_2^i\mathbf{I} \qquad \cdots \quad \cdots \qquad S_{31}^i\mathbf{I} \quad S_{32}^i\mathbf{I} \right] \tag{6.19}$$

where

$$\left.\begin{aligned}
S_1 &= \frac{1}{16}(\xi-1)(\eta-1)(\zeta-1)\left(\xi^2+\eta^2+\zeta^2+\xi+\eta+\zeta-2\right)\\
S_2 &= \frac{1}{32}a(\xi-1)^2(\xi+1)(\eta-1)(\zeta-1)\\
S_3 &= \frac{1}{32}b(\eta-1)^2(\xi-1)(\eta+1)(\zeta-1)\\
S_4 &= \frac{1}{32}c(\zeta-1)^2(\xi-1)(\eta-1)(\zeta+1)\\
S_5 &= -\frac{1}{16}(\xi+1)(\eta-1)(\zeta-1)\left(\xi^2+\eta^2+\zeta^2-\xi+\eta+\zeta-2\right)\\
S_6 &= \frac{1}{32}a(\xi+1)^2(\xi-1)(\eta-1)(\zeta-1)\\
S_7 &= -\frac{1}{32}b(\eta-1)^2(\xi+1)(\eta+1)(\zeta-1)\\
S_8 &= -\frac{1}{32}c(\zeta-1)^2(\xi+1)(\eta-1)(\zeta+1)\\
S_9 &= -\frac{1}{16}(\xi-1)(\eta+1)(\zeta-1)\left(\xi^2+\eta^2+\zeta^2+\xi-\eta+\zeta-2\right)\\
S_{10} &= -\frac{1}{32}a(\xi-1)^2(\xi+1)(\eta+1)(\zeta-1)\\
S_{11} &= \frac{1}{32}b(\eta+1)^2(\xi-1)(\eta-1)(\zeta-1)\\
S_{12} &= -\frac{1}{32}c(\zeta-1)^2(\xi-1)(\eta+1)(\zeta+1)\\
S_{13} &= \frac{1}{16}(\xi+1)(\eta+1)(\zeta-1)\left(\xi^2+\eta^2+\zeta^2-\xi-\eta+\zeta-2\right)\\
S_{14} &= -\frac{1}{32}a(\xi+1)^2(\xi-1)(\eta+1)(\zeta-1)\\
S_{15} &= -\frac{1}{32}b(\eta+1)^2(\xi+1)(\eta-1)(\zeta-1)\\
S_{16} &= \frac{1}{32}c(\zeta-1)^2(\xi+1)(\eta+1)(\zeta+1)
\end{aligned}\right\} \tag{6.20a}$$

$$\left.\begin{aligned}
S_{17} &= -\frac{1}{16}(\xi-1)(\eta-1)(\zeta+1)\left(\xi^2+\eta^2+\zeta^2+\xi+\eta-\zeta-2\right)\\
S_{18} &= -\frac{1}{32}a(\xi-1)^2(\xi+1)(\eta-1)(\zeta+1)\\
S_{19} &= -\frac{1}{32}b(\eta-1)^2(\xi-1)(\eta+1)(\zeta+1)\\
S_{20} &= \frac{1}{32}c(\zeta+1)^2(\xi-1)(\eta-1)(\zeta-1)\\
S_{21} &= \frac{1}{16}(\xi+1)(\eta-1)(\zeta+1)\left(\xi^2+\eta^2+\zeta^2-\xi+\eta-\zeta-2\right)\\
S_{22} &= -\frac{1}{32}a(\xi+1)^2(\xi-1)(\eta-1)(\zeta+1)\\
S_{23} &= \frac{1}{32}b(\eta-1)^2(\xi+1)(\eta+1)(\zeta+1)\\
S_{24} &= -\frac{1}{32}c(\zeta+1)^2(\xi+1)(\eta-1)(\zeta-1)\\
S_{25} &= \frac{1}{16}(\xi-1)(\eta+1)(\zeta+1)\left(\xi^2+\eta^2+\zeta^2+\xi-\eta-\zeta-2\right)\\
S_{26} &= \frac{1}{32}a(\xi-1)^2(\xi+1)(\eta+1)(\zeta+1)\\
S_{27} &= -\frac{1}{32}b(\eta+1)^2(\xi-1)(\eta-1)(\zeta+1)\\
S_{28} &= -\frac{1}{32}c(\zeta+1)^2(\xi-1)(\eta+1)(\zeta-1)\\
S_{29} &= -\frac{1}{16}(\xi+1)(\eta+1)(\zeta+1)\left(\xi^2+\eta^2+\zeta^2-\xi-\eta-\zeta-2\right)\\
S_{30} &= \frac{1}{32}a(\xi+1)^2(\xi-1)(\eta+1)(\zeta+1)\\
S_{31} &= \frac{1}{32}b(\eta+1)^2(\xi+1)(\eta-1)(\zeta+1)\\
S_{32} &= \frac{1}{32}c(\zeta+1)^2(\xi+1)(\eta+1)(\zeta-1)
\end{aligned}\right\} \qquad (6.20b)$$

where $\xi = 2(x-a/2)/a$, $\eta = 2(y-b/2)/b$, and $\zeta = 2(z-c/2)/c$. The generalized elastic forces can then be obtained using the virtual work as follows:

$$\mathbf{Q}_k^i = -\int_{V_0^i}\left(\frac{\partial \boldsymbol{\varepsilon}^i}{\partial \mathbf{e}^i}\right)^T \frac{\partial W^i}{\partial \boldsymbol{\varepsilon}^i}\,dV_0^i \qquad (6.21)$$

where W is an elastic energy function and dV_0^i is the infinitesimal volume at the reference configuration of element i.

6.2.3 9-Node Brick Element with Curvature Coordinates (Brick33)

Despite the C^1 continuity ensured for the 96-DOF ANCF brick element (Brick96), the element has large degrees of freedom, thereby making the element force calculation computationally intensive. On the other hand, the standard 8-node 24-DOF brick element (Brick24) requires use of locking remedies such as the enhanced assumed strain method to describe the linear stress and strain distribution over the volume. In other words, nine internal parameters are introduced to improve the compatible strain field to describe the accurate stress distribution while keeping the same number of degrees of freedom. This, however, requires additional iterative solution procedure to determine the internal EAS parameters at element level at every time step, and use of plasticity material model for modeling soil makes the solution procedure more computationally intensive. For this reason, in this study, the 8-node 24DOF brick element is extended to capture the quadratic terms in ξ, η and ζ, and the polynomial of the global position vector is re-defined as follows:

$$r = a_0 + a_1\xi + a_2\eta + a_3\zeta + a_4\xi\eta + a_5\xi\zeta + a_6\eta\zeta + a_7\xi\eta\zeta + a_8\xi^2 + a_9\eta^2 + a_{10}\zeta^2 \tag{6.22}$$

To consider the quadric terms in the preceding polynomial, an additional node defining the second derivative of the position coordinate $\mathbf{e}^{i9} = [\partial^2\mathbf{r}^{i9}/(\partial x^i)^2 \quad \partial^2\mathbf{r}^{i9}/(\partial y^i)^2 \quad \partial^2\mathbf{r}^{i9}/(\partial z^i)^2]^T$ is introduced to the center of the brick element as shown in Fig. 6.3. Accordingly, the global position vector is defined as

$$\mathbf{r}^i(\xi^i,\eta^i,\zeta^i) = \mathbf{S}^i(\xi^i,\eta^i,\zeta^i)\mathbf{e}^i \tag{6.23}$$

where $\mathbf{e}^i$ is the element nodal coordinate vector and each nodal coordinate at node k (k = 1 to 9) is defined as

$$\left.\begin{aligned} &\mathbf{e}^{ik} = (\mathbf{r}^{ik})^T, \quad k = 1,\cdots,8 \\ &\mathbf{e}^{i9} = [\partial^2\mathbf{r}^{i9}/(\partial x^i)^2 \quad \partial^2\mathbf{r}^{i9}/(\partial y^i)^2 \quad \partial^2\mathbf{r}^{i9}/(\partial z^i)^2]^T \end{aligned}\right\} \tag{6.24}$$

The shape function matrix $\mathbf{S}^i$ in Eq. 6.23 is given by

$$\mathbf{S} = \begin{bmatrix} S_1\mathbf{I} & S_2\mathbf{I} & S_3\mathbf{I} & S_4\mathbf{I} & S_5\mathbf{I} & S_6\mathbf{I} & S_7\mathbf{I} & S_8\mathbf{I} & S_9\mathbf{I} & S_{10}\mathbf{I} & S_{11}\mathbf{I} \end{bmatrix} \tag{6.25}$$

where

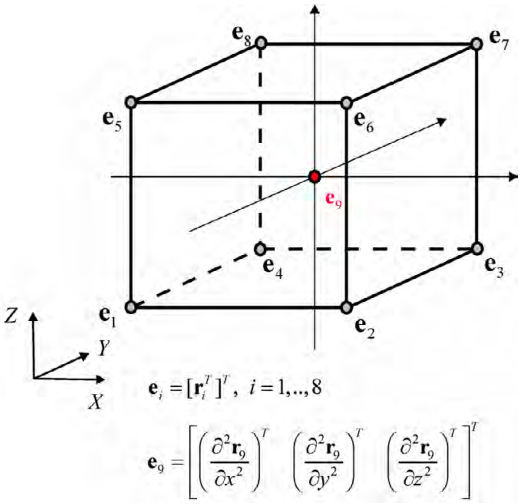

Figure 6.3 Kinematics of 9-node brick element with curvature coordinates (Brick33)

$$\left.\begin{array}{ll}
S_1^i = \frac{1}{8}(1-\xi^i)(1-\eta^i)(1-\zeta^i), & S_2^i = \frac{1}{8}(1+\xi^i)(1-\eta^i)(1-\zeta^i) \\
S_3^i = \frac{1}{8}(1+\xi^i)(1+\eta^i)(1-\zeta^i), & S_4^i = \frac{1}{8}(1-\xi^i)(1+\eta^i)(1-\zeta^i) \\
S_5^i = \frac{1}{8}(1-\xi^i)(1-\eta^i)(1+\zeta^i), & S_6^i = \frac{1}{8}(1+\xi^i)(1-\eta^i)(1+\zeta^i) \\
S_7^i = \frac{1}{8}(1+\xi^i)(1+\eta^i)(1+\zeta^i), & S_8^i = \frac{1}{8}(1-\xi^i)(1+\eta^i)(1+\zeta^i) \\
\multicolumn{2}{l}{S_9^i = \frac{1}{2}((\xi^i)^2-1), \quad S_{10}^i = \frac{1}{2}((\eta^i)^2-1), \quad S_{11}^i = \frac{1}{2}((\zeta^i)^2-1)}
\end{array}\right\} \tag{6.26}$$

It is important to notice here that the introduction of the quadratic terms allows for describing the linear distribution of the strain field, thus the locking exhibited in 8-node 24-DOF brick element can be alleviated without introducing the enhanced assumed strain approach. The similar approach such as a bubble function to add incompatible modes is employed for brick elements in literature [75]. This makes the implementation of the complex plasticity failure models such as Drucker-Prager yield criterion for deformable soil straightforward. The generalized elastic forces can then be obtained using the virtual work as follows:

$$\mathbf{Q}_k^i = -\int_{V_0^i} \left(\frac{\partial \boldsymbol{\varepsilon}^i}{\partial \mathbf{e}^i} \right)^T \frac{\partial W^i}{\partial \boldsymbol{\varepsilon}^i} dV_0^i \tag{6.27}$$

where W is an elastic energy function and dV_0^i is the infinitesimal volume at the reference configuration of element i.

6.2.4 Comparison of Brick Element Performance

To demonstrate the accuracy and computational efficiency of the three brick elements introduced in this section, numerical results of nonlinear static and dynamic analysis are presented. In the first example, a cantilever plate subjected to a point load is considered as shown in Fig. 6.4. The length, width and thickness of the plate are assumed to be 1.0 m, 1.0 m and 0.01 m. Young's modulus and Poisson's ratio 2.1×10^8 Pa and 0.3, respectively. The vertical point force F_z defined at the corner node is assumed to be 50 N. The rate of convergence of the numerical solution obtained using the three different brick elements are presented in Table 6.1 and Fig. 6.5. In those results, the reference solution is obtained by ANSYS Solid185 element with $100\times100\times1$ elements. The result of ANSYS Solid185 that is the tri-linear brick element with locking remedies is also presented in Fig. 6.5 for comparison, indicating the linear rate of convergence. It is observed from Fig. 6.5

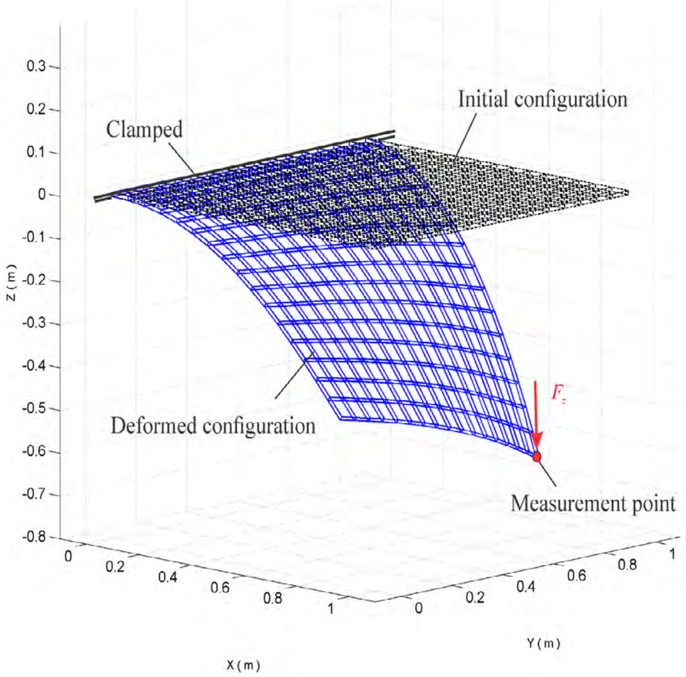

Figure 6.4 Deformed shape of a cantilevered plate subjected to a tip force

that the tri-linear 8-node brick element ensures the linear rate of convergence if the enhanced assumed strain is used (Brick24 w/ EAS), while 9-node brick element archives the linear rate of convergence without introducing any locking remedies (Brick33 w/o EAS). While the nine internal parameters are introduced to describe the linear distribution of stresses and strains over the volume in Brick24, additional nine curvature coordinates for $\partial^2\mathbf{r}/\partial x^2$, $\partial^2\mathbf{r}/\partial y^2$, and $\partial^2\mathbf{r}/\partial z^2$ are introduced to Brick33 for defining the quadratic displacement field, allowing for the linear distribution of stresses and strains over the volume. In other words, both brick elements are essentially equivalent in a sense that the linear strain distribution is enabled by the nine internal enhanced assumed strain parameters in Brick24 and by the nine additional curvature nodal coordinates in Brick33. It is also important to notice here that the tri-cubic ANCF brick element (Brick96) does not ensure the ideal cubic rate of convergence of solutions, indicating that element lockings occur, despite the fact that higher order polynomials and the larger degrees of freedom are introduced per element.

In the second numerical example, a nonlinear dynamics problem is considered. A flat plate is pinned to the ground at one of the corners as shown in Fig. 6.6 and numerical solutions of the flexible plate pendulum under the effect of gravity is discussed. The length, width and thickness of the plate are assumed to be 1.0 m, 1.0 m and 0.01 m. HHT time integrator is used with variable step size. The Young's modulus and Poisson's ratio are assumed to be 2.1×10^7 Pa and 0.3 respectively. The material density is assumed to be

Table 6.1. Static deflection of cantilevered plate subjected point load (m)

	Brick24	Brick24	Brick33	Brick96	ANSYS (SOLID185)
	w/o EAS	w/ EAS	w/o EAS	w/o EAS	w/ EAS
2x2x1	-0.00402	-0.21767	-0.21407	-0.59117	-0.18381
4x4x1	-0.01604	-0.46600	-0.44784	-0.64519	-0.40824
8x8x1	-0.05705	-0.61744	-0.61124	-0.65331	-0.60228
16x16x1	-0.13902	-0.64965	-0.64902	-0.65410	-0.64769
32x32x1	-0.29807	-0.65360	-0.65356	-0.65436	-0.65356
100x100x1					-0.65426

1,000 kg/m^3. Large deformation is observed as shown in Fig. 6.6. The global vertical positions at the tip of the plate are presented in Figs. 6.7 to 6.9 for the three brick elements (Brick24 w/ EAS, Brick33, and Brick96) under consideration for different mesh sizes. It is important to notice here that the number of Gaussian integration points for Brick24 and Brick33 is 8 ($2\times2\times2$), while that of ANCF Brick96 requires at least 27 ($3\times3\times3$) due to the use of higher order polynomials. For the minimum number of elements that reaches the convergent solutions for the three types of brick elements, the normalized CPU time is compared in Fig. 6.10. CPU time of Brick33 is used as a reference and is slightly less than that of Brick24 w/ EAS, however the higher order ANCF Brick96 element leads to computationally inefficient solutions for the nonlinear dynamics problem considered in his study. For this reason, in this study, the 9-node brick element (Brick33) is applied to the modeling of continuum deformable soil for the tire/soil interaction simulation.

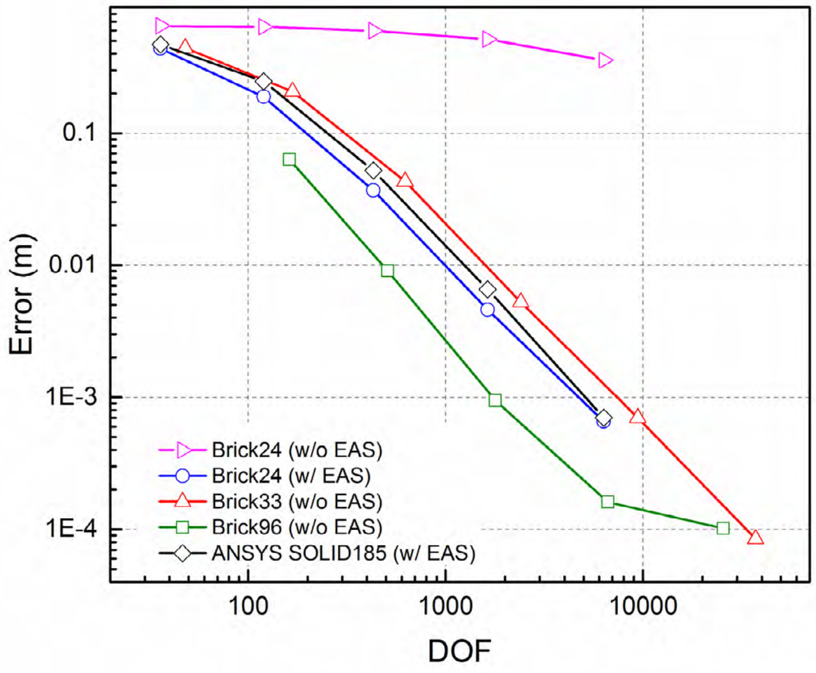

Figure 6.5 Convergence of brick element solutions

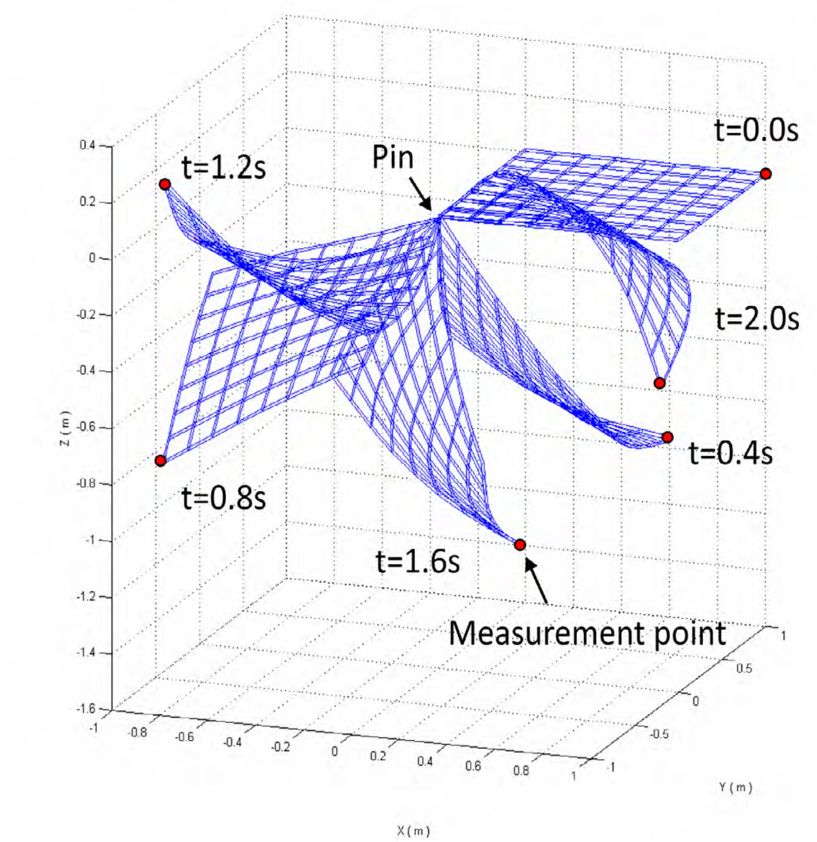

Figure 6.6 Deformed shapes

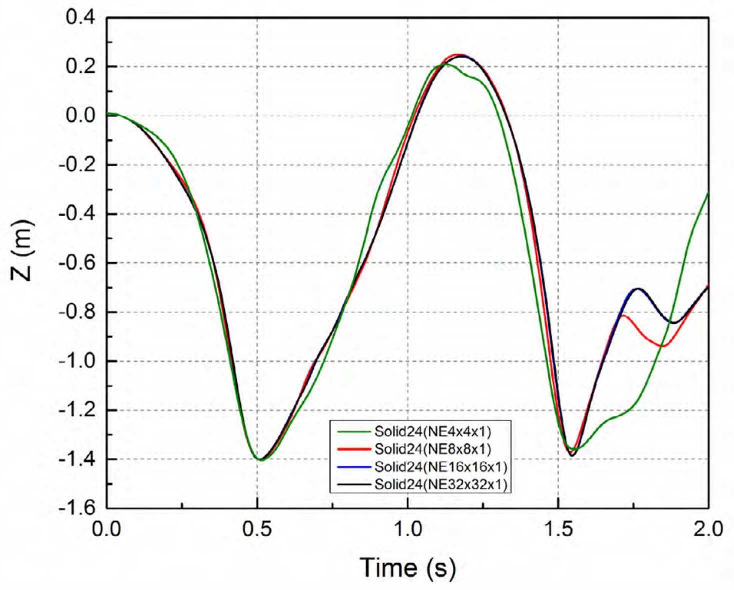

Figure 6.7 Global Z-position at the tip point (Brick24: 8-node tri-linear brick element)

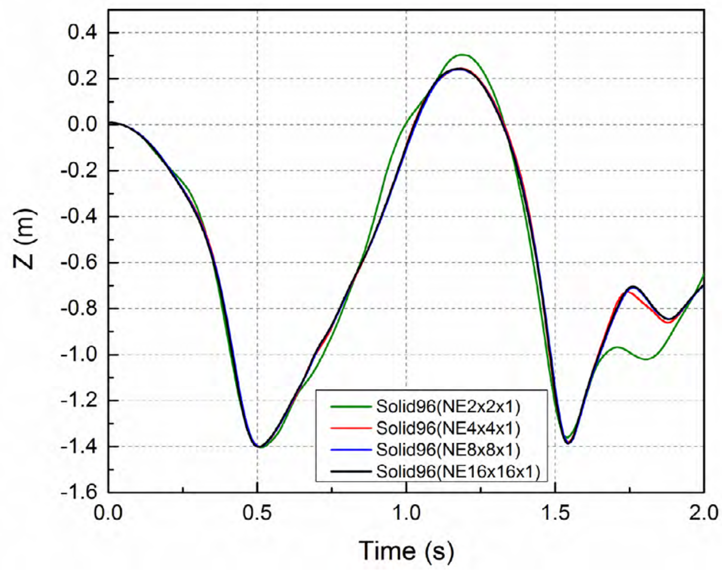

Figure 6.8 Global Z-position at the tip point (Brick96: 8-node tri-cubic brick element)

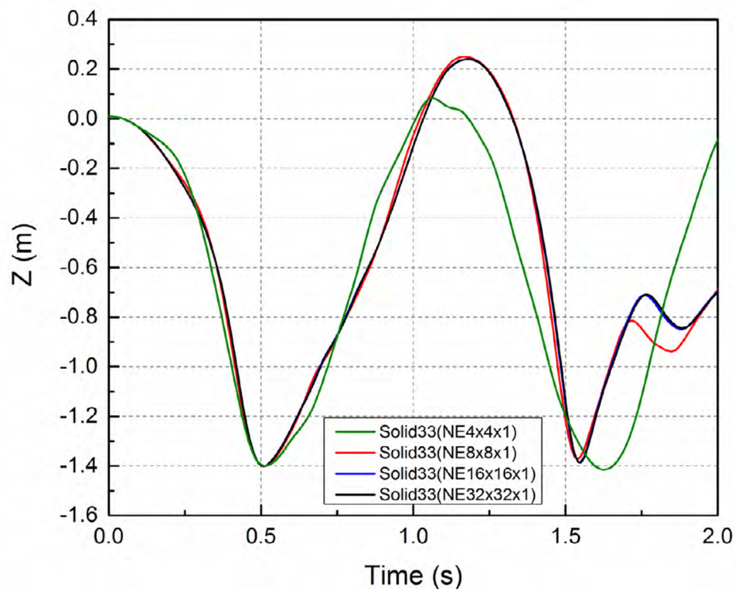

Figure 6.9 Global Z-position at the tip point (Brick33: 9-node brick element)

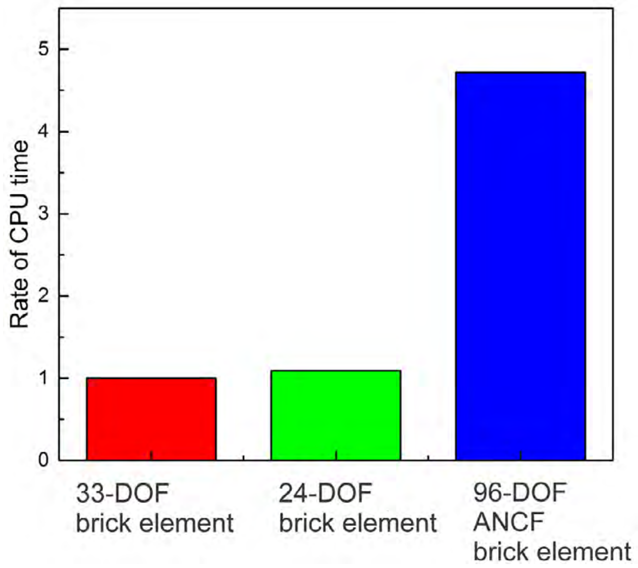

Figure 6.10 CPU time to achieve the convergent solutions

6.3 Soil Model Using Multiplicative Plasticity Theory

6.3.1 Finite Strain Plasticity Theory

To model soil behavior undergoing large plastic deformations, the multiplicative finite strain plasticity theory is utilized in this study. In large deformation problems, identification of the plastic strain involves more than just kinematic considerations [76] and elastic and plastic deformations are coupled. Lee and Liu [77] proposed that the displacement gradient tensor can be decomposed into elastic and plastic components and the intermediate stress free configuration is introduced such that the plastic state can be conceptually recovered by an elastic unloading from a current configuration. The multiplicative plasticity formulation was then applied to finite element computational framework by Simo [78] using the principle of the plastic maximum dissipation and has gained acceptance for modeling finite strain plasticity [79-84]. Since the elastic response can be described by the hyperelasticity constitutive model, this approach naturally bypasses drawbacks of hypo-plasticity formulation including erroneous dissipated elastic responses and the possible lack of objectivity of incremental constitutive equations [81-83]. Furthermore, it is shown that use of the logarithmic (Hencky) strain measure for

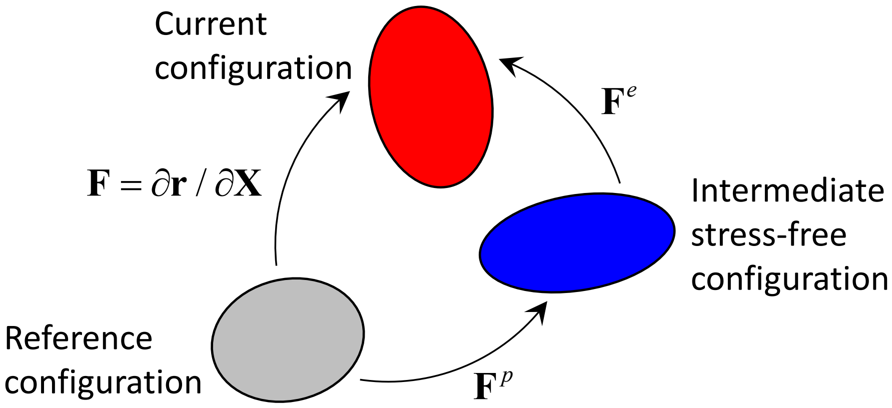

Figure 6.11 Multiplicative decomposition of displacement gradient

multiplicative plasticity formulation allows for the use of the classical return mapping scheme developed for the infinitesimal plasticity model [80].

As shown in Fig. 6.11, the position vector gradient tensor $\mathbf{F}$ is decomposed into the elastic and plastic components as follows [77]:

$$\mathbf{F} = \mathbf{F}^e\mathbf{F}^p \tag{6.28}$$

where subscripts e and p indicate the elastic and plastic parts, respectively. To define the elastic strain, the left Cauchy-Green tensor of the elastic strain $\mathbf{B}^e$ is defined as

$$\mathbf{B}^e = \mathbf{F}^e(\mathbf{F}^e)^T = \mathbf{F}(\mathbf{C}^p)^{-1}\mathbf{F}^T \tag{6.29}$$

where $\mathbf{C}^p$ is the right Cauchy-Green tensor of the plastic strain given as

$$\mathbf{C}^p = (\mathbf{F}^p)^T\mathbf{F}^p \tag{6.30}$$

from which, the elastic logarithmic strain tensor can be defined using the spectral decomposition of the left Cauchy-Green tensor $\mathbf{B}^e$ as

$$\boldsymbol{\varepsilon}_L^e = \frac{1}{2}\ln(\mathbf{B}^e) = \sum_{i=1}^{3}\ln(\lambda_i)\mathbf{e}_i \otimes \mathbf{e}_i \tag{6.31}$$

In the preceding equation, one has

$$\mathbf{B}^e = \sum_{i=1}^{3}(\lambda_i)^2\mathbf{e}_i \otimes \mathbf{e}_i \tag{6.32}$$

where λ_i ($i = 1,2,3$) is the i-th eigenvalue of spatial stretch tensor $\mathbf{V}^e$ defined by the polar decomposition $\mathbf{F}^e = \mathbf{V}^e\mathbf{R}$ and the rotation tensor $\mathbf{R}$. The vector $\mathbf{e}_i$ defines the direction of the principal stretch. Using the logarithmic strain measure, Kirchhoff stress tensor is defined for an isotropic material as

$$\boldsymbol{\tau} = \mathbf{E} : \boldsymbol{\varepsilon}_L^e \tag{6.33}$$

Using the Kirchhoff stress tensor, the generalized elasto-plastic force vector is defined as [85]

$$\mathbf{Q}_e = \int_V \left(\frac{\partial \mathbf{D}}{\partial \dot{\mathbf{e}}} \right)^T \boldsymbol{\tau} \, dV \tag{6.34}$$

where $\mathbf{D}$ is the rate of deformation tensor given by

$$\mathbf{D} = \frac{1}{2}(\mathbf{L} + \mathbf{L}^T) \tag{6.35}$$

and $\mathbf{L}$ is the velocity gradient tensor as given by $\mathbf{L} = \dot{\mathbf{F}}\mathbf{F}^{-1}$.

6.3.2 Drucker-Prager Failure Model and Return Mapping Algorithm

There are many failure models proposed for modeling soil behavior [18]. Among others, Drucker-Prager model has been widely used to describe the fundamental soil behavior for tire/soil interaction simulation. The yield function of Drucker-Prager model with an assumption of isotropic hardening is given as [79]

$$\Phi = \sqrt{J_2(\mathbf{s})} + \eta p - \xi d \tag{6.36}$$

where $J_2(\mathbf{s}) = \frac{1}{2}\mathbf{s} : \mathbf{s}$; $\mathbf{s}(\boldsymbol{\tau})$ is the deviatoric stress of the Kirchhoff stress tensor defined by $\mathbf{s}(\boldsymbol{\tau}) = \boldsymbol{\tau} - p(\boldsymbol{\tau})\mathbf{I}$; and $p(\boldsymbol{\tau})$ is the hydrostatic pressure (mean effective stress) given by $p(\boldsymbol{\tau}) = tr(\boldsymbol{\tau})/3$. The parameters η and ξ are defined using the friction angle β as follows:

$$\eta = \frac{1}{\sqrt{3}} \tan\beta \quad \text{and} \quad \xi = \frac{1}{\sqrt{3}} \tag{6.37}$$

Furthermore, the cohesion d in Eq. 6.36 is expressed as a function of the equivalent plastic strain $\bar{\varepsilon}^{pl}$, and for the linear hardening case, one has

$$d = d_0 + H\bar{\varepsilon}^{pl} \tag{6.38}$$

where d_0 is the initial cohesion and H is the slope of the plastic hardening. The Drucker-Prager yield cone is illustrated in Fig. 6.12(a). The incremental plastic strain is defined as [79]

$$\delta \boldsymbol{\varepsilon}_L^p = \Delta\gamma \mathbf{N} \tag{6.39}$$

and the plastic flow vector **N** is defined by

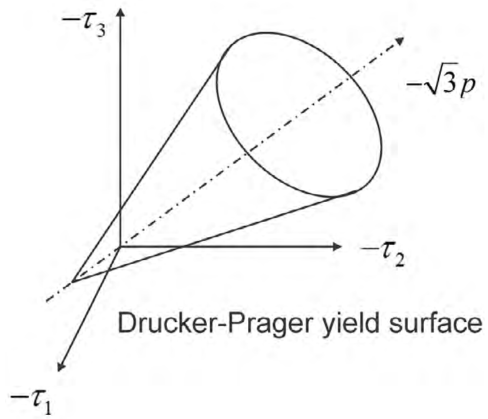

(a) Drucker-Prager yield surface

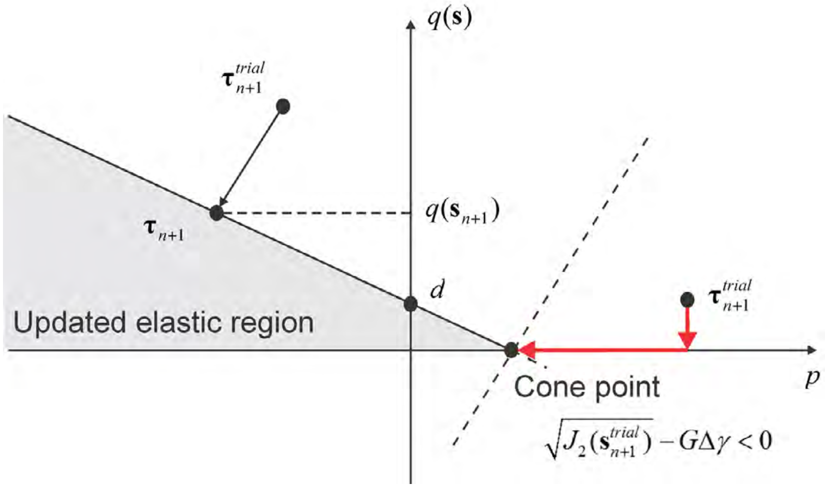

(b) Drucker-Prager return mapping process on *p*-*q* plane

Figure 6.12 Drucker-Prager failure model

$$\mathbf{N} \equiv \frac{\partial \Psi}{\partial \boldsymbol{\tau}} = \frac{1}{2\sqrt{J_2(\mathbf{s})}}\mathbf{s} + \frac{\overline{\eta}}{3}\mathbf{I} \tag{6.40}$$

where Ψ is the flow potential given by

$$\Psi \equiv \sqrt{J_2(\mathbf{s})} + \overline{\eta}\, p \tag{6.41}$$

and $\overline{\eta} = \tan\varphi / \sqrt{3}$ with the dilatancy angle φ. In the associative plastic flow, the friction angle and the dilatancy angle are assumed to be equal, and one has $\mathbf{N} = \partial \Psi / \partial \boldsymbol{\tau} = \partial \Phi / \partial \boldsymbol{\tau}$. However, in the non-associative flow rule which is common for soils, the dilatancy angle used in the flow potential is not equal to the friction angle. The use of non-associated law can avoid the excessive dilatancy exhibited in the associative rule [79].

To find the plastic strains at every time step, the return mapping algorithm for the multiplicative finite strain plasticity model is developed. As shown in Fig. 6.12(b), an elastic trial step is taken first (i.e. $\Delta\gamma_{n+1} = 0$) to check if the plastic loading occurs or not. To this end, the trial elastic left Cauchy-Green tensor at $t = t_{n+1}$ is evaluated using the accumulated plastic strains up to the previous time step $t = t_n$ as

$$(\mathbf{B}^e_{n+1})^{\text{trial}} = \mathbf{F}_{n+1}(\mathbf{C}^p_n)^{-1}\mathbf{F}^T_{n+1} \tag{6.42}$$

where the plastic strains are stored using the right Cauchy-Green tensor $\mathbf{C}^p_n$. Using the trial elastic left Cauchy-Green tensor, the trial logarithmic elastic strain tensor and Kirchhoff stress tensor are evaluated using Eqs. 6.31 and 6.33, respectively. The yield function given by Eq. 6.36 is then evaluated to determine if the Gaussian integration point under consideration is subjected to plastic loading at the current step. That is, if $\Phi^{\text{trial}}_{n+1}(\boldsymbol{\tau}^{\text{trial}}_{n+1}, \overline{\varepsilon}^{pl}_n) < 0$, an elastic loading occurs and then update the Kirchhoff stress tensor, the inverse of the plastic right Cauchy-Green tensor, and the hardening parameter as follows:

$$\boldsymbol{\tau}^e_{n+1} = \boldsymbol{\tau}^{\text{trial}}_{n+1}, \quad (\mathbf{C}^p_{n+1})^{-1} = (\mathbf{C}^p_n)^{-1}, \quad \overline{\varepsilon}^{pl}_{n+1} = \overline{\varepsilon}^{pl}_n \tag{6.43}$$

If $\Phi^{\text{trial}}_{n+1}(\boldsymbol{\tau}^{\text{trial}}_{n+1}, \overline{\varepsilon}^{pl}_n) > 0$, the plastic loading occurs, thus the plastic strain tensor is determined using the return mapping algorithm. In the Drucker-Prager yield criterion, the stress state lies on either the yield cone surface or the apex of the cone as shown in Fig.

6.12(b). In the former case, the incremental plastic multiplier $\Delta\gamma_{n+1}$ is determined by solving the following discretized equation [79]:

$$\Phi(\Delta\gamma_{n+1}) = \sqrt{J_2(\mathbf{s}_{n+1}(\boldsymbol{\tau}))} + \eta\, p_{n+1}(\boldsymbol{\tau}) - \xi d(\bar{\varepsilon}^{pl}_{n+1}) = 0 \tag{6.44}$$

where updating schemes for the deviatoric Kirchhoff stress tensor, hydrostatic pressure and equivalent plastic strain are defined as follows:

$$\begin{aligned} \mathbf{s}_{n+1}(\boldsymbol{\tau}) &= \left(1 - \frac{G\Delta\gamma_{n+1}}{\sqrt{J_2(\mathbf{s}^{trial}_{n+1})}}\right)\mathbf{s}^{\text{trial}}_{n+1}(\boldsymbol{\tau}) \\ p_{n+1}(\boldsymbol{\tau}) &= p^{\text{trial}}_{n+1}(\boldsymbol{\tau}) - K\bar{\eta}\Delta\gamma_{n+1} \\ \bar{\varepsilon}^{pl}_{n+1} &= \bar{\varepsilon}^{pl}_{n} + \xi\,\Delta\gamma_{n+1} \end{aligned} \tag{6.45}$$

From which, the consistent elastoplastic tangent moduli can be obtained as follows:

$$\mathbf{D}^{ep} = \frac{d\boldsymbol{\tau}_{n+1}}{d(\boldsymbol{\varepsilon}^e_L)^{\text{trial}}_{n+1}} = \frac{d\mathbf{s}_{n+1}}{d(\boldsymbol{\varepsilon}^e_L)^{\text{trial}}_{n+1}} + \mathbf{I}\otimes\frac{dp_{n+1}}{d(\boldsymbol{\varepsilon}^e_L)^{\text{trial}}_{n+1}} \tag{6.46}$$

where $(\boldsymbol{\varepsilon}^e_L)^{\text{trial}}_{n+1}$ is the trial logarithmic elastic strain at step n+1. The preceding expression can be written in an explicit form as

$$\begin{aligned} \mathbf{D}^{ep} &= 2G\left(1 - \frac{\Delta\gamma}{\sqrt{2}\left\|(\boldsymbol{\varepsilon}^e_L)^{\text{trial}}_{d\,n+1}\right\|}\right)\mathbf{I}_d + 2G\left(\frac{\Delta\gamma}{\sqrt{2}\left\|(\boldsymbol{\varepsilon}^e_L)^{\text{trial}}_{d\,n+1}\right\|} - GA\right)\mathbf{D}\otimes\mathbf{D} \\ &\quad - \sqrt{2}GAK\left(\eta\,\mathbf{D}\otimes\mathbf{I} + \bar{\eta}\,\mathbf{I}\otimes\mathbf{D}\right) + K\left(1 - K\eta\bar{\eta}A\right)\mathbf{I}\otimes\mathbf{I} \end{aligned} \tag{6.47}$$

where $(\boldsymbol{\varepsilon}^e_L)^{\text{trial}}_{d\,n+1}$ is the deviatoric part of the trial logarithmic strain at step n+1, given as $(\boldsymbol{\varepsilon}^e_L)^{\text{trial}}_{n+1}$; $A = 1/(G + K\eta\bar{\eta} + \xi^2 H)$; $\mathbf{D} = (\boldsymbol{\varepsilon}^e_L)^{\text{trial}}_{d\,n+1} / \left\|(\boldsymbol{\varepsilon}^e_L)^{\text{trial}}_{d\,n+1}\right\|$; and $\mathbf{I}_d$ is the 4th order deviatoric projection tensor defined by

$$\mathbf{I}_d = \mathbf{I}_S - \frac{1}{3}\mathbf{I}\otimes\mathbf{I} \tag{6.48}$$

where $\mathbf{I}_S$ is the 4th order symmetric identity tensor and $\mathbf{I}$ is the 2nd order identity tensor.

In the latter case, the stress state lies on the apex of the cone, thus the following equation is solved for the incremental plastic multiplier $\Delta\gamma_{n+1}$ [79]:

$$r(\Delta\gamma_{n+1}) = d(\bar{\varepsilon}^{pl}_{n} + \alpha_1\Delta\gamma_{n+1})\beta_1 - p^{\text{trial}}_{n+1} = 0 \tag{6.49}$$

where $\alpha_1 = \xi/\bar{\eta}$ and $\beta_1 = \xi/\eta$. In the preceding equation, updating schemes for the hydrostatic pressure and hardening parameter are defined as follows:

$$\left.\begin{aligned} p_{n+1}(\boldsymbol{\tau}) &= p_{n+1}^{\text{trial}}(\boldsymbol{\tau}) - K\Delta\gamma_{n+1} \\ \bar{\varepsilon}_{n+1}^{pl} &= \bar{\varepsilon}_{n}^{pl} + \alpha_1 \Delta\gamma_{n+1} \end{aligned}\right\} \tag{6.50}$$

Thus, the expression of consistent tangent moduli for the apex return mapping can be derived from Eq. 6.44 and expressed as follows:

$$\mathbf{D}^{ep} = K\left(1 - \frac{K}{K + \alpha_1 \beta_1 H}\right)\mathbf{I} \otimes \mathbf{I} \tag{6.51}$$

It is important to notice here that one seeks the solution on the cone yield surface first. If the solution meets $\sqrt{J_2(\mathbf{s}_{n+1}^{\text{trial}})} - G\Delta\gamma_{n+1} \geq 0$, then the stress state lies on the cone surface as shown in Fig. 6.12(b). If it is not met, the solution on the cone apex needs to be sought. Having determined the plastic multiplier, the total elastic strain tensor is updated as [79]:

$$(\boldsymbol{\varepsilon}_L^e)_{n+1} = \frac{1}{2G}\mathbf{s}_{n+1} + \frac{p_{n+1}}{3K}\mathbf{I} \tag{6.52}$$

and then the elastic left Cauchy-Green tensor at current step is updated as

$$\mathbf{B}_{n+1}^e = \sum_{i=1}^{3} \exp\left((2(\boldsymbol{\varepsilon}_L^e)_{n+1})_i\right)\mathbf{e}_i \otimes \mathbf{e}_i \tag{6.53}$$

where $((\boldsymbol{\varepsilon}_L^e)_{n+1})_i$ indicates i-th principal logarithmic strain. Using Eq. 6.42, the inverse of the plastic right Cauchy-Green tensor at $t = t_{n+1}$ is updated as

$$(\mathbf{C}_{n+1}^p)^{-1} = \mathbf{F}_{n+1}^{-1}\mathbf{B}_{n+1}^e\mathbf{F}_{n+1}^{-T} \tag{6.54}$$

In other words, the cumulative plastic strains are saved using the inverse of the plastic right Cauchy-Green tensor $(\mathbf{C}_{n+1}^p)^{-1}$. Finally, the Kirchhoff stress tensor at the current step is updated by $\boldsymbol{\tau}_{n+1} = \mathbf{s}_{n+1} + p_{n+1}\mathbf{I}$ and then the generalized elasto-plasitc force vector is evaluated using Eq. 6.34.

6.3.3 Capped Drucker-Prager Failure Model and Return Mapping Algorithm

Geomaterials undergo plastic deformations under compressive hydrostatic pressure observed as a soil compaction. However, the Drucker-Prager failure model discussed in Section 6.3.2 is unable to capture this effect, and the soil compaction behavior (compressive plastic flow) under compressive hydrostatic pressures is usually considered by introducing an elliptical cap surface to the original Drucker-Prager failure model. The yield functions of the capped Drucker-Prager model with an assumption of isotropic hardening are given as [79]:

$$\left.\begin{aligned} \Phi^a &= \sqrt{J_2(\mathbf{s})} + \eta p - \xi d \\ \Phi^b &= \frac{1}{b^2}\left[p - p_t + a\right]^2 + \left[\frac{q(\mathbf{s})}{M}\right]^2 - a^2 \end{aligned}\right\} \tag{6.55}$$

where Φ^a is the original Drucker-Prager yield function presented in Section 6.3.2, while

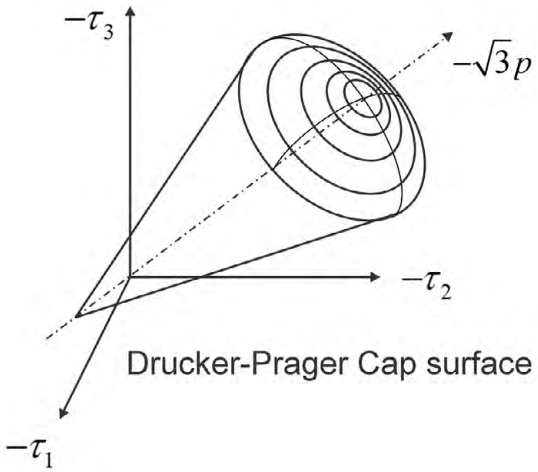

(a) Capped Drucker-Prager yield surface

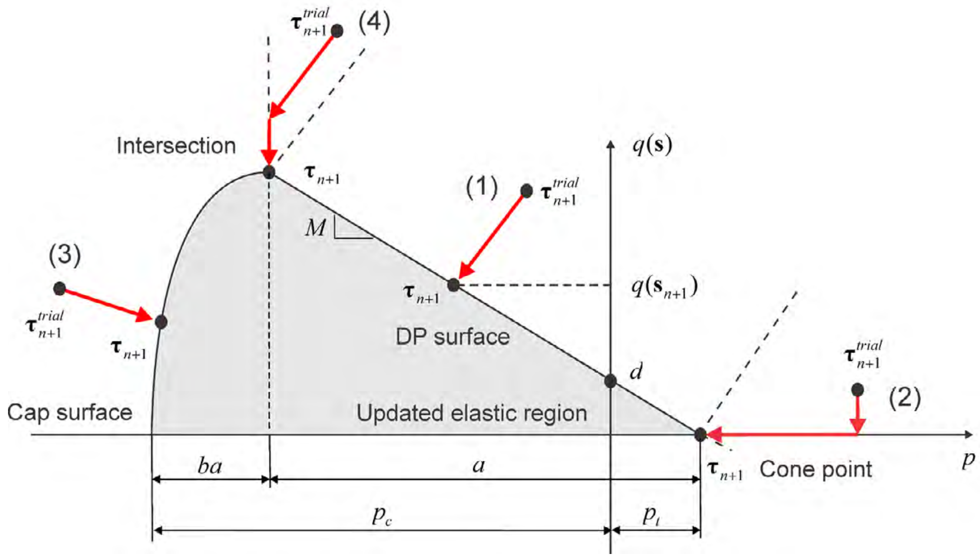

(b) Capped Drucker-Prager return mapping process

Figure 6.13 Capped Drucker-Prager failure model

Φ^b defines the elliptical cap yield function based on a modified Cam-Clay yield criterion as illustrated in Fig. 6.13(b) [79]. $p_t = (\xi/\eta)d$ is the tensile yield pressure; b is the parameter that defines the cap shape; $M = \sqrt{3}\eta$; and $q(\mathbf{s})$ is the deviator stress defined by $q(\mathbf{s}) = \sqrt{3J_2(\mathbf{s})}$. The yield surface is illustrated in Fig. 6.13(a). It is important to notice here that the linear hardening used in Section 6.3.2 is no longer applied to the capped Drucker-Prager model. In other words, the cohesion d remains constant ($d = d_0$ with $H = 0$ in Eq. 6.38), and the size of Drucker-Prager yield surface does not change even if plastic deformation occurs. On the other hand, the hardening behavior of soil can be modeled by the movement of the elliptical cap surface. The parameter $a = a(\alpha)$ is a function of a hardening variable α defining the compressive positive volumetric plastic strain as $\alpha \equiv -\varepsilon_v^p$. The hardening parameter a is then defined as follows:

$$a(\alpha) = \frac{p_c(\alpha) + p_t}{1 + b} \tag{6.56}$$

where $p_c(\alpha)$ is the compaction pressure (i.e., the yield mean effective stress). It is noted that the relationship between the compaction pressure p_c and the plastic volumetric strain ε_v^p ($= \alpha$) can be determined experimentally by the compression test as will be discussed in more detail in Section 6.4.

The return mapping algorithms for the capped Drucker-Prager model consists of four different stages as shown in Fig 6.13(b). That is,

1. Return mapping to the smoothed Drucker-Prager yield surface
2. Return mapping to the apex of the Drucker-Prager cone
3. Return mapping to the cap surface
4. Return mapping to the intersection between the Drucker-Prager yield surface and the cap surface

These four return mappings are considered to determine the stress state at every time step at all the Gaussian integration points. The return mapping algorithm is summarized in Fig 6.14. It is important to notice here that the elasto-plastic tangent moduli have to be evaluated according to the current yield surface or point that the stress lies on.

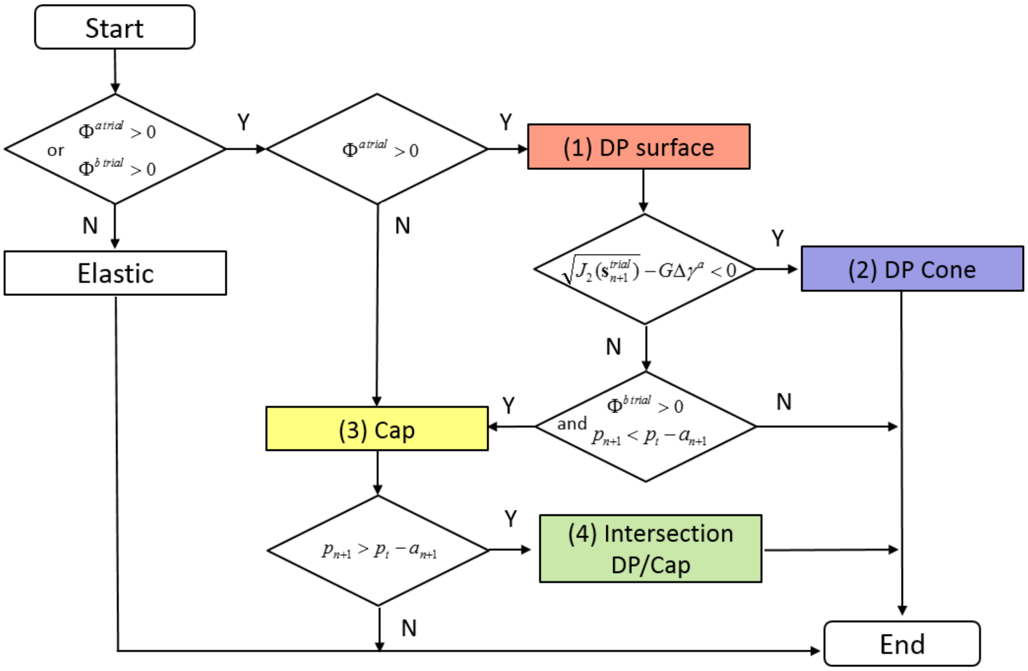

Figure 6.14 Flow chart for the return mapping of capped Drucker-Prager model

(1) The return mapping algorithm for Drucker-Prager smoothed surface

If $\Phi^a > 0$, the return mapping algorithm for the Drucker-Prager yield surface is considered first. This algorithm is essentially the same as the original Drucker Prager model shown in Section 6.3.2 except for the hardening parameter being zero. In other words, the cohesion remains constant under a plastic loading. Thus, the same algorithm is utilized as the capped Drucker-Prager model discussed in Section 6.3.2 at this first step.

(2) The return mapping algorithm to apex of the Drucker-Prager cone

If the stress does not lie on the smoothed cone yield surface (i.e., Step 1 fails) as shown in Fig.6.14, the return mapping algorithm to the apex of the Drucker-Prager yield cone is considered next. This step is also same as the original Drucker-Prager model discussed in 6.3.2.

(3) The return mapping algorithm to the cap surface

If the stress does not lie on the apex (i.e., Step 2 also fails), the return mapping to the cap surface is sought considering the plastic hardening behavior by $a(\alpha)$. To this end, the incremental plastic strain is defined as [79]

$$\delta\boldsymbol{\varepsilon}_L^p = \Delta\gamma^b \mathbf{N}^b \tag{6.57}$$

and the plastic flow vector $\mathbf{N}^b$ is defined as

$$\mathbf{N}^b \equiv \frac{\partial\Phi^b}{\partial\boldsymbol{\tau}} = \frac{3}{M^2}\mathbf{s} + \frac{2}{b^2}\left(p - p_t + a\right)\mathbf{I} \tag{6.58}$$

The associative plastic flow is usually selected for the return mapping to the elliptical cap surface. Here, the residual vectors for return mapping to the cap surface are defined as

$$\begin{bmatrix} R_1 \\ R_1 \end{bmatrix} = \begin{bmatrix} \dfrac{1}{b^2}\left[p(\alpha_{n+1}) - p_t + a(\alpha_{n+1})\right]^2 + \left[\dfrac{q(\Delta\gamma^b)}{M}\right]^2 - a(\alpha_{n+1})^2 \\ \alpha_{n+1} - \alpha_n + \Delta\gamma^b \dfrac{2}{b^2}\left[p(\alpha_{n+1}) - p_t + a(\alpha_{n+1})\right] \end{bmatrix} = \mathbf{0} \tag{6.59}$$

It is important to notice here that there are two variables to be determined. One is $\Delta\gamma^b$ defined in Eq. 6.58 and another is α_{n+1} which characterizes the hardening behavior $a(\alpha_{n+1})$. Equation 6.59 is a nonlinear vector equation, thus iterative Newton-Raphson method is used to determine those two variables. The Newton differences are written as

$$\begin{bmatrix} d\Delta\gamma^b \\ d\alpha_{n+1} \end{bmatrix} = -\begin{bmatrix} \dfrac{-12G}{M^2 + 6G\Delta\gamma^b}\left(\dfrac{q}{M}\right)^2 & \dfrac{2\overline{p}}{b^2}(K+H) - 2aH \\ \dfrac{2\overline{p}}{b^2} & 1 + \dfrac{2\Delta\gamma^b}{b^2}(K+H) \end{bmatrix}^{-1} \begin{bmatrix} R_1 \\ R_2 \end{bmatrix} \tag{6.60}$$

where $\overline{p} = p(\alpha_{n+1}) - p_t + a(\alpha_{n+1})$ and $H = \partial a(\alpha)/\partial\alpha$ defining a slope of hardening behavior. The two variables are updated by $\Delta\gamma^b = \Delta\gamma^b + d\Delta\gamma^b$ and $\alpha_{n+1} = \alpha_{n+1} + d\alpha_{n+1}$ until the residuals become less than the tolerances. The update schemes for the deviatoric Kirchhoff stress tensor and hydrostatic pressure are, respectively, defined as follows:

$$\begin{aligned} \mathbf{s}_{n+1}(\boldsymbol{\tau}) &= \frac{M^2}{M^2 + 6G\Delta\gamma^b}\mathbf{s}_{n+1}^{\text{trial}}(\boldsymbol{\tau}) \\ p_{n+1}(\boldsymbol{\tau}) &= p_{n+1}^{\text{trial}}(\boldsymbol{\tau}) + K\left(\alpha_{n+1} - \alpha_n\right) \end{aligned} \tag{6.61}$$

The consistent tangent for the cap yield surface can be obtained from Eq. 6.46 and is written as follows:

$$\begin{aligned}\mathbf{D}^{ep} &= \left(\frac{2GM^2}{M^2+6G\Delta\gamma^b}\right)\mathbf{I}_d - \left(\frac{12G^2M^2\left\|(\boldsymbol{\varepsilon}_L^e)_{d\,n+1}^{trial}\right\|}{\left(M^2+6G\Delta\gamma^b\right)^2}C_{11}\right)\mathbf{D}\otimes\mathbf{D} \\ &\quad - \left(\frac{12G^2M^2\left\|(\boldsymbol{\varepsilon}_L^e)_{d\,n+1}^{trial}\right\|}{\left(M^2+6G\Delta\gamma^b\right)^2}C_{12}\right)\mathbf{D}\otimes\mathbf{I} + \left(KC_{21}\right)\mathbf{I}\otimes\mathbf{D} + K\left(1+KC_{22}\right)\mathbf{I}\otimes\mathbf{I}\end{aligned} \tag{6.61}$$

where, $C_{11}, C_{12}, C_{21}, C_{22}$ are scalars. The cumulative plastic strains are saved using the inverse of the plastic right Cauchy-Green tensor $(\mathbf{C}_{n+1}^p)^{-1}$ and then the hardening variable α_{n+1} is also stored for use in the next time step. Finally, Kirchhoff stress tensor at the current step is updated by $\boldsymbol{\tau}_{n+1} = \mathbf{s}_{n+1} + p_{n+1}\mathbf{I}$ and then the generalized elasto-plasitc force vector is evaluated using Eq. 6.34.

(4) Return mapping to the intersection between DP yield surface and Cap surface

If the stress does not lie on the cap yield surface (i.e., Step 3 also fails), the stress must lie on the intersection between Drucker-Prager yield surface and the cap surface. The incremental plastic strain is then defined by combining two flow vectors as [79]

$$\delta\boldsymbol{\varepsilon}_L^p = \Delta\gamma^a\mathbf{N}^a + \Delta\gamma^b\mathbf{N}^b \tag{6.62}$$

and the plastic flow vector $\mathbf{N}^a$ and $\mathbf{N}^b$ are defined as

$$\mathbf{N}^a = \frac{1}{2\sqrt{J_2(\mathbf{s})}}\mathbf{s} + \frac{\bar{\eta}}{3}\mathbf{I}, \qquad \mathbf{N}^b = \mathbf{N}_d^b = \frac{3}{M^2}\mathbf{s} \tag{6.63}$$

It is noted that $\mathbf{N}^a$ is the flow vector for Drucker-Prager yield surface, while $\mathbf{N}^b$ is the flow vector of the deviatoric part for the cap surface as shown in Fig. 6.13(b). The residual vectors are defined as follows:

$$\begin{bmatrix}\Phi_{n+1}^a \\ \Phi_{n+1}^b\end{bmatrix} = \begin{bmatrix}\sqrt{J_2(\mathbf{s})} + \eta p - \xi d \\ \dfrac{1}{b^2}\left[p(\alpha_{n+1}) - p_t + a(\alpha_{n+1})\right]^2 + \left[\dfrac{q(\Delta\gamma)}{M}\right]^2 - a(\alpha_{n+1})^2\end{bmatrix} = \mathbf{0} \tag{6.64}$$

To find $\Delta\gamma^a$ and $\Delta\gamma^b$, the Newton differences of these variables are given as

$$\begin{bmatrix} d\Delta\gamma^a \\ d\Delta\gamma^b \end{bmatrix} = -\begin{bmatrix} -K\eta\bar{\eta} - \dfrac{GM^2}{M^2+6G\Delta\gamma^b} & \dfrac{2\sqrt{3}GM^2(\sqrt{3}G\Delta\gamma^a - q^{trial})}{(M^2+6G\Delta\gamma^b)^2} \\ \dfrac{2\sqrt{3}GM^2(\sqrt{3}G\Delta\gamma^a - q^{trial})}{(M^2+6G\Delta\gamma^b)^2} - \dfrac{2K\bar{\eta}\bar{p}}{b^2} & \dfrac{12GM^2(\sqrt{3}G\Delta\gamma^a - q^{trial})^2}{(M^2+6G\Delta\gamma^b)^3} \end{bmatrix}^{-1} \begin{bmatrix} \Phi^a \\ \Phi^b \end{bmatrix} \tag{6.65}$$

where $\bar{p} = p - p_t + a$. The two variables are updated by $\Delta\gamma^a = \Delta\gamma^a + d\Delta\gamma^a$ and $\Delta\gamma^b = \Delta\gamma^b + d\Delta\gamma^b$. Having determined the plastic multipliers, the deviatoric stress, the hydrostatic stress and the hardening parameter are updated as follows:

$$\begin{aligned} \mathbf{s}_{n+1}(\boldsymbol{\tau}) &= \left(\frac{M^2}{M^2+6G\Delta\gamma^b}\right)\left(1 - \frac{G\Delta\gamma^a}{\sqrt{J_{2\,n+1}^{trial}}}\right)\mathbf{s}_{n+1}^{\text{trial}}(\boldsymbol{\tau}) \\ p_{n+1}(\boldsymbol{\tau}) &= p_{n+1}^{\text{trial}}(\boldsymbol{\tau}) - K\bar{\eta}\Delta\gamma^a \\ \alpha_{n+1} &= \alpha_n - \bar{\eta}\Delta\gamma^a \end{aligned} \tag{6.66}$$

The consistent tangent for the intersection between the Drucker-Prager yield surface and the cap surface is written as follows:

$$\begin{aligned} \mathbf{D}^{ep} = {} & 2G\frac{M^2}{M^2+6G\Delta\gamma^b}\left(1 - \frac{\Delta\gamma^b}{\sqrt{2}\left\|(\boldsymbol{\varepsilon}_L^e)_{d\,n+1}^{trial}\right\|}\right)\mathbf{I}_d + \left(\frac{\sqrt{2}GM^2}{M^2+6G\Delta\gamma^b}\frac{\Delta\gamma^a}{\left\|(\boldsymbol{\varepsilon}_L^e)_{d\,n+1}^{trial}\right\|}\right)\mathbf{D}\otimes\mathbf{D} \\ & + \left(-\frac{\sqrt{2}GM^2C_{11}}{M^2+6G\Delta\gamma^b} - \frac{12G^2M^2C_{21}}{(M^2+6G\Delta\gamma^b)^2}\left(\left\|(\boldsymbol{\varepsilon}_L^e)_{d\,n+1}^{trial}\right\| - \sqrt{2}G\Delta\gamma^a\right)\right)\mathbf{D}\otimes\mathbf{D} \\ & + \left(-\frac{\sqrt{2}GM^2C_{12}}{M^2+6G\Delta\gamma^b} - \frac{12G^2M^2C_{22}}{(M^2+6G\Delta\gamma^b)^2}\left(\left\|(\boldsymbol{\varepsilon}_L^e)_{d\,n+1}^{trial}\right\| - \sqrt{2}G\Delta\gamma^a\right)\right)\mathbf{D}\otimes\mathbf{I} \\ & - K\bar{\eta}C_{11}\,\mathbf{I}\otimes\mathbf{D} + K\left(1 - \bar{\eta}C_{12}\right)\mathbf{I}\otimes\mathbf{I} \end{aligned} \tag{6.67}$$

where $C_{11}, C_{12}, C_{21}, C_{22}$ are scalars. The cumulative plastic strains are saved and then the generalized elasto-plasitc force vector is evaluated using Eq. 6.34.

6.3.4 Plate Sinkage Test of Soil

To demonstrate the use of the continuum soil model developed using the 9-node brick element with capped and uncapped Drucker-Prager failure criteria and the multiplicative finite strain plasticity theory, a plate sinkage test of soil is carried out and numerical results are compared with ABAQUS models. A square plate ($0.25 \times 0.25 \times 0.01$ m) on the soil in a square box ($0.8 \times 0.8 \times 0.6$ m) is pressed vertically as shown in Fig. 6.15 to obtain the pressure-sinkage relationship. A quarter model is used by imposing the symmetric boundary condition as shown in Fig. 6.15. In the ABAQUS model for comparison, the tri-linear brick element using the reduced integration with hourglass control (C3D8R) is used together with capped and uncapped Drucker-Prager yield criteria.

In the first example, uncapped Drucker-Prager failure model is considered. The Young's modulus, Poisson's ratio, material density are 1.379×10^7 Pa, 0.3, and 200 kg/m^3, respectively. The initial cohesion is assumed to be zero (i.e., $d_0 = 0.0\ \mathrm{N/m^2}$) and linear hardening is assumed with a coefficient of $H = 1.0\times10^5\ \mathrm{N/m^2}$. The friction angle β is assumed to be 10 degrees. The dilatancy angle is assume to be zero for non-associative flow model, while 10 degree angle is assumed for the associative model. The deformed shape of the soil at the plate sinkage of 0.1 m obtained using the soil model developed in this study is compared with the ABAQUS soil model. It is observed from Fig. 6.16 that the large plastic soil deformation occurs and the deformed shapes of both models agree well. Furthermore, the pressure and sinkage relationship is presented in Fig. 6.17 for both present and ABAQUS models. It is shown in this figure that use of $10\times10\times8$ elements leads to a convergent solution obtained using $16\times16\times12$ elements, and the results obtained using the soil model developed in this study agree well with those of ABAQUS model for both associative and non-associative plastic flow models. Furthermore, due to the soil dilatancy, the associative flow model leads to higher pressure for the same sinkage as expected.

In the second example, the capped Drucker-Prager failure model is tested. The Young's modulus, Poisson's ratio, material density are 54.1 MPa, 0.293, and 2,149 kg/m^3, respectively. The number of element is the same as the first example. The deformed shapes at 0.1m sinkage using the capped Drucker-Prager failure model are compared with the ABAQUS model using the capped Drucker-Prager failure model in Fig. 6.18. The results agree well in shape and magnitude. The pressure and sinkage relationship are also in good agreement with the ABAQUS reference solution as shown in Fig. 6.19.

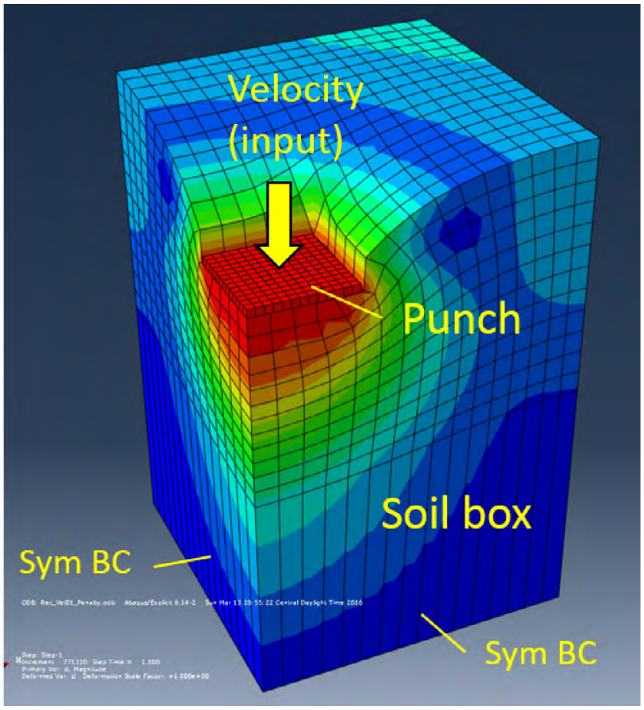

Figure 6.15 Plate sinkage test model

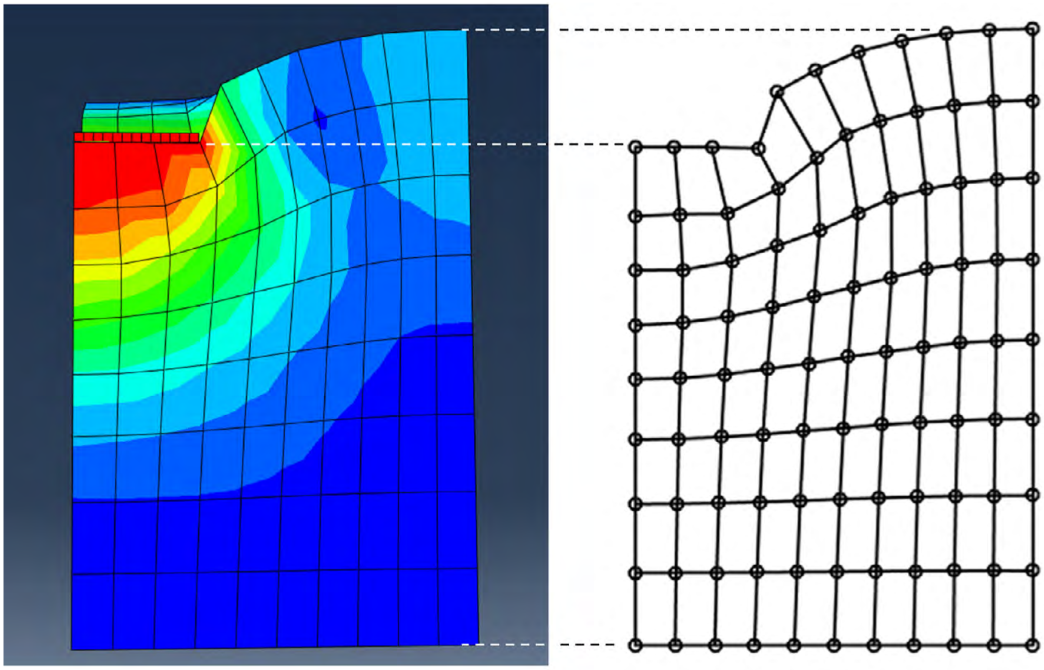

(a) ABAQUS model
(C3D8R element)

(b) Present model
(Brick33 element)

Figure 6.16 Deformed shape of soil at plate sinkage of 0.1 m
(Drucker-Prager model)

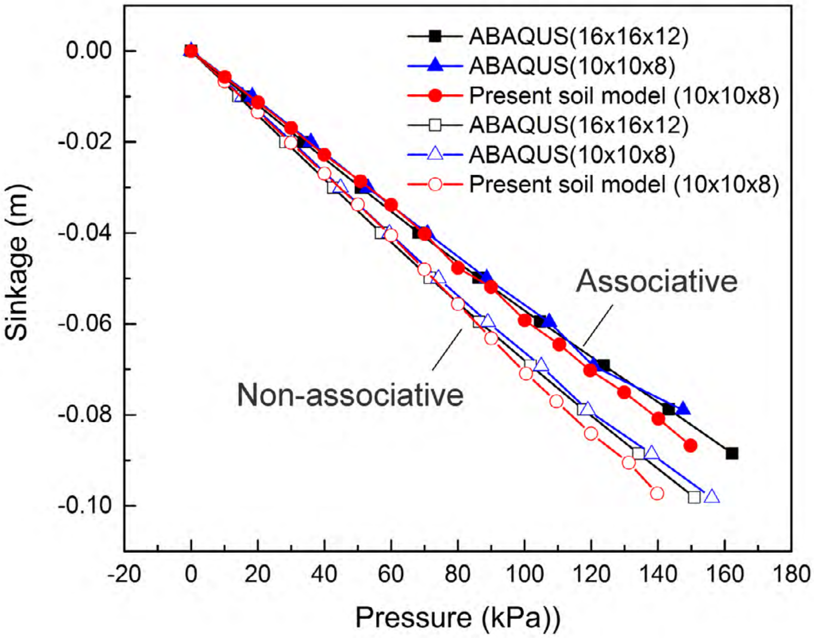

Figure 6.17 Pressure-sinkage relationship (comparison with ABAQUS model)

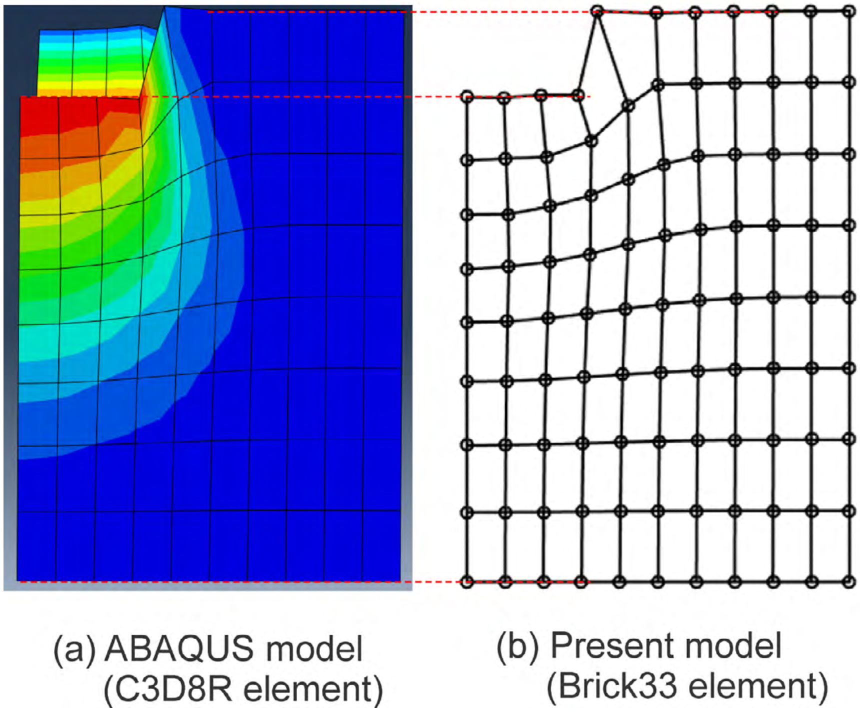

Figure 6.18 Deformed shape of soil at plate sinkage of 0.1 m (capped Drucker-Prager model)

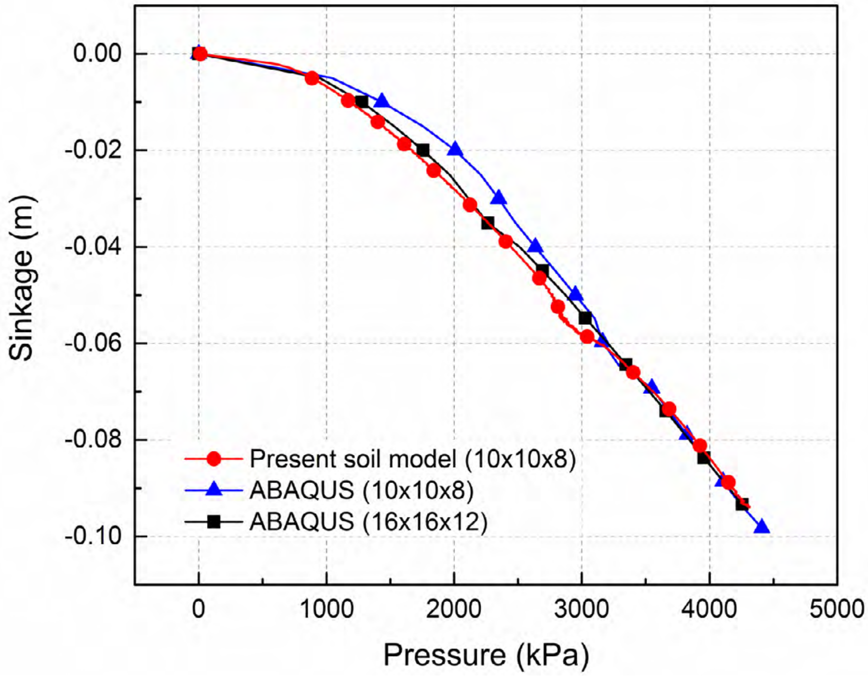

Figure 6.19 Pressure-sinkage relationship using capped Drucker-Prager model (comparison with ABAQUS model)

6.4 Triaxial Compression Test and Soil Validation

6.4.1 Triaxial Compression Test of Soil

The triaxial compression test is used to determine the strength and the stress-strain behavior of soil under uniform confining pressures [89]. The triaxial compression test is conducted by Delta Geotechnics. As shown in Fig. 6.20, the cylindrical soil specimen subjected to a uniform confining pressure is vertically compressed until failure. To this end, the soil specimen is fully saturated first by supplying water from the bottom tube shown in Fig. 6.20. The water circulates through the soil and is drained from the top tube. After that, a uniform confining pressure (σ_3) is applied to consolidate the cylindrical soil specimen and excessive water is drained from both tubes. The deviator stress ($\sigma_d = \sigma_1 - \sigma_3$) is applied vertically such that the stress element in the soil is subjected to the major principal stress σ_1 in the vertical direction. In this process, both drain valves are open and the volume of the drained water is measured to calculate the volume change of the soil specimen during loading (i.e., consolidated-drained (CD) test). The three confining pressures (25, 50 and 200 kPa) are considered in this test to identify parameters of the continuum soil model with the capped Drucker-Prager failure criterion including the Young's modulus, shear modulus of rigidity, friction angle, cohesion. The specification of the soil specimen is summarized in Table 6.2.

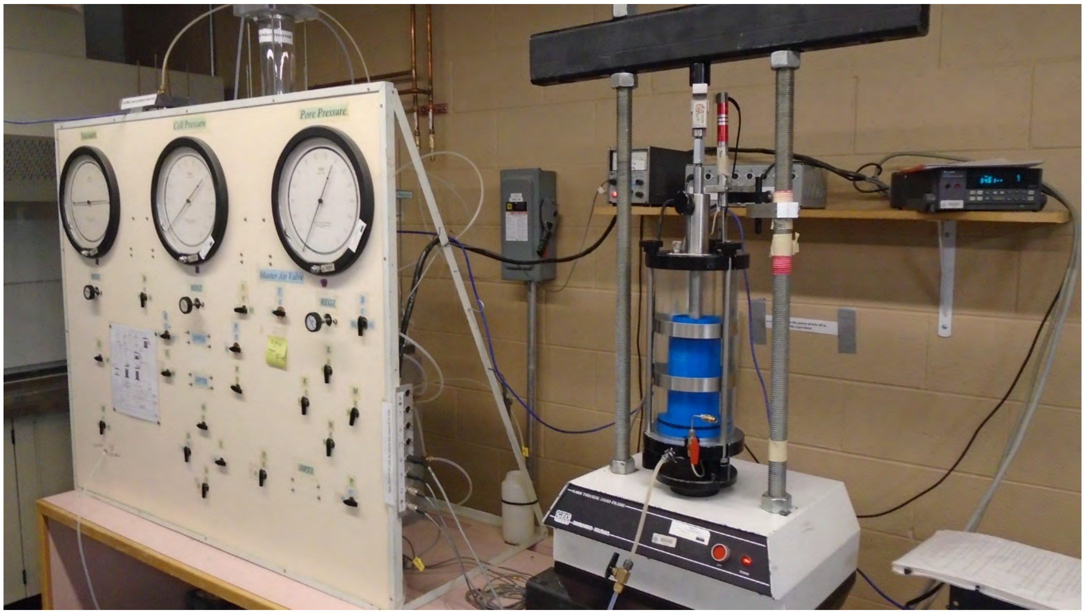

Figure 6.20 Triaxial soil test

Table 6.2 Specification of soil specimen

Specimen diameter	71.10 mm
Specimen height	142.27 mm
Water content	11.20%
Initial area	39.70 cm^2
Initial volume	564.86 cm^3
Density	2.149 g/cm^3
Dry density	1.933 g/cm^3
Confining pressure	25 kPa, 50 kPa, and 200 kPa

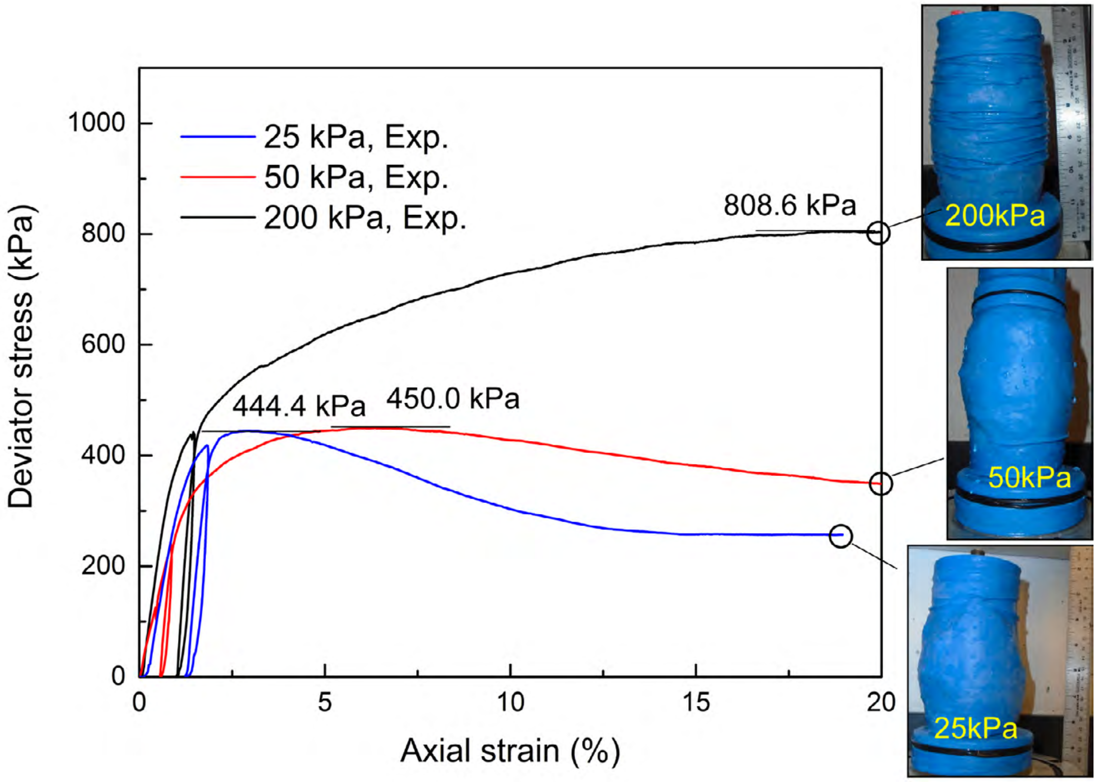

Figure 6.21 Deviator stress vs axial strain curves

The deviator stress versus the axial strain relationship for the three different confining pressures are presented in Fig. 6.21. It is observed from this figure that the yield strength increases as the confining pressure increases due to the increase in soil consolidation. Furthermore, since the soil is partially saturated for the low confining pressure case, difference in the strength for 25 and 50 kPa confining pressures is small. To identify the cohesion and friction angle at failure, the deviator stress, principal stress and mean effective stress at failure are summarized for the three confining pressures in Table 6.3. Using this result, the deviator stress and the mean effective stress at failure are plotted, and the linear regression is carried out to identify the cohesion from the intercept and the friction angle from the slope as shown in Fig. 6.22. The cohesion and friction angle are, respectively, identified as $d_0 = 211\,(\text{kPa})$ and $\beta = 51.8^\circ$. The Young's modulus and shear modus of rigidity are also identified using the slope of the stress-strain curve.

Table 6.3 Triaxial compression test results at failure

	Confining pressure σ_3 kPa	Deviator stress at failure $q = \sigma_1 - \sigma_3$ kPa	Major principal stress at failure σ_1 kPa	Mean effective stress at failure $p = (\sigma_1 + 2\sigma_3)/3$ kPa
Test 1	25	444.4	469.4	173.1
Test 2	50	450.0	500.0	200.0
Test 3	200	808.6	1008.6	469.5

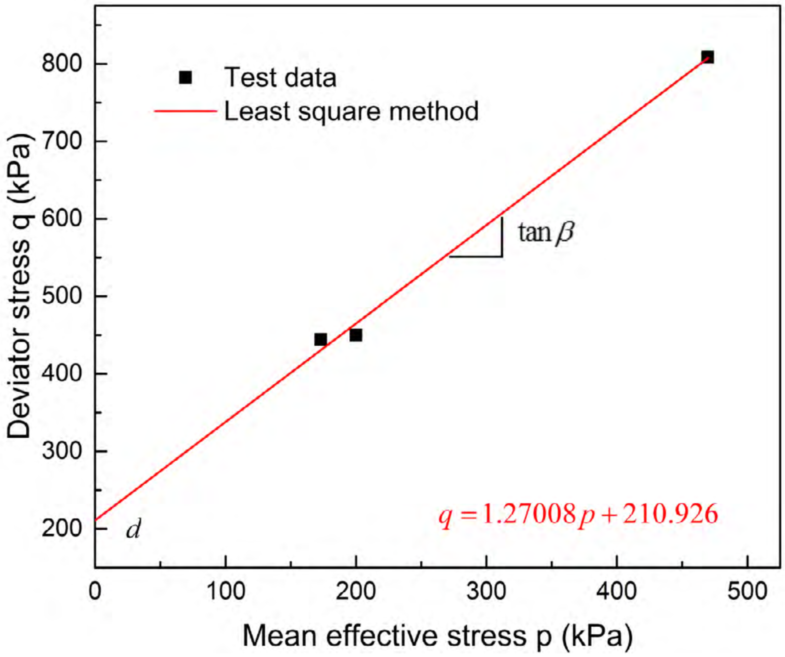

Figure 6.22 Deviator stress vs mean effective stress at failure

In order to identify the strain hardening curve, the plastic volumetric strain ε_v^p is approximated as a function of the mean effective stress p as [89]

$$\varepsilon_v^p = \frac{C_c - C_s}{2.3(1+e_0)} \ln \frac{p}{p_0} \tag{6.68}$$

where C_c and C_s are identified experimentally using the compression test of the soil, while e_0 and p_0 are, respectively, the void ratio and the mean effective stress at the initial state. The change in the void ratio obtained using the one-dimensional compression test of the same soil specimen is plotted as a function of the mean effective stress in Fig. 6.23. This test result is obtained by Delta Geotechnics. In this figure, the loading stage is shown as black rectangular symbols, while the unloading stage is shown as red circular symbols. Using this test result, the linear regression is performed to determine the slopes at the loading and unloading stages that correspond to C_c and C_s, respectively, as shown in Fig. 6.23. Using this one-dimensional compression test result, C_c and C_s, are identified as 0.2035 and 0.00268.

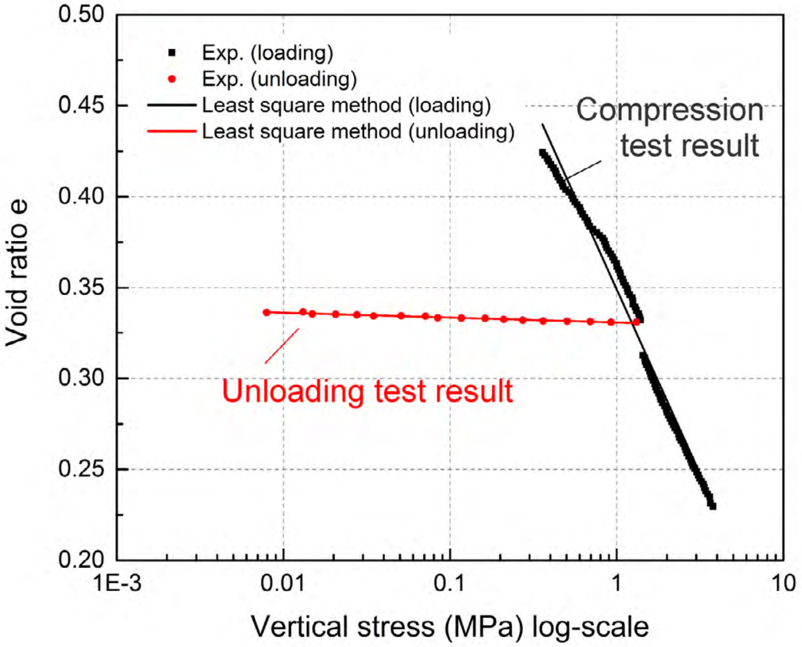

Figure 6.23 Void ratio vs vertical stress obtained by one-dimensional compression test

6.4.2 Triaxial Compression Test Simulation

Using all the parameters identified by the triaxial compression test as well as the one-dimensional compression test for the soil hardening characteristics, the triaxial compression test model is developed using the 9-node brick soil element with the capped Drucker-Prager failure criterion as shown in Fig. 6.24 for validating the soil model simulation capability. The model parameters identified for this soil specimen are summarized in Table 6.4. The deviator stress and axial stress strain relationship obtained using the 9-node brick soil element with the capped Drucker-Prager failure model is presented in Fig. 6.25 and is compared with the test data at 200 kPa confining pressure. It is observed from this figure that the nonlinear plastic and hardening behavior of the soil under triaxial compression test condition is well captured using the soil model developed and implemented in this study, and the result agrees reasonably well with the test result.

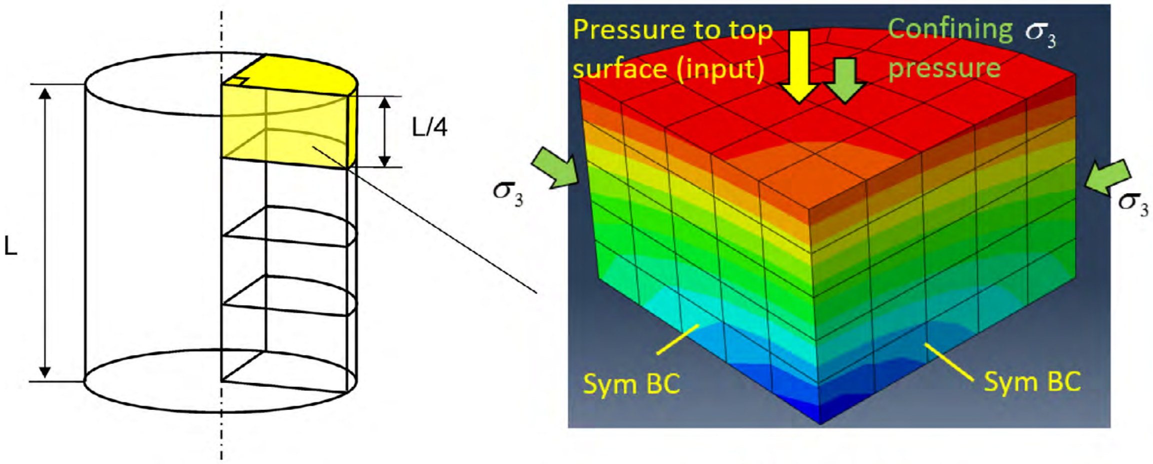

(a) Soil specimen (b) Triaxial test model

Figure 6.24 Triaxial test model

Table 6.4 Triaxial test model parameters

General	Density ρ	2,149 kg/m^3
Elastic	Young's modulus E	54.1 MPa
	Poisson's ratio ν	0.293
Capped DP Plasticity	Cohesion d	210.926 kPa
	Friction angle β	51.7848 deg
	Compression index C_c	0.20351
	Swelling index C_s	0.00268
	Initial void ratio e_0	0.424
	Initial mean effective stress p_0	0.358 MPa

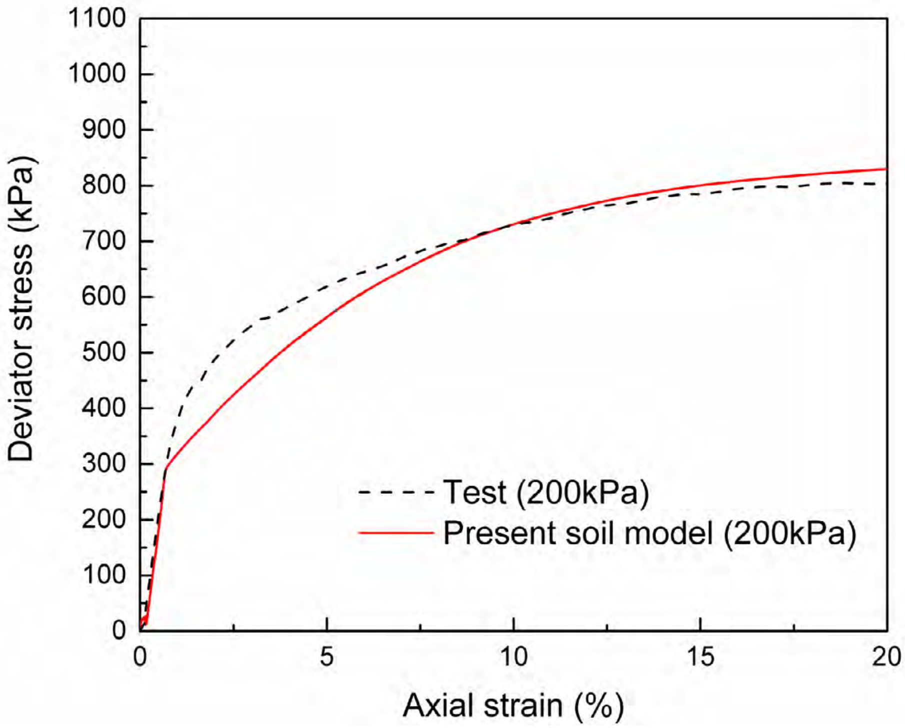

Figure 6.25 Stress-strain result of triaxial test model (200kPa confining pressure)

CHAPTER 7
CONTINUUM BASED TIRE/SOIL INTERACTION SIMULATION CAPABILITY FOR OFF-ROAD MOBILITY SIMULATION

7.1 Introduction

In this chapter, a physics-based tire/soil interaction simulation capability is proposed using the deformable tire and soil models developed in this study for use in off-road mobility simulation on deformable terrains. To define the frictional contact forces between the deformable tire and soil models, contact nodes are defined on the shell element to define the tire tread block geometry and on the soil element surface. The penalty approach is then utilized to define normal contact forces. Use of the high-fidelity physics-based tire/soil simulation model in off-road mobility simulation, however, leads to a large computational model to account for a wide area of terrains, and it makes the use of the high-fidelity tire/soil simulation model less attractive due to high computational costs resulting from the large dimensional deformable soil model. To address this issue, a numerical procedure is developed such that only soil behavior in the vicinity of the rolling tire is solved to reduce the overall computational soil model dimensionality without loss of generality. This approach is called a component soil model in this study. It is shown that use of the component soil model leads to a significant reduction in computational time while ensuring the accuracy.

7.2 Modeling of Tire/Soil Interaction

7.2.1 Contact Model between Deformable Tire and Soil

To model the contact with deformable soil, the outer surface of the finite-element tire model is discretized into numerous contact nodes defined on the shell element surface as shown in Fig. 7.1. These contact nodes are different from the finite element nodes and they are used to define the tire tread geometry and contact forces with soil elements. Using this approach, a detailed tread pattern required for off-road tire simulation can be described without increasing the number of elements for the tire model. The same procedure is used to define the contact nodes on the soil element contact surface. To detect contact points, an interpenetration between the contact nodes on the tire tread and on the soil surfaces is evaluated. As shown in Fig. 7.2, for contact node *i* on the tire tread surface, the nearest contact node *j* on the soil is detected, and then the distance δ^{ij} normal to the soil surface at contact node *j* is evaluated as

$$\delta^{ij} = (\mathbf{r}^i - \mathbf{r}^j)\cdot\mathbf{n}^j \tag{7.1}$$

where $\mathbf{n}^j$ is a unit normal to the surface at contact node *j*. If the sign of the distance function is negative (i.e., $sgn(\delta^{ij}) = -1$), two contact nodes are in contact and the normal contact force $\mathbf{F}_n$ is defined as a compliant force function as follows:

$$\mathbf{F}_n = (k\delta^{ij} + c\dot{\delta}^{ij})\mathbf{n}^j \tag{7.2}$$

where $\dot{\delta}^{ij} = (\dot{\mathbf{r}}^i - \dot{\mathbf{r}}^j)\cdot\mathbf{n}^j$, k is a spring contact, and c is a damper coefficient. The tangential forces at the contact point can be calculated based on either LuGre friction force model or simplified slip-dependent kinetic friction force model. In the latter case, one has

$$\mathbf{F}_t = -\mu_t(\mathbf{v}_t)\left\|\mathbf{F}_n\right\|\frac{\mathbf{v}_t}{\left\|\mathbf{v}_t\right\|} \tag{7.3}$$

where the tangential slip velocity vector is defined by $\mathbf{v}_t = \dot{\mathbf{r}}^{ij} - (\dot{\mathbf{r}}^{ij}\cdot\mathbf{n}^j)\mathbf{n}^j$ as shown in Fig. 7.2. The coefficient of friction is assumed as a function of slip velocity $\mathbf{v}_t$ as [12]

$$\mu(\mathbf{v}_t) = \alpha\tan^{-1}(\beta\left\|\mathbf{v}_t\right\|) \tag{7.4}$$

where the parameters α and β are determined by the curve fitting. In this study, α is assumed as $\alpha = 2\mu_0/\pi$ for the kinetic friction coefficient μ_0, and β is determined by the slope around zero slip. The total contact force vector can then be defined as $\mathbf{F} = \mathbf{F}_t + \mathbf{F}_n$ using Eqs. 7.2 and 7.3, and then the generalized contact force vectors for tire and soil elements are defined using the principle of virtual work.

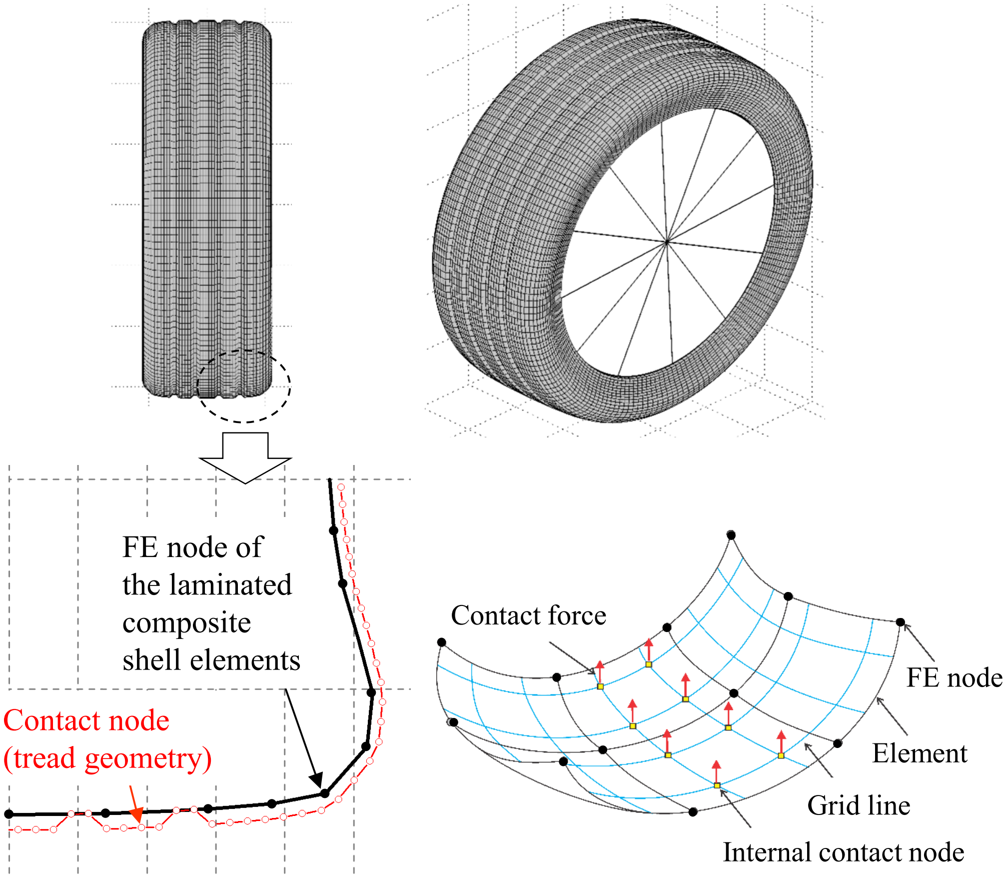

(a) Tread block geometry using contact nodes

(b) Contact nodes

Figure 7.1 Modeling tread geometry using contact nodes

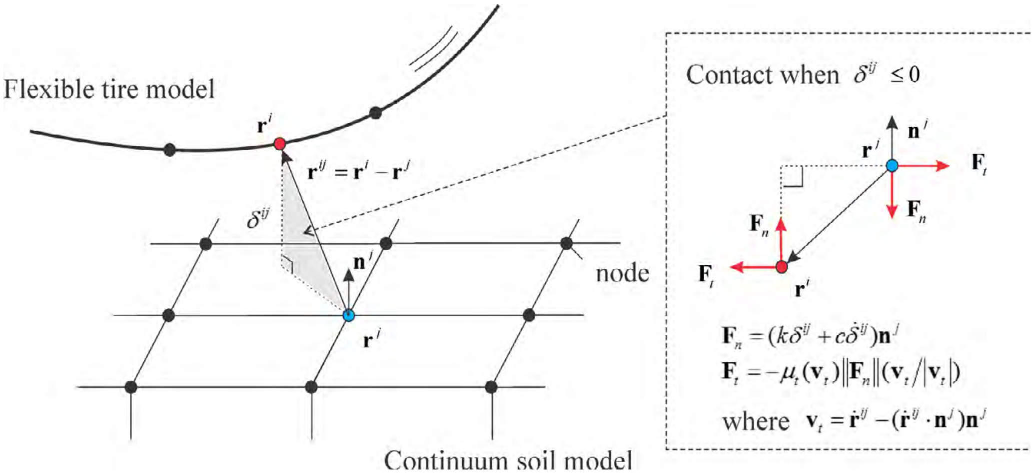

Figure 7.2 Contact force model for tire soil interaction

7.2.2 Component Soil Approach

Use of the high-fidelity physics-based tire/soil simulation model in off-road mobility simulation leads to a very large computational model to consider a wide area of terrains. Thus, the computational cost dramatically increases as the size of the soil model increases. In addition to the parallel computing utilized in this study to improve the computational efficiency, the large computational cost inherent to the tire/soil interaction simulation needs to be improved from a modeling perspective as well. When the rolling tire comes into contact with deformable soil, the soil undergoes plastic deformation around the contact region and the permanent soil deformation propagates as the tire travels. Since the large plastic soil deformation introduces energy dissipation, the propagation of the plastic soil deformation stops around the contact region and the soil far from the contact region has no contribution to the tire/soil interaction behavior. In other words, one can solve the soil behavior only in the vicinity of the rolling tire in order to reduce the overall computational soil model dimensionality. That is, soil elements far behind the tire can be removed from the equations of motion after the tire passes, and then new soil elements are added to the portion that the tire is heading to. The similar idea was applied to the discrete element (DE) soil model by Wasfy, et al. to reduce the overall computational cost of the tire/soil interaction simulation [90]. Having removed the soil elements behind from the equations of motion, the nodal coordinates and plastic strains of the removed soil elements are saved such that the previous soil state can be recovered any time when the other tire comes and rolls over this soil portion. In other words, the soil element freezes temporary and then defreezes if the other tire comes closer and travels over this soil element. This allows for considering multiple pass scenarios on deformable terrains without loss of generality.

To utilize this procedure, the moving soil patch size (length and width) around the rolling tire needs to be predetermined, and this localized soil patch is called a "component soil model" in this study. On the cut section of the component soil model, the symmetric boundary condition is imposed. In order for the tire to always lie around the center of the component soil surface, the component soil model needs to be updated as the tire travels. To this end, the minimum horizontal distance from the center of the tire rim to the edges of the component soil model is monitored. If the minimum horizontal distance becomes less than a threshold, the component soil model is updated by removing soil elements behind and adding new elements to the portion that the tire is heading to, as illustrated in Fig. 7.3. By doing so, the number of degrees of freedom of the soil model remains small and constant throughout the simulation regardless the overall area of soil considered in the off-road mobility simulation. This leads to a significant saving of memory usage and reduction of the computational time as will be discussed in Section 7.3.2.

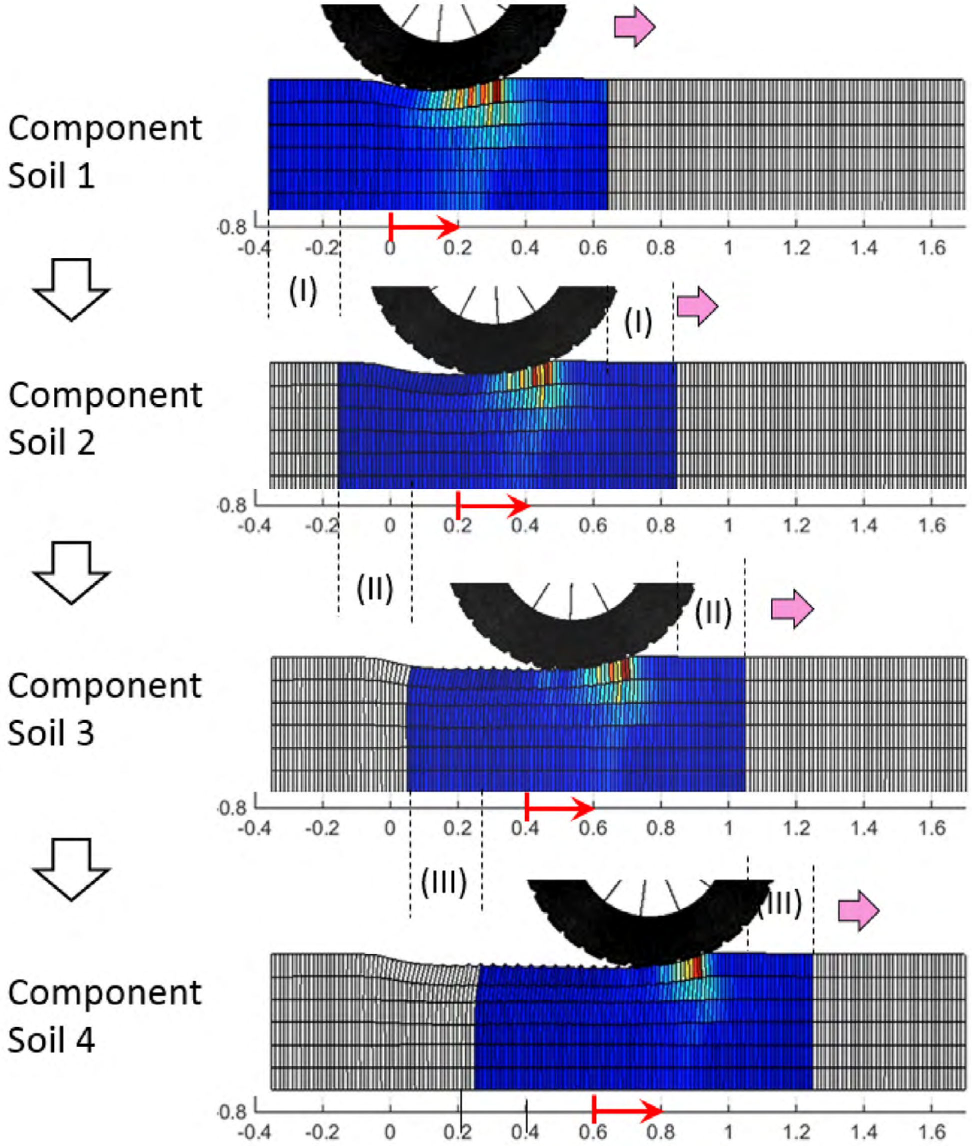

Figure 7.3 Updates of component soil model

7.3 Numerical Examples

7.3.1 Off-Road Tire Model

For the tire soil interaction simulation, an off-road tire model is developed using the laminated composite shell element in a way discussed in Section 5.4.1. The off-road tire considered in this study is 235/75R15. The tire geometry, the cross-section geometry, and the layer property are shown in Fig. 7.4. As shown in Fig. 7.4, the tire cross-section is divided into the tread, shoulder, sidewall, and bead sections. The number of layers, cord angles, thickness, and material properties, which vary through the tire structure, are specified in each section. The tread section consists of a carcass ply, two steel belts, a belt cover, and tread blocks. The carcass ply and steel belt are modeled as an orthotropic material with polyester and steel cords embedded in rubber, respectively. A rubber layer is considered between the upper and lower steel belts and between the carcass ply and the lower steel belt. The shoulder section is modeled by a carcass ply layer and rubber layer. The sidewall section is modeled by a carcass ply layer. The bead section is modeled by two carcass ply layers and a rubber layer as shown in Fig. 7.4. The deformed cross section is shown in Fig. 7.5. For comparison with test results, the air pressure is set to 180 and 230 kPa. The normal contact pressure distribution in the longitudinal and lateral direction at 4 kN wheel load are shown in Figs. 7.6 and 7.7 and compared with the test results. The tire model results agree well with the test results in magnitude and shape. Furthermore, the contact patch lengths along the longitudinal and lateral axes are compared with the test results for various wheel loads and various air pressure in Figs. 7.8 and 7.9 respectively. It is observed from these figures that the results agree well with the test results for different loads in both directions and the nonlinear effect is also captured for large wheel loads using the present tire model for both air pressures (i.e., 230 and 180 kPa). The vertical load and deflection relationship is presented in Fig. 7.10 for various wheel loads under various air pressures and they are compared with test results. The result matches reasonably well with the test data. For modeling the tread pattern of off-road tire, the tread location is measured and the tread block geometry is created using the contact nodes as explained in Section 7.2.1. This off-road tire model is used in the following examples to demonstrate the use of the tire and soil simulation capability.

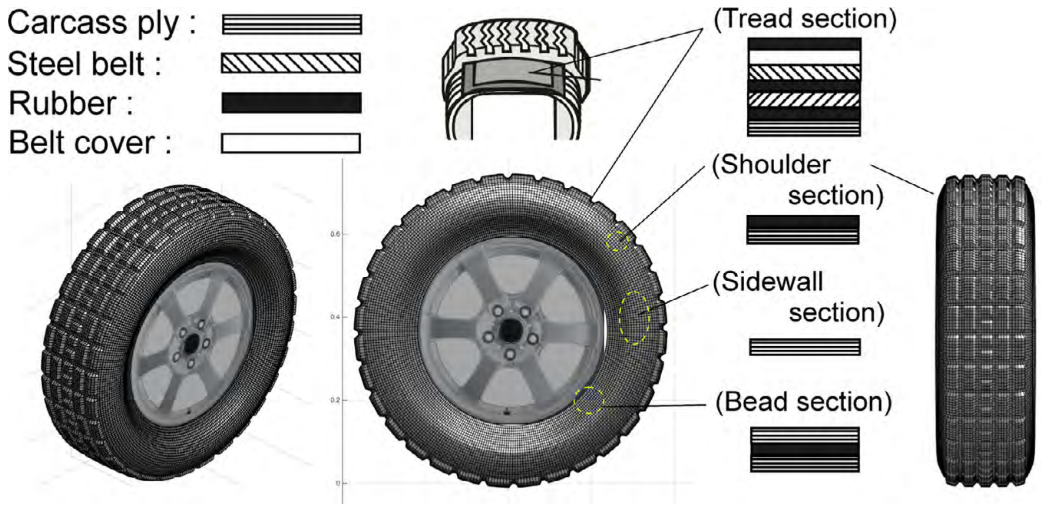

Figure 7.4 Physics-based off-road tire model using the laminated composite shell element

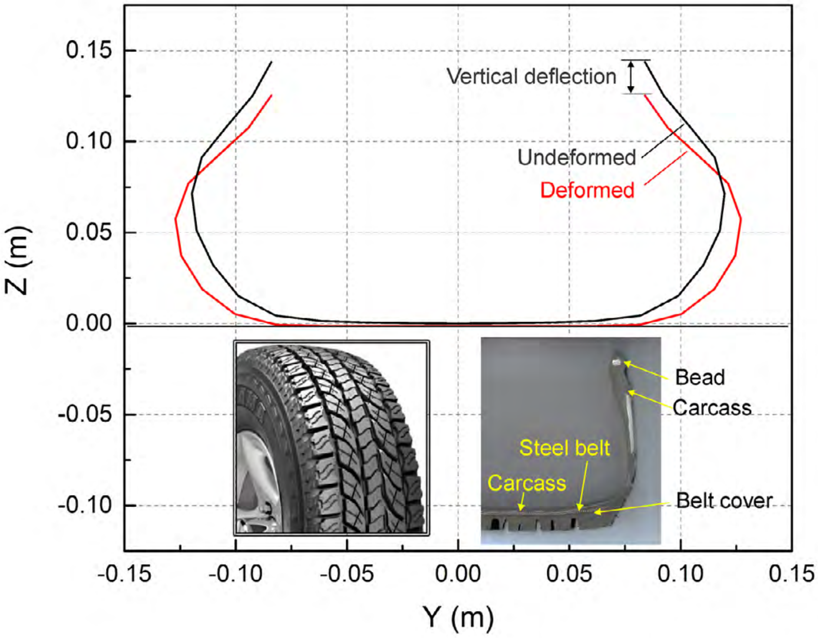

Figure 7.5 Deformed shape of off-road tire cross section

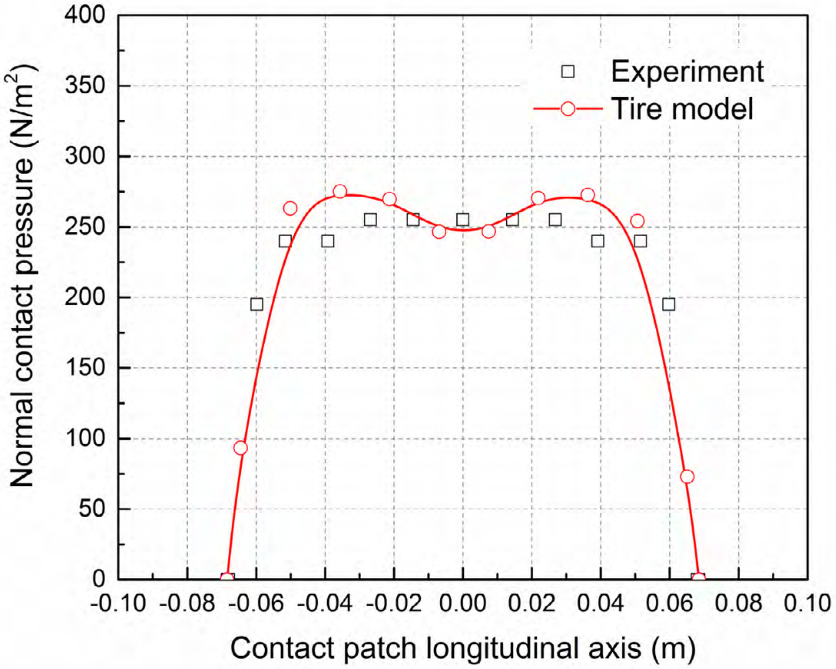

Figure 7.6 Normal contact pressure in a longitudinal direction (4kN)

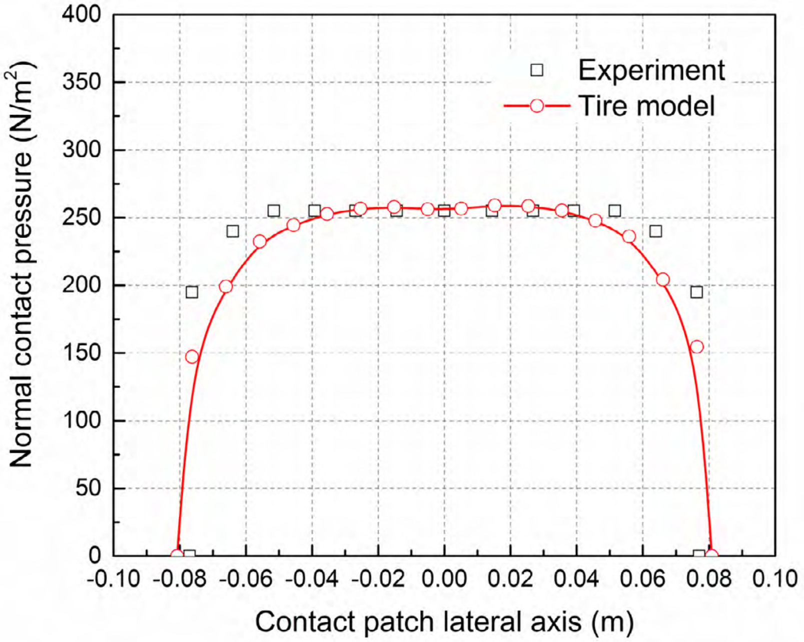

Figure 7.7 Normal contact pressure in a lateral direction (4kN)

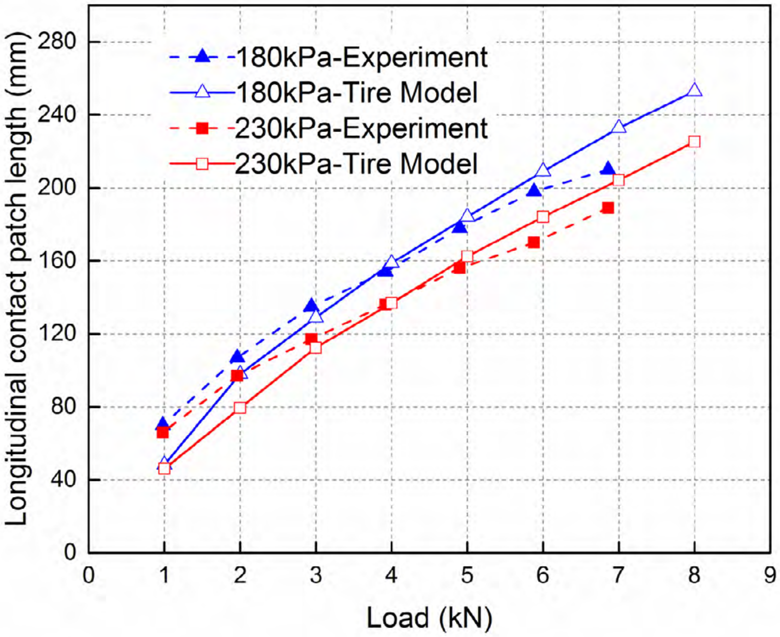

Figure 7.8 Load-longitudinal contact patch length for off-road tire model

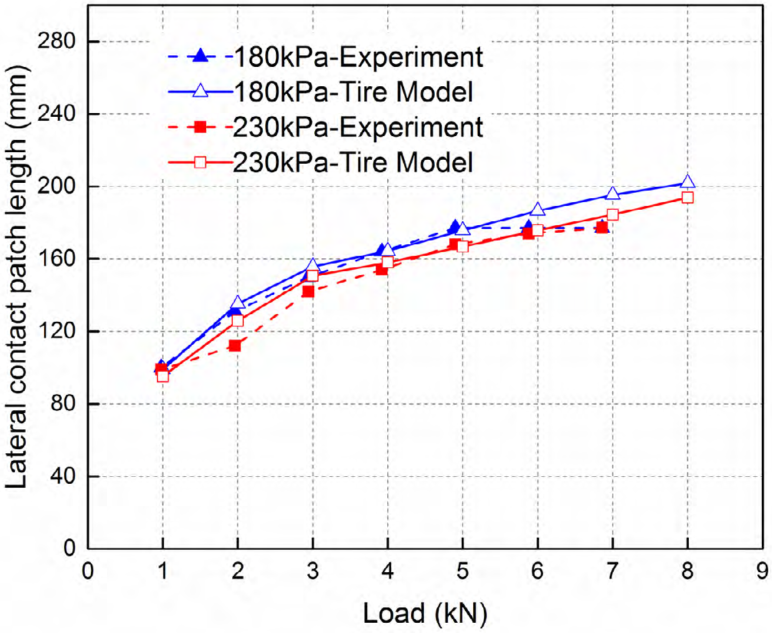

Figure 7.9 Load-lateral contact patch length for off-road tire model

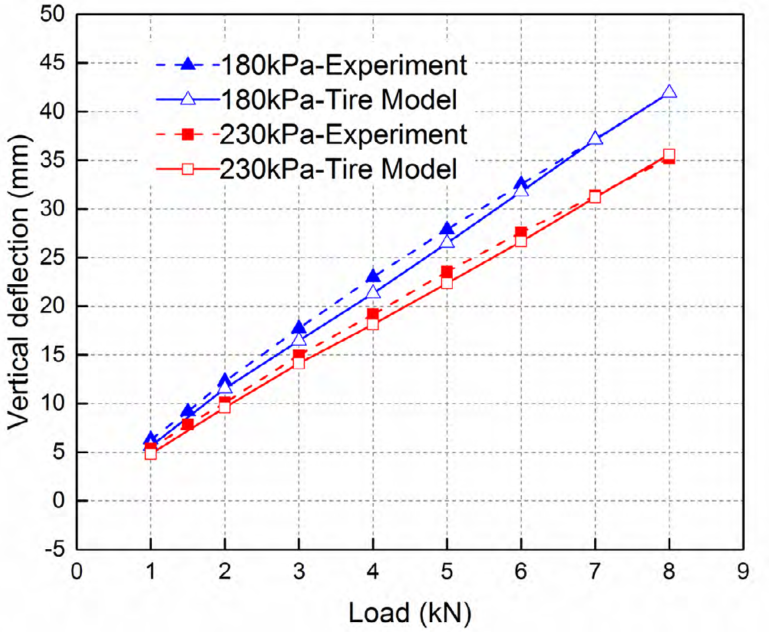

Figure 7.10 Load-vertical deflection curve for off-road tire model

7.3.2 Tire/Soil Interaction Simulation

In this subsection, several numerical examples are presented in order to demonstrate the use of the physics-based tire/soil interaction simulation capability developed in this study. The off-road tire model discussed in Section 7.3.2 is used and a constant traveling speed of 5 m/s is assumed. The air pressure and normal load are assumed to be 230 kPa and 4 kN, respectively. The coefficient of friction is assumed to be 0.3. The parameters of the deformable terrain model are summarized in Table 7.1 [86]. The width and height of the soil model are assumed to be 0.4 m and 0.4 m, respectively. 40 elements are used in the width direction, while 6 elements are used in the height direction. In the longitudinal (traveling) direction, 80 elements are used for 1 meter long soil. That is, the soil element is 12.5 mm in length and 10 mm in width to capture the tread pattern geometry on the soil footprint as shown in Fig. 7.11.

Table 7.1 Material model parameters

Initial cohesion d_0 (Pa)	5000
Yield surface coefficient η	0.0
Yield surface coefficient ξ	1.155
Young's modulus E (MPa)	13.79
Poisson's ratio ν	0.3
Density ρ (kg/m^3)	200

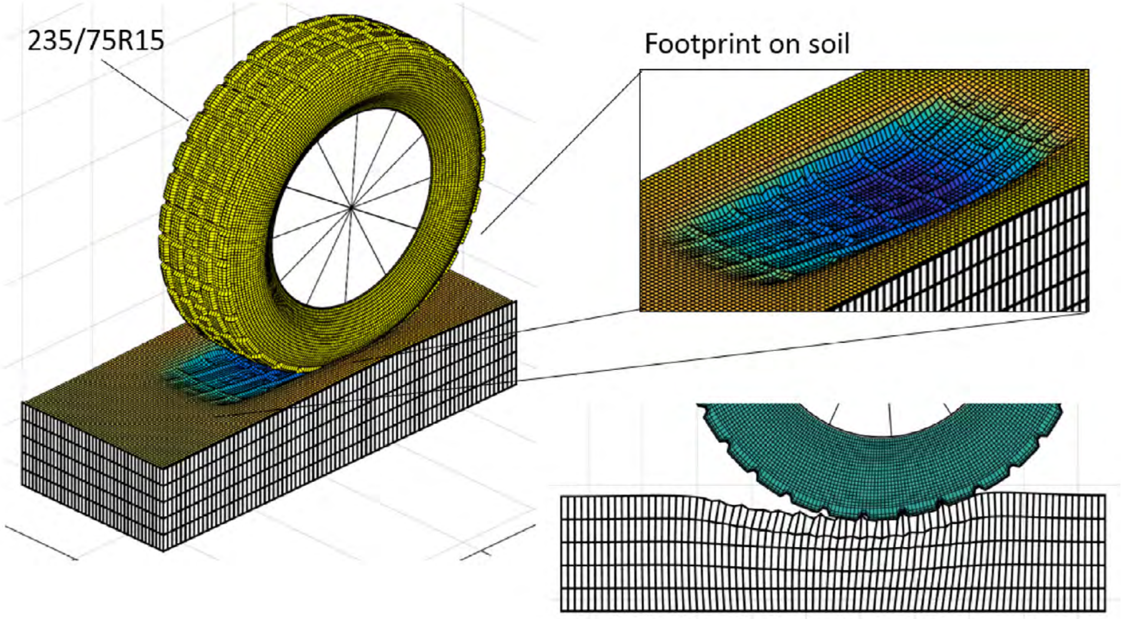

Figure 7.11 Tire/soil interaction model

In Fig. 7.12, the tire and soil deformation using the component soil model approach is presented. It is shown that the moving soil patch is updated as the tire travels. In order to discuss the effect of length in the component soil model on accuracy, 0.8 m, 1.0 m and 1.2 m long component soil models are considered and compared with the complete soil model. The soil element size (i.e., 12.5 mm in length and 10 mm in width) are kept constant for all the models and symmetric boundary condition is imposed on the cut section of the component soil model. The tire rim vertical position and the rolling

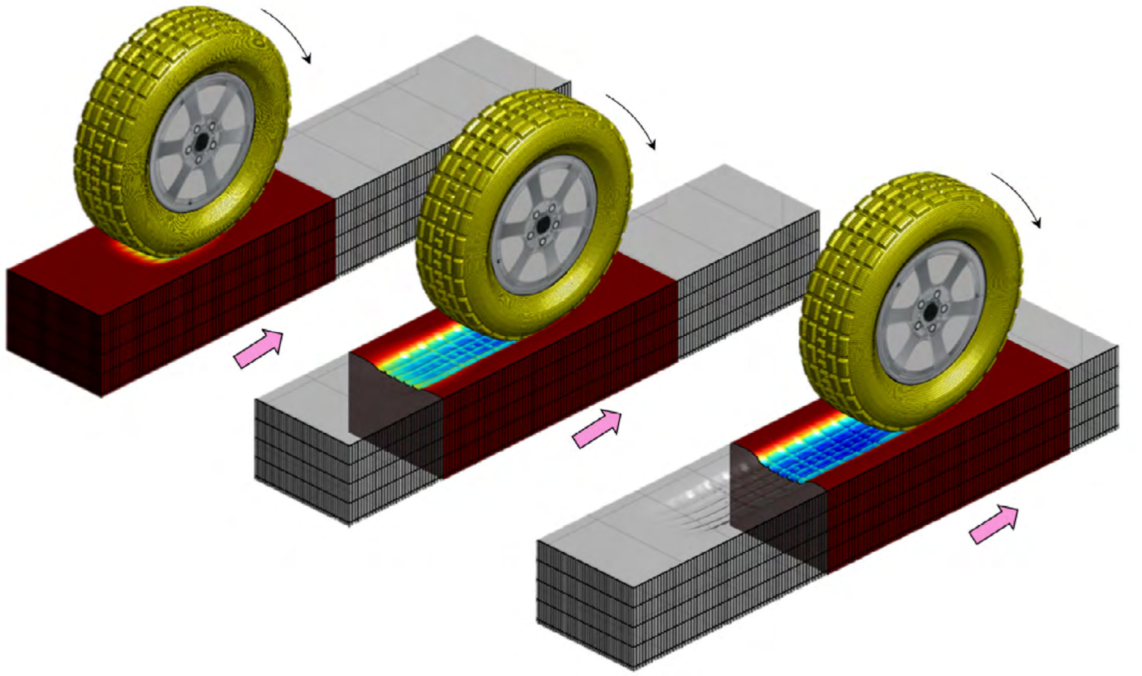

Figure 7.12 Tire/soil interaction model using component soil approach

resistance defined by the ratio of the longitudinal tire force to the vertical (F_x / F_z) for the traveled distance of 1 m are shown in Figs. 7.13, 7.14 and 7.15 for the three component soil models, and they are compared with the complete soil model as the reference solution. In this simulation, 2 m long soil bin is considered and the tire is dropped on the soil at the initial configuration, resulting in approximately 0.05 m sinkage of the vertical position of the tire rim from the initial position as observed between time t = 0 and 0.2 seconds. The rolling resistance at the steady state rolling is approximately 0.26, which is close to the coefficient of friction assumed in this model. It is observed from Figs. 7.13, 7.14 and 7.15 that use of 0.8 m long component soil model leads to noticeable deviations in the vertical position and the rolling resistance from the reference solutions obtained using the complete soil model, while use of 1.2 m long component soil model leads to identical solutions to the complete soil model. The computational time for the three models are, respectively, 28.0, 39.0 and 42.8 hours. The use of longer component soil model leads to longer computational time as expected, while in this simulation scenario, the 1.0 m long soil model also predicts the overall tire and soil behavior well, despite the small deviation as shown in Fig. 7.14. The selection of the component soil size depends on the simulation model parameters and loading scenarios, involving the tradeoff between the model accuracy and computational time. Furthermore, using the 1.0 m long component soil model, the tire sinkage and rolling resistance under various wheel loads are presented in Fig. 7.16. It is clearly observed that the tire sinkage and rolling resistance increase as the vertical force increases.

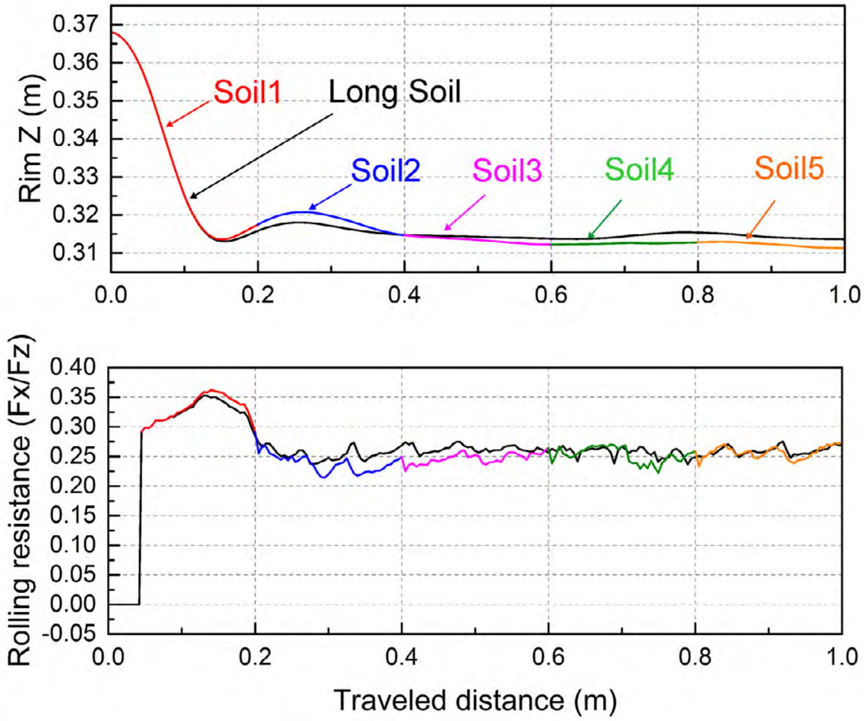

Figure 7.13 Tire sinkage and rolling resistance with 0.8 m long (64x40x6)

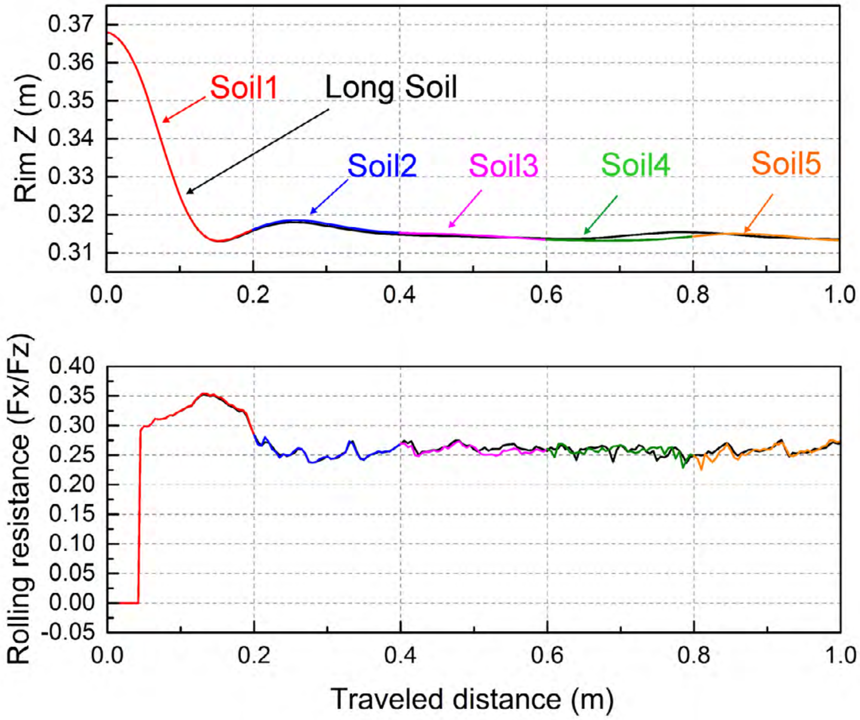

Figure 7.14 Tire sinkage and rolling resistance with 1.0m long (80x40x6)

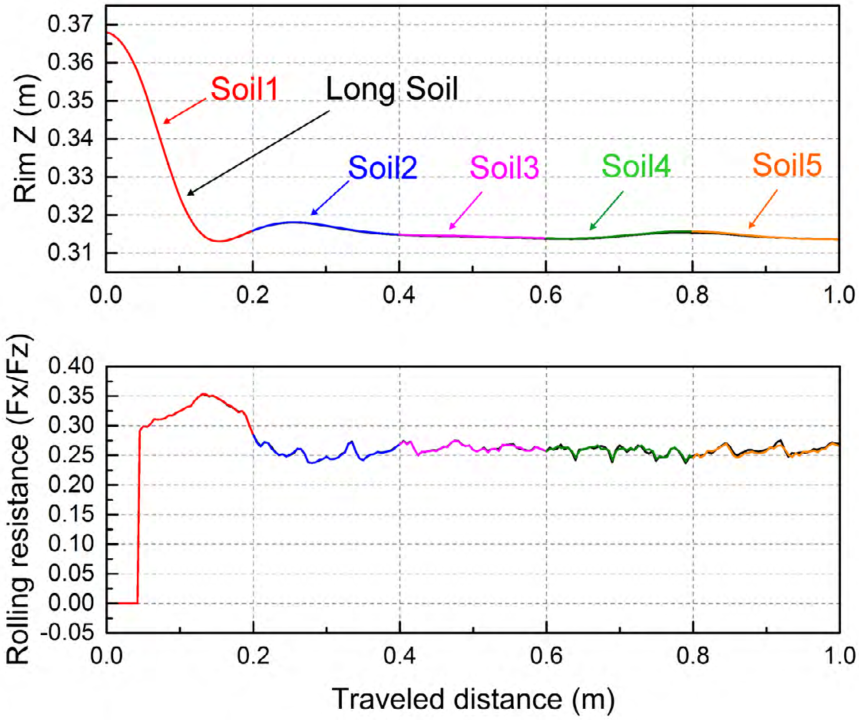

Figure 7.15 Tire sinkage and rolling resistance with 1.2m long (96x40x6)

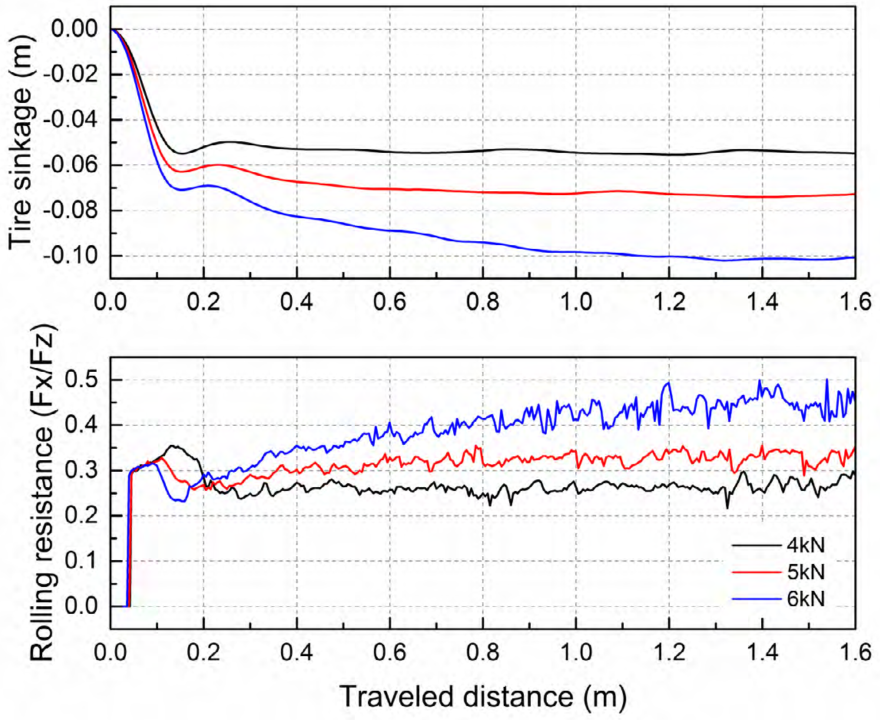

Figure 7.16 Tire sinkage and rolling resistance for various wheel loads

To further discuss the computational time of the high-fidelity physics-based tire/soil simulation capability using the component soil model approach, the computational time for the soil bin length of 1.0 m, 2.0 m, and 3.0 m are presented in Fig. 7.17 for the complete soil model and the 1.0 m long component soil model. Intel Core i7-3770, 3.4GHz is used with OpenMP parallel computing capability for 4 threads. The numbers of degrees of freedom of the soil elements for the soil bin length of 1.0 m, 2.0 m, and 3.0 m are, respectively, 242,541, 484,221 and 725,901, while the number of degrees of freedom of the 1 m long component soil model is 242,541 regardless of the length of the soil bin. The degrees of freedom of the tire model is 12,000. It is observed from Fig. 7.17 that the CPU time exponentially increases as the traveled distance increases in the complete soil model, while the CPU time increases almost linearly as an increase of the traveled distance in the component soil model. This is attributed to the fact that the soil model dimensionality remains constant regardless of the traveled distance. The significant reduction in computational time is achieved for longer simulation using the component soil model as demonstrated in this example, and it enables the use of the high-fidelity physics-based tire/soil interaction simulation model in the large-scale off-road mobility simulation.

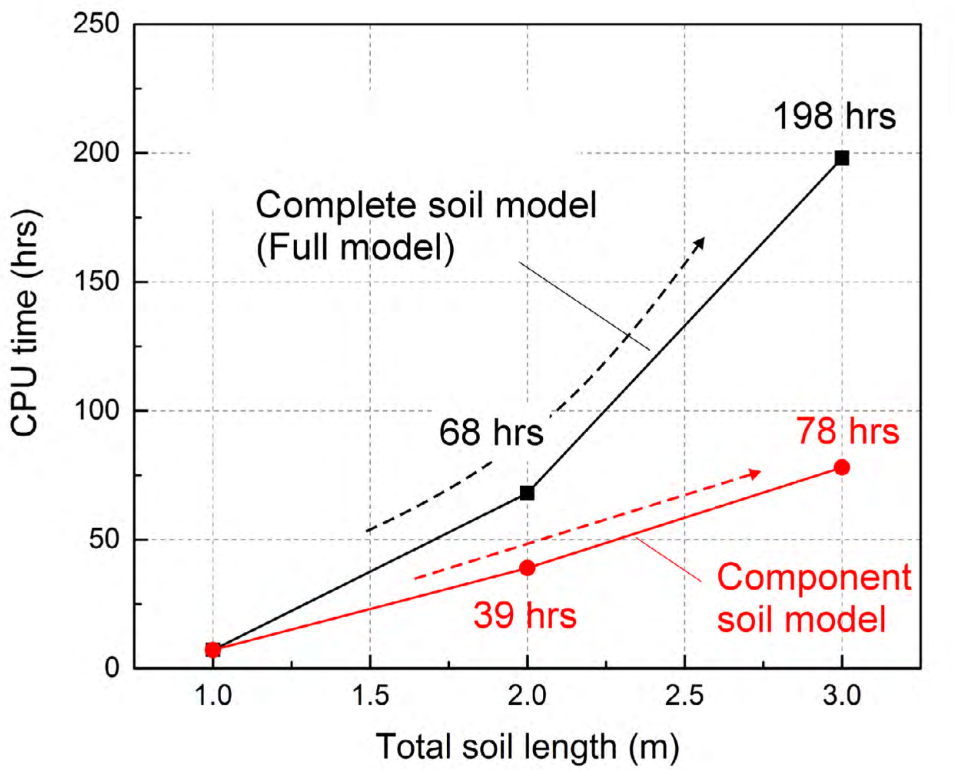

Figure 7.17 CPU time comparison between long soil model and component soil model

CHAPTER 8
CONCLUSIONS AND FUTURE WORK

8.1 Summary and Conclusions

Despite the fact detailed finite element tire models using explicit finite element software have been widely utilized for structural design of tires by tire manufactures, it is recognized in the tire industry that existing state-of-the-art explicit finite element tire models are not capable of predicting the transient tire force characteristics accurately under severe vehicle maneuvering conditions due to the numerical instability that is essentially inevitable for explicit finite element procedures for severe loading scenarios and the lack of transient (dynamic) tire friction model suited for FE tire models. Furthermore, to integrate the deformable tire models into multibody full vehicle simulation, co-simulation technique could be an option for commercial software. However, there exit various challenges in co-simulation for the transient vehicle maneuvering simulation in terms of numerical stability and computational efficiency. The transient tire dynamics involves rapid changes in contact forces due to the abrupt braking and steering input, thus use of co-simulation requires very small step size to ensure the numerical stability and energy balance between two separate simulation using different solvers. For this reason, a high-fidelity physics-based tire model that can be fully integrated into multibody dynamics computer algorithms is developed in this study for vehicle dynamics simulation without resorting to ad-hoc co-simulation procedures.

To this end, a continuum mechanics based shear deformable laminated composite shell element is developed based on the finite element absolute nodal coordinate formulation for modeling the complex fiber reinforced rubber tire structure in Chapter 2. The element consists of four nodes, each of which has the global position coordinates and the transverse gradient coordinates along the thickness introduced for describing the orientation and deformation of the cross section of the shell element. The global position field on the middle surface and the position vector gradient at a material point in the element are interpolated by bi-linear polynomials. The continuum mechanics approach is used to formulate the generalized elastic forces, allowing for the consideration of nonlinear constitutive models in a straightforward manner. The element locking exhibited in the element can be eliminated using the assumed natural strain (ANS) and enhanced assumed strain (EAS) approaches. In particular, the combined ANS and EAS approach is introduced to alleviate both curvature and Poisson's thickness lockings arising from the erroneous transverse normal strain distribution. The shell element developed is further generalized to a laminated composite shell element for application to the modeling of fiber-reinforced rubber (FRR) structure of the physics-based flexible tire model. The complex deformation coupling exhibited in fiber-reinforced composite materials can be automatically considered in the shear deformable laminated composite shell element using the continuum mechanics approach, and the element lockings are systematically eliminated by ANS and EAS approaches, thereby leading to a locking-free shear deformable composite shell element. Furthermore, various nonlinear material models can be considered for each layer in a way same as solid elements. Several numerical examples are presented in Chapter 3 in order to demonstrate the accuracy and the rate of convergence of numerical solutions obtained by the continuum mechanics based bi-linear shear deformable shell element proposed in this study. In particular, the effect of locking remedy and the element performance including the rate of convergence of the finite element solutions are compared with those of ANSYS for nonlinear problems and analytical solutions for linear problems for various benchmark problems.

Using the shear deformable laminated composite shell element based on the absolute nodal coordinate formulation, a physics-based flexible tire model for the transient braking and cornering analysis is developed for use in multibody vehicle dynamics simulation in Chapter 4. To account for the transient tire friction characteristics including the friction-induced hysteresis that appears in severe maneuvering conditions, the distributed parameter LuGre tire friction model is integrated into the flexible tire model. To this end, the contact patch predicted by the structural tire model is discretized into small strips across the tire width, and then each strip is further discretized into small elements to convert the partial differential equations of the LuGre tire friction model to the set of first-order ordinary differential equations. By doing so, the structural deformation of the flexible tire model and the LuGre tire friction force model are dynamically coupled in the final form of the equations, and these equations are integrated simultaneously forward in time at every time step.

In Chapter 5, a systematic and automated procedure for parameter identification of LuGre tire friction model introduced in Chapter 4 is developed for accurate and reliable prediction of transient tire forces. Since several fitting parameters are introduced to account for the nonlinear friction characteristics, the correlation of the model parameters with physical quantities are not clear, making the parameter identification of the LuGre tire friction model difficult. That is, inappropriate initial estimates may lead to parameters that have nothing to do with physical quantities even though the LuGre model are fitted well with measured tire force curves. To this end, friction parameters used in the LuGre tire force model are estimated using the measured slip-dependent friction characteristics first and used for the nonlinear least square fitting. The adhesion parameter is then estimated using the slope around the zero slip ratio. The nonlinear least square fitting is used to identify all the parameters for the entire slip range such that the maximum tire force peak can agree with the measurement data. Furthermore, the modified friction characteristic curve function is proposed for wet road conditions, in which the linear decay in friction is exhibited in the large slip velocity range. It is shown that use of the proposed numerical procedure leads to an accurate prediction of the LuGre model parameters for measured tire force characteristics under various loading and speed conditions. Furthermore, the fundamental tire properties including the load-deflection curve, the contact patch lengths, contact pressure distributions, and natural frequencies are validated against the test data. Several numerical examples for the hard braking and cornering simulation including the antilock braking control are presented to demonstrate the robust simulation capability of the physics-based flexible tire model developed in this study.

The physics-based flexible tire model is further extended for application to off-road mobility simulation in Chapters 6 and 7. In Chapter 6, a locking-free 9-node 33-DOF brick element is developed with the curvature coordinates at the center node for modeling a continuum soil using the capped Drucker-Prager failure criterion. Introduction of the curvature coordinates allows for considering the quadratic terms in the polynomial for the assumed displacement field, thus the linear distribution of the stresses and strains, which cannot be captured in the standard tri-linear 8-node 24-DOF brick element, can be considered. This eliminates the reliance on the enhanced assumed strain method to alleviate the element lockings exhibited in the standard tri-linear 8-node brick element, thereby making the formulation and implementation of the continuum soil model straightforward. Several benchmark test results are presented to demonstrate the use of the 9-node brick element with curvature coordinates. Furthermore, the multiplicative finite strain plasticity theory is utilized to consider the large soil deformation exhibited in the tire/soil interaction simulation using the capped Drucker-Prager failure criterion. The implementation of the capped Drucker-Prager failure is verified by comparison with the soil elements in ABAQUS for the plate sinkage benchmark test of soil. In order to identify soil parameters including cohesion and friction angle, the triaxial soil test is carried out. Using the soil parameters identified including the plastic hardening parameters by the compression soil test, the continuum soil model developed is validated against the test data for the triaxial compression test condition. The stress-strain curve agrees well with the triaxial soil test result.

In Chapter 7, using the physics-based deformable tire and soil models, the tire/soil interaction simulation capability is developed and implemented in the general multibody dynamics computer algorithm. Use of the high-fidelity physics-based tire/soil simulation model in off-road mobility simulation, however, leads to a very large computational model to consider a wide area of terrains. Thus, the computational cost dramatically increases as the size of the soil model increases. To address this issue, the component soil model is proposed such that soil elements far behind the tire can be removed from the equations of motion sequentially, and then new soil elements are added to the portion that the tire is heading to. That is, the soil behavior only in the vicinity of the rolling tire is solved in order to reduce the overall model dimensionality associated with the finite element soil model. It is shown that use of the component soil model leads to a significant reduction in computational time while ensuring the accuracy, making the use of the physics-based deformable tire/soil simulation capability feasible in off-road mobility simulation.

8.2 Future Work

While the physics-based tire and soil models developed in this study are tested and validated extensively against the test results using the test facility for the tire and soil individually, validation of the tire/soil interaction simulation model has not be completed yet. This involves more extensive tests using the mobility soil bin test facility to measure the tire sinkage and rolling resistance on deformable terrains for various test conditions. For validating the computational model, the mobility soil bin test will be carried out using the off-road tire introduced in Section 7.3 and the soil used in the triaxial soil test presented in Section 6.4. These computational models are validated against the test data individually as discussed in Section 6.4 and 7.3, and their model parameters are also identified. The soil bin test involves measuring the static wheel load and tire sinkage curve for various tire air pressures; and the rolling resistance of the tire on soil in various wheel load and air pressure conditions. Tire forces are measured by force transducers embedded in the instrumented rim.

In addition, the integration of the physics-based flexible tire model developed in this study in a high-performance computing (HPC) off-road mobility simulation framework is crucial to enable the evaluation of overall vehicle performance and mobility capability in various terrain conditions. While use of the component soil model leads to significant reduction in the computational time, use of the physics-based tire/soil simulation capability for full vehicle simulation including four tires and detailed suspension models still requires significant computational power. For this reason, the tire and soil models developed in this study are currently implemented into the physics-based HPC off-road mobility simulation software called *Chrono* such that deformable tire and soil interaction simulation capability can be utilized in multibody full vehicle simulation in a single computational framework. Furthermore, the integration with *Chrono* software allows for the use of discrete element (DE) soil models consisting of millions of particles and DE soil models are needed for severe vehicle maneuvering scenarios involving high slippages.

Development of a systematic parameter identification and validation procedure for the physics-based tire/soil simulation model developed in this study is also needed. A tire has a complex structure and various model parameters need to be identified to create the physics-based tire model. In addition, soil parameters are stochastic in nature and spatially distributed. Furthermore, an uncertainty quantification of terrains requires extensive measurement, thus in most cases, only limited number of test data under limited test conditions is available, and uncertainties of the tire and soil model parameters make the validation process of the tire/soil interaction simulation very difficult and challenging. This issue, however, has not been thoroughly addressed in the field of study, and is of crucial importance in use of the physics-based tire and soil simulation model.

APPENDIX
ELASTIC MIDDLE SURFACE APPROACH FOR SHEAR DEFORMABLE SHELL ELEMENT

A.1 Introduction

In Appendix, the elastic middle surface approach used for formulating the elastic forces of the shear deformable shell element discussed in Chapter 2 is presented with a plane stress assumption [87]. While the continuum mechanics approach is utilized to consider fiber reinforced rubber (FRR) material which is indispensable for tire modeling, the elastic middle surface approach discussed below can be applied to the thin to moderately thick shell structures. For some applications, this shell formulation would be suited from computational standpoint since the integration along the thickness can be performed analytically and Poisson's locking can be automatically eliminated by the plane stress assumption. However, this formulation requires a special formulation to consider nonlinear material models.

A.2 Elastic Middle Surface Approach

Using Green-Lagrange strain tensor, the six strain components in the middle surface of the shell element *i* can be defined as follows:

$$\hat{\mathbf{E}}_m^i(x^i, y^i, 0) = \frac{1}{2}\left((\mathbf{F}_m^i)^T \mathbf{F}_m^i - \mathbf{I}\right) \tag{A.1}$$

where $\mathbf{F}_m^i$ is the global position vector gradient tensor at a material point in the middle surface of the shell element *i* and is given as

$$\mathbf{F}_m^i(x^i, y^i, 0) = \frac{\partial \mathbf{r}_m^i}{\partial \mathbf{X}^i} = \bar{\mathbf{J}}_m^i (\mathbf{J}_m^i)^{-1} \tag{A.2}$$

where $\mathbf{r}_m^i = \mathbf{S}^i(x^i, y^i, 0)\mathbf{e}^i = \mathbf{S}_m^i(x^i, y^i)\mathbf{e}_p^i$. $\bar{\mathbf{J}}_m^i$ and $\mathbf{J}_m^i$ are covariant base tensors of the material point in the middle surface at the deformed and reference configurations, respectively. These tensors are defined as

$$\bar{\mathbf{J}}_m^i = \frac{\partial \mathbf{r}_m^i}{\partial \mathbf{x}^i} = \begin{bmatrix} \mathbf{g}_1^i & \mathbf{g}_2^i & \mathbf{g}_3^i \end{bmatrix} \tag{A.3}$$

where $\mathbf{g}_1^i = \partial \mathbf{r}_m^i / \partial x^i$, $\mathbf{g}_2^i = \partial \mathbf{r}_m^i / \partial y^i$, $\mathbf{g}_3^i = \partial \mathbf{r}_m^i / \partial z^i$ and

$$\mathbf{J}^i_m = \frac{\partial \mathbf{X}^i_m}{\partial \mathbf{x}^i} = \begin{bmatrix} \mathbf{G}^i_1 & \mathbf{G}^i_2 & \mathbf{G}^i_3 \end{bmatrix} \tag{A.4}$$

where the vector $\mathbf{X}^i_m$ represents the global position vector of element i at the reference configuration in the middle surface and is given by $\mathbf{X}^i_m = \mathbf{S}^i(x^i, y^i, 0)\mathbf{e}^i_0$ with the initial element nodal coordinates $\mathbf{e}^i_0$. Furthermore, one can define $\mathbf{G}^i_1 = \partial \mathbf{X}^i_m / \partial x^i$, $\mathbf{G}^i_2 = \partial \mathbf{X}^i_m / \partial y^i$ and $\mathbf{G}^i_3 = \partial \mathbf{X}^i_m / \partial z^i$. Substituting Eq. A.2 into Eq. A.1, one can obtain

$$\hat{\mathbf{E}}^i_m(x^i, y^i, 0) = (\mathbf{J}^i_m)^{-T}\tilde{\mathbf{E}}^i_m(\mathbf{J}^i_m)^{-1} \tag{A.5}$$

where

$$\tilde{\mathbf{E}}^i_m(x^i, y^i, 0) = \frac{1}{2}\left((\bar{\mathbf{J}}^i_m)^T\bar{\mathbf{J}}^i_m - (\mathbf{J}^i_m)^T\mathbf{J}^i_m\right) \tag{A.6}$$

The Green-Lagrange strains given by Eq. A.5 are transformed to those defined with respect to the orthogonal frame $\mathbf{A}^i_m$ defined at the reference configuration as follows:

$$\mathbf{E}^i_m(x^i, y^i, 0) = (\mathbf{B}^i_m)^{-T}\tilde{\mathbf{E}}^i_m(\mathbf{B}^i_m)^{-1} \equiv \varepsilon^i_{rs}, \quad r, \mathrm{s} = x, y, z \tag{A.7}$$

where

$$\mathbf{B}^i_m = (\mathbf{A}^i_m)^T\mathbf{J}^i_m \equiv B^i_{rs}, \quad r, \mathrm{s} = 1, 2, 3 \tag{A.8}$$

The tensor transformation given by Eq. A.7 can be re-expressed in terms of the engineering strain vector $\boldsymbol{\varepsilon}^i_m$ and the covariant strain vector $\tilde{\boldsymbol{\varepsilon}}^i_m$ as:

$$\boldsymbol{\varepsilon}^i_m = (\mathbf{T}^i_m)^{-T}\tilde{\boldsymbol{\varepsilon}}^i_m \tag{A.9}$$

where $\mathbf{T}^i_m$ is a 6 by 6 matrix is defined as

$$\mathbf{T}^i_m = \begin{bmatrix} (B^i_{11})^2 & (B^i_{12})^2 & 2B^i_{11}B^i_{12} & (B^i_{13})^2 & 2B^i_{11}B^i_{13} & 2B^i_{12}B^i_{13} \\ (B^i_{21})^2 & (B^i_{22})^2 & 2B^i_{21}B^i_{22} & (B^i_{23})^2 & 2B^i_{21}B^i_{23} & 2B^i_{22}B^i_{23} \\ B^i_{11}J^i_{21} & B^i_{12}B^i_{22} & B^i_{11}B^i_{22} + B^i_{12}B^i_{21} & B^i_{13}B^i_{23} & B^i_{11}B^i_{23} + B^i_{13}B^i_{21} & B^i_{12}B^i_{23} + B^i_{13}B^i_{22} \\ (B^i_{31})^2 & (B^i_{32})^2 & 2B^i_{31}B^i_{32} & (B^i_{33})^2 & 2B^i_{31}B^i_{33} & 2B^i_{32}B^i_{33} \\ B^i_{11}B^i_{31} & B^i_{12}B^i_{32} & B^i_{11}B^i_{32} + B^i_{12}B^i_{31} & B^i_{13}B^i_{33} & B^i_{11}B^i_{33} + B^i_{13}B^i_{31} & B^i_{12}B^i_{33} + B^i_{13}B^i_{32} \\ B^i_{21}B^i_{31} & B^i_{22}B^i_{32} & B^i_{21}B^i_{32} + B^i_{22}B^i_{31} & B^i_{23}B^i_{33} & B^i_{21}B^i_{33} + B^i_{23}B^i_{31} & B^i_{22}B^i_{33} + B^i_{23}B^i_{32} \end{bmatrix} \tag{A.10}$$

The orthogonal frame $\mathbf{A}^i_m$ is defined using the cross-section frame [47]. In the cross-section frame, the unit vector along the Z-axis of the orthogonal frame $\mathbf{A}^i_m$ is parallel to the third covariant base vector $\mathbf{G}^i_3$, thus the orthogonal frame describes the orientation of the cross-section of the shell. That is, the unit vector $\mathbf{k}^i_s$ along the Z-axis of the cross-section frame is defined as

$$\mathbf{k}^i_s = \frac{\mathbf{G}^i_3}{\left|\mathbf{G}^i_3\right|} \tag{A.11}$$

Two other axes are defined using Gram-Schmidt orthogonalization procedure as follows:

$$\mathbf{j}^i_s = \frac{\mathbf{G}^i_2 - ((\mathbf{G}^i_2)^T\mathbf{k}^i_s)\mathbf{k}^i_s}{\left|\mathbf{G}^i_2 - ((\mathbf{G}^i_2)^T\mathbf{k}^i_s)\mathbf{k}^i_s\right|} \quad \text{and} \quad \mathbf{i}^i_s = \mathbf{j}^i_s \times \mathbf{k}^i_s \tag{A.12}$$

from which, one has

$$\mathbf{A}^i_m = \begin{bmatrix} \mathbf{i}^i_s & \mathbf{j}^i_s & \mathbf{k}^i_s \end{bmatrix} \tag{A.13}$$

Since the orthogonal frame $\mathbf{A}^i_m$ is defined at the reference configuration, the orientation matrix is an identity matrix if the element is initially flat.

Since the six strain components are defined in the middle surface, the bending and twisting deformations of the shell element need to be introduced. To this end, the three curvature components with respect to the orthogonal frame $\mathbf{A}^i_m$ are defined as

$$\mathbf{K}^i_m(x^i, y^i, 0) = (\mathbf{C}^i_m)^{-T}\tilde{\mathbf{K}}^i_m(\mathbf{C}^i_m)^{-1} \equiv \kappa^i_{rs}, \quad r, \mathrm{s} = x, y \tag{A.14}$$

where $\mathbf{C}^i_m$ is a 2 by 2 matrix that can be extracted from the matrix $\mathbf{B}^i_m$ and is defined by $\mathbf{C}^i_m \equiv C^i_{rs} = B^i_{rs}$ for $r, \mathrm{s} = 1, 2$. In the preceding equation, the matrix $\tilde{\mathbf{K}}^i_m$ is defined as

$$\tilde{\mathbf{K}}^i_m = \begin{bmatrix} \tilde{\kappa}^i_{xx} - \tilde{\kappa}^i_{0xx} & \tilde{\kappa}^i_{xy} - \tilde{\kappa}^i_{0xy} \\ \tilde{\kappa}^i_{xy} - \tilde{\kappa}^i_{0xy} & \tilde{\kappa}^i_{yy} - \tilde{\kappa}^i_{0yy} \end{bmatrix} \tag{A.15}$$

where

$$\left.\begin{aligned} &\tilde{\kappa}^i_{xx} = -\left(\frac{\partial}{\partial x^i}\left(\frac{\partial \mathbf{r}^i_m}{\partial z^i}\right)\right)^T \frac{\partial \mathbf{r}^i_m}{\partial x^i}, \qquad \tilde{\kappa}^i_{yy} = -\left(\frac{\partial}{\partial y^i}\left(\frac{\partial \mathbf{r}^i_m}{\partial z^i}\right)\right)^T \frac{\partial \mathbf{r}^i_m}{\partial y^i} \\ &\tilde{\kappa}^i_{xy} = \frac{1}{2}\left(-\left(\frac{\partial}{\partial x^i}\left(\frac{\partial \mathbf{r}^i_m}{\partial z^i}\right)\right)^T \frac{\partial \mathbf{r}^i_m}{\partial y^i} - \left(\frac{\partial}{\partial y^i}\left(\frac{\partial \mathbf{r}^i_m}{\partial z^i}\right)\right)^T \frac{\partial \mathbf{r}^i_m}{\partial x^i}\right) \end{aligned}\right\} \tag{A.16}$$

and

$$\left.\begin{aligned}
&\tilde{\kappa}^{i}_{0xx} = -\left(\frac{\partial}{\partial x^{i}}\left(\frac{\partial \mathbf{X}^{i}_{m}}{\partial z^{i}}\right)\right)^{T}\frac{\partial \mathbf{X}^{i}_{m}}{\partial x^{i}}, \qquad \tilde{\kappa}^{i}_{0yy} = -\left(\frac{\partial}{\partial y^{i}}\left(\frac{\partial \mathbf{X}^{i}_{m}}{\partial z^{i}}\right)\right)^{T}\frac{\partial \mathbf{X}^{i}_{m}}{\partial y^{i}} \\
&\tilde{\kappa}^{i}_{0xy} = \frac{1}{2}\left(-\left(\frac{\partial}{\partial x^{i}}\left(\frac{\partial \mathbf{X}^{i}_{m}}{\partial z^{i}}\right)\right)^{T}\frac{\partial \mathbf{X}^{i}_{m}}{\partial y^{i}} - \left(\frac{\partial}{\partial y^{i}}\left(\frac{\partial \mathbf{X}^{i}_{m}}{\partial z^{i}}\right)\right)^{T}\frac{\partial \mathbf{X}^{i}_{m}}{\partial x^{i}}\right)
\end{aligned}\right\} \tag{A.17}$$

A.3 Locking Remedy

In the shear deformable bi-linear shell element based on continuum mechanics approach, the following lockings are exhibited as discussed in Chapter 2: (1) in-plane normal/shear locking, (2) transverse shear locking, (3) Poisson's thickness locking and (4) curvature thickness locking. In this section, the locking remedy for the shell element based on the elastic middle surface approach is discussed.

A.3.1 In-Plane Normal/Shear Locking

As in the continuum mechanics approach, in-plain normal/shear locking can be alleviated by the enhanced assumed strain (EAS) approach. The compatible in-plane strains in the middle surface $\boldsymbol{\varepsilon}^{ic}_{p}$ obtained by differentiating the assumed global position vector is modified as follows as follows:

$$\boldsymbol{\varepsilon}^{i}_{p} = \boldsymbol{\varepsilon}^{ic}_{p} + \boldsymbol{\varepsilon}^{i\mathrm{EAS}}_{p} \tag{A.18}$$

where $\boldsymbol{\varepsilon}^{i\mathrm{EAS}}_{p}$ is the enhanced assumed strain vector defined by

$$\boldsymbol{\varepsilon}^{i\mathrm{EAS}}_{p}(\boldsymbol{\xi}^{i}) = \mathbf{G}^{i}(\boldsymbol{\xi}^{i})\boldsymbol{\alpha}^{i} \tag{A.19}$$

In the preceding equation $\boldsymbol{\alpha}^{i}$ is the vector of internal parameters that define the assumed strain field of element i and the matrix $\mathbf{G}^{i}(\boldsymbol{\xi}^{i})$ is defined as:

$$\mathbf{G}^{i}(\boldsymbol{\xi}^{i}) = \frac{\left|\mathbf{J}^{i}_{0}\right|}{\left|\mathbf{J}^{i}(\boldsymbol{\xi}^{i})\right|}(\mathbf{T}^{i}_{0mp})^{-T}\mathbf{N}^{i}(\boldsymbol{\xi}^{i}) \tag{A.20}$$

where $\mathbf{J}^{i}(\boldsymbol{\xi}^{i})$ and $\mathbf{J}^{i}_{0}$ are, respectively, the position vector gradient tensor at the reference configuration evaluated at the Gauss integration point $\boldsymbol{\xi}^{i}$ and that evaluated at the center of the element ($\boldsymbol{\xi}^{i} = \mathbf{0}$). $\mathbf{T}^{i}_{0mp}$ is the 3 by 3 transformation matrix defined by the sub-matrix of the 6 by 6 transformation matrix given by Eq. A.10 associated with the in-plane strain vector $\boldsymbol{\varepsilon}_p^i$, and this matrix has to be evaluated at the center of the element [44,54,88]. The explicit form of the transformation matrix is given as follows:

$$\mathbf{T}_{mp0}^i = \begin{bmatrix} (B_{11}^i)^2 & (B_{12}^i)^2 & 2B_{11}^i B_{12}^i \\ (B_{21}^i)^2 & (B_{22}^i)^2 & 2B_{21}^i B_{22}^i \\ B_{11}^i B_{21}^i & B_{12}^i B_{22}^i & B_{11}^i B_{22}^i + B_{12}^i B_{21}^i \end{bmatrix}_{\boldsymbol{\xi}=\mathbf{0}} \tag{A.21}$$

where $B_{rs}^i = (\mathbf{B}_m^i)_{rs} = ((\mathbf{A}_m^i)^T \mathbf{J}_m^i)_{rs}, \quad r,s = 1,2$ as defined by Eq. A.8. The matrix $\mathbf{N}^i(\boldsymbol{\xi}^i)$ consists of polynomial terms of the enhanced strain field in parametric domain. The simplest enhancement which introduces four internal parameters $\boldsymbol{\alpha}^i$ is given as follows:

$$\mathbf{N}^i(\boldsymbol{\xi}^i) = \begin{bmatrix} \xi^i & 0 & 0 & 0 \\ 0 & \eta^i & 0 & 0 \\ 0 & 0 & \xi^i & \eta^i \end{bmatrix} \tag{A.22}$$

The effect of the number of internal parameters on the elastic force accuracy is discussed in literature [54]. It is important to notice here that the matrix $\mathbf{N}^i(\boldsymbol{\xi}^i)$ should fulfill the following condition

$$\int \mathbf{N}^i(\boldsymbol{\xi}^i)\, d\boldsymbol{\xi}^i = \mathbf{0} \tag{A.23}$$

such that the assumed stress vanishes over the reference volume of the element and it passes the patch test [44].

A.3.2 Transverse Shear Locking

The transverse shear locking can be removed by the assumed natural strain (ANS) approach. The covariant strains evaluated at Barlow points where the strain field terms are correct are tied to assumed natural strain interpolation points through the use of Lagrange interpolation. The assumed covariant natural transverse shear strain field can re-expressed as follows:

$$\left.\begin{aligned} \tilde{\gamma}_{xz}^{i\mathrm{ANS}} &= \frac{1}{2}\left(1-\eta^i\right)\tilde{\gamma}_{xz}^{iC} + \frac{1}{2}\left(1+\eta^i\right)\tilde{\gamma}_{xz}^{iD} \\ \tilde{\gamma}_{yz}^{i\mathrm{ANS}} &= \frac{1}{2}\left(1-\xi^i\right)\tilde{\gamma}_{yz}^{iA} + \frac{1}{2}\left(1+\xi^i\right)\tilde{\gamma}_{yz}^{iB} \end{aligned}\right\} \tag{A.24}$$

where $\tilde{\gamma}_{xz}^{iC}$, $\tilde{\gamma}_{xz}^{iD}$, $\tilde{\gamma}_{yz}^{iA}$ and $\tilde{\gamma}_{yz}^{iB}$ are the covariant transverse shear strains at the tying points.

A.3.3 Poisson’s Thickness Locking

Poisson’s thickness locking is not essentially exhibited in case of elastic middle surface approach since in-plane strains and the transverse normal strain are decoupled due to the plane strain assumption. It is known that Poisson’s thickness locking occurs when Poisson ratio has some value, which introduces the coupling of the in-plane strains to the transverse normal strain. For instance, in the case of pure bending, the axial strains due to bending are linearly distributed along the thickness, and it leads to the linearly varying transverse normal strain due to the coupling induced by Poisson’s ratio. However, the use of the linear interpolation along the thickness leads to constant thickness strains which make the element behave overly stiff since the thickness strain does not vanish on the neutral axis. Continuum mechanics-based shear deformable element with EAS allows for incorporating the linearly varying transverse normal strain to alleviate Poisson’s thickness locking effectively as discussed in Section 2.2. On the other hand, due to the plane stress assumption made in the shell element, the in-plane strains and the transverse normal strain are decoupled, thus the Poisson’s thickness locking is not essentially exhibited. This is one of the most economical ways of treating the Poisson´s locking for applications where the plane stress assumption is fulfilled. For thick shell structures with nonlinear material models, this assumption is no longer valid and the continuum mechanics approach needs to be used.

A.3.4 Curvature Thickness Locking

Curvature thickness locking is also exhibited in case of initially curved configuration as the same as continuum mechanics approach. The transverse gradient vectors can be erroneously elongated when the shell element is subjected to bending and twisting deformation. The assumed natural strain (ANS) method is applied, the covariant transverse normal strains at the four nodal points are interpolated by the Lagrange polynomial as follows:

$$\tilde{\varepsilon}_{zz}^{i\mathrm{ANS}} = S_1^{i\mathrm{ANS}}\tilde{\varepsilon}_{zz}^{i1} + S_2^{i\mathrm{ANS}}\tilde{\varepsilon}_{zz}^{i2} + S_3^{i\mathrm{ANS}}\tilde{\varepsilon}_{zz}^{i3} + S_4^{i\mathrm{ANS}}\tilde{\varepsilon}_{zz}^{i4} \qquad \text{(A.25)}$$

where $\tilde{\varepsilon}_{zz}^{k}$ indicates the compatible transverse normal strain at node k and S_k^{ANS} is the shape function associated with it.

A.4 Equation of Motion

Using Eqs. A.9 and A.15, the generalized elastic forces $\mathbf{Q}_k^i$ for the initially curved shell element can be defined using the virtual work as follows:

$$\begin{aligned}\delta W^i &= -h^i \int (\delta \boldsymbol{\varepsilon}_p^i)^T \mathbf{D}_p \boldsymbol{\varepsilon}_p^i \, dA_0^i - h^i \int (\delta \boldsymbol{\gamma}_t^i)^T \mathbf{D}_\gamma \boldsymbol{\gamma}_t^i \, dA_0^i \\ &\quad - h^i \int \delta \varepsilon_{zz}^i E \varepsilon_{zz}^i \, dA_0^i - \int (\delta \boldsymbol{\kappa}^i)^T \mathbf{D}_\kappa \boldsymbol{\kappa}^i \, dA_0^i \\ &= (\delta \mathbf{e}^i)^T \mathbf{Q}_k^i \end{aligned} \qquad (A.26)$$

where A_0^i is the infinitesimal area of element i in the reference configuration and the following engineering strain and curvature vectors are defined:

$$\boldsymbol{\varepsilon}_p^i = [\varepsilon_{xx}^i \quad \varepsilon_{yy}^i \quad 2\varepsilon_{xy}^i]^T, \; \boldsymbol{\gamma}_t^i = [2\varepsilon_{xz}^i \quad 2\varepsilon_{yz}^i]^T, \; \boldsymbol{\kappa}^i = [\kappa_{xx}^i \quad \kappa_{yy}^i \quad 2\kappa_{xy}^i]^T \qquad (A.27)$$

where $\boldsymbol{\varepsilon}_p^i$ represents the vector of the in-plane strains, $\boldsymbol{\gamma}_t^i$ the vector of transverse shear strains and $\boldsymbol{\kappa}^i$ the vector of curvatures. For a linear Hookean material model in plane stress condition with constant shell thickness h, the following matrices of elasticity are defined:

$$\mathbf{D}_p = \frac{E}{1-\nu^2}\begin{bmatrix} 1 & \nu & 0 \\ \nu & 1 & 0 \\ 0 & 0 & (1-\nu)/2 \end{bmatrix}, \; \mathbf{D}_\gamma = \frac{E}{2(1+\nu)}\begin{bmatrix} c_{xz} & 0 \\ 0 & c_{yz} \end{bmatrix}, \; \mathbf{D}_\kappa = \frac{h^3}{12}\mathbf{D}_p \qquad (A.28)$$

where E is Young's modulus; ν Poisson′s ratio; c_{xz} and c_{yz} the transverse shear strain distribution correction factors. The integration is performed over the middle surface of the element and the stress distribution along the thickness of the shell is assumed constant in this model. This assumption can be considered as a reasonable approximation for thin shell structures with linear Hookean material model. It is also important to notice that since the elastic forces are evaluated only in the middle surface, the total number of integration points is less than that of the continuum mechanics based shell element. Several numerical examples of the use of elastic middle surface approach are demonstrated in Section 3.1, showing that element lockings are eliminated by the approaches discussed in this Appendix.

REFERENCES

1. Lugner, P., Pacejka, H. and Plochl, M., 2005, "Recent Advances in Tyre Models and Testing Procedures", *Vehicle System Dynamics*, vol. 43, no. 6-7, pp. 413-436.

2. Pacejka, H. B., 2002, *Tire and Vehicle Dynamics*, Society of Automotive Engineers (SAE), Warrendale, PA.

3. Gruber, P., Sharp, R. S. and Crocombe, A. D., 2012, "Normal and Shear Forces in the Contact Patch of a Braked Racing Tyre. Part 1: Results from a Finite-Element Model", *Vehicle System Dynamics*, vol. 50, pp. 323–337

4. Gruber, P., Sharp, R. S. and Crocombe, A. D., 2012, "Normal and Shear Forces in the Contact Patch of a Braked Racing Tyre. Part 2: development of a physical tyre model", *Vehicle System Dynamics*, vol. 50, pp. 339–356

5. Clark, S. K. (ed.), *Mechanics of Pneumatic Tires*, 1981, US DOT HS805 952 NHTSA.

6. Lee, C.R., Kim, J.W., Hallquist, J.O., Zhang, Y. and Farahani, A.D., 1997, "Validation of a FEA Tire Model for Vehicle Dynamic Analysis and Full Vehicle Real Time Proving Ground Simulations", *SAE Technical Paper 971100*

7. Koishi, M., Kabe, K. and Shiratori, M., 1998, "Tire Cornering Simulation Using an Explicit Finite Element Analysis Code", *Tire Science and Technology*, vol. 26, pp. 109-119

8. Gruber, P., Sharp, R. S. and Crocombe, A. D., 2012, "Shear Forces in the Contact Patch of a Braked Racing Tyre", *Vehicle System Dynamics*, vol. 50, pp. 1761-1778

9. Tanner, J.A., 1996, "Computational Methods for Frictional Contact with Applications to the Space Shuttle Orbiter Nose-Gear Tire", *NASA Technical Report 3573*, pp. 1-52

10. Gipser, M., 2005, "FTire: A Physically Based Application-Oriented Tyre Model for Use with Detailed MBS and Finite-Element Suspension Models", *Vehicle System Dynamics*, vol. 43, pp. 76-91

11. Gallrein, A. and Baecker, M., "CDTire: A Tire Model for Comfort and Durability Applications", *Vehicle System Dynamics*, vol. 45, Supplement, 2007, pp. 69-77

12. Oertel, C. and Fandre, A., 1999, "Ride Comfort Simulations and Step Towards Life Time Calculations: RMOD-K and ADAMS", *Proceedings of International ADAMS conference*, Berlin, Germany

13. Huston, R. L. *Multibody Dynamics*, 1990 (Butterworth Heinemann, Stonham).

14. Roller, M., Betsch, P., Gallrein A. and Linn, J., 2014, "On the Use of Geometrically Exact Shells for Dynamic Tyre Simulation", *Ch. 9 in Multibody Dynamics, Computational Methods in Applied Sciences 35*, Terze, Z., (ed.), pp. 205-236, Springer-Verlag

15. Roller, M., Betsch, P., Gallrein, A. and Linn, J., 2015, "An Enhanced Tire Model for Dynamic Simulation Based on Geometrically Exact Shells", *Proceedings of ECCOMAS Thematic Conference on Multibody Dynamics*, June 29-July 2, Barcelona, Spain

16. Bekker, M. G. 1969, *Introduction to Terrain-Vehicle Systems*, The University of Michigan Press, Ann Arbor.

17. Wong, J. Y. 2008, *Theory of Ground Vehicle. 4th ed.* Hoboken, NJ: John Wiley & Sons.

18. Contreras, U. Li, G., Foster, C.D. Shabana,A.A. Jayakumar, P. and Letherwood, M.D., 2013, “Soil Models and Vehicle System Dynamics”, *Applied Mechanics Reviews*, vol. 65, 040802-1.

19. Xia, K., 2011, “Finite Element Modeling of Tire/Terrain Interaction: Application to Predicting Soil Compaction and Tire Mobility”, *Journal of Terramechanics*, vol. 48, pp.113-123.

20. Shoop S.A., Richmond,P.W., Lacombe, J., 2006, “Overview of Cold Regions Mobility Modeling at CRREL”, *Journal of Terramechanics*, vol. 43, pp. 1-26.

21. Varghese, A.G., Turner, J.L., Way,T.R., Johnson,C.E., Dorfi, H.R., 2012, “Traction prediction of a smooth rigid wheel in soil using coupled Eulerian-Lagrangian analysis”, *Proceedings of 2012 SIMULIA Community Conference*, pp. 1-15.

22. Wasfy, T.M., Wasfy.H.M., Peters, J.M., 2014, “Coupled Multibody Dynamics and Discrete Element Modeling of Vehicle Mobility on Cohesive Granular Terrains”, *Proceedings of the ASME 2014 IDETC & CIE Conference*, Buffalo, DETC2014-35146.

23. Negrut, D.,Serban, R., Mazhar, H., Heyn, T., 2014, “Parallel Computing in Multibody System Dynamics: Why, When and How”, *ASME Journal of Computational and Nonlinear Dynamics,* 9:041007-1.

24. Heyn, T., Anitescu, M., Tasora. A, Negrut, D., 2013, “Using Krylov subspace and spectral methods for solving complementarity problems in many-body contact dynamics simulation”, *International Journal for Numerical Methods in Engineering*, vol. 95, pp. 541-561.

25. Nakashima, H., and Oida, A., 2004, “Algorithm and Implementation of Soil-Tire Contact Analysis Code Based on Dynamic FE-DE Method”, *Journal of Terramechanics*, vol. 41, pp. 127-137.

26. El-Gindy, M., Lescoe, R., Oljer, F., Jojansson, I., Trlvedl, M., 2011, “Soil Modeling Using FEA and SPH Techniques for a Tire-Soil Interaction”, *Proceedings of the ASME 2011 IDETC & CIE Conference*, Washington, DETC2011-47104

27. Belytschko, T., Liu, W.K., Moran, B., 2000, *Nonlinear Finite Elements for Continua and Structures*, Wiley

28. Shabana, A. A., *Dynamics of Multibody Systems*, 2005, Cambridge University Press, New York.

29. Gerstmayr, J., Sugiyama, H. and Mikkola, A., 2013, "Review on the Absolute Nodal Coordinate Formulation for Large Deformation Analysis of Multibody Systems", *ASME Journal of Computational and Nonlinear Dynamics*, vol. 8, pp. 031016-1-12.

30. Mikkola, A. M. and Shabana, A. A., 2003, "A Non-Incremental Finite Element Procedure for the Analysis of Large Deformation of Plates and Shells in Mechanical System Applications", *Multibody System Dynamics*, vol. 9, pp.283-309.

31. Sugiyama, H. and Suda, Y., 2009, "Nonlinear Elastic Ring Tire Model Using the Absolute Nodal Coordinate Formulation", *IMechE Journal of Multi-Body Dynamics*, vol. 223, pp. 211-219

32. Yamashita, H., Matsutani, Y. and Sugiyama, H., 2015, "Longitudinal Tire Dynamics Model for Transient Braking Analysis: ANCF-LuGre Tire Model", *ASME Journal of Computational and Nonlinear Dynamics*, vol. 10, pp. 031003-1-11

33. Mikkola, A.M.; Matikainen, M.K., 2006, "Development of Elastic Forces for a Large Deformation Plate Element Based on the Absolute Nodal Coordinate Formulation". *ASME Journal of Computational and Nonlinear Dynamics*, vol. 1, pp. 103-108, 2006

34. Dmitrochenko, O. and Pogorelov, D. Y., 2003, "Generalization of Plate Finite Elements for Absolute Nodal Coordinate Formulation", *Multibody System Dynamics*, vol. 10, pp. 17-43

35. Dufva, K., and Shabana, A. A., 2005, "Analysis of Thin Plate Structures Using The Absolute Nodal Coordinate Formulation", *IMechE Journal of Multi-body Dynamics*, vol. 219, pp. 345-355.

36. Schwab, A. L., Gerstmayr, J., and Meijaard, J. P., 2007, "Comparison of Three-Dimensional Flexible Thin Plate Elements for Multibody Dynamic Analysis: Finite Element Formulation and Absolute Nodal Coordinate Formulation", *Proceedings of the ASME 2007 International Design Engineering Technical Conferences & Computers and Information in Engineering Conference*, Las Vegas, Nevada, USA

37. Nachbagauer, K., Gruber, P., and Gerestmayr, J., 2013, "Structural and Continuum Mechanics Approaches for a 3D shear Deformable ANCF Beam Finite Element: Application to Static and Linearized Dynamic Examples", *ASME Journal of Computational and Nonlinear Dynamics*, vol. 8, pp.021004-1-7

38. Dmitrochenko, O., Matikainen, M., and Mikkola, A., 2012, "The Simplest 3- and 4-Noded Fully Parameterized ANCF Plate Elements", *Proceedings of the ASME 2012 International Design Engineering Technical Conferences & Computers and Information in Engineering Conference*, Chicago, IL, USA

39. Hauptmann, R., Doll, S., Harnau, M., Schweizerhof, K., 1998, "A Systematic Development of 'Solid-Shell' Element Formulations for Linear and Non-Linear Analyses Employing Only Displacement Degrees of Freedom", *International Journal for Numerical Methods in Engineering*, vol. 42, pp. 49–69

40. Hauptmann, R., Doll, S., Harnau, M., Schweizerhof, K., 2001, "Solid-Shell Elements with Linear and Quadratic Shape Functions at Large Deformations with Nearly Incompressible Materials", *Computers & Structures*, vol. 79, pp. 1671-1685

41. Vu-Quoc, L., and Tan, X. G., 2003, "Optimal Solid Shells for Non-Linear Analyses of Multilayer Composites I. Statics", *Computer Methods in Applied Mechanics and Engineering*, vol. 192, pp. 975-1016

42. Vu-Quoc, L., and Tan, X.G., 2003, "Optimal Solid Shells for Non-Linear Analyses of Multilayer Composites. II. Dynamics", *Computer Methods in Applied Mechanics and Engineering*, vol. 192, pp. 1017-1059

43. Tan, X.G., and Vu-Quoc, L., 2005, "Efficient and Accurate Multilayer Solid-Shell Element: Nonlinear Materials at Finite Strain", *International Journal for Numerical Methods in Engineering*, vol. 63, pp. 2124-2170

44. Simo, J. C., and Rifai, M. S. and Fox, D.D., 1990, "On a Stress Resultant Geometrically Exact Shell Model. Part IV: Variable Thickness Shells with Through-the-Thickness Stretching", *International Journal for Numerical Methods in Engineering*, vol. 81, pp. 91-126

45. Betsch, P., and Stein, E., 1995, "An Assumed Strain Approach Avoiding Artificial Thickness Straining for A Non-Linear 4-Node Shell Element", *Communications in Numerical Methods in Engineering*, vol. 11, pp. 899-909

46. Betsch, P., and Stein, E., 1996, "A Nonlinear Extensible 4-Node Shell Element Based on Continuum Theory and Assumed Strain Interpolations", *Journal of Nonlinear Science*, vol. 6, pp. 169-199

47. Sugiyama, H., Escalona, J. L. and Shabana, A. A., 2003, "Formulation of Three-Dimensional Joint Constraints Using the Absolute Nodal Coordinates", *Nonlinear Dynamics*, vol. 31, pp. 167-195

48. Sugiyama, H. and Yamashita, H., 2011, "Spatial Joint Constraints for the Absolute Nodal Coordinate Formulation using the Non-Generalized Intermediate Coordinates", *Multibody System Dynamics*, vol. 26, pp. 15-36

49. Yamashita, H., Valkeapää, A., Jayakumar, P., Sugiyama, H. and 2015, "Continuum Mechanics Based Bilinear Shear Deformable Shell Element Using Absolute Nodal Coordinate Formulation", *ASME Journal of Computational and Nonlinear Dynamics*, vol. 10, 051012-1-9.

50. Ahmad, S., Irons, B. M., Zienkiewicz O. C., 1970, “Analysis of Thick and Thin Shell Structures by Curved Finite Elements”. *International Journal for Numerical Methods in Engineering*. vol. 2, pp. 419–451

51. Shabana, A. A., Mikkola, A. M., 2003, “On the Use of the Degenerate Plate and the Absolute Nodal Coordinate Formulations in Multibody System Applications”, *Journal of Sound and Vibration*. vol. 259, pp. 481–489.

52. Sze, K. Y., 2002, “Three-Dimensional Continuum Finite Element Models for Plate/Shell Analysis”, *Progress in Structural Engineering and Materials*, vol. 4, pp. 400-407

53. Mostafa, M., Sivaselvan, M. V. and Felippa, C. A., 2013, “A Solid-Shell Corotational Element Based on ANDES, ANS and EAS for Geometrically Nonlinear Structural Analysis”, *International Journal for Numerical Methods in Engineering*, vol. 95, pp. 145-180

54. Andelfinger, U., and Ramm, E., 1993, “EAS-Elements for Two-Dimensional, Three-Dimensional, Plate and Shell Structures and Their Equivalence to HR-Elements”, *International Journal for Numerical Methods in Engineering*, vol. 36, pp. 1311-1337

55. Dvorkin, E. N., and Bathe, K. J., 1984, “A Continuum Mechanics Based Four-Node Shell Element for General Non-Linear Analysis”, *Engineering Computations*, vol. 1, pp. 77-88

56. Bathe, K. J. and Dvorkin, E. N., 1986, “A Formulation of General Shell Elements - The Use of Mixed Interpolation of Tensorial Components”, *International Journal for Numerical Methods in Engineering*, vol. 22, pp. 697-722

57. Bischoff, M., Ramm, E., 1997, “Shear Deformable Shell Elements for Large Strains and Rotations”, *International Journal for Numerical Methods in Engineering*, vol. 40, pp. 4427-4449

58. Cook, R. D., Malkus, D. S., Plesha, M. E., and Witt, R. J., 2002, *Concepts and Applications of Finite Element Analysis Fourth Edition*, Wiley

59. Bonet, J., and Wood, D. R., 1997, *Nonlinear Continuum Mechanics for Finite Element Analysis*, Cambridge University Press

60. Jones, R. M., 1999, *Mechanics of Composite Materials*, Taylor and Francis

61. Noor, A.K. and Burton, W.S., 1989, "Assessment of Shear Deformation Theories for Multilayered Composite Plates", *Applied Mechanics Review*, vol. 42, pp. 1-13

62. Noor, A.K. and Burton, W.S., 1990, "Assessment of Computational Models for Multilayered Composite Shells", *Applied Mechanics Review*, vol. 43, pp. 67-97

63. Bathe, K.J., *Finite Element Procedures*, 1996, Prentice Hall

64. Stander, N., Matzenmiller, A., Ramm, E, 1988, “An Assessment of Assumed Strain Methods in Finite Rotation Shell Analysis”, *Engineering Computations*, vol. 6, pp.58-66

65. Matikainen, M.K., Valkeapää, A. I., Mikkola, A. M., and Schwab, A. L., 2013, “A Study of Moderately Thick Quadrilateral Plate Elements Based on the Absolute Nodal Coordinate Formulation”, *Multibody System Dynamics*, pp. 1–30

66. Yamashita, H., Jayakumar, P., Sugiyama, H., 2016, “Physics-Based Flexible Tire Model Integrated With LuGre Tire Friction For Transient Braking and Cornering Analysis”, *ASME Journal of Computational and Nonlinear Dynamics*, vol. 11, 031017-1-17

67. Hilber, H. M., Hughes, T. J. R., and Taylor, R. L., 1977, "Improved Numerical Dissipation for Time Integration Algorithms in Structural Dynamics", *Earthquake Engineering and Structural Dynamic*, vol. 5, pp. 265–284

68. Canudas-de-Wit, C., Tsiotras, P., Velenis, E., Basset, M. and Gissinger, G., 2003, "Dynamic Friction Models for Road/Tire Longitudinal Interaction", *Vehicle System Dynamics*, vol. 39, pp. 189-226.

69. Deur, J., Asgari, J., Hrovat, D., 2004, "A 3D Brush-Type Dynamic Tire Friction Model", *Vehicle System Dynamics*, vol. 42, pp. 133-173

70. Rajapakshe, M. P., Gunaratne, M., and Kaw, A. K., 2010, "Evaluation of LuGre Tire Friction Model with Measured Data on Multiple Pavement Surfaces", *Tire Science and Technology*, vol. 38, pp. 213-227

71. Deur, J., Ivanović, V., Troulis, M., Miano, C., Hrovat, D. and Asgari, J., 2005, "Extensions of the LuGre Tyre Friction Model Related to Variable Slip Speed along the Contact Patch Length", *Vehicle System Dynamics*, vol. 43, pp. 508-524

72. Deur, J., Ivanović, V., Pavković, D., Hrovat, D., Asgari, J., Troulis, M. and Miano, C., 2005, "Experimental Analysis and Modelling of Longitudinal Tyre Friction Dynamics for Abrupt Transients", *Vehicle System Dynamics*, vol. 43, pp. 525-539

73. Simo, J. C., and Rifai, M. S., 1990, “A Class of Mixed Assumed Strain Methods and The Method of Incompatible Modes”, *International Journal for Numerical Methods in Engineering*, vol. 29, pp. 1595-1638

74. Olshevskiy, A., Dmitrochenko, O., Kim, C.W., 2014,”Three-Dimensional Solid Brick Element Using Slopes in the Absolute Nodal Coordinate Formulation”, *ASME Journal of Computational and Nonlinear Dynamics*. vol. 9, pp. 021001

75. Wilson, E. L., Taylor, R. L., Doherty, W. P. Ghabussi, T., 1973, “Incompatible Displacement Models”, *Numerical and Computer Methods in Structural Mechanics*, pp. 43-57

76. Naghdi, P. M., 1990, "A Critical Review of the State of Finite Plasticity", *Journal of Applied Mathematics and Physics (ZAMP)*, vol. 41, pp. 315-394

77. Lee, E. H. and Liu, D. T., 1967, "Finite Strain Elastic-Plastic Theory Particularly for Plane Wave Analysis", *Journal of Applied Physics*, vol. 38, pp. 19-27

78. Simo, J. C., 1988, "A Framework for Finite Strain Elastoplasticity Based on Maximum Plastic Dissipation and the Multiplicative Decomposition: Part I Continuum Formulation", *Computer Methods in Applied Mechanics and Engineering*, vol. 66, pp. 199-219

79. de Souza Neto, E. A., Peric, D. and Owen, D. R. J., 2008, *Computational Methods for Plasticity: Theory and Applications*, Wiley

80. Simo, J. C., 1992, "Algorithms for Static and Dynamic Multiplicative Plasticity That Preserve the Classical Return Mapping Schemes of the Infinitesimal Theory", *Computer Methods in Applied Mechanics and Engineering*, vol. 99, pp. 61-112.

81. Nagtegaal, J. C. and De Jong, J. E., 1982, "Some Aspects of Non-Isotropic Work Hardening in Finite Strain Plasticity", *Plasticity of Metal at Finite Strain*, Stanford University Press, pp. 65-102

82. Nemat-Nasser, S., 1982, "On Finite Deformation Elasto-Plasticity", *International Journal of Solids and Structures*, vol. 18, pp. 857-872

83. Nagtegaal, J. C., 1982, "On the Implementation of Inelastic Constitutive Equations with Special Reference to Large Deformation Problems", *Computer Methods in Applied Mechanics and Engineering*, vol. 33, pp. 469-484

84. Simo, J. C. and Hughes, T. J. R., 1998, *Computational Inelasticity*, Springer

85. Crisfield, M. A., 1996, *Non-Linear Finite Element Analysis of Solids and Structures, Volume 2*, Wiley

86. Shoop, S. A. 2001, “Finite Element Modeling of Tire-Terrain Interaction”, ERDC/CRREL TR-01-16, US. Army Corps of Engineers, Engineer Research and Development Center

87. Valkeapää, A., Yamashita, H., Jayakumar, P. and Sugiyama, H., 2015, "On the Use of Elastic Middle Surface Approach in the Large Deformation Analysis of Moderately Thick Shell Structures using Absolute Nodal Coordinate Formulation", *Nonlinear Dynamics*, vol. 80, pp. 1133-1146

88. Simo, J. C. and Armero, F., 1992, “Geometrically Non-Linear Enhanced Strain Mixed Methods and the Method of Incompatible Modes.” *International Journal for Numerical Methods in Engineering*. vol. 33, pp. 1413–1449.

89. Helwany, S., 2007, *Applied Soil Mechanics with ABAQUS Applications*, John Wiley and Sons, New York.

90. Wasfy, M. T., Jayakumar, P., Mechergui, D. and Sanikommu, S., 2016, “Prediction of Vehicle Mobility on Large-Scale Soft-Soil Terrain Maps Using Physics-Based Simulation”, *Proceeding to 2016 NDIA Ground Vehicle Systems Engineering and Technology Symposium*.